ECHELLE SPECTROSCOPY OF THE CENTRAL STARS OF PLANETARY NEBULAE

Thesis by

James K. McCarthy

In Partial Fulfillment of the Requirements

for the Degree of

Doctor of Philosophy

California Institute of Technology

Pasadena, California

1988

(Submitted May 17, 1988)

Acknowledgement

One does not carry out a project such as this single-handedly; in my particular case, it was accomplished with a great deal of really superb help from a large number of people. Below I shall attempt to thank most of them, but owing to space limitations, time limitations, and the pressures of trying to finish on time (well, a year after "on time," to be honest) I am certain I shall overlook many individuals who contributed their time and talents to this project or in many ways contributed to my enjoyment of the years spent working on it. They know who they are, and I am grateful.

It is a pleasure to acknowledge the guidance I received from Dr. Jeremy Mould, my advisor, throughout my graduate student years. From the selection of a scientific subject, through fund raising for the instrument, data reduction and analysis, and up to the last issue of interpretation of the results, Jeremy's interest, suggestions, and patience have been most appreciated. He also played very significant roles in arranging for my visit to Munich — a key element in the successful completion of the work described herein — as well as in my efforts to secure and decide upon a post-doctoral position.

Regarding the P60 echelle spectrograph phase of this project, credit for many of the design concepts must be shared with Dr. Stephen Shectman, who in some important areas "paved the way" with the Las Campanas echelle. Although our collaboration was sporadic at times, I always found working with Shec an incredible learning experience owing to his wealth of really creative instrument design ideas. In very much the same way, the summer I spent at JPL working for Mr. James Janesick on CCDs was very profitable; not only is Jim one of (if not *the*) scientific community's foremost CCD gurus, but he's also one of the nicest "bosses" for whom I've ever had the pleasure to work. Thanks also to Tom Elliott and Taher Daud for

many intriguing conversations regarding the properties of these very wonderful — and often mysterious and surprising — CCD devices.

Caltech faculty members Drs. J. Beverly Oke and Judith Cohen were always there to answer instrument design questions. Bev's experience with instruments at Palomar and echellette modification to the P60 and Digital Spectrographs played an important role in getting this project off the ground, and Judy's investment of time and energy into the Palomar 60-inch telescope are in large part responsible for much of what can currently be done with that telescope, a CCD camera, and a MicroVAX — the echelle spectrograph included.

But when it comes to direct, hands-on assistance with the P60 echelle spectrograph, a great deal of credit and my most heartfelt thanks go to Mr. Gaston Araya, who spent many hours of machine work fabricating most of the mechanical components of the instrument. Frequently this was accomplished faster than I could draw the designs of these components, but still Gaston maintained a careful attention to detail; as a result he was often able to point out details which had escaped me or otherwise resulted in errors in the drawings I gave him. The fact that he wouldn't settle for accuracy which was within tolerance and "good enough" but instead would strive to make everything "right on" made subsequent assembly of his handiwork much simpler indeed.

What wrinkles remained to be ironed out once the instrument was built and the funds exhausted were seldom a problem for the very capable engineering staff of Palomar Observatory. My thanks for assistance above and beyond the call of duty go to Messrs. Earle Emery and Mike Carr, who helped me turn an assembled instrument into a working one. The fact that Earle was willing to take charge of the CCD9 Dewar design and Mike the spectrograph mounting stand (and later the T.V. guider redesign) allowed me to work on other problems during that hectic period

when the instrument was making monthly trips back and forth to Palomar.

The Palomar electronics engineering staff, Messrs. Fred Harris, David Levy, and Greg van Idsinga, are also to be commended for their many valued contributions to the P60 echelle spectrograph project. Fred's CCD Dewar electronics and Dave's stepping motor electronics for the rotating slit wheel were both exactly what was called for, and Greg assembled much of these electronics flawlessly as far as I have been able to tell.

Operations at Palomar with the echelle spectrograph went smoother thanks to the technical contributions of Messrs. Dave Tennant, Mike Doyle, John Henning, and many others, under the very experienced direction of mountain superintendent Mr. Bob Thickston. I have no doubt at all that I shall be leaving the instrument in quite capable hands. Special thanks go to each of the night assistants, not only for their help in obtaining echelle spectra but also for the hours of interesting conversation and their having put up with my eclectic choice of music and radio programs: Jeff Phinney, Skip Staples, Jean Mueller, Juan Carrasco, Russ Day, and all the rest have done outstanding jobs.

The dedication with which Messrs. Larry Blakeé and Bill Qualls have attempted to keep up with my observing schedule — especially back in the days when it never seemed like the instrument was going to be ready in time — is really appreciated, and a great deal of the rough going early on with the echelle was smoothed over as a result of their efforts, patience, and sense of humor. Hopefully this dedication hasn't come at the expense of Larry's health or Bill's being able to enjoy his retirement; best wishes go out to both of them, on the job and more importantly off the job. It is also a pleasure to acknowledge the fine work of Dr. Bob Brucato, Ms. Lilo Hauck, and Ms. Ann Palfreyman in regards to Palomar administration.

The painstaking work reducing Palomar data was much easier than it might

otherwise have been thanks to the well thought out organizational structures upon which Dr. Keith Shortridge based the FIGARO data reduction system. Even though Keith's home in Australia prevented much close collaboration with the particular problems of echelle data reduction, his skills and high standards, which are obvious from the software he left behind here on DEIMOS, were an inspiration for solving those problems. I'm sure I speak for many when I say that we are grateful for the amount of FIGARO support he has continued to give us from the land of Oz. Closer to home, Chris Lee and Tim Pearson are due a tremendous amount of credit for their OBSERVING and PGPLOT packages, respectively, not to mention the countless hours they spent trying to make the computer tasks of the rest of us easier.

I would like to thank Dr. Rolf Kudritzki and his colleagues at the Universität Sternwarte München for their hospitality during my two-month visit, and hope in the not-too-distant future to visit them again. I continue to be impressed by the quality of science that goes on at their Institute. When and if I do make a second visit, I'll bring with me rectified data plotted to scale in hardcopy form, in the hope of being able to concentrate more on science and less on computer software than was possible the first time. Drs. Roberto Mendez and Dirk Husfeld are to be acknowledged for their continuing interest in my work and ever informative BITNET messages. Best wishes to friends Martin Roth and Talat Saygah as they earn their astronomische doktorande.

Scientifically, I've learned much during my years at Caltech not only from Jeremy Mould but also from Drs. Jesse Greenstein, Bev Oke, Wal Sargent, Ann Boesgaard, and in the last few weeks from conversations with Colin Masson. Due to the Caltech Astronomy Department's great depths of knowledge and experience, "much" never seems like enough, however. Not to be overlooked, though, are the countless intriguing, lively and enjoyable discussions with less senior

folk: especially fellow classmates Pawan Kumar, Mary Barsony, and Fernando Selman; prior optical astronomy students Don Schneider, Abi Saha, Alex Filippenko, Mike Rich, Rick Edelson, and Alain Porter; post-docs past and present Dave Tytler, Jules Halpern, Neill Reid, and Jim Schombert; and among the many newer students Kent Budge, Ming Sheng Han, Deborah Padgett, Alain Picard, Josh Roth, Chuck Steidel, and others. Meanwhile, our scientific pursuits here have been made much more pleasant by Ms. Helen Knudsen and the effort she puts into the Astronomy Library and the computerized literature search programs, as well as by numerous other thankless tasks performed all in a day's work by Ms. Margaret Katz, Jill King, and Marilynne Rice, for which I am grateful.

Throughout my years at Caltech I have been fortunate enough to have close friends with whom to share interests outside of astronomy; thanks go to Judi and Zack, Grace, Lise, Laura and Jeff, Mary Ann, Gerry, Bill, Linda, Nanilee, Roy and Sharon, Roz and Steve, and Randi and Jerry for extending to me their friendship in spite of long periods of absence when the research was all-encompassing. Hopefully we will continue to stay in touch. The members of my family, and my parents in particular, have likewise been very supportive and tolerant during those long months, and throughout my academic training. I am also appreciative of the very pleasant surroundings Don and Traute have afforded me these last four years in Altadena, along with the opportunity to earn a "simultaneous degree in horticulture."

Finally, I would like to acknowledge the financial support of a National Science Foundation Graduate Fellowship during the period 1982–1985, the large gift of an anonymous donor to the P60 echelle spectrograph project, a matching amount from the Virginia Steele Scott Fund, the further support that project received from a Caltech President's Fund award, and finally the travel funds from Commission 38 of the I.A.U. which made possible my visit to Munich, West Germany.

Abstract

Presented in this work are the results of a spectroscopic study of the central stars of planetary nebulae (CSPN) conducted at high resolution. From detailed comparisons of their photospheric absorption line profiles observed at high signal-to-noise with the NLTE model atmosphere line profiles of Kudritzki, et al., in Munich, West Germany, the photospheric effective temperatures (T_{eff}), surface gravities (g), and helium abundances (y) were derived. Placement of the CSPN in the distance-independent log(g) – log(T_{eff}) diagram allowed central star masses and evolutionary ages to be deduced via comparisons with published evolutionary model calculations. Spectroscopic distances to the CSPN were estimated from the best fit model fluxes, leading to dynamical expansion ages for the surrounding nebulae which were typically much greater than the corresponding CSPN evolutionary ages. Two possible reasons for this timescale disagreement were quantitatively investigated: (1) the nebulae could have experienced a phase of rapid photo-ionization of material ejected while the stars were still on the AGB, or (2) the AGB – CSPN evolutionary transition times could have been increased by small additional amounts of residual envelope material remaining after the superwind mass loss phase.

An important preliminary phase of this project was the design and construction of a CCD echelle spectrograph for the Palomar 1.5 m telescope. The spectrograph was designed to cover the wavelength range 3200 Å to 7000 Å, utilizing 57 diffracted orders from the echelle grating. Fused quartz prism cross-dispersing elements and an all-transmitting camera lens system contribute to the extremely high throughput of the instrument; the combined telescope and echelle spectrograph efficiency is approximately 20% from above the atmosphere. Details of the echelle spectrograph optical and mechanical designs are presented.

The scientific objectives of the CSPN study with this new instrument required a

thorough investigation into the data reduction process for CCD echelle spectra, and a set of Fortran subroutines were written for this purpose as part of the FIGARO data reduction package. The philosophy and algorithms employed in these routines are discussed, and a detailed description of each of the commands is provided in an Appendix for future reference.

Table of Contents

To Mom & Dad

"Bows and flows of angel hair
And ice cream castles in the air
And feather canyons everywhere
I've looked at clouds that way ...

"But now they only block the sun
They rain and snow on everyone
So many things I would have done
But clouds got in my way ..."

– Joni Mitchell, "Both Sides Now"

I. Introduction

Planetary nebulae (PN) are among the most beautiful objects in the night sky: faint "clouds" of nebulosity often dumbbell or hourglass shaped, but more commonly taking the form of spherical shells. At their center is a faint blue star, from which the nebulae originated and from which they currently receive the ionizing radiation that powers their nebulous emission. The study of these central stars is the objective of this work, a study which has historically been hampered by the bright emission lines from the "clouds in the way."

A. Scientific Motivation

The central stars of planetary nebulae (CSPN) are an important class of object because they constitute an evolutionary link between the asymptotic giant branch (AGB) and white dwarf stages of stellar evolution. The nebula is a very short lived phenomenon, lasting up to 30,000 years, and so the central stars are at a well defined "instant" of their evolution. They present a unique opportunity to glimpse the results of mass loss on the AGB and to study separately envelope and core material for what was once the same AGB star. Eventually the former will dissipate and enrich the inter-stellar medium, and the latter will cool, be restructured by gravitational settling, and finally join the ranks of the white dwarf stars.

Recently these later stages of stellar evolution have been the focus of much theoretical work (e.g., Iben and Renzini, 1983), and computer models have been developed which trace the evolution of a hypothetical star through the planetary nebula phase (Schönberner, 1979; Wood and Faulkner, 1986). The models make definite predictions of central star mass, radius, temperature, and surface composition for each set of initial conditions selected. Observationally, the need now exists to determine, to the extent possible, the evolutionary status of a sample of CSPN

in order to compare their distribution with these theoretical evolutionary models. Such comparisons will play a vital role in refining the theories and extending our understanding of the physical processes responsible for AGB evolution, the formation of planetary nebulae, and the ancestry of the white dwarfs.

B. CSPN as Progeny of AGB Stars

It was first suggested by Shklovskiĭ (1956) that the planetary nebulae were the offspring of some types of red giant stars. A few years earlier, Aller (1954) had postulated an evolutionary link between planetary nebulae and certain symbiotic stars. These initial speculations were later confirmed and strengthened by Abell and Goldreich (1966), although it was not clear to these authors how then to explain the horizontal branch (HB) stars. They suggested the possibility that *"stars evolve through a giant phase at least twice,"* the first time starting from the main sequence and the second time starting from the horizontal branch, and that planetary nebulae are the end result of the second giant phase. The evolution of a horizontal branch star through this second giant phase was subsequently demonstrated by Paczynski and Ziolkowski (1968), and it would later come to be known as the Asymptotic Giant Branch (AGB) phase.

The complete details of the transition from AGB star to planetary nebula are still not understood, although an important piece of this puzzle has been the realization that AGB evolution ends in a phase with very strong mass loss, at a rate $\dot{M}$ up to 10^{-4} solar masses per year ($M_\odot$/yr; see Knapp, et al., 1982; Knapp, 1985). The mechanism thought to be responsible for this "superwind" mass loss is radiation pressure acting on dust which condenses out of the outer atmosphere when gaseous material is carried to large radii by Mira-like pulsations (Wood, 1979). As the star evolves up the AGB and its luminosity reaches the point where these pulsations begin, the pulsation period is relatively short (anywhere from 150 to

600 days for "classical" Mira variables) and the mass loss rates are of the order $\dot{M} \sim 10^{-7} M_{\odot}/yr$. With increasing luminosity, however, the classical Miras are believed to evolve (see Bedijn, 1986) into objects known as OH/IR Mira variables, which have periods up to 2000 days and mass loss rates up to $\dot{M} \sim 10^{-4}$ $M_{\odot}/yr$.

These OH/IR Mira variables are part of a general class of OH/IR stars (Schutz, et al., 1976) so obscured by circumstellar material that they are invisible at optical wavelengths but are seen as infrared (IR) sources (first detected by the Caltech 2.2μm survey; see Neugebauer, et al., 1965). Furthermore, this circumstellar material is the origin of strong 1612 MHz OH maser emission (Wilson and Barrett, 1968). A small number of non-variable OH/IR stars have cooler envelopes (see the IRAS two-color diagram of Olnon, et al., 1984) than either the classical Miras or the OH/IR Miras, which together form a continuous sequence in the IRAS two-color diagram. This sequence is interpreted as clear evidence of an increasing mass loss rate as classical Miras evolve into variable OH/IR stars (see Baud and Habing, 1983). Based on the cooler envelopes for the non-variable OH/IR stars and their departure from the mass loss sequence common to the Miras and variable OH/IR stars, Bedijn (1987) has concluded that the non-variable OH/IR stars have ceased losing mass by this Mira pulsation mechanism, thereby stopping the influx of warm stellar material into the expanding circumstellar shell (now a proto-planetary nebula), allowing it to cool. Van der Veen, et al. (1987), cite the drop in OH/IR star envelope mass below a critical amount as a possible explanation for the cessation of Mira pulsations and mass loss.

A dynamical model for the development of a planetary nebula from the interaction of a fast, hot, low density CSPN wind with material ejected by an earlier slow, cool, high density AGB star wind has been proposed by Kwok, et al. (1978), and later extended by Kwok (1983). With this model as a starting point, Balick (1987) and Balick, et al. (1987), have attempted to explain the variety of morpholo-

gies found among the planetary nebulae by the interaction of the CSPN and AGB winds with relaxed constraints on spherical symmetry. More rigorous calculations for individual nebulae have been performed by Phillips and Reay (1977), Kahn and West (1985), and Masson (1988), among others. Lastly, Chu, et al. (1984), have presented data showing an increase in expansion velocity with increasing nebular radius, as the interacting stellar winds model predicts.

C. CSPN as Ancestors of White Dwarfs

There has been a suspected evolutionary link between the central stars of planetary nebulae and the white dwarf stars for a long time. Schatzman (1958), however, argued against such a hypothesis in favor of direct formation of the white dwarfs, while Greenstein (1960) supported the idea that CSPN do in fact evolve into white dwarfs. The latter position was strengthened by *both* the theoretical work of Hayashi, et al. (1962), in which evolutionary tracks for CSPN were found to have a constant luminosity, increasing temperature phase followed by a constant radius and degenerate cooling phase leading to the white dwarfs, *and* the observational work of O'Dell (1963) which calculated, on the basis of Zanstra temperatures and distance estimates for a sample of known nebulae, a PN birthrate that was able to account for a large fraction of the known white dwarfs.

More recently debate has focused on the problem of explaining the wide variety of spectral types found among the white dwarfs (see Greenstein, 1960) on the basis of their pre-white dwarf evolution. According to Sion and Liebert (1977), the ratio of DA (hydrogen atmosphere) to DB (helium atmosphere) white dwarf stars is between 3:1 and 4:1 at temperatures above 12,000 K, while for temperatures between 5500 K and 8000 K the non-DA types dominate by a ratio of 5:3 (Wehrse and Liebert, 1980). Liebert (1979) interprets this as evidence of convective mixing in the cool ($T_{eff} \leq$ 12,000 K) white dwarf atmospheres, as predicted by Baglin and Vauclair (1973) and

Koester (1976). The consensus is thus that the cool non-DA stars are comprised by a mixture of hotter non-DA stars which have cooled *plus* hotter DA stars which have cooled and undergone convective mixing (Liebert, 1979; see also Greenstein, 1986).

However, this still leaves unsettled the question of whether the hot DA and non-DA stars have separate origins. Since most types of CSPN show hydrogen lines in their spectra, is there a process by which hot non-DA stars can evolve from stars of type DA ? Vauclair and Reisse (1977) have shown that the time required by diffusion for He to gravitationally settle out of a mixed H/He atmosphere is very short compared to evolutionary timescales. Convective mixing of a hot white dwarf hydrogen atmosphere with helium from a deeper layer seems ruled out by the same studies which predicted mixing at cooler temperatures (Baglin and Vauclair, 1973; Koester, 1976). Accretion of material from the interstellar medium cannot play an important role, since this fresh material would contain more H than He (although Michaud and Fontaine (1979) have postulated that ionized white dwarf coronae could selectively inhibit the accretion of hydrogen; see also Strittmatter and Wickramasinghe, 1971).

The role which CSPN-like stellar winds might play in removing the hydrogen atmosphere from a hot DA predecessor to produce a hot DB white dwarf has not been quantitatively investigated. It is interesting to note that the only type of CSPN which do not as a rule exhibit strong hydrogen lines in their spectra are the WC class (Aller, 1968; Heap, 1977a,b; see especially Mendez, et al., 1986); the dominant feature of this class are the strong P-Cygni line profiles of CII, CIII, CIV, OIII, OIV, OV, OVI, HeI, and HeII, indicative of stellar winds having terminal velocities up to 3000 km/s and mass loss rates of between 10^{-9} and 10^{-7} $M_{\odot}$/year (Cerruti-Sola and Perinotto, 1985).

From theoretical models of the pulsating DA white dwarfs known as ZZ Ceti stars, Winget and Fontaine (1982) have been able to determine that the mass of the hydrogen envelope on the surface of these stars is indeed quite small, between 10^{-10} and 10^{-8} of the mass of the star. Since it is generally accepted that all DA white dwarfs pulsate as they cool through the ZZ Ceti instability strip, this hydrogen envelope mass likely applies to DA white dwarfs in general. Therefore it seems that only a very fine line (namely, the removal of the last $\leq 10^{-8}$ $M_\odot$ of hydrogen from the envelope) separates the evolutionary paths leading to DA or non-DA white dwarfs. Note in this context the work of Koester, et al. (1979), and Oke, et al. (1984), who report nearly identical mean masses for DA and DB white dwarfs of 0.58 ± 0.10 $M_\odot$ and 0.55 ± 0.10 $M_\odot$, respectively. Thus a large difference in progenitor core mass does not appear to be an explanation able to account for the difference between the DA and DB white dwarf types.

Iben (1984) has proposed that it is possible for a CSPN to return to the AGB as a consequence of a late helium shell flash, and suggests that these "born-again" CSPN occur frequently enough to account for the observed fraction of non-DA white dwarfs. The evolutionary models of Wood and Faulkner (1986) likewise return to the AGB under conditions of a late helium shell flash. But Wood and Faulkner also reported that they were unable to evolve a 2 $M_\odot$ AGB star beyond a core mass of 0.89 $M_\odot$, since at this point its luminosity at the base of the hydrogen layer exceeded the Eddington limit. On this basis they suggested that such massive stars would lose all of their hydrogen envelope by a radiation pressure driven stellar wind, and consequently evolve through the CSPN phase into DB white dwarfs. However, as was pointed out above, there does not seem to be any observational evidence supporting a large mass difference between the DA and DB white dwarfs.

D. CSPN as Ionizing Sources of Planetary Nebulae

The fact that stars in this brief phase of evolution between the AGB and the white dwarf stages are surrounded by a planetary nebula has made it possible for quite some time to infer their stellar properties indirectly by studying the nebular emission. Zanstra temperatures, Stoy temperatures, Shklovskiĭ distances, and even evolutionary ages inferred from the nebular radii and expansion velocities, are all attempts to use nebular information to reveal parameters of interest for understanding the central stars. But each of these techniques is therefore subject to the added uncertainties, which are often very large, regarding the properties of the nebula (e.g., its dust content, optical depth, ionized mass, etc.). In this section many of these *indirect* methods will be reviewed, although the driving motivation for the current study is to further the application of techniques which permit the CSPN to be observed *directly*, independent (or more accurately, *in spite of*) the emission from the surrounding planetary nebula.

The Zanstra method (Zanstra, 1931) determines the effective temperature of the central star by relating the Hβ flux of the nebula to the number of hydrogen recombinations per second in the nebular volume, under the assumption that this number equals the number of hydrogen ionizing photons ($\lambda \leq 911$ Å) emitted per second by the CSPN. The ratio of this number of Hβ photons to the stellar flux at some visible wavelength is a distance-independent function of the star's effective temperature and flux distribution; the latter was assumed by Zanstra to be a blackbody, and therefore an estimate of the effective temperature (here denoted $T_Z(H)$) could be derived. In a similar manner it is possible to define a Zanstra temperature based on the ionization and recombination of HeII (here denoted $T_Z(He^+)$).

There are, however, several possible pitfalls in this approach. First of all there is the assumption that the number of recombinations is in fact equal to the number of

ionizing photons emitted by the star. Any dust grains present in the nebular volume will absorb ionizing photons and re-emit this energy in the infrared, or similarly the assumption could fail due to the nebula being optically thin shortward of the ionization edge and allowing some of the ionizing photons to escape without ionizing a hydrogen atom. This second possibility is typically thought to be the reason why $T_Z(H) > T_Z(He^+)$; the nebula is less likely to be optically thin shortward of the HeII ionization edge ($\lambda \leq 228$ Å). A third possibility is that the central star might not be the only source of ionizing photons; some CSPN show evidence of a hot (300,000 K) stellar wind, the radiation from which could add a significant ultraviolet (UV) flux to that radiated by the star itself, thereby increasing the number of ionizations occuring in the nebula (Adam and Köppen, 1985).

Another second potentially flawed assumption of the Zanstra method is that the stellar flux distribution is identical to that of a blackbody spectrum. Although most workers measuring Zanstra temperatures continue to assume a blackbody spectrum (see e.g., Kaler, 1983, and Hummer, 1983, for two recent examples) in preference to a more realistic model atmosphere flux distribution, there is often a substantial difference between the two. This is especially true in the ionizing ultraviolet region of the spectrum, where typically the model atmospheres emit more ionizing photons than does a blackbody with the same effective temperature. Using non-LTE (hereafter NLTE) model atmospheres with luminosities close to the Eddington limit, Husfeld, et al. (1984), suggest that the large "Zanstra discrepancy" (i.e., $T_Z(H) \ll T_Z(He^+)$) often derived for PN with Of-type central stars can be explained on the basis of a HeII emission edge at $\lambda = 228$ Å in such models. Similarly, Henry and Shipman (1986, 1987) find that pure hydrogen model atmospheres, analogous to those developed for DA white dwarfs, emit sufficiently more UV photons relative to blackbodies that more typical Zanstra discrepancies can in most cases be explained on this basis alone.

Third and finally, the Zanstra method relies on a measurement of the stellar continuum flux in the visible, which is often difficult to obtain via photoelectric photometry through large apertures due to contamination from the nebular emission lines. This is especially true in cases where the nebula is of high surface brightness and the star is faint, a combination one would expect for stars of the highest temperatures (Renzini, 1983). Kaler (1987) has investigated the problems caused by nebular contamination in some detail, and recently Shaw and Kaler (1985, 1988) have attempted to correct their photometry of CSPN for a nebular contribution predicted on the basis of the measured Hβ flux of the nebula. Except for the most compact high surface brightness nebulae, CCD photometry through filters selected to avoid the brightest nebular emission lines (e.g., Walton, et al., 1986) is a much preferred solution, however.

The Stoy method of deriving central star temperatures (Stoy, 1933) avoids this last difficulty; in fact, it is not even necessary to detect the central star at all in order to derive a Stoy temperature. Also known as the "energy balance method," the Stoy technique considers the excess energy of the ionizing photons (i.e., the difference between the actual photon energy and the 13.6 eV required to ionize an atom of hydrogen), which after ionization is translated into the kinetic energy of the ionized electron and so is a major contributor to the heating of the nebula. Since the nebula cools primarily as a result of escaping radiation following the collisional excitation of heavy elements, the cooling rate can be determined by observing as many collisionally excited lines as possible in the nebular spectrum. The central star temperature then follows from the requirement that the heating and cooling rates be equal for thermal equilibrium; the integrated excess energy of all stellar ionizing photons is a function of the effective temperature of the star and the assumed stellar ultraviolet energy distribution.

Most of the objections raised above in the discussion of the Zanstra method

also pose problems for the determination of accurate Stoy temperatures, apart from the need for a stellar magnitude. Preite-Martinez and Pottasch (1983) have derived temperatures by the energy balance method for a large sample of planetary nebulae central stars, and although they assumed that CSPN radiate as blackbodies, they parametrized their observational constraint upon the temperature — the ratio of collisionally excited heavy element line fluxes to the Hβ line flux — in such a way that model atmosphere Stoy temperatures could be derived for comparison purposes as well. These authors also found that the model atmosphere Stoy temperatures were lower for any given object, since as pointed out above the model ultraviolet fluxes are greater than those of a blackbody at the same effective temperature.

Direct measurements of the "color temperature" of the central stars of planetary nebulae are possible, in principle, from the observed shape of the continuum energy distribution. Unfortunately, this approach is difficult in practice; the slope of the stellar continuum in the visible (as indicated by the B–V color, for instance) is no longer sensitive to temperature at such high temperature, reflecting only the λ^{-1} slope of the Rayleigh-Jeans tail of the stellar energy distribution. Above the earth's atmosphere, however, ultraviolet continuum measurements with the IUE satellite have in a few cases enabled CSPN color temperatures to be determined (Heap, 1981). The amount of correction to apply for interstellar reddening is the primary source of uncertainty in this approach.

Finally, perhaps the most direct method of all is to obtain the central star spectrum at sufficiently high resolution to reveal stellar line profiles, which yield a temperature estimate in a straightforward manner from the HeI vs. HeII ionization equilibrium, if lines of both species are present and can be measured (Aller, 1968; Mendez, et al., 1981). The details of this method will be more fully discussed below; here it need only be noted that this approach is *completely independent* of the properties of the surrounding nebula, the distance to the object, the extinction

law along the line of sight or its variations, and even the exact nature of the far ultraviolet energy distribution and its departures from a blackbody. It only depends on the reliability of the model atmosphere calculation of line strengths, and in this respect different models seem to agree quite well with each other in the few cases where the models overlap in the available surface gravity – effective temperature ($\log(g) - \log(T_{eff})$) parameter space (see Section III of Wesemael, et al., 1980).

E. Stellar Evolution During the CSPN Phase

In order to study the evolutionary status of the central stars of planetary nebulae, a temperature measurement alone is insufficient, however. To place the central stars in the HR diagram, one needs a luminosity estimate as well. Several workers have attempted to obtain values for the luminosities of CSPN, but are seriously hampered by the lack of accurate distances to most objects in addition to the aforementioned difficulties with CSPN photometry. Only in a few cases where the CSPN has a main sequence companion whose distance is known from its spectroscopic parallax, or when the nebula is a member of a cluster with a known distance, can CSPN distances be determined to better than a factor of two.

The distances to most PN are derived by statistical methods whose calibration is based on the handful of more accurate distances available. One such method that has found widespread use is the Shklovskiĭ method (Shklovskiĭ, 1956; or see Chapter V of Pottasch, 1984), in which it is assumed that the ejected masses of all PN have the same value, usually taken to be 0.2 $M_{\odot}$. Measurements of the PN Hβ flux and angular radius can then be used to calculate the actual nebular radius in linear units, from which a distance estimate follows directly. But once again optical depth effects play an important role, since crucial to the application of the Shklovskiĭ method is the assumption that all of the 0.2 $M_{\odot}$ of material surrounding the central star is ionized. If the nebula is ionization bounded rather than density

bounded, the ionized mass could be substantially less than 0.2 $M_{\odot}$, leading to an overestimate of the distance.

The HR diagram derived by Kaler (1983) and reproduced as Figure 1-1 is based on Zanstra temperatures and Shklovskiĭ distances. The error bars, while large, are indicative only of the errors inherent in the observational data and do not include allowances for systematic errors. From the discussion above, there is ample reason to suspect these might be large as well.

Schönberner (1981) has attempted to study the evolutionary status of the central stars of planetary nebulae by comparing them to evolutionary tracks in the $\log(M_V)$ – $\log(t)$ plane. To derive an absolute magnitude M_V, he first measures the apparent visual magnitude V and, based on a distance estimate, converts it to M_V. Then to calculate the ages t of the CSPN, he first measures the angular radius of the nebula and, again based on a distance estimate, converts it to a linear radius. By assuming a constant expansion velocity, this linear radius can finally be converted into an age. His results are reproduced as Figure 1-2, and in addition to the uncertainties pointed out above regarding both the existing magnitude and distance estimates required, the comparison to evolutionary tracks also involves an arbitrary zero point for the time axis, which Schönberner takes to be the point at which the T_{eff} of the central star first reaches 5,000 K and thus begins to move rapidly away from the AGB. This well defined *evolutionary* time in the post-AGB evolution is arbitrarily assumed to coincide with zero nebular radius (i.e., with $t = 0$ in the *dynamical* sense of PN expansion) when the evolutionary model tracks are superimposed upon the data. The fact that the horizontal axis is plotted as $\log(t)$ suggests that the significance of this arbitrary zero point is not widely appreciated.

Lastly, there is the worrisome assumption of a single constant expansion velocity for all nebulae over their entire history; note that the error bar in the corner

of Schönberner's diagram (Figure 1-2 here) is an error in log(t), and so this error would become larger linearly with time were the data plotted on a linear time axis rather than a logarithmic one. The mass distribution that Schönberner derives, in which almost all CSPN are confined between 0.55 and 0.65 $M_{\odot}$, is considerably narrower than the mass distribution of the white dwarfs (Weidemann, 1984).

Once again, there does exist a more direct approach to the study of the evolutionary status of the central stars of planetary nebulae, based on a comparison of their line profiles to model atmospheres. With a temperature from the HeI vs. HeII ionization equilibrium determined, the width of the hydrogen line wings is then a function of surface gravity. CSPN analyzed in this way (Mendez, et al., 1981, 1983, 1985; Kudritzki, 1987; Mendez, et al., 1988) can therefore be located in the log(g) – log(T_{eff}) plane and compared to evolutionary tracks for a variety of stellar masses. Note again that such a technique is completely independent of the distance to each object and the properties of the surrounding nebula (e.g., expansion velocity, ejection timescale, ionized mass, optical depth, dust, etc.). The details of this approach will be discussed below.

F. Objectives of This Work

Because knowledge of the physical nature of the central stars of planetary nebulae is crucial to our understanding of late stages of stellar evolution, the primary objective of this work is the NLTE model atmosphere analysis of high resolution CSPN spectra. This approach has the important advantage over all others of being a *distance-independent* means of determining stellar effective temperatures and surface gravities. It will therefore allow the placement of the central stars in the log(g) – log(T_{eff}) diagram and the determination of their evolutionary status independent of any assumptions about the properties of the surrounding nebulae. As a result of comparing the CSPN locations to evolutionary tracks through the log(g)

– $\log(T_{eff})$ plane, distance- and nebula-independent masses and evolutionary ages can be derived also. The masses of CSPN are most important for establishing the link between the CSPN and the white dwarf stars, while the ages are important for understanding more about the planetary nebula phase itself. Both are important in the context of post-AGB evolution.

Secondary objectives will be to determine stellar radii and model fluxes from which nebula-independent estimates of the distance can be computed. The nebular radii and ionized masses can then be derived on the basis of these distance determinations, and the evolutionary status of the nebulae compared to that of the central stars. Finally, it is hoped that as a result of such a comparison, it will be possible to comment on the poorly understood transition from the tip of the AGB to the planetary nebula phase of stellar evolution.

Previous work on the NLTE model atmosphere analysis of CSPN by Mendez and by Kudritzki and their collaborators in Munich has included only the brightest CSPN accessible from the European Southern Observatory (ESO) in Chile. In order to complement their work with northern hemisphere CSPN spectra taken from Palomar Observatory *and* in an attempt to overcome the possible selection effects which might arise from selection criteria based only upon apparent magnitude, the recent set of distance determinations by Daub (1982) was examined as part of this study in order to define a distance limited statistical sample.

Daub presents distances for 299 planetary nebulae based on a variation of the Shklovskiĭ method, using 5 GHz radio fluxes to overcome the errors which arise from interstellar extinction and absorption within the nebulae themselves. Figure 1-3 shows the number of PN interior to a sphere of radius d as a function of d, as compared to a d^2 distribution. The scale height of PN locally is roughly 125 pc (Cahn and Kaler, 1971; Daub, 1982); for larger values of d the number of PN can

be expected to increase as d^2 if the sample is complete. From this figure one can conclude that the Daub sample is complete out to a distance of nearly 1.5 kpc.

Conservatively adopting 1.3 kpc as a cutoff distance, one finds that there are 94 planetaries in Daub's sample with $d \leq 1.3$ kpc. Of these, 64 are in the sky accessible from Palomar. Tables 1-1 through 1-3 contain this sample of 64 CSPN broken down by apparent magnitude, while Table 1-4 contains those southern PN with declinations less than -25 degrees. Note that as many as 90% of the 64 CSPN listed in Tables 1-1 through 1-3 are bright enough to be observed spectroscopically, given sufficient observing time at Palomar.

In order to be better able to carry out this and other observing projects requiring high resolution, high signal-to-noise ratio spectra from Palomar Observatory, this CSPN study began with the design and construction of an echelle spectrograph for the Palomar sixty-inch (1.5m) telescope. This major undertaking will be described in Chapter **II**, and the data reduction software which was written specifically for this new instrument will be described in Chapter **III**. The use of this instrument and data reduction software to pursue the above scientific objectives pertaining to the central stars of planetary nebulae will be returned to in Chapter **IV**. What work yet remains to be done will be the subject of the concluding Chapter **V**.

TABLE 1-1

Central Stars of Planetary Nebulae (Acker, et al., 1982) with B < 14
Distances by Daub (1982) less than 1.3 kpc

Number (1)	Name (2)	l(II) (3)	b(II) (4)	R.A. 1985.0 (5)	Decl. (6)	P.N. Dia. (7)	U (8)	B (9)	V (10)	R (11)	Spectrum (12)	Dist(kpc) (13)
2	NGC 40	120 + 9 1		0 12 11.3	72 26 20	> 37 "	11.1	11.8	11.8	0.0	WC8	1.070
8	NGC 246	118 - 74 1		0 46 20.9	-11 57 35	250 "	10.4	11.6	12.0	11.9	OIV+K	0.460
21	NGC 1360	220 - 53 1		3 32 36.0	-25 55 10	390 "	9.7	11.0	11.3	11.8	sd O	0.257
28	NGC 1514	165 - 15 1		4 8 20.3	30 44 14	>114 "	9.9	10.0	9.4	0.0	AIII+sdO	0.671
43	IC 418	215 - 24 1		5 26 46.6	-12 42 31	12 "	7.9	9.2	9.4	0.0	O7f,WC7	0.412
51	IC 2149	166 + 10 1		5 55 17.1	46 6 11	> 8 "	10.0	11.0	11.0	0.0	O7 fp	1.120
74	NGC 2346	215 + 3 1		7 8 36.7	0 46 54	> 54 "	11.3	11.1	11.3	0.0	A5 V	1.300
81	NGC 2392	197 + 17 1		7 28 17.5	20 56 36	> 13 "	9.1	10.2	10.5	0.0	O7 f	1.220
86	VV 1-7	235 + 1 1		7 40 34.0	-18 57 30	250 "	9.8	8.2	8.4	8.2	A-0 IV	0.575
127	NGC 3242	261 + 32 1		10 24 2.7	-18 34 4	> 15 "	10.5	11.8	12.0	0.0	Cont. ?	0.730
145	NGC 4361	294 + 43 1		12 23 44.1	-18 42 10	> 45 "	11.7	13.0	13.4	0.0	O6	0.908
148	A 35	303 + 40 1		12 52 44.9	-22 47 30	800 "	10.8	10.5	9.6	10.4	G8III+sd	0.207
156	A 36	318 + 41 1		13 39 52.4	-19 48 10	293 "	10.0	11.4	11.6	12.0	sd O7	0.312
216	NGC 6210	43 + 37 1		16 43 51.7	23 49 38	> 16 "	10.1	10.5	9.9	0.0	O7f,WC7	1.190
296	NGC 6572	34 + 11 1		18 11 22.5	6 50 58	8 "	10.3	10.2	9.1	0.0	Of+WR	0.474
279	NGC 6543	96 + 29 1		17 58 33.6	66 38 1	> 18 "	10.1	11.3	11.1	0.0	O7f+WR	0.640
308	NGC 6629	9 - 5 1		18 24 48.7	-23 12 32	> 15 "	11.9	12.8	12.3	0.0	O	1.180
330	Hu 2-1	51 + 9 1		18 49 9.4	20 49 39	3 "	11.3	12.6	12.6	0.0	Of+WN b	1.180
350	M 1-67	50 + 3 1		19 10 50.8	16 50 0	82 "	12.1	12.2	11.1	0.0	WR-N8	0.836
366	NGC 6790	37 - 6 1		19 22 11.0	1 29 6	7 "	12.9	13.6	13.5	0.0	Cont.	1.130
376	VV 503	64 + 5 1		19 34 9.9	30 28 59	8 "	9.1	10.1	9.9	0.0	WC 9	0.733
381	NGC 6818	25 - 17 1		19 43 7.3	-14 11 19	> 17 "	11.8	13.0	13.1	0.0	Cont.	1.290
383	NGC 6826	83 + 12 1		19 44 23.8	50 29 18	> 10 "	9.0	10.2	10.5	0.0	O6 fp	1.080
387	NGC 6833	82 + 11 1		19 49 20.8	48 55 22	0 s	12.8	13.9	14.0	0.0	Cont.?	1.160
393	NGC 6853	60 - 3 1		20 0 0.0	0 0 0	0 *	0.0	13.7	0.0	0.0	*****	0.217
405	IC 4997	58 - 10 1		20 19 27.1	16 41 6	2 "	0.0	12.3	11.9	0.0	WC10+Of	1.210
417	NGC 7008	93 + 5 2		21 0 6.4	54 28 56	83 "	12.9	13.7	13.6	0.0	O7	0.793

TABLE 1-1 (Continued)

Number (1)	Name (2)	l(II) (3)	b(II) (4)	R.A. 1985.0 (5)	Decl. (6)	P.N. Dia. (7)	U (8)	B (9)	V (10)	R (11)	Spectrum (12)	Dist(kpc) (13)
419	NGC 7009	37	- 34 1	21 3 21.8	-11 25 33	> 24 "	9.6	11.0	11.5	0.0	Cont.	0.759
421	NGC 7027	84	- 3 1	21 6 27.9	42 10 32	15 "	0.0	12.0	0.0	0.0	---	0.178
441	NGC 7293	36	- 57 1	22 28 49.4	-20 54 55	>770 "	11.8	13.1	13.4	13.7	---	0.150
451	NGC 7662	106	- 17 1	23 25 10.4	42 27 9	> 20 "	11.7	12.7	11.7	0.0	Cont.	0.837

TABLE 1-2

Central Stars of Planetary Nebulae (Acker, et al., 1982) with 14 < B < 17
Distances by Daub (1982) less than 1.3 kpc

Number (1)	Name (2)	l(II) (3)	b(II) (4)	R.A. 1985.0 (5)	Decl. (6)	P.N. Dia. (7)	U (8)	B (9)	V (10)	R (11)	Spectrum (12)	Dist(kpc) (13)
11	NGC 650	130 -	10 1	1 41 24.4	51 29 35	< 65 "	0.0	15.9	16.3	0.0	Cont.	0.974
26	NGC 1501	144 +	6 1	4 5 42.9	60 52 40	52 "	14.3	15.1	14.5	0.0	WC6,OVI	1.100
38	A 7	215 -	30 1	5 2 27.3	-15 37 27	770 "	13.9	15.2	15.4	16.7	DA,sdO	0.207
70	K 1-8	223 -	2 1	7 2 34.7	-10 33 41	80 "	0.0	16.8	0.0	15.9	---	1.160
87	NGC 2438	231 +	4 2	7 41 9.9	-14 41 53	> 66 "	0.0	15.1	15.0	0.0	Cont.	1.170
88	NGC 2440	234 +	2 1	7 41 15.2	-18 10 24	> 14 "	0.0	15.2	14.0	0.0	Cont.	1.010
93	A 24	217 +	14 1	7 50 51.4	3 2 47	>229 "	15.8	16.9	17.2	18.4	---	0.487
118	A 33	238 +	34 1	9 38 24.9	-2 44 35	268 "	14.3	15.4	15.5	15.4	sd Op	0.695
135	NGC 3587	148 +	57 1	11 13 54.6	55 5 54	194 "	14.2	15.5	15.7	0.0	---	0.572
243	NGC 6369	2 +	5 1	17 28 25.8	-23 44 52	> 29 "	16.2	16.5	14.7	0.0	WR+OVI	0.422
253	Hb 4	3 +	2 1	17 40 57.4	-24 41 35	6 "	15.6	16.2	14.9	0.0	---	1.300
271	Hb 6	7 +	1 1	17 54 13.0	-21 44 31	6 "	16.0	16.4	14.7	0.0	Cont.	1.100
288	M 1-40	8 -	1 1	18 7 30.9	-22 17 3	5 "	0.0	16.6	15.6	0.0	---	1.060
333	NGC 6720	63 +	13 1	18 53 2.2	33 0 31	> 70 "	13.0	14.3	14.7	0.0	Cont.	0.790
334	IC 1295	25 -	4 2	18 53 47.3	-8 51 0	> 86 "	0.0	15.0	0.0	17.5	---	1.080
340	NGC 6741	33 -	2 1	19 1 50.0	0 28 8	6 "	0.0	16.0	14.7	0.0	---	1.250
363	NGC 6781	41 -	2 1	19 17 44.5	6 30 37	>109 "	15.1	15.9	14.9	0.0	---	0.671
373	NGC 6804	45 -	4 1	19 30 52.6	9 11 42	> 31 "	13.5	14.3	14.0	0.0	O9	1.160
384	A 65	17 -	21 1	19 45 38.8	-23 10 10	104 "	15.0	16.0	15.9	15.7	Opk	1.210
388	NGC 6842	65 +	0 1	19 54 27.5	29 14 51	50 "	14.6	15.5	16.0	0.0	---	1.280
399	NGC 6884	82 +	7 1	20 9 55.2	46 24 59	6 "	0.0	15.8	15.7	0.0	WNb	1.120
420	NGC 7026	89 +	0 1	21 5 47.5	47 47 30	21 "	0.0	14.6	14.2	0.0	WC7+OVI	1.270
431	IC 5117	89 -	5 1	21 31 56.7	44 31 48	3 "	14.0	14.7	13.9	0.0	WR	1.000
445	NGC 7354	107 +	2 1	22 39 44.5	61 12 15	> 20 "	0.0	16.1	15.0	0.0	Cont.	0.881

TABLE 1-3

Central Stars of Planetary Nebulae (Acker, et al., 1982) with B > 17
Distances by Daub (1982) less than 1.3 kpc

Number (1)	Name (2)	l(II) (3)	b(II) (4)	R.A. 1985.0 (5)	Decl. (6)	P.N. Dia. (7)	U (8)	B (9)	V (10)	R (11)	Spectrum (12)	Dist(kpc) (13)
58	A 13	204 - 8 1		6 3 58.8	3 56 51	154 "	19.0	20.1	19.9	18.8	---	0.957
69	K 2-2	221 - 4 1		6 51 40.8	9 58 56	414 "	0.0	18.2	0.0	20.0	---	0.452
144	K 2-4	275 + 72 1		12 17 32.6	11 8 7	690 "	0.0	17.7	0.0	17.7	---	0.237
266	NGC 6445	8 + 3 1		17 48 21.8	-20 0 20	> 33 "	0.0	19.1	0.0	0.0	Cont.	1.230
284	NGC 6537	10 + 0 1		18 4 19.9	-19 50 20	> 9 "	0.0	0.0	19.5	0.0	---	0.652
355	NGC 6772	33 - 6 1		19 13 50.2	-2 43 56	> 62 "	0.0	18.4	0.0	0.0	---	1.200
389	A 66	19 - 23 1		19 56 38.7	-12 39 4	250 "	16.9	17.7	17.4	18.5	---	0.577
424	NGC 7048	88 - 1 1		21 13 42.9	46 13 34	61 "	0.0	18.3	0.0	0.0	---	1.180

TABLE 1-4

Central Stars of Planetary Nebulae (Acker, et al., 1982) with Decl. < -25
Distances by Daub (1982) less than 1.3 kpc

Number (1)	Name (2)	l(II) (3)	b(II) (4)	R.A. 1985.0 (5)	Decl. (6)	P.N. Dia. (7)	U (8)	B (9)	V (10)	R (11)	Spectrum (12)	Dist(kpc) (13)
117	NGC 2867	278 - 5 1		9 21 0.2	-58 14 56	17 "	12.9	13.2	13.8	0.0	WC 3,OVI	1.220
119	IC 2501	281 - 5 1		9 38 21.5	-60 1 23	< 25 "	0.0	0.0	14.0	0.0	---	0.832
124	NGC 3132	272 + 12 1		10 6 23.7	-40 21 45	> 56 "	10.3	10.0	10.1	0.0	A2V+sd O	1.030
133	IC 2621	291 - 4 1		10 59 45.1	-65 10 5	5 "	12.9	14.1	13.6	0.0	---	1.190
140	NGC 3918	294 + 4 1		11 49 34.1	-57 5 51	16 "	9.4	10.8	10.8	0.0	---	0.583
154	NGC 5189	307 - 3 1		13 32 38.0	-65 53 52	140 "	13.4	14.1	14.4	0.0	WC2,OVI	0.511
160	NGC 5315	309 - 4 2		13 52 49.8	-66 26 27	5 "	10.9	12.0	11.3	0.0	WC 4 ?	0.694
171	He 2-115	321 + 2 1		15 4 9.7	-55 7 40	< 5 "	17.3	17.1	16.0	0.0	---	1.230
172	He 2-117	321 + 2 2		15 4 51.5	-55 55 44	< 5 "	19.0	17.4	17.7	0.0	---	0.987
175	NGC 5882	327 + 10 1		15 15 48.5	-45 35 37	14 "	11.5	11.7	12.2	0.0	Cont.	0.920
183	He 2-131	315 - 13 1		15 35 35.8	-71 51 57	6 "	9.7	10.3	10.6	0.0	O7.5fep	0.909
184	He 2-133	324 - 1 1		15 40 46.3	-56 33 55	< 10 "	16.0	14.2	12.8	0.0	B9III	1.090
188	Sp 1	329 + 2 1		15 50 33.7	-51 28 43	72 "	13.5	14.3	13.9	0.0	Cont.?	1.160
200	NGC 6072	342 + 10 1		16 11 59.5	-36 11 23	> 40 "	0.0	17.5	17.5	0.0	---	1.160
203	Mz 3	331 - 1 1		16 16 4.4	-51 57 5	25 "	13.3	13.3	14.1	0.0	B0	0.854
224	IC 4637	345 + 0 1		17 4 5.9	-40 51 45	14 "	12.2	12.8	12.3	0.0	Cont.?	1.030
233	NGC 6302	349 + 1 1		17 12 43.3	-37 5 5	44 "	0.0	0.0	0.0	0.0	O VI	0.399
257	Tc 1	345 - 8 1		17 44 28.6	-46 5 1	9 "	9.9	11.1	11.1	0.0	P Cyg	0.586
260	M 1-26	358 - 0 2		17 44 59.7	-30 11 51	4 "	12.4	13.0	12.1	0.0	P Cyg	0.866
264	Hb 5	359 - 0 1		17 46 59.0	-29 59 36	20 "	0.0	0.0	0.0	0.0	Cont.	0.845
462	NGC 2899	277 - 3 1		0 0 0.0	0 0 0	120	0.0	0.0	0.0	0.0	---	0.860
465	NGC 3699	292 + 1 1		0 0 0.0	0 0 0	68	0.0	0.0	0.0	0.0	---	1.270
468	NGC 6153	341 + 5 1		0 0 0.0	0 0 0	25	0.0	0.0	0.0	0.0	---	0.960
469	NGC 6164	336 - 0 1		0 0 0.0	0 0 0	370	0.0	0.0	0.0	0.0	---	0.223
522	K 3-17	39 + 2 1		0 0 0.0	0 0 0	19	0.0	0.0	0.0	0.0	---	0.940
550	M 3-39	358 + 5 1		0 0 0.0	0 0 0	20	0.0	0.0	0.0	0.0	---	1.220
564	Sh 2-71	36 - 1 1		0 0 0.0	0 0 0	155	0.0	0.0	0.0	0.0	---	0.744

TABLE 1-4 (Continued)

Number (1)	Name (2)	l(II) (3)	b(II) (4)	R.A. 1985.0 (5)	Decl. (6)	P.N. Dia. (7)	U (8)	B (9)	V (10)	R (11)	Spectrum (12)	Dist(kpc) (13)
565	Sh 2-266	195	- 0 1	0 0 0.0	0 0 0	80	0.0	0.0	0.0	0.0	---	0.971
567	VV 1-4	197	- 2 1	0 0 0.0	0 0 0	130	0.0	0.0	0.0	0.0	---	0.619
568	VV 1-5	196	- 1 1	0 0 0.0	0 0 0	310	0.0	0.0	0.0	0.0	---	0.326
569	YM 29	205	+ 14 1	0 0 0.0	0 0 0	615	0.0	0.0	0.0	0.0	---	0.247

Bibliography

Abell, G.O., and Goldreich, P., 1966. *Pub. Astron. Soc. Pac.*, v. **78**, p. 232.

Adam, J., and Köppen, J., 1985. *Astron. Astrophys.*, v. **142**, p. 461.

Aller, L.H., 1954. *Pub. Dominion Astrophys. Obs.*, v. **9**, p. 321.

Aller, L.H., 1968. In *I.A.U. Symp. No. 34, Planetary Nebulae*, eds. D.E. Osterbrock and C.R. O'Dell (Dordrecht: Reidel), p. 339.

Baglin, A., and Vauclair, G., 1973. *Astron. Astrophys.*, v. **27**, p. 307.

Balick, B., 1987. *A. J.*, v. **94**, p. 671.

Balick, B., Preston, H.L., and Icke, V., 1987. *A. J.*, v. **94**, p. 1641.

Baud, B., and Habing, H.J., 1983. *Astron. Astrophys.*, v. **127**, p. 73.

Bedijn, P.J., 1986. In *1st IRAS Conf., Light on Dark Matter*, ed. F.P. Israel (Dordrecht: Reidel), p. 119.

Bedijn, P.J., 1987. *Astron. Astrophys.*, v. **186**, p. 136.

Cahn, J.H., and Kaler, J.B., 1971. *Ap. J. Suppl. Ser.*, v. **22**, p. 319.

Cerruti-Sola, M., and Perinotto, M., 1985. *Ap. J.*, v. **291**, p. 237.

Chu, Y.H., Kwitter, K.B., Jacoby, G.H., and Kaler, J.B., 1984. *Pub. Astron. Soc. Pac.*, v. **96**, p. 598.

Daub, C.T., 1982. *Ap. J.*, v. **260**, p. 612.

Greenstein, J.L., 1960. In *Stars and Stellar Systems, v.* **6**, *Stellar Atmospheres*, ed. J.L. Greenstein (Chicago: Univ. Chicago Press), p. 676.

Greenstein, J.L., 1986. *Ap. J.*, v. **304**, p. 334.

Hayashi, C., Hoshi, R., and Sugimoto, D., 1962. *Prog. Theor. Phys. Osaka, Suppl. Ser.*, n. 22.

Heap, S.R., 1977a. *Ap. J.*, v. **215**, p. 609.

————, 1977b. *Ap. J.*, v. **215**, p. 864.

————, 1981. In *NASA Conf. Publ. 2171, The Universe at Ultraviolet Wavelengths*, p. 415.

Henry, R.B., and Shipman, H.L., 1986. *Ap. J.*, v. **311**, p. 774.

————, 1987. In *I.A.U. Symp. No. 131, Planetary Nebulae*, ed. S. Torres-Peimbert, in press.

Hummer, D.G., 1983. In *I.A.U. Symp. No. 103, Planetary Nebulae*, ed. D.R. Flower (Dordrecht: Reidel), p. 211.

Husfeld, D., Kudritzki, R.P., Simon, K.P., and Clegg, R.E.S., 1984. *Astron. Astrophys.*, v. **134**, p. 139.

Iben, I., and Renzini, A., 1983. *Ann. Rev. Astron. Astrophys.*, v. **21**, p. 271.

Iben, I., 1984. *Ap. J.*, v. **277**, p. 333.

Kahn, F.D., and West, K.A., 1985. *MNRAS*, v. **212**, p. 837.

Kaler, J.B., 1983. *Ap. J.*, v. **271**, p. 188.

————, 1987. In *I.A.U. Symp. No. 131, Planetary Nebulae*, ed. S. Torres-Peimbert, in press.

Knapp, G.R., Phillips, T.G., Leighton, R.B., Lo, K.Y., and Wannier, P.G., 1982. *Ap. J.*, v. **252**, p. 616.

Knapp, G.R., 1985. *Ap. J.*, v. **293**, p. 273.

Koester, D., 1976. *Astron. Astrophys.*, v. **52**, p. 415.

Koester, D., Shulz, H., and Weidemann, V., 1979. *Astron. Astrophys.*, v. **76**, p. 232.

Kudritzki, R.P., 1987. In *I.A.U. Symp. No. 131, Planetary Nebulae*, ed. S. Torres-Peimbert, in press.

Kwok, S., Purton, C.R., and FitzGerald, P.M., 1978. *Ap. J. (Letters)*, v. **219**, p. L125.

Kwok, S., 1983. *Ap. J.*, v. **258**, p. 280.

Liebert, J., 1979. In *I.A.U. Colloq. No. 53, White Dwarfs and Variable Degenerate Stars,* eds. H.M. Van Horn and V. Weidemann (New York: Univ. Rochester Press), p. 146.

Masson, C.R., 1988. Preprint.

Mendez, R.H., Kudritzki, R.P., Gruschinske, J., and Simon, K.P., 1981. *Astron. Astrophys.*, v. **101**, p. 323.

Mendez, R.H., Kudritzki, R.P., and Simon, K.P., 1983. In *I.A.U. Symp. No. 103, Planetary Nebulae,* ed. D.R. Flower (Dordrecht: Reidel), p. 343.

Mendez, R.H., Kudritzki, R.P., and Simon, K.P., 1985. *Astron. Astrophys.*, v. **142**, p. 289.

Mendez, R.H., Miguel, C.H., Heber, U., and Kudritzki, R.P., 1986. In *Hydrogen Deficient Stars and Related Objects,* ed. K. Hunger, et al. (Dordrecht: Reidel), p. 323.

Mendez, R.H., Kudritzki, R.P., Herrero, A., Husfeld, D., and Groth, H.G., 1988. *Astron. Astrophys.*, v. **190**, p. 113.

Michaud, G., and Fontaine, G., 1979. *Ap. J.*, v. **229**, p. 694.

Neugebauer, G., Martz, D.E., and Leighton, R.B., 1965. *Ap. J.*, v. **142**, p. 399.

O'Dell, C.R., 1963. *Ap. J.*, v. **138**, p. 67.

Oke, J.B., Koester, D., and Weidemann, V., 1984. *Ap. J.*, v. **281**, p. 276.

Olnon, F.M., Baud, B., Habing, H.J., de Jong, T., Harris, S., and Pottasch, S.R., 1984. *Ap. J. (Letters),* v. **278**, p. L37.

Paczynski, B., and Ziolkowski, J., 1968. In *I.A.U. Symp. No. 34, Planetary Nebulae,* eds. D.E. Osterbrock and C.R. O'Dell (Dordrecht: Reidel), p. 396.

Phillips, J.P., and Reay, N.K., 1977. *Astron. Astrophys.*, v. **59**, p. 91.

Pottasch, S.R., 1984. *Planetary Nebulae,* (Dordrecht: Reidel).

Preite-Martinez, A., and Pottasch, S.R., 1983. *Astron. Astrophys.*, v. **126**, p. 31.

Renzini, A., 1983. In *I.A.U. Symp. No. 103, Planetary Nebulae*, ed. D.R. Flowers (Dordrecht: Reidel), p. 267.

Schatzman, E., 1958. *White Dwarfs*, (Amsterdam: North Holland Press), p. 162.

Schönberner, D., 1979. *Astron. Astrophys.*, v. **79**, p. 108.

————, 1981. *Astron. Astrophys.*, v. **103**, p. 119.

Schultz, G.V., Kreysa, E., and Sherwood, W.A., 1976. *Astron. Astrophys.*, v. **50**, p. 171.

Shaw, R.A., and Kaler, J.B., 1985. *Ap. J.*, v. **295**, p. 537.

————, 1988. In preparation.

Shklovskiĭ, I.S., 1956. *Astr. Zhurnal, U.S.S.R.*, v. **33**, p. 315.

Sion, E.M., and Liebert, J., 1977. *Ap. J.*, v. **213**, p. 468.

Stoy, R.H., 1933. *MNRAS*, v. **93**, p. 588.

Strittmatter, P.A., and Wickramasinghe, D.T., 1971. *MNRAS*, v. **152**, p. 47.

Van der Veen, W.E.C.J., Habing, H.J., and Geballe, T., 1987. In *Planetary and Proto Planetary Nebulae: From IRAS to ISO*, ed. A. Preite-Martinez (Dordrecht: Reidel), p. 69.

Vauclair, G., and Reisse, C., 1977. *Astron. Astrophys.*, v. **61**, p. 415.

Walton, N.A., Reay, N.K., Pottasch, S.R., and Atherton, P.D., 1986. *Proc. Joint NASA/ESA/SRC Conf., New Insights in Astrophysics*, ESA SP-263.

Wehrse, R., and Liebert, J., 1980. *Astron. Astrophys.*, v. **83**, p. 184.

Weidemann, V., 1984. *Astron. Astrophys.*, v. **134**, p. L1.

Wesemael, F., Auer, L.H., Van Horn, H.M., and Savedoff, M., 1980. *Ap. J. Suppl. Ser.*, v. **43**, p. 159.

Wilson, W.J., and Barrett, A.H., 1968. *Science*, v. **161**, p. 778.

Winget, D.E., and Fontaine, G., 1982. In *Pulsations in Classical and Cataclysmic Variable Stars*, (Boulder: Univ. Colorado/JILA), p. 46.

Wood, P.R., 1979. *Ap. J.*, v. **227**, p. 220.

Wood, P.R., and Faulkner, D.J., 1986. *Ap. J.*, v. **307**, p. 659.

Zanstra, H., 1931. *Z. Astrophys.*, v. **2.**, p. 1.

Figure Captions

Figure 1-1: An HR Diagram based on Zanstra Temperatures and Shklovskiĭ distances, reprinted from Figure 3 of Kaler (1983).

Figure 1-2: An $M_v - t_{\rm dyn}$ diagram for CSPN evolution, reprinted from Figure 7 of Schönberner (1981).

Figure 1-3: The number of planetary nebulae in the distance measurement sample of Daub (1982) as a function of distance, compared with a d^2 curve.

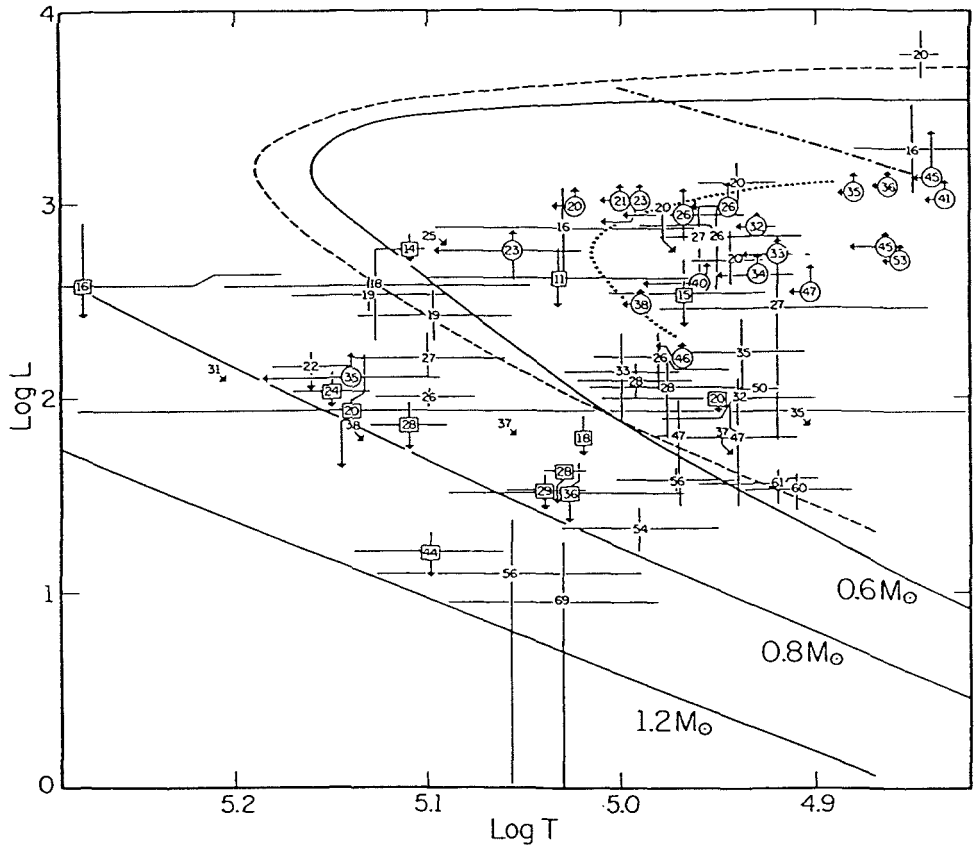

FIG. 6.—The planetary nuclei on the log L-log T plane, indicated by numbers that express the nebular radii in units of 0.01 pc. The solid curves are the Paczyński 1971 tracks for 0.6, 0.8 and 1.2 $M_\odot$. The dashed curve is Iben and Renzini's 1982 track for a 0.6 $M_\odot$ core, and the dotted curve is Schönberner and Weidemann's 1981*b* extrapolated track for 0.55 $M_\odot$. The horizontal and vertical arrows indicate optically thick and thin nebulae, and the consequent upper and lower limits on T and L, as discussed in the text (§§ III*g* and IV*b*). Boxes around the numbers denote nebulae that are optically thick in the hydrogen Lyman ultraviolet, for which L is an upper limit. Circles indicate nebulae that are thin in the He^+ Lyman continuum, for which T and L are lower limits. The dot-dashed line, which originates at the Abell 78 point, is the locus along which the star moves as optical depth is taken into account and the temperature is increased from the lower limit; all circled points may be moved parallel to this line. The arrows pointing downward at 45° indicate nebulae for which only upper limits on $F(\lambda 4686)$ He II, and T_*(He II) are available. These points may be moved down and to the right roughly parallel to the Iben-Renzini 0.6 $M_\odot$ cooling track.

Figure 1-1

D. Schönberner: Evolution of Central Stars of Planetary Nebulae

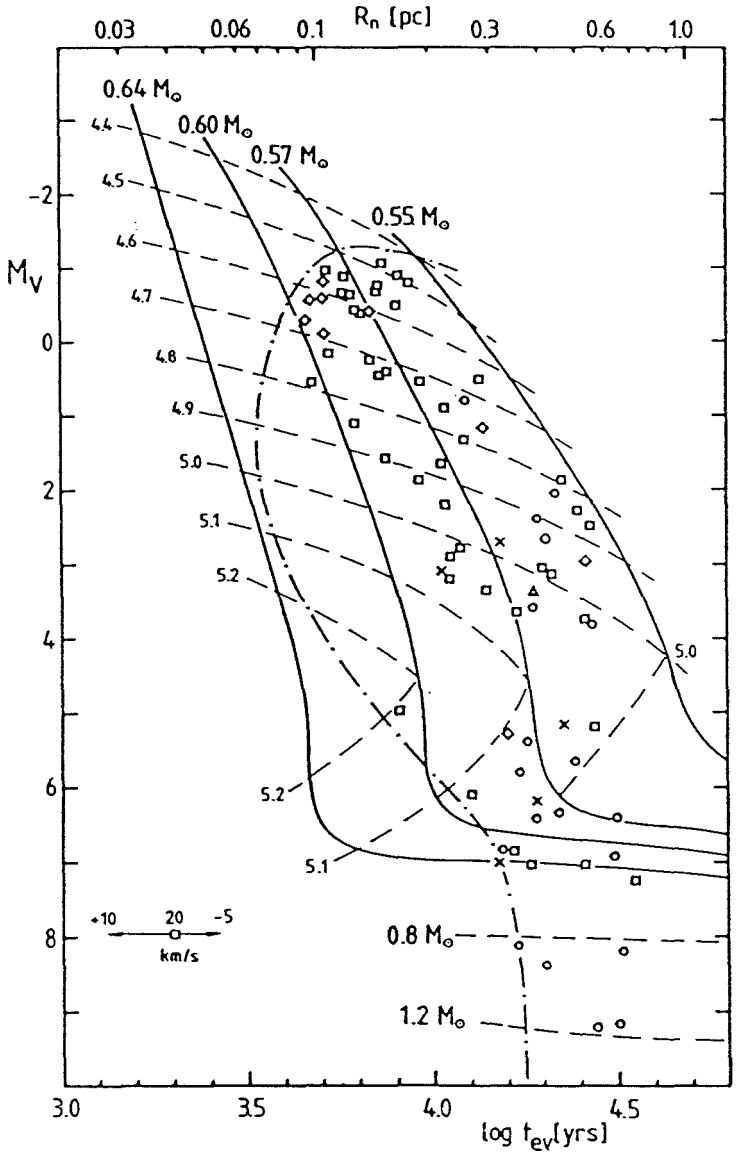

Fig. 7. M_v, t_{ev}-diagram for different post-AGB evolutionary tracks, extracted from Fig. 3a, with the estimated border (dash dotted line) between optically thick and thin PN, as explained in the text. Lines of constant T_{eff} are indicated (dashed). All PN of Figs. 2 which are belonging to the optical thin region, are plotted after a distance increase of 20% and a PN expansion velocity of 20 km s^{-1} have been applied. The arrows in the lower left corner give some impression how expansion velocities may influence the loci of individual objects.

Figure 1-2

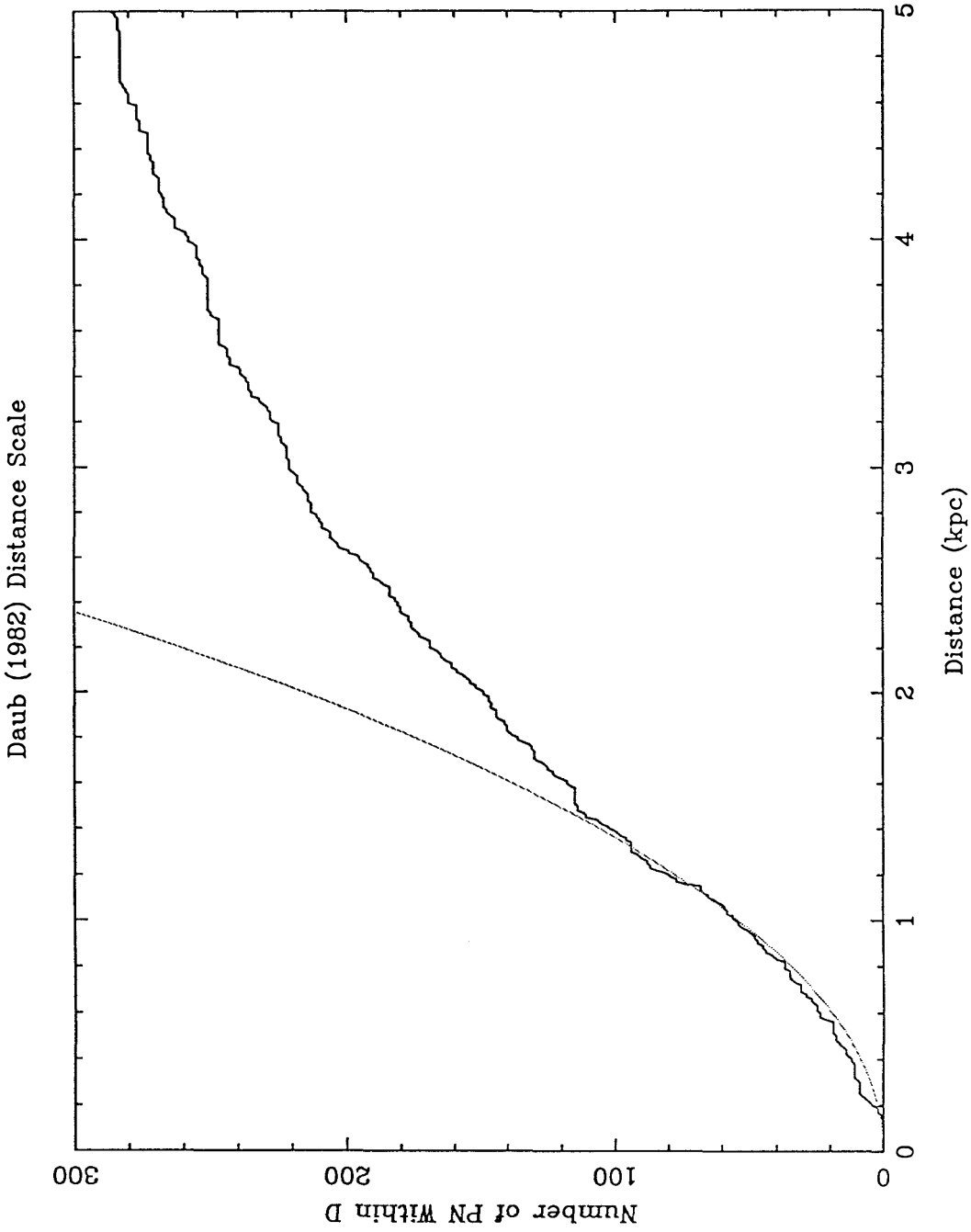
Daub (1982) Distance Scale
Distance (kpc)
Number of PN Within D
0
100
200
300
0
1
2
3
4
5

Figure 1-3

II. The P60 Echelle Spectrograph

A. Design Objectives

The past decade has witnessed tremendous advances in ground-based astronomical instrumentation as a result of the development of the charge coupled device, or CCD, imaging detector. Of the various different CCD designs and formats currently available, the one best suited to low light level scientific applications is the Texas Instruments 800 × 800 backside illuminated three phase sensor (TI3ϕCCD), developed in conjunction with NASA's Jet Propulsion Laboratory for use in the Hubble Space Telescope's Wide-Field/Planetary Camera instrument (for an in-depth discussion of the TI3ϕCCD, see Blouke, et al., 1978, 1983, and Janesick, et al., 1984).

These devices are characterized by excellent linearity, high quantum efficiency (Q.E.), especially in the red part of the spectrum, and low noise. The discovery of backside charging (Janesick, et al., 1985) and later the so-called "flash gate" (Janesick, et al., 1986) as a means for increasing the blue response of non-phosphor coated CCDs has made it possible to consider the design of astronomical spectrographs which could operate over a very broad wavelength range. The stability, linearity, and high Q.E. of CCDs makes it possible to achieve very high signal-to-noise ratios which, when coupled with high resolution, enable detailed stellar atmosphere analysis to be carried out. Such advances in detector technology prompted the design of a new spectrograph for the Palomar sixty-inch telescope (hereafter, P60) which would be optimized to make the best possible use of currently available CCDs such as the 800 × 800 TI3ϕCCD.

Because CCDs are two dimensional detector arrays capable of high Q.E. over a broad wavelength range, it was clear that the echelle spectrograph configuration,

which combines high resolution with large wavelength coverage (see below), would make the best possible use of the full CCD format for high resolution spectroscopy. The initial investigations into the design of such an instrument indicated that with a reciprocal dispersion of $\lambda/\Delta\lambda = 40,000$ per pixel (for a two-pixel resolution of $\mathcal{R} = 20,000$), the wavelength range from 3200 Å to 7000 Å could be imaged simultaneously onto the CCD.

The "echelle" design (Harrison, 1949) uses a diffraction grating blazed at a large angle ($63°26' = \tan^{-1}2$ is typical) which works in high diffracted orders (48 to 104 in this design). When diffracted in the direction of the blaze, these orders are all overlapping; a second grating or a set of prisms is then used to disperse the light in a perpendicular direction, separating the echelle orders perpendicular to the echelle dispersion direction. The second grating or prism set is referred to as the "cross-dispersing" element. This design is able to achieve high resolution owing to the high order numbers in which the echelle grating is used, while it simultaneously achieves large wavelength coverage by imaging many such echelle orders at once onto the CCD detector. What must be sacrificed is the maximum length of the slit that can be used, since adjacent orders are imaged close together in the slit dimension. For work on point sources with brightnesses well above the sky background, the short slit length is not a serious limitation.

The echelle design is inherently a very efficient one; not only are there many orders being exposed at once, but equally important is the fact that each order is utilized in the direction of the echelle blaze function. This is to be compared to single order gratings which in practice are very often employed far from the blaze wavelength at which they have optimum response. Therefore the internal optics of the P60 echelle spectrograph were designed with this potential for high efficiency always in mind; the goal was to reach as faint as 14^{th} magnitude in V with a signal-to-noise ratio S/N = 30 in a one hour exposure for the resolution

quoted above (N.B., the CCD can electronically "bin" adjacent pixels together and so reach fainter magnitudes at the expense of spectral resolution).

Finally, keeping mechanical flexure to a minimum was a design objective because the reciprocal dispersion figure of 40,000 per pixel translates into a radial velocity difference of 7.5 km/s per pixel, and so it was anticipated that the P60 echelle spectrograph would find wide application for radial velocity measurements. If the spectrograph does not suffer from mechanical flexure, radial velocity errors of ~ 0.1 pixel can be achieved through the use of cross-correlation techniques (e.g., Tonry and Davis, 1979). Since the P60 echelle spectrograph was not anticipated to be a large instrument, its weight load on the telescope's Cassegrain focus would not likely become a limiting factor and thus it could be profitably over-designed from a structural standpoint in order to guarantee maximum rigidity.

The following §**II.B** describes how these design objectives were met as far as the optical design of the instrument was concerned, while §**II.C** describes the mechanical design of the spectrograph. The actual performance of the completed instrument is evaluated in §**II.D**.

B. The Optical Design

The echelle grating in the P60 echelle spectrograph is used in the unconventional "Quasi-Littrow" configuration. In the "conventional" configuration, the optical axis of the collimator makes an angle α with the grating normal, the optical axis of the camera makes an angle β with the grating normal, and both axes are co-planar with the grating normal ($\gamma = 0$); see the diagram of the grating geometry in Figure 2-1. For this configuration, the grating equation:

$$\frac{m\lambda}{a} = \left(\sin\alpha + \sin\beta\right)\cos\gamma \qquad (2.1a)$$

reduces to:

$$\frac{m\lambda}{a} = \sin\alpha + \sin\beta \ , \quad \gamma = 0 \tag{2.1b}$$

where m is the order number and a the grove spacing (see e.g., Schroeder, 1970, or Chaffee and Schroeder, 1976). "Littrow" is characterized by $\alpha = \beta = \theta_B$, where θ_B is the blaze angle of the grating. Note that in a true Littrow configuration, $\gamma = 0$ also and the camera and collimator beams are coincident; in practice, some separation is necessary and so therefore $\alpha \gtrsim \beta$ in most conventional ($\gamma = 0$) designs.

However, the solution decided upon in the P60 echelle design was to maintain Littrow with $\alpha = \beta = \theta_B$ and to achieve the necessary separation between the camera and collimator beams with an angle γ tilt perpendicular to the plane containing the grating normal. In this configuration, the optical axis of the collimator, the optical axis of the camera, and the grating *facets* all lie in the same plane. Because the angle $\gamma \neq 0$, this configuration is referred to as "Quasi-Littow" as distinct from true Littrow with $\gamma = 0$. The grating equation (2.1a) can be re-written:

$$\lambda_c = \frac{2a\sin\theta_B}{m}\cos\gamma \ , \quad \alpha = \beta_c = \theta_B \tag{2.2}$$

for the central wavelength λ_c of order number m. The decision to use a Quasi-Littrow over a conventional configuration was made on the basis of the higher efficiency offered by the Quasi-Littrow geometry; in a preliminary design study for the proposed AAT Coude echelle spectrograph, Walker and Diego (1983; see also Walker, et al., 1986) compared the peak efficiencies of the Quasi-Littrow configuration with that of a conventional design, and found values of 95% and 65%, respectively. Walker and Diego also calculated the efficiencies at the order free spectral range (F.S.R.) boundary (i.e., where the intensity matches that in the next order for an identical wavelength), and found efficiencies of 38% and 46% for the Quasi-Littrow and conventional configurations, respectively. Ironically, Walker and Diego used these efficiencies to argue in favor of the conventional design for the AAT Coude echelle being proposed, since there would be less intensity varation

from order center to order edge across the F.S.R. (65% to 46% as opposed to 90% to 38%), and that instrument was being designed for use with a photon counting detector. However, since the P60 echelle spectrograph would be used with a CCD detector, the higher dynamic range across the F.S.R. of the Quasi-Littrow configuration was not a concern; the increase in *average* efficiency across the entire order (a factor of 1.2, according to Walker and Diego, 1983) was thought to be a more important criterion in favor of the Quasi-Littrow configuration than the problem of greater center-to-edge variation.

The available gratings were analyzed with equation (2.2), and the one giving the most appropriate number of orders over the wavelength range 3200 Å to 7000 Å was the grating with $a^{-1} = 52.65$ lines/mm having a blaze angle $\theta_B = 63°26'$. This grating covers the required wavelength range in 57 orders, numbers $48 \leq m \leq 104$, with each order F.S.R. having an angular extent:

$$\begin{aligned} \Delta\beta(m) &= \frac{\lambda_c}{a \cos\beta_c \cos\gamma} \\ &= \frac{2 \tan\theta_B}{m} \ , \quad \alpha = \beta_c = \theta_B \ , \end{aligned} \tag{2.3}$$

which is equivalent to a free spectral range in wavelength given by:

$$\begin{aligned} \Delta\lambda(m) = \frac{\lambda}{m} &= \frac{\lambda_c^2}{a(\sin\beta_c + \sin\alpha)\cos\gamma} \\ &= \frac{\lambda_c^2}{2a \sin\theta_B \cos\gamma} \ , \quad \alpha = \beta_c = \theta_B \ . \end{aligned} \tag{2.4}$$

Note that the orders with low order numbers m will have the greatest angular extent $\Delta\beta(m)$; from equation (2.2) it follows that these are the red (i.e., long wavelength) orders. For the longest order ($m = 48$), equation (2.3) gives an angular extent $\Delta\beta = 4.77°$; in the P60 echelle spectrograph it was desired that the length of this order be matched to the length of the CCD so that the wavelength coverage would be continuous for $\lambda \leq 7000$ Å. The 12mm length of the CCD (800 pixels each 15 μm

square) then required a camera system having an effective focal length (E.F.L.) of 144 mm, independent of the beam diameter.

The collimator focal length was determined next by requiring that a given slit width match so many CCD pixels; the focal ratio of the P60 Cassegrain is 8.675 and so the image scale can be derived from the telescope focal length $f_{\rm tel}$ as follows:

$$\begin{aligned} s &= \frac{1}{f_{\rm tel}} \text{ radians} \\ &= \frac{206,265 \text{ arcsec/radian}}{(60'')(8.675)(25.4\,\text{mm}/'')} \\ &= 15.6 \text{ arcsec/mm} \ . \end{aligned} \tag{2.5}$$

The minimum sampling acceptable for radial velocity observations (Schechter, 1984) required that the 1.5 arcsecond slit width typically most appropriate at the P60 map onto 2 CCD pixels. Note that a 1.5 arcsecond slit measures $1.5/(15.6\,\text{mm}^{-1})$, or 96 μm, in the collimator focal plane. Two CCD pixels measure 30 μm in the spectrograph camera image plane, and so the collimator focal length needs to be $(96/30) = 3.2$ times the camera effective focal length to achieve the required sampling. For a camera E.F.L. of 144 mm, this translates into a collimator focal length of 461 mm. Since the beam of light emerging from the slit will retain the f/8.675 focal ratio of the telescope at Cassegrain, the beam size following the collimator will be $(461\,\text{mm}/8.675) = 53.1$ mm, or about two inches. Note that this is the beam size prior to any dispersion by the echelle grating and cross-dispersing element, and so the camera diameter must in general be larger than this to avoid losses due to vignetting.

Turning now to the means for achieving the required cross-dispersion, the available choices were a low dispersion reflection grating, transmission grating, or a set of one or more prisms. From the m^{-1} dependence of both equations (2.2) and (2.3), it follows that the free spectral range of the echelle grating decreases towards the blue (i.e., larger order numbers m). Hence the fairly uniform dispersion

of a grating cross-disperser would result in orders close together in the blue and increasingly farther apart towards the red, in proportion to λ_c^2 by equation (2.4) above. The dispersion of glass prisms, on the other hand, decreases towards the red, approximately in proportion to λ^{-3} (cf., Smakula, 1962). When this is combined with equation (2.4), the resulting order separation still decreases towards the red, but only in proportion to λ_c^{-1}. Therefore an echelle spectrograph designed to cover a wavelength range greater than a factor of two benefits a great deal from the more uniform order-to-order separation provided by prism cross-dispersing elements. A second advantage is that prism cross-dispersing elements are much more efficient than cross-dispersing gratings: such prisms can be anti-reflection coated and achieve significantly higher throughput than the peak efficiency of diffraction gratings, which would also introduce their own blaze function and so provide poor response over more than a factor of two in wavelength.

However, most glass prisms (indeed most ordinary crown and flint glass optical elements) suffer from poor near ultraviolet transmission ($\lambda \leq 3600$ Å); recall that the desired wavelength coverage of the P60 echelle spectrograph was 3200 Å to 7000 Å. Thus quartz (a.k.a., synthetic fused silica) was the material of choice for the cross-dispersing prisms, since it offers high transmission far into the ultraviolet. Unfortunately quartz is not a very dispersive material, and so two quartz prisms each with a 60° apex angle working in tandem were required to achieve adequate cross-dispersion (i.e., separate $\lambda = 3200$ Å and $\lambda = 7000$ Å beams by the same $\Delta\beta$ angular size of the CCD as seen through the camera optics, which had their E.F.L. specified above to accommodate the longest echelle order, $m = 48$).

The poor near ultraviolet transmission of ordinary crown and flint glasses was also a factor in the design of the camera optical system. It was decided that an all-transmitting lens system would be the most efficient type of camera optics to use in the P60 echelle spectrograph, for several reasons. First of all, the throughput

of a series of anti-reflection coated lenses is very high; typical losses are only 1–2% or less for each air/glass interface involved, whereas the reflection losses from a mirror are at least 10% per reflecting surface. Secondly, the central obstruction common to almost all reflecting camera designs would cause severe losses when used in this instrument, because of the small monochromatic beam size (53 mm) and the fact that only a small fraction of the incident wavelengths remain on-axis (in which case the central obstruction of the camera coincides to some degree with the central obstruction of the telescope) in the echelle format. In addition to quartz, only calcium fluoride (a.k.a., Fluorite) transmits far into the ultraviolet. There are, however, some "light flint" and "ultraviolet crown" glasses such as LLF6 and UBK7 which still allow 84% and 92% transmission through 5 mm of material at 3200 Å, respectively (N.B., these latter two glasses are those used in the achromatic Schmidt corrector lens of the 48-inch Oschin Telescope at Palomar Observatory). As will be explained below, the final design of the P60 echelle spectrograph camera lens system makes use of all four of these materials and achieves image spot sizes of less than two pixels full width at half maximum intensity (FWHM).

The final phase before the detailed design of individual optical components could be undertaken was to make a series of scale drawings laying out the full spectrograph optical path. The objective was to arrange the individual components in such a way that the optical path would be folded into as small and symmetric a configuration as possible, thus making the overall spectrograph structure more compact and less subject to mechanical flexure. This was attempted for a variety of different collimating alternatives, and finally it was decided that the optimum choice would be a folded off-axis paraboloid reflecting collimator. The folding flat mirror would deflect the beam emerging from the spectrograph slit by 90°, so that instead of moving farther away from the focal plane of the telescope it would move parallel to the underside of the telescope primary mirror. This would eliminate the large

"moment arm" common to conventional spectrographs without folded collimator beam paths, and so greatly reduce the forces giving rise to flexure. Reflecting optics were chosen for the collimator elements partly because of the compact geometry that resulted from their use, but primarily because it is an important requirement in echelle spectrographs that the light striking the grating be precisely collimated. Any lack of collimation will be manifested as astigmatism after reflection from the echelle grating, due to the fact that the echelle grating is used in very high orders (Wheeler, 1975). It is possible that the chromatic aberration of a lens collimator could give rise to such astigmatic effects (Ramsey, 1986), and so the absence of chromatic aberration in reflecting optics was a compelling reason to use them for the collimator in spite of their lower throughput.

It was also concluded on the basis of the full optical system layouts that the preferred placement of the two cross-dispersing prisms was one before and the second after the echelle grating. Although unorthodox — it is customary to locate all the cross-dispersing elements after the echelle grating, unless a single prism is used in double pass (see e.g., Learner, 1972; Bardas, 1977; Shectman, 1983) — this arrangement, shown schematically in Figure 2-2, has several advantages. First of all, the complete system was able to fit inside a significantly smaller enclosure since both the collimator and camera beams are deviated by an equal amount by one prism rather than the camera beam alone being deviated by twice this amount, as would be the case were both prisms to follow the grating. Secondly, both prisms are closer to the echelle grating in this arrangement, and so the size of the second does not need to be any larger than the first. More importantly, the clear aperture of the camera lens system is reduced since it too is closer to the echelle grating. Finally, this optical layout makes available the novel possibility of adding a second mode of operation to the instrument: because both the camera and collimator optical axes are deviated equally by a cross-dispersing prism, the two beams will

still converge should both prisms be removed from the echelle beam path (see Figure 2-2). It would be possible to locate an ordinary single order grating at this non-cross-dispersed point of intersection (point "G" in Figure 2-2) in order to make a non-echelle mode of operation available within the same instrument. As it has not yet been implemented, full discussion of this mode will be postponed until §**V.A** below, although it will be mentioned occasionally in regards to echelle mode components designed and built with this non-echelle mode in mind.

There is, however, one disadvantage resulting from the placement of one of the two cross-dispersing prisms before the echelle grating. Recall that the echelle grating is being used in the Quasi-Littrow configuration, and the angle γ in equations (2.1a) and (2.2) is non-zero. As a consequence of this arrangement, the slit images in the focal plane of the camera will be tilted with respect to the echelle dispersion direction by an angle χ given by:

$$\begin{aligned} \tan\chi = \frac{d\beta}{d\gamma} &= \lambda \frac{d\beta}{d\lambda} \tan\gamma \\ &= 2\tan\theta_B \tan\gamma \,, \quad \alpha = \beta_c = \theta_B \\ &= 4\tan\gamma \,, \qquad \theta_B = 63°26' \end{aligned} \tag{2.6}$$

(Rense, 1966). In the final layout, the minimum collimator to camera angle which could be achieved without requiring excessively large and expensive optical elements was $2\gamma = 19°32'$; thus $\gamma = 9.77°$ and $\chi = 34.5°$. While it is possible to rotate the entrance slit by an angle $-\chi$ to produce a slit image perpendicular to the orders, this increases the width of the slit from w to w', where

$$w' = \frac{w}{\cos\chi} \,, \tag{2.7}$$

and decreases the length of the slit image from ℓ to ℓ', where

$$\ell' = \ell\cos\chi \,. \tag{2.8}$$

The fact that one prism precedes the echelle grating causes the angle γ to vary by approximately $\pm 1.2°$ as a function of wavelength, since this prism pre-disperses the light which strikes the grating; hence by equation (2.6) above, χ also varies as a function of wavelength. Since the slit length is very short, this small variation in χ was not expected to degrade the resolution significantly. Note however that radial velocity errors can be introduced if echelle data are wavelength calibrated by arc data not extracted from the same CCD rows because of this small and variable inclination of the slit images (see §**III.B** below for means of avoiding this with the *TEMPLATE* keyword in ECHTRACT). For comparison purposes, note that the double pass prism pre-dispersed echelle spectrographs designed by Bardas (1977) has $\gamma = 17°$ while that by Shectman (1983) has $\gamma \sim 5°$.

From the final arrangement of optical elements shown in Figure 2-2, it was possible to decide upon the rectangular dimensions or clear apertures of each element required to maintain an unvignetted field of view out to the corners of the CCD array. The optical elements could then be procured. A list of the relevant specifications for all the optical elements and the source for each has been compiled and can be found in Appendix A for future reference; here it is only necessary to describe in full the custom design for the camera lens system.

The all-transmitting camera lens system (McCarthy, 1985) was designed specifically for its role in the P60 echelle spectrograph using the *ACCOS V* † raytracing and optical design program. As mentioned above, the desired E.F.L. for the full format echelle wavelength coverage of 3200 Å to 7000 Å was 144 mm, and the short wavelength limit restricted the choice of available glass materials to those few with high transmission shortward of 3600 Å (e.g., fused silica, Fluorite, UBK7, LLF6, and others). The pre-dispersed beam diameter was 53 mm, and this beam is dispersed

† *ACCOS V* is a registered trademark of Scientific Calculations, Inc., and is licensed for use at Caltech's Jet Propulsion Laboratory.

by an amount $\pm\Delta\beta/2 \sim 2.4°$ by the echelle grating and quartz cross-dispersing prisms. For a nominal separation of 30 cm between the echelle grating and first lens element, the beam size and dispersion then require a camera lens clear aperture of at least 95 mm for unvignetted operation out to the corners of the CCD.

The design approach was to first define an aperture stop 53 mm in diameter located at the grating position, 30 cm in front of the first lens element. Parallel light emerging from this stop would then pass through the lens system in a manner similar to monochromatic beams dispersed by the echelle grating. In order to achieve a throughput as high as possible, it was necessary to keep the number of air/glass interfaces to a minimum, and so individual lens elements were kept in cemented groups where at all possible. The maximum acceptable image diameter was two pixels r.m.s. (30 μm); it was thought that a 1.5 pixel spot diameter of 22.5 μm should be the design objective. Unfortunately, a single cemented doublet of the required diameter and E.F.L. proved unable to provide satisfactory image diameters, as did a lone cemented triplet. However, a longer E.F.L. quartz/Fluorite/quartz triplet was capable of good performance over the required field angle, and was a suitable first component of the camera lens system for several reasons. First and foremost was the low dispersion of Fluorite; a positive Fluorite element could possess a large power without simultaneously introducing a large amount of dispersion. One disadvantage of the use of Fluorite, however, is its hydroscopic property, which causes it to absorb water from its surroundings, soften, and dissolve over time. Hence a cemented triplet lens containing a positive Flourite element surrounded by a pair of quartz elements offered the advantages of Flourite, yet could effectively seal this element from contact with the surrounding atmosphere.

With such a triplet as the first component of the camera system, it would be necessary to considerably shorten the E.F.L. with subsequent lens elements. Following the example of Rayton (1930; see also Bowen, 1952, Butcher, 1974, and

Shectman, 1983, by whom the concept was first suggested to this author), it was decided to incorporate an "aplanatic sphere" into the lens system design close to the CCD focal plane. It is a direct consequence of Snell's Law of Refraction that a spherical surface of radius R refracts light destined for a point on a concentric sphere of radius nR onto a concentric sphere of radius $\frac{1}{n}R$, where n is the index of refraction of the glass aplanatic sphere (see Figure 2-3; adapted from Figure 4.9 of Born and Wolf, 1980). This reduction in image scale and therefore E.F.L. by the factor $\left(\frac{1}{n}\right)^2$ is accomplished without the introduction of any additional spherical aberration; its uncorrected chromatic aberration could be compensated for in the design of the preceding triplet lens, and the curvature of field introduced could be compensated for by a curved rear surface in the aplanatic sphere itself (Butcher, 1974) as well as by a separate field flattening element used in place of the CCD cover glass (Oke, 1984). Due to the large (i.e., several cm) thickness required for the aplanatic sphere, fused silica was the material of choice in order to maintain high transmission at the shortest wavelengths. Furthermore, it was decided in consultation with Oke (1984) that the aplanatic sphere could serve also as the window to the CCD Dewar, thereby reducing the number of air/glass interfaces and allowing the aplanatic sphere to occupy a position much closer to the CCD.

However, the combined lens system performance was still unsatisfactory for values of the E.F.L. ≤ 200 mm. Owing to the advantages which an alternate, longer E.F.L. camera would potentially offer in terms of a greater order-to-order separation in pixels on the CCD focal plane (Kudritzki, 1984), it was decided to optimize this "long" camera system (Figure 2-4, top) at an effective focal length of 200 mm, and then to add an additional positive lens group between the triplet and aplanat so as to achieve the 144 mm E.F.L. "short" camera system required for full field coverage (Figure 2-4, bottom). Table 2-1 shows the radii, thickness, and glasses for the elements of the optimized long camera system, and Table 2-2 contains the r.m.s.

spot diameters predicted for the long camera design. Note from Table 2-1 that optimized radii which were very close to the same value have been set equal to the same value, radii which were very large have been set equal to infinity (i.e., flat surfaces), and the system re-optimized so as to compensate for these slight changes. These changes were intended to reduced the amount of custom tooling required to grind, polish, and test the complete lens system, thereby also reducing the cost of such fabrication. Also note that the final lens radii and thicknesses were optimized using not the catalog refractive indices, but rather the so-called "melt indices" for the actual glass blanks purchased for use in this system.

The parameters for the lens elements of the long camera were held constant when the additional positive lens component of the short camera was optimized, except for the triplet-to-aplanat spacing. This new component, a cemented LLF6/UBK7 doublet, was located between the triplet and aplanat with relative spacings chosen such that its rear surface could remain flat, which would reduce the cost of fabrication. Shown in Table 2-3 are the final radii, thicknesses, and glasses for the short camera system (optimized using the melt indices shown), and Table 2-4 contains the final r.m.s. spot diameters predicted for the short camera design. Using the final thicknesses of the LLF6/UBK7 doublet, one finds that its on-axis transmission at 3200 Å is 94%, at 3300 Å is 98%, and at 3500 Å is 99%, (N.B., all of these values neglect surface reflection losses). The remaining fused silica and calcium fluoride elements are not expected to suffer any significant internal transmission losses over the 3200 Å to 7000 Å wavelength range of importance here.

The camera lens elements were fabricated by Mr. Don Loomis of Custom Optics in Tucson, Arizona (see Appendix A for the address of Custom Optics as well as all the other vendors utilized during this project), who cited manufacturing tolerances of $\pm 0.1\%$ in the radii of curvature, $\pm 50\,\mu$m in the individual element thicknesses, and centering tolerances of $\pm 25\,\mu$m for each element. Evaluation of the lens de-

sign confirmed that its performance was insensitive to changes of these amounts, provided the spacings separating the lens groups could be adjusted to compensate for the small radii and thickness errors. Such adjustment would normally be performed to focus the lens system, and so fabrication could proceed without the need to tighten any of these tolerances.

Following the mechanical design, construction, and assembly of the P60 echelle spectrograph as described in §**II.C** below, the instrument was used with drafting tape spacers between each of the glass elements which were designed to be cemented together, in order to test the camera system performance in actual use. Following the successful completion of focus tests, the camera system was disassembled so that the outer air/glass surfaces could be anti-reflection (AR) coated.

The AR coating was custom designed and applied by Newport Thin Film Lab in Chino, California (see Appendix A). The coating consists of 4 thin film layers, optimized for use over the bandpass 3200 Å to 7000 Å. Because the actual AR coating design is proprietary, not much is known about the composition of any of the four layers, except that: (1) the outer layer is MgF_2 and so the coating is durable; (2) none of the AR layers absorbs significantly over the wavelength range 3200 Å to 7000 Å; and (3) none of the layers consists of radioactive isotopes which might contribute to spurious "cosmic ray" -like events in the CCD. The third design requirement was a concern due to the mere 1 mm separation between the rear of the field flattener (CCD cover glass) and the CCD detector itself. Figure 2-5 shows the measured *transmission* of a quartz test piece coated on two sides along with the camera system lens elements.

In an analogous fashion, the two large fused silica cross-dispersing prisms were also anti-reflection coated by Newport Thin Film Lab. Although the design of the prism coating uses the same four materials as does the lens system coating, the

thicknesses of the prism layers are smaller because the AR coating of the prisms was optimized for minimum reflection at the angle of incidence i at which the prisms operate. Under conditions of minimum deviation, i is given by:

$$\sin i = n_\lambda \sin\left(\frac{A}{2}\right) \tag{2.9}$$

where A is the apex angle of the prism ($A = 60°$ here), and n_λ is the index of refraction of the prism material (fused silica here). Since the refractive index of the prism is a function of wavelength λ, the angle of incidence i is as well, by equation (2.9). In the case of the P60 echelle spectrograph, $\lambda \simeq 4000$ Å is located in the center of the CCD when the design wavelength range of 3200 Å to 7000 Å is selected; since $n_\lambda = 1.469618$ for fused silica at 4047 Å, it follows from equation (2.9) that $i = 47.°3$. Figure 2-6 shows the measured *transmission at* $i \sim 45°$ of a quartz test piece coated on two sides along with the cross-dispersing prisms.

Finally, after being AR coated, the lens system doublet and triplet group elements could be cemented together. However, this posed a potentially serious problem because of the large expansion coefficient of calcium fluoride with temperature and the much smaller expansion coefficient of fused silica. The solution suggested by Loomis (1985) based on his experience was to use *Dow Corning Sylgard*† *184 silicone elastomer*, a clear silicone cement which remains elastic even after it has cured and thus could adjust to the differential expansion of the quartz and Fluorite glasses with temperature. Appendix B contains for future reference the data sheet on this material provided by the Dow Corning Corporation. The actual cementing together of lens elements was performed with the assistance and advice of Shectman (1987); it was necessary to insert small tape shims between the elements to be cemented in order to maintain a cement thickness at least as large as the shim thickness, and the cement was allowed to cure in an unheated area overnight (T $\sim$ 18°C) in order that

† *Sylgard* is a registered trademark of the Dow Corning Corporation.

the cement layer's unstressed equilibrium not be at the high temperature extreme of the range it will be exposed to in operation.

When the cement had set and the lens system was reinstalled in the P60 echelle spectrograph, a substantial decrease in the amount of scattered light in the inter-order minima rows was observed (down to less than 3% of the adjacent order maxima rows; see below, §**III.B**). A summary of the P60 echelle optical design parameters appears in Table 2-5 for future reference. The predicted CCD image formats for both the short and long cameras can be found in Figures 2-7 and 2-8, respectively. Further details of the instrument's optical performance will be discussed in §**II.D** below.

C. The Mechanical Design

It was pointed out in §**II.B** above that, as a result of the decision to use a folding mirror between the slit and the collimating mirror and to use the echelle grating in the Quasi-Littrow configuration, all of the major optical elements shown in the Figure 2-2 layout lie in a single plane only a short distance below the Cassegrain focus of the P60 telescope. This arrangement is very convenient from a mechanical standpoint, as it allows all of the optical components to be mounted to a single surface held beneath the slit. From the position of the folding mirror 9 inches beneath the slit in Figure 2-2, it follows that thereafter the optical axis remains this distance underneath the telescope focal plane.

The first major decision from a mechanical standpoint, made after a brief consultation with Friswold (1985), was to use a 1-inch-thick aluminum plate held between the slit and folding mirror as this single mounting surface for all of the optical components. The top of this plate (hereafter referred to as the "primary mounting plate") was to be held 4.5 inches below the slit, so that its underside —

the "primary mounting surface" — would then be 3.5 inches above the optical axis after reflection by the folding mirror. This 3.5-inch separation was thought to be small enough to allow rigidity to be easily maintained when the optical component mounts were later designed, yet large enough to accommodate a 7.0-inch-diameter circle centered on the optical axis. The CCD Dewar, approximately 6.0 inches in diameter, was by far the largest component expected to require centering on the optical axis.

Connecting this primary mounting plate to the Cassegrain focus of the telescope would be a rectangular box-like structure containing the slit mechanism, shutter, etc., and having at its top a rectangular mounting flange fully compatible with that of the existing P60 spectrograph mounting flange. This compatibility would permit the echelle spectrograph to mount onto the existing "spectrograph mounting base," which contains incandescent flat field and arc line calibration sources as well as T.V. guider optics. The latter would also require that the slit of the P60 echelle spectrograph be tilted by the same 10° angle with respect to the optical axis of the telescope as the slit of the existing P60 spectrograph, in order to properly direct the light reflected from the slit to the T.V. guider relay optics and camera.

The next decisions dealt with how much additional "structural" framework would be required in addition to the 1-inch-thick primary mounting plate and its rectangular connection to the spectrograph mounting base on the back of the telescope. To make these decisions, it was necessary to determine how much the primary mounting plate would flex in the absence of any additional structural framework; recall that keeping mechanical flexure to a minimum was an important design objective. Such information followed directly from the expression for Young's Modulus of Elasticity, M, for a rectangular plate:

$$M = \frac{4mg\ell^3}{sa^3b} = 10^7 \text{ psi for Aluminum} \tag{2.10}$$

where mg is the force causing a deflection s of the plate whose dimension in the direction of the force is a, whose length from its support to the place where the force is being applied is ℓ, and whose remaining width dimension is b. From the optical layout of Figure 2-2, the overall dimensions of the 1-inch-thick primary mounting plate will need to be approximately 16 × 40 inches. Taking note that the plate will be supported roughly in the middle of its 40-inch length, equation (2.10) may be solved for the deflection s of the primary mounting plate with $a = 1''$, $b = 16''$, and $\ell = 20''$ yielding:

$$\begin{aligned} s &= \frac{4mg\ell^3}{Ma^3b} \\ &= \frac{4(mg)(20'')^3}{(10^7 \text{ psi})(1'')^3(16'')} \\ &= 5.08\,\mu\text{m} \times \left(\frac{mg}{\text{lb.}}\right). \end{aligned} \tag{2.11}$$

Thus for a force $(mg) = 50$ lbs., $s = 254\,\mu$m, which is 17 CCD pixels. On this basis it was concluded that the primary mounting plate needed to be substantially stiffened with *structurally important* side plates at the very least. Consider next a 0.5-inch-thick aluminum side plate enclosing a lower section extending 7 inches below the primary mounting plate. Substitution into equation (2.11a) with a now equal to 8.0 inches and b equal to 0.5 inches yields:

$$s = 0.318\,\mu\text{m} \times \left(\frac{mg}{\text{lb.}}\right) \tag{2.12}$$

or $s = 15.8\,\mu$m for a force $(mg) = 50$ lbs., which is roughly 1 CCD pixel and still larger than one would like. Although it was realized that this calculation was a very conservative one — four 0.5 × 8.0 inch side plates welded to the primary mounting plate would result in a structure much stiffer than a single side plate alone, and (mg) is likely to be less than 50 lbs. in actual fact — it was nevertheless decided to increase the length a of the side plates from 8.0 inches to 11.0 inches by extending

them an extra 3.0 inches *above* the primary mounting plate, so that:

$$s = 0.122\,\mu\text{m} \times \left(\frac{mg}{\text{lb.}}\right) . \tag{2.13}$$

For these extended side plates, $s = 6.1\,\mu$m for a force $(mg) = 50$ lbs. Furthermore, diagonal stiffeners were added in the extra space created above the primary mounting plate; these were 3.0 inches tall in the corners where they joined the side plates and rose to 4.5 inches tall where they joined the rectangular box-like structure connecting the spectrograph's primary mounting plate to the telescope's mounting base. In this manner the spectrograph structural enclosure shown in Figures 2-9 and 2-10 (P60 echelle drawings JKM-13 and JKM-14, respectively) was determined to possess more than the required stiffness.

Several things should be noted from Figures 2-9 and 2-10. First of all, the upper box-like structure with the flange to connect to the telescope's spectrograph mounting base is rotated by 32°44′ with respect to the primary mounting plate and the lower enclosure. This is because the slit orientation determines the upper part of the structure, while the lower part of the structure is aligned for convenience and economy with the optical axis of the camera lens system (cf., Figure 2-2, noting that the collimator folding mirror is 13°12′ off the collimator axis, and the camera to collimator angle $2\gamma = 19°32'$). Secondly, note how the primary mounting plate (JKM-01 in Figures 2-9 and 2-10) is held in an eighth inch deep channel in the four side plates. In this way the lower enclosure could be light-tight without the need for continuous welds running the entire lengths of the side plates, and in addition assembly and alignment prior to the actual welding would be easier with the aid of this groove. Finally the two lower partitions JKM-18 and JKM-19 on which mount the collimator and Dewar, respectively, were not to be welded but rather bolted in place, so that they would not be warped by the heat of welding and instead would provide accurately flat mounting surfaces for the optics.

Except where noted otherwise below, all the excellent machine work for the P60 echelle spectrograph was performed by Mr. Gaston Araya of Gaston Araya Machining in Altadena, California (see Appendix A). The aluminum welding of the spectrograph structure was done by Mr. Ralph Ortega of Caltech's Central Engineering Services (CES). Note that "stitch welds" were used where strength but not light-tightness was required, and "full welds" where both were necessary; the former technique introduced much less warpage than the latter. Following the welding process, the spectrograph structure was annealed in order to relax the stresses built up by the localized heat of welding.

The heat of welding did, as expected, warp the primary mounting plate slightly, enough to prevent the primary mounting surface from serving as an accurate reference surface for the spectrograph optics. The machine shop at Mount Wilson and Las Campanas Observatories (MWLCO) had a milling machine large enough to machine flat the top of the mounting flange (JKM-06) and then, working from the underside, machine the primary mounting surface accurately flat and parallel to the top flange. With this and other tasks requiring a large machine completed, the spectrograph structure was returned to Gaston Araya Machining for the months of remaining work fabricating and installing the optical component mounts. For the sake of clarity, the design details of each of these will be discussed below in the sequence in which they are encountered by the light beam entering the spectrograph, starting above the slit.

Recessed into the top mounting flange of the spectrograph is a light-tight top cover over the slit compartment. This cover is in three sections (see Figure 2-11; P60 echelle drawing JKM-50), the center one containing a moveable "barn door" which when closed protects the slit compartment from dust, and when opened (by pulling the handle of a lever located above the level of the side plates) allows light from the telescope to reach the entrance slit of the spectrograph. Note that the

top of the closed barn door is recessed slightly, so that dust which collects there is not swept into the slit compartment when the barn door is opened. The two cover sections on either side of the center were designed to be removeable independent of the center section, so that for access to the slit compartment they could be removed first and so allow the barn door lever to be disconnected from the center section where it is attached to the moveable barn door itself. Note that the screws joining the cover sections together are shorter in length than the screws joining the cover sections to the inside of the mounting flange; this is to prevent the former from interfering with the motion of the slits beneath them. The screws beneath which the barn door lever travels are shorter still.

The slits in the P60 echelle spectrograph were modelled after the slits used in the P200 Double Spectrograph; the slits are small openings in hardened and polished stainless steel disks. Figure 2-12 (from P60 echelle drawing JKM-52) shows the design of these slit disks, which have an outer diameter of 1.75 inches and were machined from a bar of 17-4 P.H. alloy stainless steel by Gaston Araya Machining. The series of channels 0.250 inches long were cut in the back of the disks with ball-end milling tools by Johnson Products in Monrovia, California, and the disks were then hardened to a hardness specification of H-900. Johnson Products then ground the front of the disks to within 0.005 inches of the deepest point of the channel. Next the ground front of each disk was polished by Mr. Gene Fair, formerly of Pomona, California (see Appendix A for Fair Optical's latest known address). Note that the polishing of the slit disks was done prior to the cutting of the slits, unlike the procedure followed for the P200 disks. Polishing the P60 slit disks was done first because the slits themselves were so small (the image scale of the P60 is nearly six times less than the image scale of P200 Cassegrain); if polishing followed the cutting of the slits, it was doubtful that the slits could ever be cleaned of polishing abrasive. The polishing was also significantly easier before the slits were cut, since

there was no danger of a turned down edge at the slit jaws.

After polishing, the slit disks were taken to Mertsoc Tool Company in Escondido, California, with little or no results after two months. This order was then cancelled, and the polished slit disks taken to EDM Labs in Garden Grove, California, where the actual slits were cut. The P200 slits, being so much larger, were cut by a process called "wire EDM" (Electrical Discharge Machining), in which cutting occurs as a current passes from a wire electrode to the metal being machined. Wire 0.005 inches in diameter is the smallest most firms use, although a few do work with wire as small as 0.002 inches diameter. However, a one-arcsecond slit at the Cassegrain focus of the P60 needs to be 64 μm in width, or 0.0025 inches. No firm could be found able to make such a slit, since it had to be located in the center of the disk and the cut could not extend out to one side; had it even been possible to thread the 0.002 inch diameter wire through a hole that size in the disk, the slit would have had semicircular ends or worse. Thus a less common process called "conventional EDM" was required, where the cutting is done with a metal blade electrode and not a long wire. EDM Labs were able to make such electrodes with rectangular cross-sections of the required slit width and length, and to cut into the center of the slit disks from above. Eight short slits for the P60 echelle spectrograph "echelle mode" were cut; the slit widths which resulted from these eight cuts are listed in Table 2-6.

At the same time these slits were being made, identical polished disks having channels 1.000 inches in length were fabricated as well, for the proposed "ordinary grating/long slit mode" of the P60 echelle spectrograph. The spectrograph optics remain unvignetted for a slit up to an inch in length. Table 2-7 lists the widths of these long slits; note that their length of 0.929 inches corresponds to 6 arcminutes in the focal plane of the P60 Cassegrain.

Six slit disks — which can be either short or long or a combination of the two kinds — are held on a rotating brass wheel in the slit compartment of the spectrograph. The slit wheel is inclined by the 10° required to direct the light reflected from the slit disk in use to the T.V. guider relay optics inside the spectrograph mounting base, and the wheel has six detents around its circumference, one at 90° from each disk. A spring-loaded roller bearing 90° from the optical axis of the telescope falls into these detents to lock the wheel in place after it has rotated from one slit position to another (see Figure 2-11, top view). Note that the brass slit wheel is rotated by a coaxial pulley powered by a stepping motor, with a 12:1 pitch diameter ratio between the pulley and the motor sprocket. This ratio was necessary in order to make the P60 echelle spectrograph slit wheel as compatible as possible with the 12-position rotating filter wheel in an off-axis X-Y guider stage being built for CCD imaging with the P60 (Cohen, 1986). However, in consultation with Shectman (1986) it was decided to follow the example of McLellan (1966) in the multi-channel spectrograph (MCSP) aperture wheel assembly and link the pulley to the brass slit wheel using a pin from the pulley into an oversize hole in the slit wheel. In this way, the slit wheel would come to rest at a final position based only on the roller falling into the detent in the edge of the slit wheel; the oversize hole would decouple the pulley from the slit wheel when the former stopped moving.

Palomar electronics engineer Mr. David Levy designed the electrical cable hookup to the stepping motor which drives the slit wheel, and has subsequently installed a photoelectric "home" sensor which initializes the wheel to one particular slit position starting from any unknown orientation. The cable arrangement is such that there is one set of connectors at the outside edge of the spectrograph above the CCD Dewar location, which is used to connect and disconnect the instrument from the stepper motor driver when the instrument is mounted or dismounted from the telescope. A second set of connectors is to be found within the slit compartment

itself, attached to the underside of the tilted slit wheel mounting bracket, which allows the slit assembly to be disconnected from the spectrograph and removed for service or access to the region beneath it. This mounting bracket is held in place on top of two leg supports (Figure 2-11) with seven large allen head cap screws, which when unscrewed permit removal of the slit wheel assembly. The legs in turn bolt onto the top of the primary mounting plate from underneath, and should not in general ever require removal. These bolts are countersunk into the primary mounting surface so as not to interfere with the locations of other optical components mounted to it. Note finally that a Uniblitz one inch diameter shutter (model 225L-0-0-T-5,X) is attached to the top of the tilted slit wheel mounting bracket, and its electrical cables follow the same path and obey the same rules as the stepper motor cables.

Located beneath the slit wheel assembly, still within the slit compartment, is a filter slide capable of holding four 1 × 2 inch filters, which are half of the standard 2 × 2 inch size in order to save space. Figures 2-13 and 2-14 (P60 echelle drawings JKM-37 and JKM-38) show the filter slide itself, which is made of brass and slides between an aluminum baseplate and two nylon runners, in order to achieve a motion which is stiff but not binding. The four filters to be used will follow the sequence employed by Oke (1985a) for order separation in the existing P60 spectrograph: (1) open; (2) 2 mm of GG 385; (3) 3 mm of GG 455; and (4) 5 mm of OG 570. The filter slide operates with a push rod located below the top level of the side plates; when the ordinary grating receptacle is built and these filters become necessary, they will be installed and detents provided in the push rod to indicate the four filter positions. Note, however, that these filters will not be located in a parallel light beam, and so the collimator focus will change as a function of their optical thicknesses. At present all four of the filter slide compartments are empty.

After passing through the filter slide, the diverging beam of light from the slit

passes through a 1 × 2 inch opening in the one inch thick primary mounting plate and enters the lower half of the spectrograph enclosure. Here it is allowed to continue 3.500 inches down from the primary mounting surface before it is reflected 90° by the flat folding mirror and is directed towards the collimating mirror. This folding mirror is held in a rectangular aluminum holder (Figure 2-15; P60 echelle drawing JKM-45) by five nylon screws; the holder was designed without any means of adjustment (other than shims where it attaches to the primary mounting surface, if necessary), and so the mirror position is essentially fixed. Note that to remove the folding mirror, the nylon screws need to be loosened slightly and the aluminum bottom bracket containing the five screws disassembled from the rest of the mounting fixture. However, if it is only necessary to remove the mirror from the spectrograph (e.g., for transportation off the mountain), an easier solution, and one less likely to scratch the mirror surface, is to remove the entire rectangular holder by means of the three bolts which attach it to the primary mounting plate.

The collimating mirror cell was not designed specifically for use in the P60 echelle spectrograph, but rather comes from a long forgotten application in another instrument. Its various pieces were reassembled for use in the P60 echelle spectrograph by Palomar senior research engineer Mr. Earle Emery. It is very similar (apart from its square and not circular mounting flange) to the collimator cell used on the existing P60 spectrograph and the P200 Digital Spectrograph. The mirror itself is mounted in an inner brass cell which fits snugly into an outer cell attached to the spectrograph. Four rectangular pins from the inner cell slide along through four channels in the outer cell. The focus adjustment is made using two threaded rings on the outside of the outer cell which push against the four pins, thereby moving the inner cell with respect to the outer cell. The forward of the two threaded rings has a scale ruled around its circumference which allows the focus position to be read in conjunction with a fixed scale on the outer cell. At present the collimator cell

is attached to the partition JKM-18 of the spectrograph in an adjustable fashion, permitting accurate alignment of the collimating mirror's optical axis; eventually the final position will be duplicated by a fixed light-tight spacer which will maintain the mirror's aligned position permanently.

After reflection by the collimating mirror, the parallel light beam passes through the first of the two cross-dispersing prisms. Because the conversion from the echelle mode to the proposed ordinary grating mode requires both prisms to be moved out of the spectrograph beam path, the two prisms are mounted together in a moveable fixture (Figure 2-16; P60 echelle drawing JKM-26) which can rotate them both out of the echelle spectrograph beam. Each of the two prisms is held in this fixture by means of a "kinematic" mounting arrangement: the prism position is defined by six adjustable points, designed following the example used in the Las Campanas 100″ Dupont telescope echelle spectrograph (Shectman and Friswold, 1985). The defining points are the round polished ends of stainless steel bolts, and opposite each is an adjustable spring which provides enough compression against the prism to maintain contact with the defining point at all times. Complicating the design of this kinematic mount and the placement of the adjustable points was the fact that the two prisms were required to be very close together, with the apex of one prism less than a quarter of an inch from the base of the other prism. However, the design is still relatively simple owing to the fact that the prisms remain in a fixed position when the spectrograph is being used in the echelle mode (i.e., once they are installed and adjusted, it is not necessary to rotate them in order to change the range of orders imaged onto the CCD, for instance).

The prism mount is in turn held in place by an analogous kinematic arrangement: the spindles and bearings on which the prism mount rotates to move the prisms out of the echelle mode beam define its position perpendicular to this axis of rotation. Rotation around this axis is terminated by a pair of ball-end studs which

fall into a V-groove in one side of the prism mount, and it is held against these studs by a captured threaded rod emerging at an angle from the side of the spectrograph structure. Finally, motion parallel to the axis of rotation and the V-groove is prevented by a clamp which holds the bottom bracket of the prism mount tightly against the primary mounting surface. The brass knob located on the upper surface of the primary mounting plate controls this clamp: turning it *counter-clockwise* as viewed from above *tightens* the clamp, and vice versa.

Note the threaded ring with locking setscrew which fits over the end of the prism rotation spindle emerging from the primary mounting plate. It is very important that this locking ring not be overlooked when re-installing the prism mount. This ring has been included in the design as a last line of defense against disaster should the bottom cover be removed while the spectrograph is upright and the prism mount is unclamped, a procedure which is still dangerous and should not be attempted: the prism mount *should always be returned to the echelle mode position and clamped to the primary mounting plate* before the bottom cover is removed.

During its rotational movement from one mode to the other, the prism mount moves over the primary mounting surface and bottom cover resting on teflon pads which Mr. Earle Emery incorporated into the prism mount design. As a result, the amount of wear suffered by the primary mounting surface is drastically reduced, and the rotation no longer binds. When clamped in place, the upper teflon pad is compressed and the prism mount comes to rest on three aluminum pads incorporated into the design at the same time.

After being dispersed and deviated by the first of the two cross-dispersing prisms, the collimated beam is diffracted by the echelle grating. This grating is also supported in a kinematic mount (see Figure 2-17; P60 echelle drawing JKM-20), based on a preliminary design by Friswold (1985), which was substantially modified

following the suggestion by Oke (1985b) that if two of the three points in the triangle underneath the grating which define its tilt were made accessible, the third could be left inaccessible and fixed without compromising the degree of possible adjustment. Because the spectrograph optical design images more than the free spectral range of all orders with $m \geq 48$ onto the CCD at once, it is only necessary to adjust the grating once so that the blaze peak is imaged onto the center column of the CCD array. No further adjustment of the kinematic points defining the grating position is ever required. Unlike the prism mount, the grating mount has been welded together, taking full advantage of the complete freedom of adjustment the kinematic mount offers to compensate for warpage and misalignment during the welding process. Only the bottom surface, which attaches to the primary mounting surface, was re-machined flat following the welding.

When designing the manner in which the grating mount would be attached to the primary mounting plate, it was realized that rotation around an axis perpendicular to the primary mounting surface would maintain the relations $\alpha = \beta_c = \theta_B$ and yet allow the angle γ to be changed. This in turn would change the particular wavelength which enters the camera system on-axis after passing through the second cross-dispersing prism; in effect, the result would be varying the range of echelle orders which are imaged onto the CCD. Hence the grating mount was not simply bolted in a fixed position but rather bolted to the primary mounting plate with one fixed bolt (that closest to the incoming light) to define an axis of rotation and two slotted holes (those farthest away) to accommodate a slight rotation around this axis. A micrometer was mounted in the side wall of the spectrograph nearest the grating mount, and a spring was installed opposite this micrometer to maintain contact between it and the grating mount. When the three mounting bolts are loosened slightly, adjustment of the micrometer moves the grating mount, changing the angle γ. This can be seen most clearly in the assembly drawing of Figure 2-18 (P60

echelle drawing JKM-100); when the motion is completed, the bolts are tightened to hold the grating mount fixed. Users of the echelle spectrograph are therefore not restricted to the 3200 Å to 7000 Å wavelength range for which the echelle mode of the instrument was originally designed.

Following diffraction by the grating, the light passes through the second of the two cross-dispersing prisms held in the kinematic prism mount described above (see again Figure 2-16), and then enters the camera lens system. It was decided that the first triplet lens component would be mounted separately and moved to focus the camera, while the doublet lens would be mounted in a separate cell attached to the front of the CCD Dewar (cf., Figure 2-18). Recall that the aplanatic sphere would act as the Dewar window, and the additional field flattening element would also serve as the CCD cover glass. Since the aplanatic sphere and cover glass are fused quartz, the UV flood lamp used to backside charge the CCD (Janesick, et al., 1985) can penetrate these elements; however, the doublet lens cell in front of the aplanat must be removed for UV flooding because the LLF6/UBK7 doublet lens does not transmit far ultraviolet light. *Care must be exercised when unscrewing the doublet cell from the rest of the Dewar optics,* since the front surface of the aplanatic sphere is quite near the place where the doublet cell separates from the Dewar. UV flooding is not required, however, for flash gated CCDs (Janesick, et al., 1986).

The triplet lens is mounted in a brass cell, held in place by a retaining ring attached to the front by three nylon screws. The brass cell is in turn mounted in an aluminum fixture which is bolted onto a ball slide attached to the primary mounting surface. This assembly is shown in Figures 2-19, 2-20, and 2-21 (all from P60 echelle drawing JKM-32). Set screws in the side of the aluminum mount are capable of pressing against the outside of the ball slide to align the triplet lens axis with the axis of the remaining camera elements. A battery operated digital readout manual micrometer (for which technical literature can be found in Appendix B)

pushes against a stainless steel arm attached to the moveable aluminum fixture, and a spring on the other side of this arm keeps it in contact with the micrometer. The micrometer spindle is attached via two bevel gears to a brass knob on the outside of the spectrograph, near the window in which the digital readout of the micrometer appears.

When the lens mount moving on the ball slide reaches the desired focus position, it can then be clamped in place by tightening two brass knobs emerging from the bottom plate of the spectrograph. These knobs are attached to rods passing alongside the lens cell and into the primary mounting plate. Held between the bottom cover and the top of the aluminum lens mounting fixture is a stainless steel clamp plate, which clamps the aluminum mount fixture onto two stainless steel pads positioned on the primary mounting surface alongside the ball slide. Following a concept originated by Friswold (1985) for the Dupont echelle spectrograph, the moveable aluminum fixture and fixed stainless steel pads are separated by a few thousandths of an inch clearance when the clamps are loose; tightening the clamps compresses the ball slide by this amount and the aluminum fixture comes to rest on the stainless steel pads. Therefore in the clamped configuration, the lens mount is not in any way dependent on the ball slide for support in maintaining its position. The technique used to achieve the desired few thousandths clearance was to underestimate the total height of the ball slide, and then to machine away the surface of the aluminum mounting fixture which rests on the ball slide until the proper fit was attained. The final height of the lens axis above the primary mounting surface is only a function of the heights of the stainless steel pads and the aluminum surface which rests upon them, and does not depend on the height of the ball slide or the final thickness of the aluminum fixture left between it and the lens. Note that because only a few thousandths of an inch separate the moveable lens mount from the fixed clamp pads, the clamps themselves do not need to be

tightened beyond "finger tight" in order to hold the lens firmly in place.

The details of the Dewar mounting design for the remaining lens elements were worked out by Mr. Earle Emery. Figure 2-22 shows an enlarged view of the front portion of the Dewar and these optics in cross-section, with the O-ring seal between the aplanatic element and the vacuum Dewar indicated. Because of these internal optics at the front of the Dewar, it is currently compatible only with the P60 echelle spectrograph, although in principle the optical design information provided in Tables 2-1 and 2-3 would enable future P60 instruments to incorporate this Dewar and CCD package, which carries the designation "CCD9" at Palomar. In §**V.B** below a revised method for attaching the CCD9 Dewar to the wall of the spectrograph is presented.

The CCD detector and readout electronics used in the echelle spectrograph CCD9 Dewar are duplicates of the standard Palomar CCD electronics design by Palomar senior electronics engineer Mr. Fred Harris. On-chip binning is permitted and is switch-selectable from within the single CCD9 saddlebag; the switch code depends on the read-out EPROM program in use at the time. Note that in the echelle mode, on-chip binning in the slit dimension is not recommended because of the difficulty this would introduce in extracting the orders from the two-dimensional frame (see §**III.B** below). Binning in the echelle dispersion direction does allow an increase in signal-to-noise ratio at the expense of resolution.

The final mechanical component of the spectrograph is the aluminum stand on which it is supported when not attached to the telescope, which was designed by Palomar design engineer Mr. Mike Carr. All three legs of this stand contain stiff springs inside protective sheaths, which serve to prevent fingers from getting pinched as the springs compress when the echelle spectrograph is mated to the telescope. Note that for greater access to the primary mounting compartment (i.e.,

inside the lower section of the instrument), or for transport of the instrument off the mountain, it is possible to remove these sheaths and replace the stiff springs by more flexible springs, and then support the spectrograph *inverted* on the aluminum stand. In this configuration the springs act as shock-absorbers, and the overall height of the stand + spectrograph is greatly reduced.

D. P60 Echelle Spectrograph Performance

In actual practice the spectrograph optics have proved quite capable of producing images with FWHM less than two pixels over nearly the full CCD detector array. The question of the $\lambda \leq 3600$ Å imaging capability of the camera lens system remains unanswered, however, because of the lack of CCD sensitivity in the near ultraviolet (see below). Another unanswered question at present concerns the origin of small ($\lesssim 0.5$ pixel) variations in the image FWHM along any given echelle order. These small changes nevertheless affect the continuum level of the extracted orders by several percent (see §**III.B** below); possible causes include misalignment of the camera system components, ripple in the surface of the CCD itself, or problems inherent in the camera lens design. The latter origin is thought to be the least likely, since the FWHM variations are not symmetric with respect to the center of the CCD, nor were they as large with previous CCD sensors used in Dewar CCD9 in the past as they are with the most recent one (sensor #305; Janesick, 1987).

The reciprocal dispersion has been measured to be $\lambda/\Delta\lambda = 38,800$ per pixel in actual fact, very nearly the nominal 40,000 dispersion expected based on the optical design. When coupled with the two pixel or less FWHM images of the spectrograph optics, this dispersion is sufficient to achieve the desired spectral resolution of roughly 20,000.

The primary respect in which the P60 echelle spectrograph has failed to meet

expectations is with regard to the near ultraviolet sensitivity of the CCD, which severely compromises the wavelength coverage for which the instrument was designed. In attempts to overcome this problem, three different CCD sensors have been used in Dewar CCD9, each of which has been too thick to achieve the "Q.E. pinned" condition of maximum blue sensitivity. CCD9 sensor #305 is the best so far, having 20% Q.E. at 9000 Å, 55% at 6000 Å, and 15% at 4000 Å, according to measurements made at J.P.L. (Janesick, 1987). Note that the response in the corners of the CCD array is much better than in the center, because typically the corners of a TI3ϕCCD are thinner than the central region of the device.

To offset this lack of near ultraviolet sensitivity, the echelle grating has been moved with the micrometer adjustment described above (see §**II.C**) to bring echelle orders $35 \leq m \leq 94$ and beyond into view on the CCD detector. While this adjustment extends the long wavelength limit from 7000 Å to over 9500 Å, note that beyond 7000 Å the wavelength coverage is not continuous because the order free spectral range ($\Delta\beta$ in equation (2.3) above) is larger in angular extent than the CCD. It is also true that beyond 7000 Å the order center to order center separation is less than the length of the slit, but in practice the amount of order to order contamination that results from this is not serious at the adjacent order centers.

If the wavelength coverage has fallen short of expectations, the high throughput of the P60 echelle spectrograph has equalled or exceeded them. Figure 2-23 shows the total system (i.e., P60 telescope mirrors, echelle spectrograph, and detector CCD9) peak efficiency of each order as a function of wavelength. This figure is based on a 2000^{s} exposure of the $V = 12.^{m}3$ flux standard v Ma 2, courtesy of Dr. I. Neill Reid of Caltech. The observed flux was calculated from the mean continuum level $\langle DN \rangle$ in each order as follows:

$$\langle f_{\rm obs} \rangle = \frac{\langle DN \rangle \times 1.89 e^{-}/DN}{t_{\rm sec} \times A_{\rm P60} \times \text{Å/pixel}} \tag{2.14}$$

where $t_{\rm sec} = 2000$ is the exposure time in seconds, and $A_{\rm P60} = 16,600\,{\rm cm}^2$ is the surface area of the P60 telescope. Equation (2.14) then becomes:

$$\langle f_{\rm obs} \rangle = 5.693 \times 10^{-8}\ e^-/{\rm sec}/{\rm cm}^2/{\rm \AA}\ \times \frac{\langle DN \rangle}{{\rm \AA/pixel}}\ . \tag{2.15}$$

The expected fluxes follow from the calibration of Oke (1974), giving fluxes $f^\circ_{\rm mJy}$ in milli-Janskys (1 mJy $= 10^{-26}$ erg/sec/cm^2/Hz), so that:

$$\begin{aligned} f_{\rm exp} &= f^\circ_{\rm mJy} \times 10^{-26} \left(\frac{c}{\lambda^2}\right)\left(\frac{\lambda}{hc}\ {\rm photons/erg}\right) \\ &= 1.509\ {\rm photons/sec/cm}^2/{\rm \AA}\ \times \frac{f^\circ_{\rm mJy}}{\lambda_{\rm A}}\ . \end{aligned} \tag{2.16}$$

For example, at wavelengths near Hα, $\langle DN \rangle = 2768$, and Å/pixel = 0.171, yielding $\langle f_{\rm obs} \rangle = 9.24 \times 10^{-4}\ e^-/{\rm sec}/{\rm cm}^2/{\rm \AA}$, while $f^\circ_{\rm mJy} = 45.709$ and $\lambda_{\rm A} = 6565$ so that $f_{\rm exp} = 1.04 \times 10^{-2}$ photons/sec/cm^2/Å. The efficiency:

$$\eta_{\rm tot} = \langle f_{\rm obs} \rangle / f_{\rm exp} = 0.088 \tag{2.17}$$

at Hα, or 8.8%, as shown in Figure 2-23. The decline of $\eta_{\rm tot}$ for $\lambda \leq 5000$ Å as well as for $\lambda \geq 6500$ Å is due to the decrease in Q.E. of the CCD; from the peak $\eta_{\rm tot}$ of 11% at $\lambda = 6000$ Å and the Q.E.(6000 Å) = 0.55 for CCD9 as measured at J.P.L. (Janesick, 1987), one can conclude that the P60 telescope and echelle spectrograph together deliver approximately 20% of the incoming light to the CCD detector array.

Finally, the P60 echelle spectrograph has proven to be quite resistant to the effects of mechanical flexure. Preliminary tests conducted by this author have revealed only a 0.2 pixel shift in the echelle dispersion direction and a 1.0 pixel shift in the cross-dispersion direction between the zenith and hour angles of six hours east or west. This was subsequently confirmed with detailed measurements by Dr. I. Neill Reid, which are presented in Table 2-8. Note that the primary scientific focus of this work dealt not with radial velocity measurements but rather with

determining accurate stellar line profiles. Therefore the major thrust of the data reduction process described in Chapter **III** dealt with background subtraction and continuum normalization issues.

TABLE 2-1

Radii, Thicknesses, and Materials for Long Camera System

Surface (1)	Radius, cm (2)	Thickness, cm (3)	Material (4)	n(4047 A) (5)
1	0.00000000	30.00000000	AIR	1.000000
2	14.10648862	1.25000000	SILICA	1.469621
3	6.84380600	3.10000000	CAFL2	1.441610
4	-9.24157625	1.25000000	SILICA	1.469621
5	0.00000000	23.47041832	AIR	1.000000
6	4.66677588	6.00000000	SILICA	1.469621
7	6.84380600	0.70000000	AIR	1.000000
8	-14.10648862	0.20000000	SILICA	1.469621
9	0.00000000	0.10000000	AIR	1.000000
10	0.00000000	0.00000000	AIR	1.000000

Surface (6)	MELT INDICES 4047 A (7)	3650 A (8)	5461 A (9)	3200 A (10)	7000 A (11)
2	1.469621	1.474536	1.460079	1.482740	1.455290
3	1.441610	1.444996	1.434944	1.450560	1.431760
4	1.469621	1.474536	1.460079	1.482740	1.455290
6	1.469621	1.474536	1.460079	1.482740	1.455290
8	1.469621	1.474536	1.460079	1.482740	1.455290

TABLE 2-2

Long Camera rms Spot Diameters[a,b]

CCD Field Angle (1)	Wavelength 320.0 nm (2)	365.0 nm (3)	404.7 nm (4)	546.1 nm (5)	700.0 nm (6)
on axis:	18.9 (10.3)	14.3 (6.1)	4.5 (3.7)	32.9 (1.4)	22.9 (4.0)
halfway:	22.1 (12.4)	18.1 (7.2)	8.7 (5.0)	27.4 (6.5)	18.3 (9.6)
at edge:	31.0 (19.4)	29.2 (11.6)	21.8 (9.1)	16.0 (13.0)	18.9 (18.3)

[a] Monochromatic rms spot diameters are listed above in microns as a function of field angle and wavelength at the "best focus."

[b] Numbers in parentheses indicate the rms spot diameters possible if focussing is optimized for that wavelength and field position in particular.

TABLE 2-3

Radii, Thicknesses, and Materials for Short Camera System

Surface (1)	Radius, cm (2)	Thickness, cm (3)	Material (4)	n(4047 A) (5)
1	0.00000000	30.00000000	AIR	1.000000
2	14.10648862	1.25000000	SILICA	1.469621
3	6.84380600	3.10000000	CAFL2	1.441610
4	-9.24157625	1.25000000	SILICA	1.469621
5	0.00000000	9.87202477	AIR	1.000000
6	28.13402568	1.00000000	LLF6	1.549770
7	7.34320820	1.50000000	UBK7	1.529860
8	0.00000000	5.25000000	AIR	1.000000
9	4.66677600	6.00000000	SILICA	1.469621
10	6.84380600	0.70000000	AIR	1.000000
11	-14.10648862	0.20000000	SILICA	1.469621
12	0.00000000	0.10000000	AIR	1.000000
13	0.00000000	0.00000000	AIR	1.000000

	MELT INDICES				
Surface (6)	4047 A (7)	3650 A (8)	5461 A (9)	3200 A (10)	7000 A (11)
2	1.469621	1.474536	1.460079	1.482740	1.455290
3	1.441610	1.444996	1.434944	1.450560	1.431760
4	1.469621	1.474536	1.460079	1.482740	1.455290
6	1.549770	1.558850	1.533440	1.575969	1.525943
7	1.529860	1.535870	1.518390	1.546258	1.512705
9	1.469621	1.474536	1.460079	1.482740	1.455290
11	1.469621	1.474536	1.460079	1.482740	1.455290

TABLE 2-4

Short Camera rms Spot Diameters[a,b]

CCD Field Angle (1)	Wavelength 320.0 nm (2)	365.0 nm (3)	404.7 nm (4)	546.1 nm (5)	700.0 nm (6)
on axis:	3.5 (0.7)	26.6 (3.1)	22.3 (4.9)	19.4 (8.4)	30.3 (10.4)
halfway:	10.6 (8.3)	26.2 (4.3)	26.2 (4.4)	16.8 (9.0)	26.8 (12.3)
at edge:	32.7 (26.7)	26.4 (16.0)	24.3 (10.6)	10.8 (8.3)	18.1 (13.4)

[a] Monochromatic rms spot diameters are listed above in microns as a function of field angle and wavelength at the "best focus."

[b] Numbers in parentheses indicate the rms spot diameters possible if focussing is optimized for that wavelength and field position in particular.

TABLE 2-5

Echelle Spectrograph Design Parameters

Spectrograph Parameter (1)	Value (2)
Grating grooves/mm	52.65 /mm
Grating blaze angle	63.43 deg
Camera/Collimator angle	19.53 deg
Camera E.F.L.	144.01 mm
Collimator F.L.	461.52 mm
P60 Cassegrain scale	64.1 um/"
CCD Image scale	1.5 px/"
CCD Pixel size	15 um sq.
CCD Array size	800 x 800 pixels
CCD Physical size	12 mm sq.
Prism apex angles	60.00 deg

TABLE 2-6

Dimensions of Short Slits (Echelle Mode)

Disk ID Label (1)	Width arcsec. (2)	Width inches (3)	Length arcsec. (4)	Length inches (5)
S-1	0.81 +/- 0.03	0.0021	7.28 +/- 0.03	0.0188
S-2	1.43	0.0037	7.36	0.0190
S-3	2.13	0.0055	7.90	0.0204
S-6	2.48	0.0064	7.86	0.0203
S-5	3.76	0.0097	7.86	0.0203
S-7	0.77 dia.	0.0020	--	--
*S-8	0.74 +/- 0.03	0.0019	7.24 +/- 0.03	0.0187
*S-4	2.94	0.0076	7.44	0.0192

* These slits are not currently installed on the six position rotating slit wheel of the P60 echelle spectrograph.

TABLE 2-7

Dimensions of Long Slits (Oridinary Grating Mode) *

Disk ID Label (1)	Width arcsec. (2)	Width inches (3)	Length arcsec. (4)	Length inches (5)
L-1	9.22 +/- 0.03	0.0238	360 +/- 0.3	0.930
L-2	0.74	0.0019	360	0.929
L-3	1.32	0.0034	360	0.929
L-4	2.05	0.0053	360	0.929
L-5	3.33	0.0086	360	0.929
L-6	9.22	0.0238	360	0.929
L-8	3.99	0.0103	360	0.929
L-9	3.33	0.0086	360	0.929
L-10	4.65	0.0120	360	0.929
L-7	2.0 +/- 0.3	0.005	360 +/- 3	0.93

* These slits are not currently installed on the six position rotating slit wheel of the P60 echelle spectrograph.

TABLE 2-8

Flexure Shifts of P60 Echelle Spectrograph[a,b,c]

Decl. (1)	Hour Angle -3 (2)	-2 (3)	-1 (4)	0 (5)	1 (6)	2 (7)	3 (8)
+75	0.159	< 0.115 >		0.055	< 0.022 >		-0.028
+50	0.122	0.099	0.063	0.027	0.010	-0.032	-0.098
+32	0.080	0.056	0.029	0.000	-0.060	-0.119	-0.180
0	0.043	0.040	0.006	-0.044	-0.052	-0.062	-0.039
-20		< -0.007 >		-0.077	< -0.094 >		

a Flexure shifts in the echelle dispersion direction in pixels (1 pixel = 15 microns), relative to the zenith (Decl. = +32, Hour Angle = 0).

b Numbers in angle brackets, < >, represent +/- 1.5 Hour Angles.

c Based measurements provided by Dr. I. Neill Reid of He+Ne+Ar+Hg arc images cross-correlated in the order containing the D lines of NaI.

Bibliography

Bardas, D., 1977. *Pub. Astron. Soc. Pac.*, v. **89**, p. 104.

Blouke, M.M., Breitzmann, J.F., and Hall, J.E., 1978. *Proc. IEEE ISSCC*, v. **36**.

Blouke, M.M., Janesick, J.R., Hall, J.E., Cowens, M.W., and May, P.J., 1983. *Opt. Engr.*, v. **22**, p. 607.

Born, M., and Wolf, E., 1980. *Principles of Optics*, 6^{th} *ed.* (Oxford: Pergammon Press).

Bowen, I.S., 1952. *Ap. J.*, v. **116**, p. 1.

Butcher, H.R., 1974. *Ph.D. Thesis*, Australian National Univ., Canberra.

Chaffee, F.H., and Schroeder, D.J., 1976. *Ann. Rev. Astron. Astrophys.*, v. **14**, p. 23.

Cohen, J.G., 1986. Private communication.

Friswold, C.L., 1985. Private communication.

Harrison, G.R., 1949. *J. Opt. Soc. Am.*, v. **39**, p. 522.

Janesick, J.R., Elliott, T., Collins, S.A., Marsh, H., Blouke, M.M., and Freeman, J., 1984. *Proc. SPIE*, v. **501**.

Janesick, J.R., Elliott, T., Daud, T., and McCarthy, J.K., 1985. *Proc. SPIE*, v. **570**, p. 46.

Janesick, J.R., Elliott, T., Daud, T., and Campbell, D., 1986. *Proc. SPIE*, v. **627**, p. 543.

Janesick, J.R., 1987. *J.P.L. Memorandum, dated 26-April-1987*, unpublished.

Kudritzki, R.P., 1984. Private communication.

Learner, R.C.M., 1972. In *Auxiliary Instrumentation for Large Telescopes*, eds. S. Lausten and A. Reiz (Geneva: European Southern Obs.), p. 131.

Loomis, D., 1985. Private communication.

McCarthy, J.K., 1985. *Proc. SPIE,* v. **554**, p. 155.

McLellan, W.H., 1966. *MCSP Drawing # 105485,* unpublished.

Oke, J.B., 1974. *Ap. J. Suppl. Ser.,* v. **27**, p. 21.

Oke, J.B., 1984. Private communication.

Oke, J.B., 1985a. *P60 Spectrograph Manual,* unpublished.

Oke, J.B., 1985b. Private communication.

Ramsey, L.W., 1986. Private communication.

Rayton, W.B., 1930. *Ap. J.,* v. **72**, p. 59.

Rense, W.A., 1966. *Space Sci. Rev.,* v. **5**, p. 234.

Schechter, P.L., 1984. Private communication.

Schroeder, D.J., 1970. *Pub. Astron. Soc. Pac.,* v. **82**, p. 1253.

Shectman, S.A., 1983. Private communication.

Shectman, S.A., and Friswold, C.L., 1985. Private communication.

Shectman, S.A., 1986. Private communication.

Shectman, S.A., 1987. Private communication and assistance.

Smakula, A., 1962. *Opt. Acta.,* v. **9**, p. 205.

Tonry, J., and Davis, M., 1979. *A. J.,* v. **84**, p. 1511.

Wheeler, C.C., 1975. *"Formulae for Astronomical Grating Spectrographs"* (Perkin-Elmer Corporation, Applied Optics Division), unpublished.

Walker, D.D., and Diego, F.G., 1983. *"An Evaluation of Possible Designs for the Proposed Echelle Spectrograph at the AAT"* (University College London), unpublished report dated 12/83.

Walker, D.D., Diego, F.G., Charalambous, A., Hirst, C., and Fish, A., 1986. *Proc. SPIE,* v. **627**, p. 291.

Figure Captions

Figure 2-1: The grating nomenclature used in the text. For Quasi-Littrow, $\alpha = \beta = \theta_B$ and $\gamma \neq 0$.

Figure 2-2: A schematic representation of the P60 echelle spectrograph optical layout. The labels denote the following: (M) collimator diagonal mirror; (C) off-axis paraboloid collimating mirror; (P_1) first cross-dispersing prism; (E) echelle grating; (P_2) second cross-dispersing prism; (T) camera triplet lens; (D) camera doublet lens; and (A) camera aplanatic sphere.

Figure 2-3: A demonstration of the aplanatic principle, reprinted from Figure 4.9 of Born and Wolf (1980).

Figure 2-4: The camera lens system optical design. Note that the conversion from the short camera to the long camera is accomplished by removing the doublet lens and relocating the CCD Dewar at the new focus position farther from the triplet lens.

Figure 2-5: The combined transmission of the two anti-reflection coatings applied to the camera system optics, measured by Newport Thin Film Lab at normal incidence.

Figure 2-6: The combined transmission of the two anti-reflection coatings applied to the prisms cross-dispersers, measured by Newport Thin Film Lab at 45° incidence.

Figure 2-7: The predicted echelle format on the CCD detector based on the optical design of §**II.A** and §**II.B**. Each tilted line is a separate echelle order, and the (*) at the end of each order marks the end of the free spectral range of that order. The small tick marks are at 5 Å intervals; the larger ones are at 50 Å and 100 Å intervals. The orders $48 \leq m \leq 104$ are shown, covering the short camera wavelength range of 3200 Å to 7000 Å.

Figure 2-8: Same as Figure 2-7 except the reduced imaging area of the long camera is indicated. Note that continuous wavelength coverage is now possible only from 5300 Å to 3300 Å.

Figure 2-9: The top view of the spectrograph structure; a full scale version of this figure exists as P60 echelle drawing JKM-13.

Figure 2-10: The side view of the spectrograph structure; a full scale version of this figure exists as P60 echelle drawing JKM-14.

Figure 2-11: Side and top views of the slit compartment; the side view shows the spectrograph mounting flange, barn door cover, rotating slit assembly, and location of the filter slide. The top view shows the detents and tangent arm assembly. Both views exist full scale as P60 echelle drawing JKM-50.

Figure 2-12: The design of the individual slit disks. Eight of these were made with channels 0.250″ long for the short slits, while ten of them have channels 1.000″ long for the long slits. A full scale version of this figure exists as P60 echelle drawing JKM-52.

Figure 2-13: The top view of the spectrograph filter slide. Note that the slide is designed to accomodate four 1 × 2 inch filters. A full scale version of this figure exists as P60 echelle drawing JKM-37.

Figure 2-14: The end view of the spectrograph filter slide; a full scale version of this figure exists as P60 echelle drawing JKM-38 (?).

Figure 2-15: The collimator diagonal mirror mount; a full scale version of this figure exists as P60 echelle drawing JKM-45.

Figure 2-16: The top view of the cross-dispersing prism kinematic mounting. The prisms themselves are shown cross-hatched. A full scale version of this figure exists as P60 echelle drawing JKM-26.

Figure 2-17: The echelle grating kinematic mount, with holds the grating at a constant angle of $\theta_B = 63°26'$ with respect to the incoming optical axis. A full scale verion of this figure exists as P60 echelle drawing JKM-20.

Figure 2-18: The top view of the complete P60 echelle spectrograph assembly. Note the small space between the collimator diagonal, prism mount, and triplet camera lens mount. Also shown are the modified Dewar mounting arrangement and the micrometer adjustment for the echelle grating rotation. A full scale version of this figure exists as P60 echelle drawing JKM-100.

Figure 2-19: The camera system triplet lens mount (side view), showing the focus and clamp mechanisms. A full scale version of this figure exists as P60 echelle drawing JKM-32.

Figure 2-20: The camera system triplet lens mount (end view), also from P60 echelle drawing JKM-32.

Figure 2-21: The camera system triplet lens mount (top view), also from P60 echelle drawing JKM-32.

Figure 2-22: The rear elements of the camera lens system integrated with the front of Dewar CCD9, as per the design by Mr. Earle Emery. This figure was adapted from P60 echelle drawing JKM-100.

Figure 2-23: The total system efficiency of the Palomar 60-inch telescope, P60 echelle spectrograph, and CCD9 as a function of wavelength. The crosses are the peak efficiency of each echelle order, based on an echelle spectrum of the standard star v Ma 2 taken by Dr. I. Neill Reid.

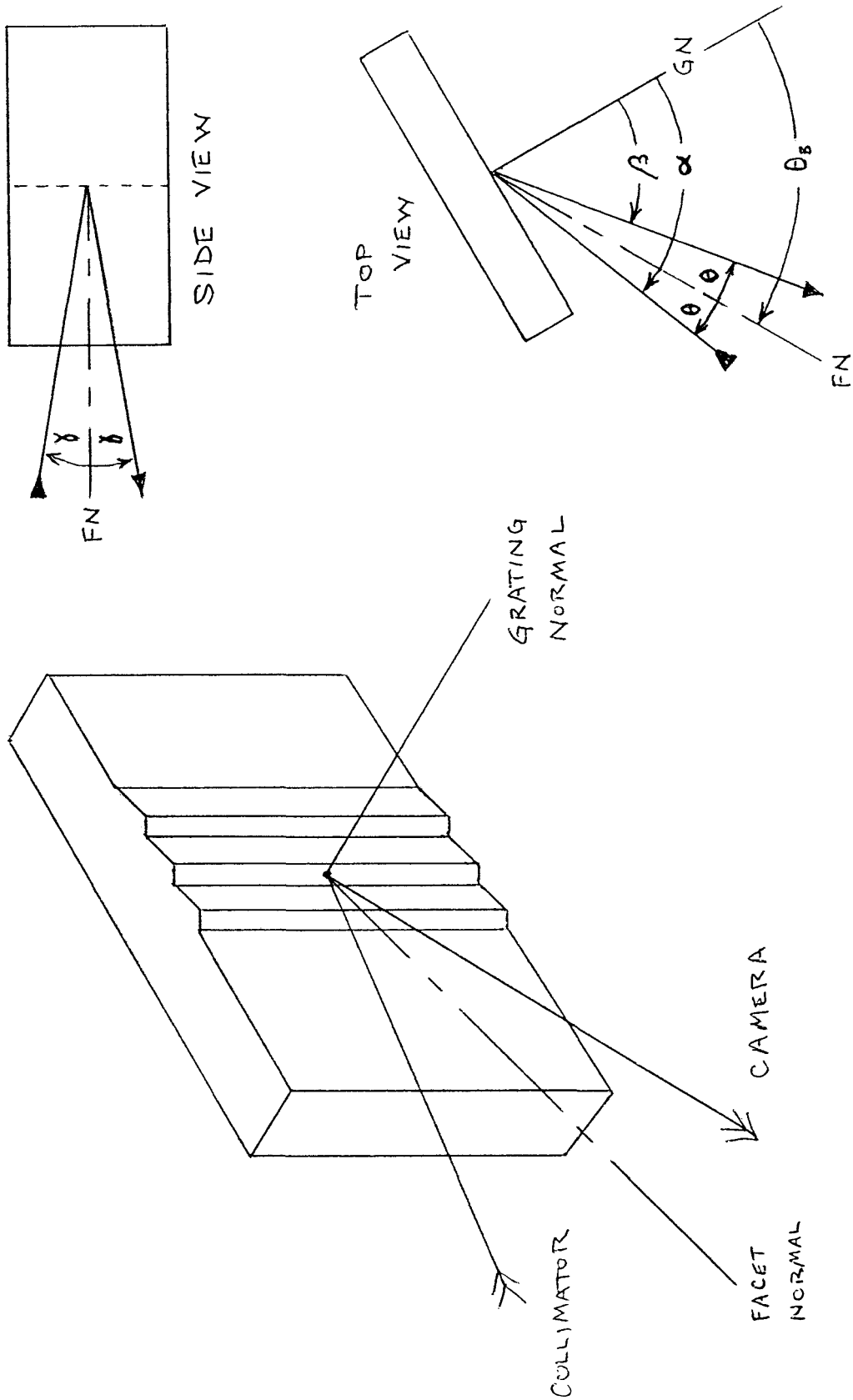
SIDE VIEW
γ
δ
FN
TOP VIEW
GN
β
α
θB
θ
θ
FN
GRATING NORMAL
CAMERA
COLLIMATOR
FACET NORMAL

Figure 2-1

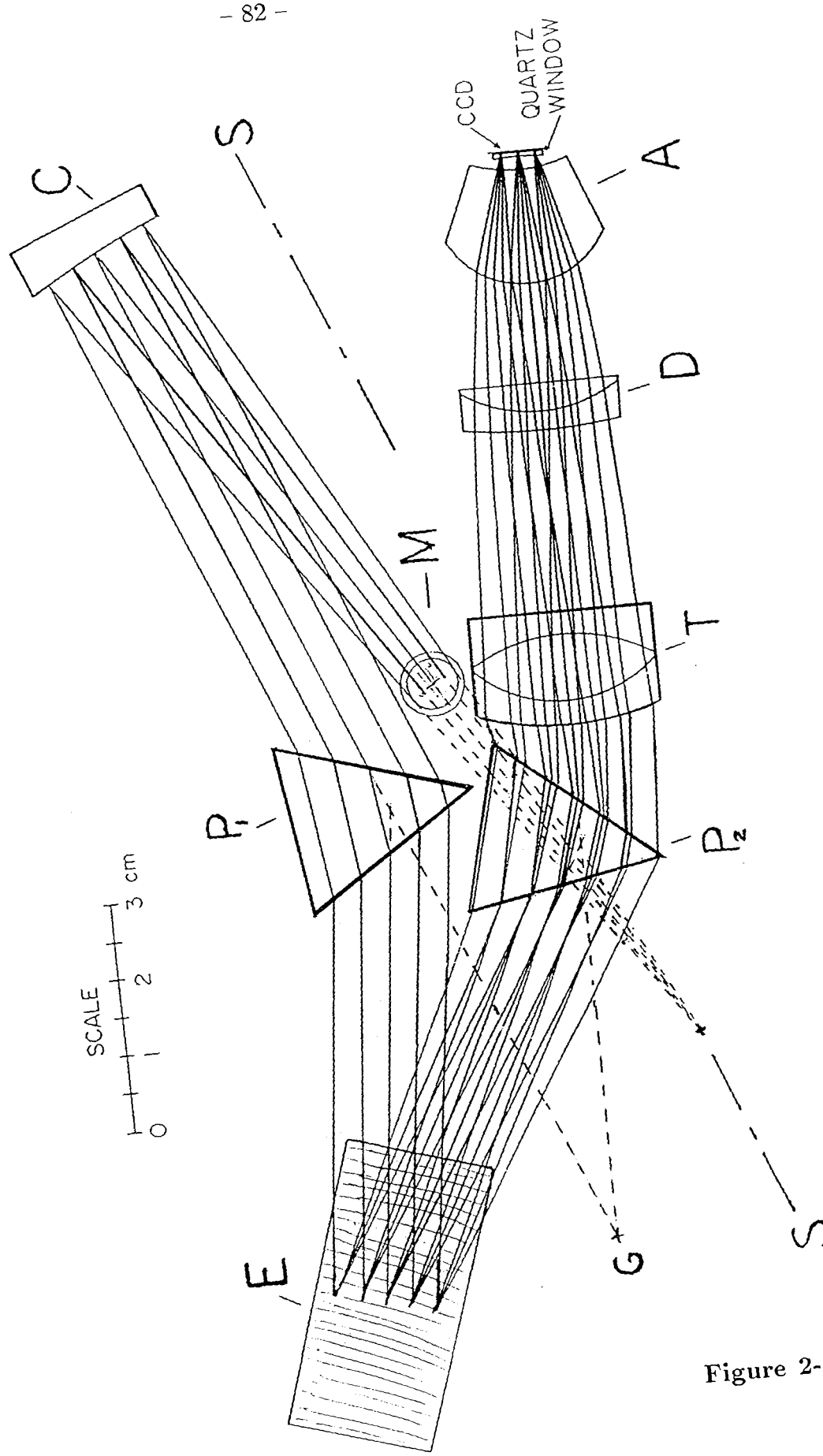

Figure 2-2

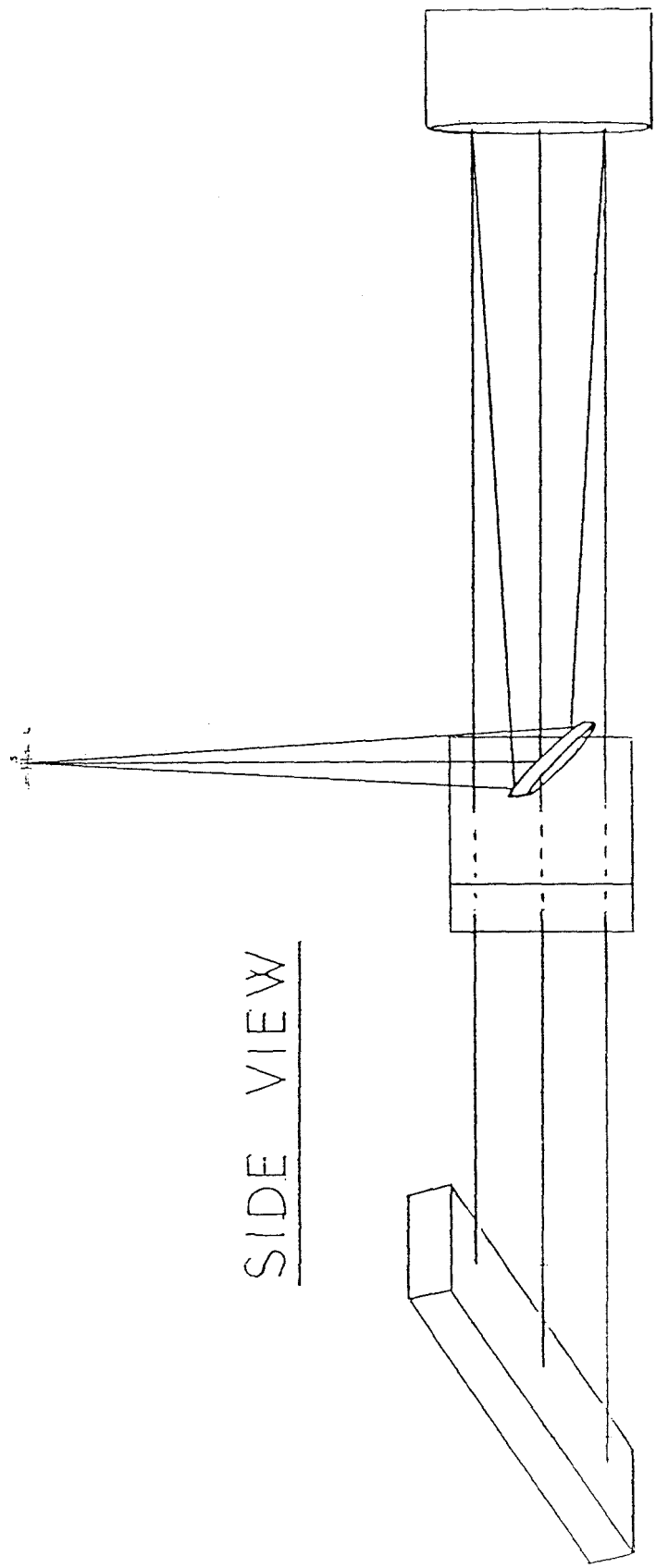

Figure 2-2
(continued)

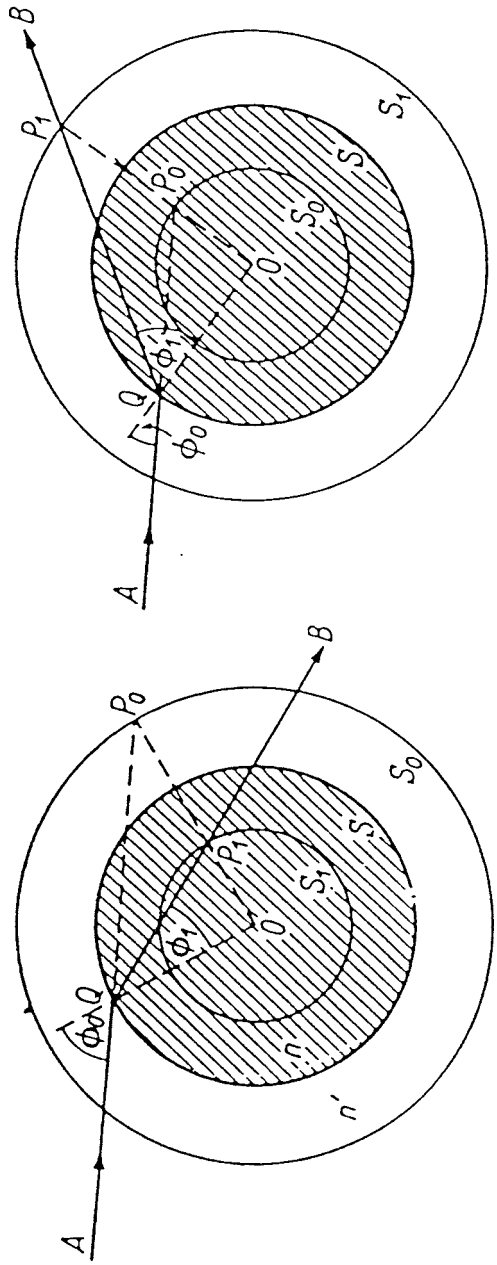

Fig. 4.9. Refraction at a spherical surface. Aplanatic points.

Figure 2-3

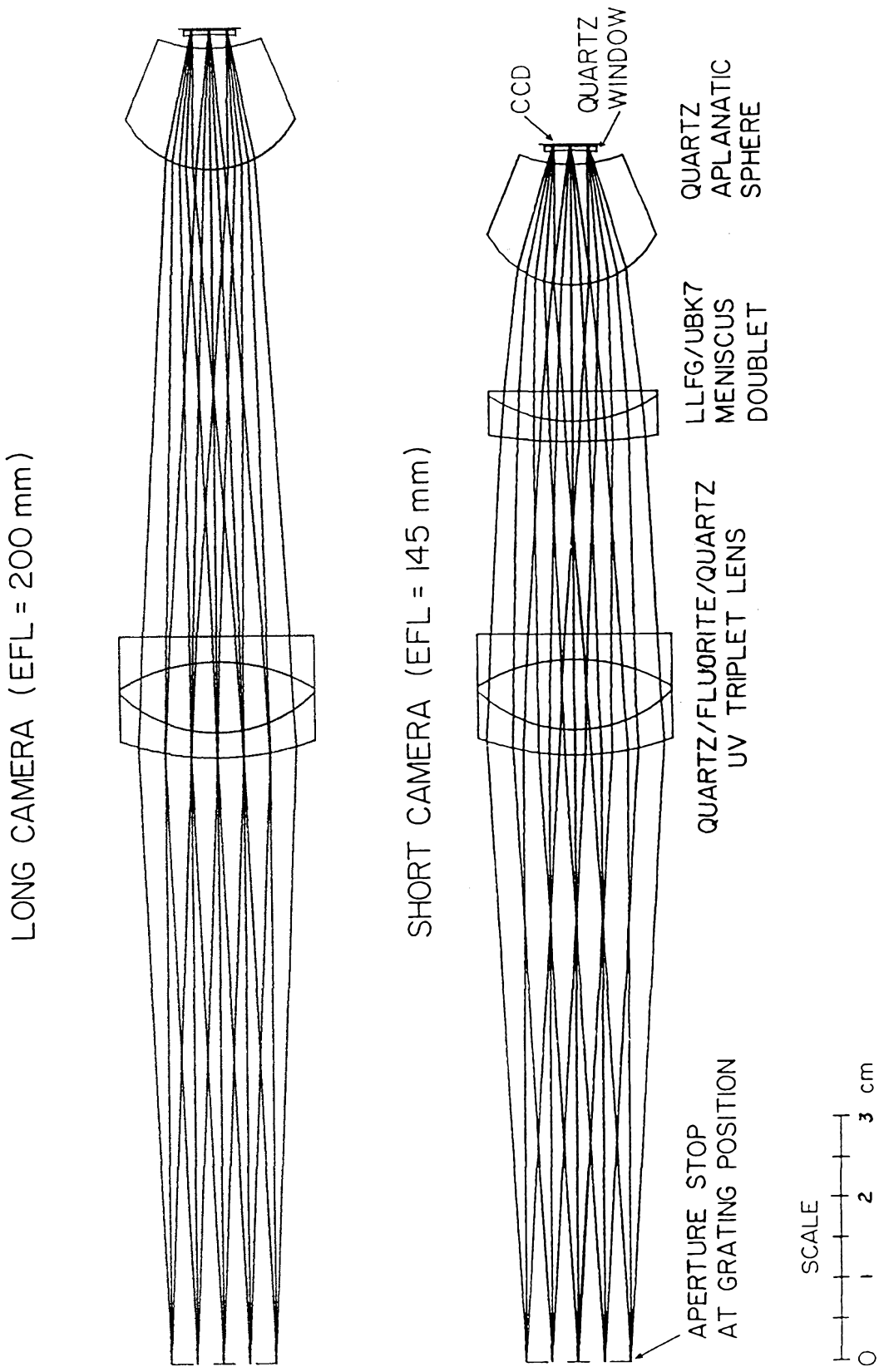
LONG CAMERA (EFL = 200 mm)
SHORT CAMERA (EFL = 145 mm)
CCD
QUARTZ WINDOW
QUARTZ APLANATIC SPHERE
LLFG/UBK7 MENISCUS DOUBLET
QUARTZ/FLUORITE/QUARTZ UV TRIPLET LENS
APERTURE STOP AT GRATING POSITION
SCALE
0
1
2
3 cm

Figure 2-4

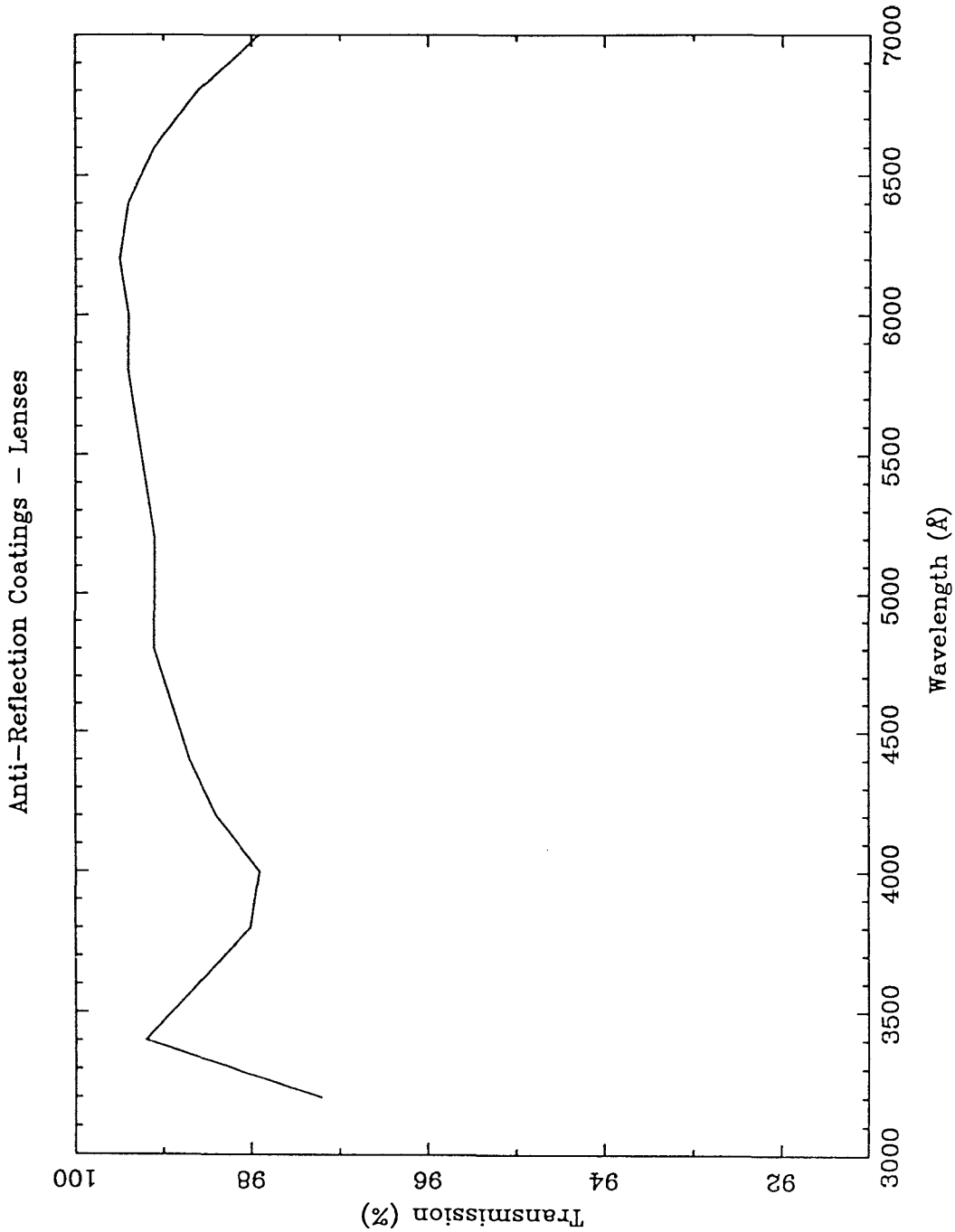
Anti-Reflection Coatings – Lenses
Transmission (%)
100
98
96
94
92
3000
3500
4000
4500
5000
5500
6000
6500
7000
Wavelength (Å)

Figure 2-5

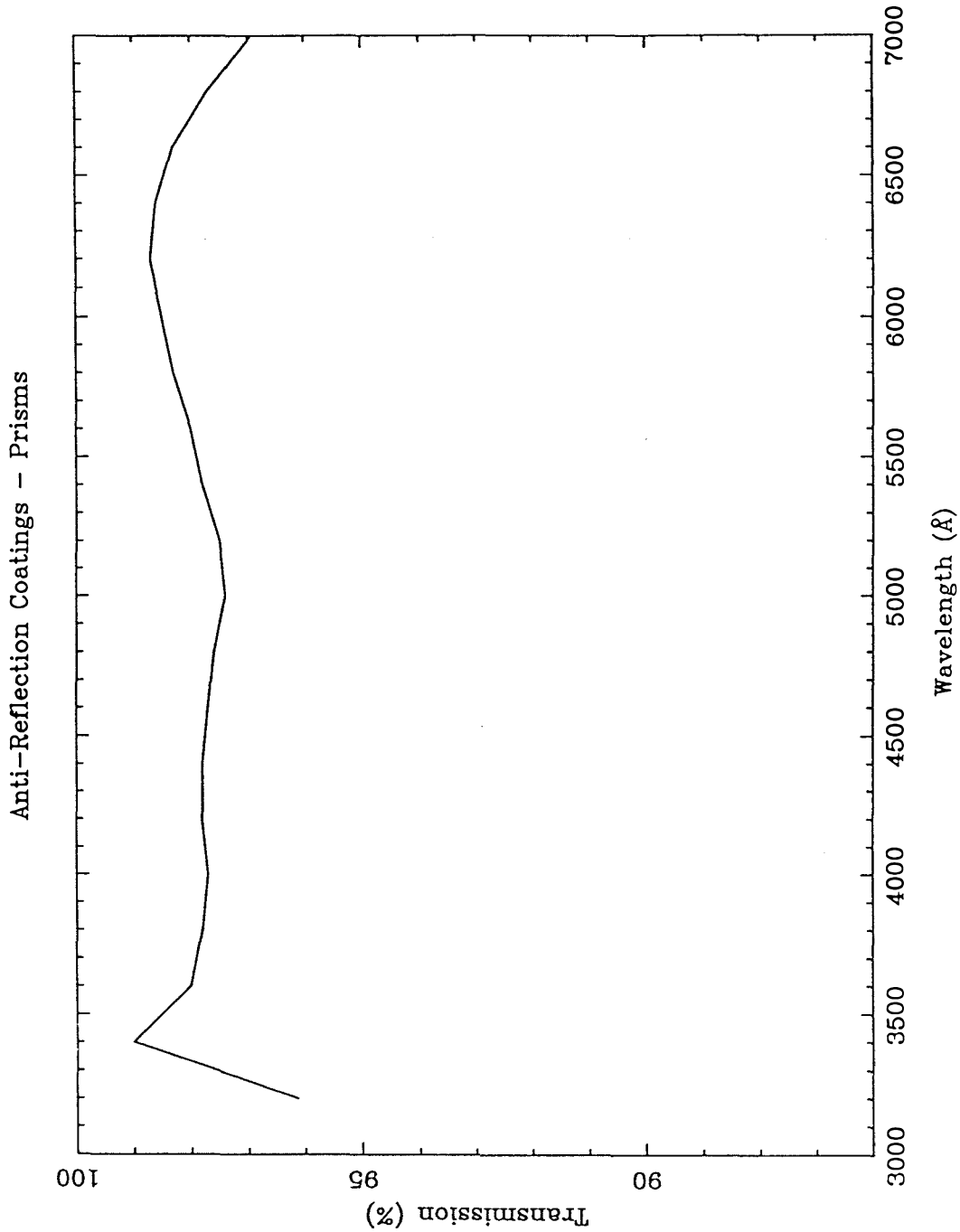
Anti-Reflection Coatings - Prisms
Transmission (%)
100
95
90
3000
3500
4000
4500
5000
5500
6000
6500
7000
Wavelength (Å)

Figure 2-6

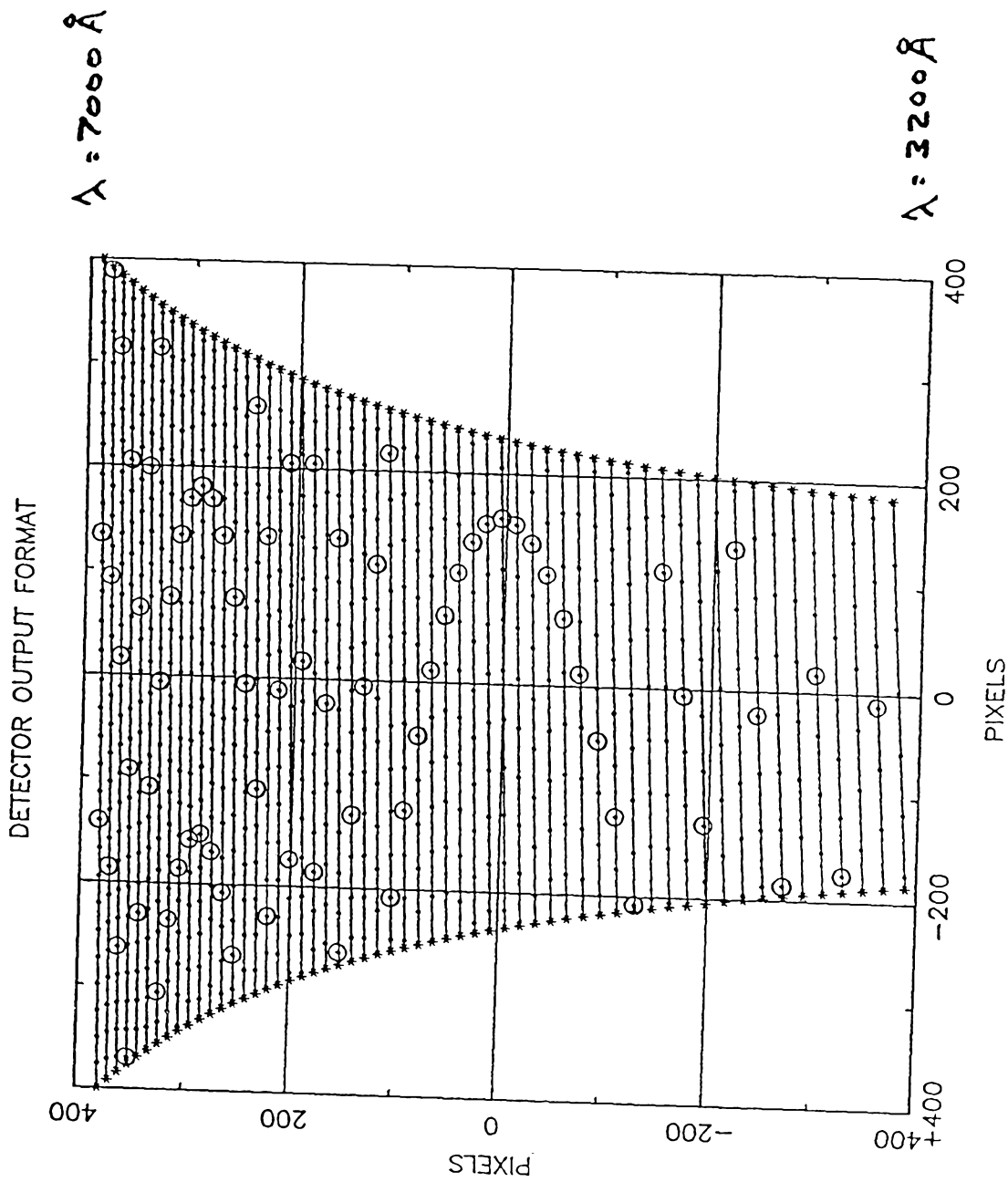
λ = 7000 Å
λ = 3200 Å
DETECTOR OUTPUT FORMAT
PIXELS
PIXELS
400
200
0
−200
−400
400
200
0
−200
−400

Figure 2-7

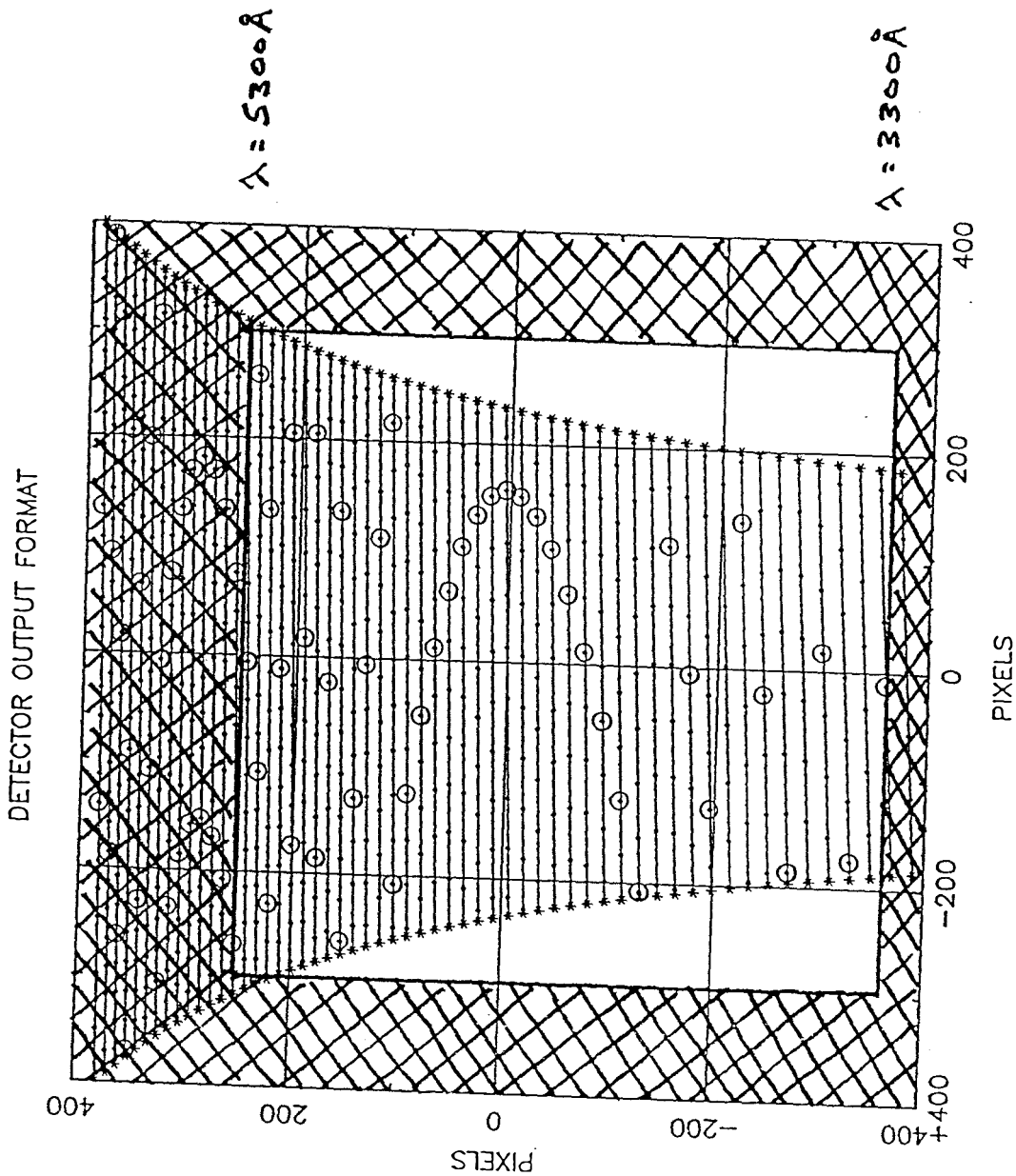
λ = 5300Å
λ = 3300Å
DETECTOR OUTPUT FORMAT
PIXELS
400
200
0
−200
−400
PIXELS
400
200
0
−200
−400

Figure 2-8

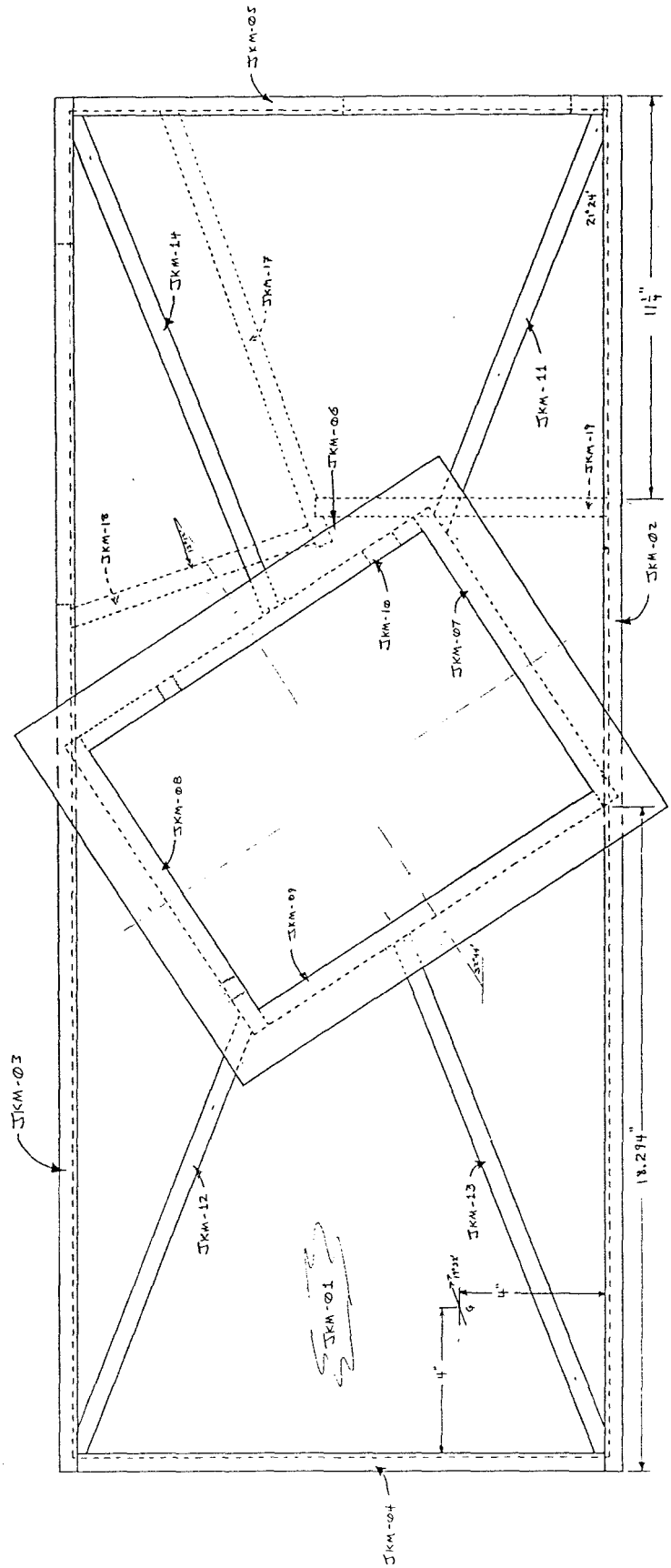
JKM-05
JKM-14
JKM-17
JKM-11
JKM-06
JKM-19
JKM-15
JKM-10
JKM-07
JKM-02
JKM-08
JKM-09
JKM-03
JKM-12
JKM-13
JKM-01
JKM-04
11½"
18.294"
4"
4"

Figure 2-9

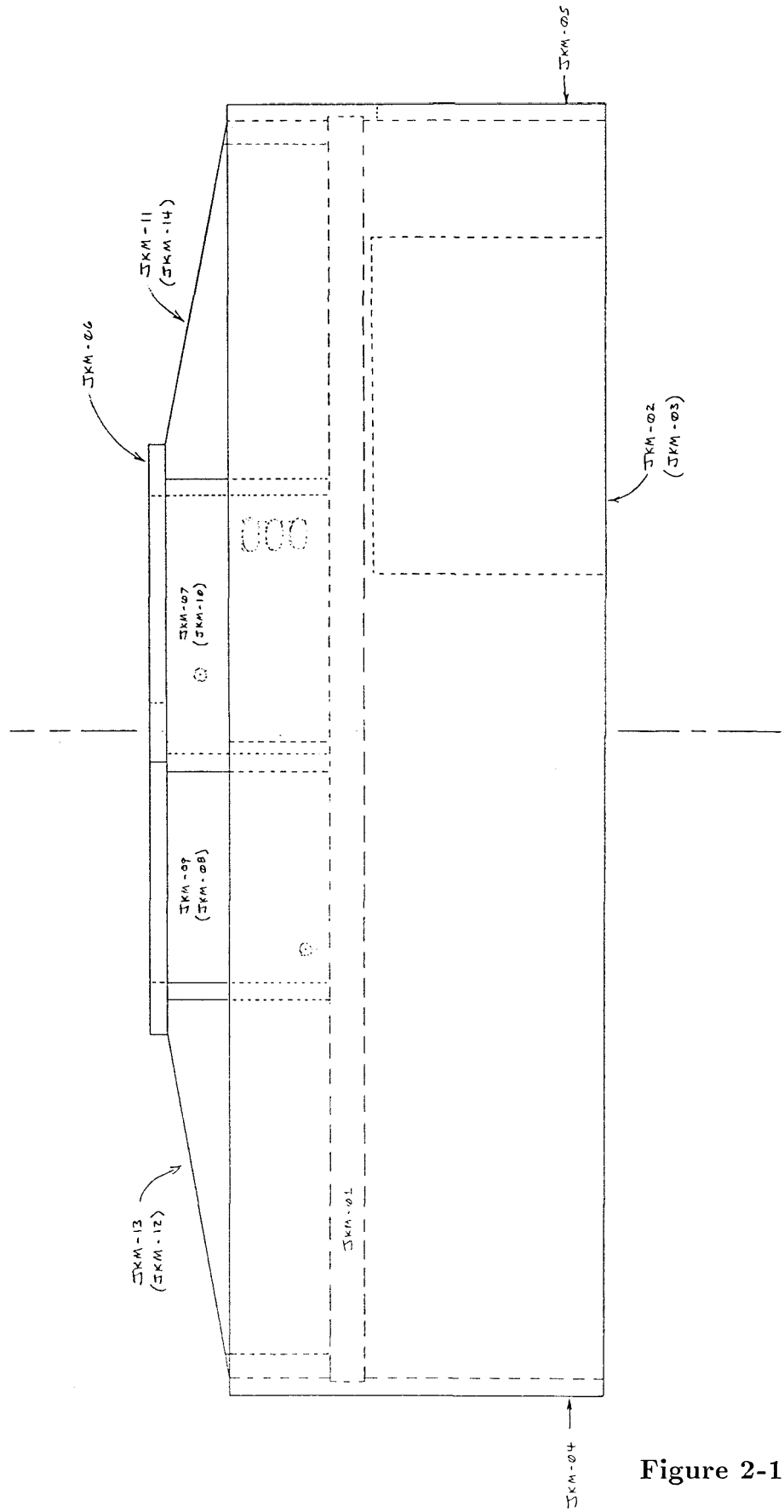
JKM-05
JKM-11
(JKM-14)
JKM-06
JKM-02
(JKM-03)
JKM-07
(JKM-10)
JKM-09
(JKM-08)
JKM-13
(JKM-12)
JKM-01
JKM-04

Figure 2-10

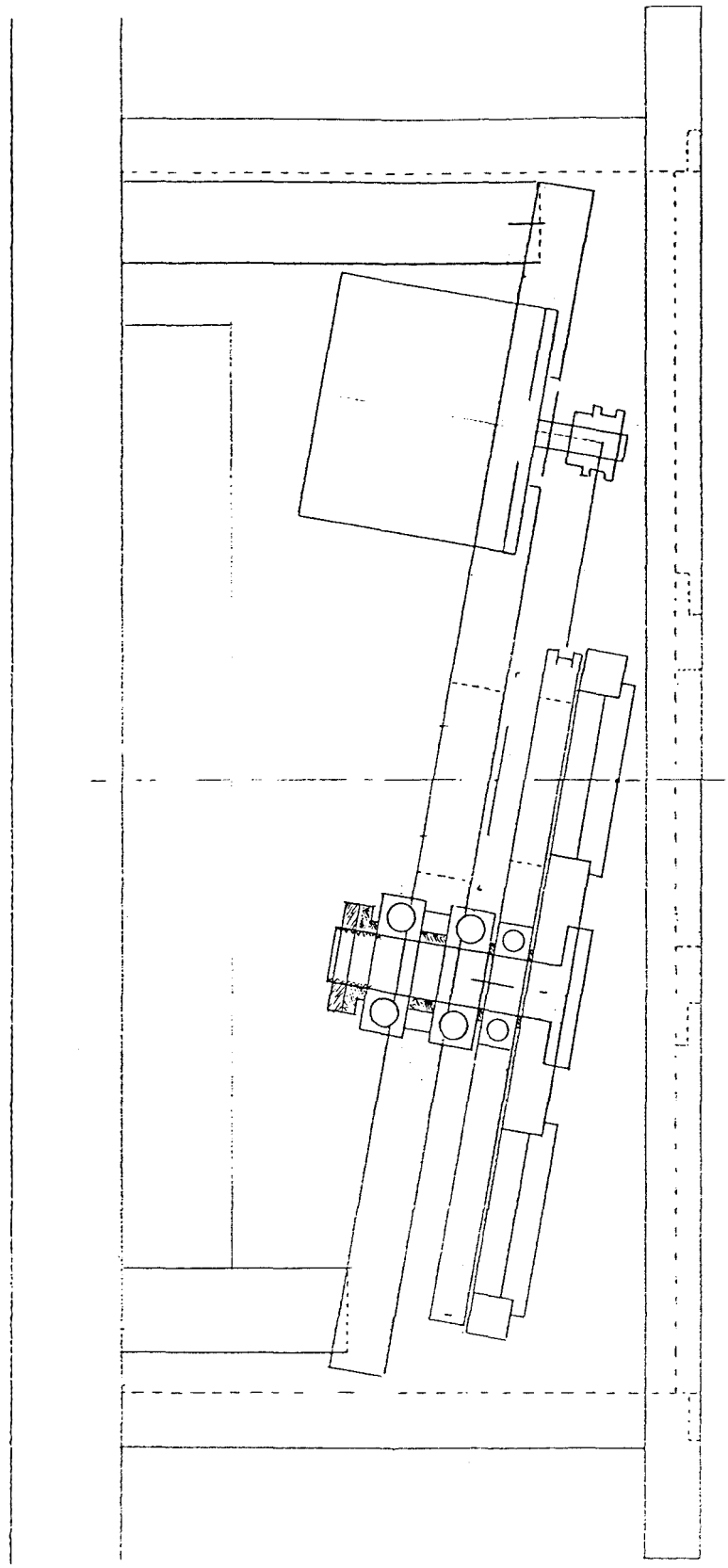

Figure 2-11

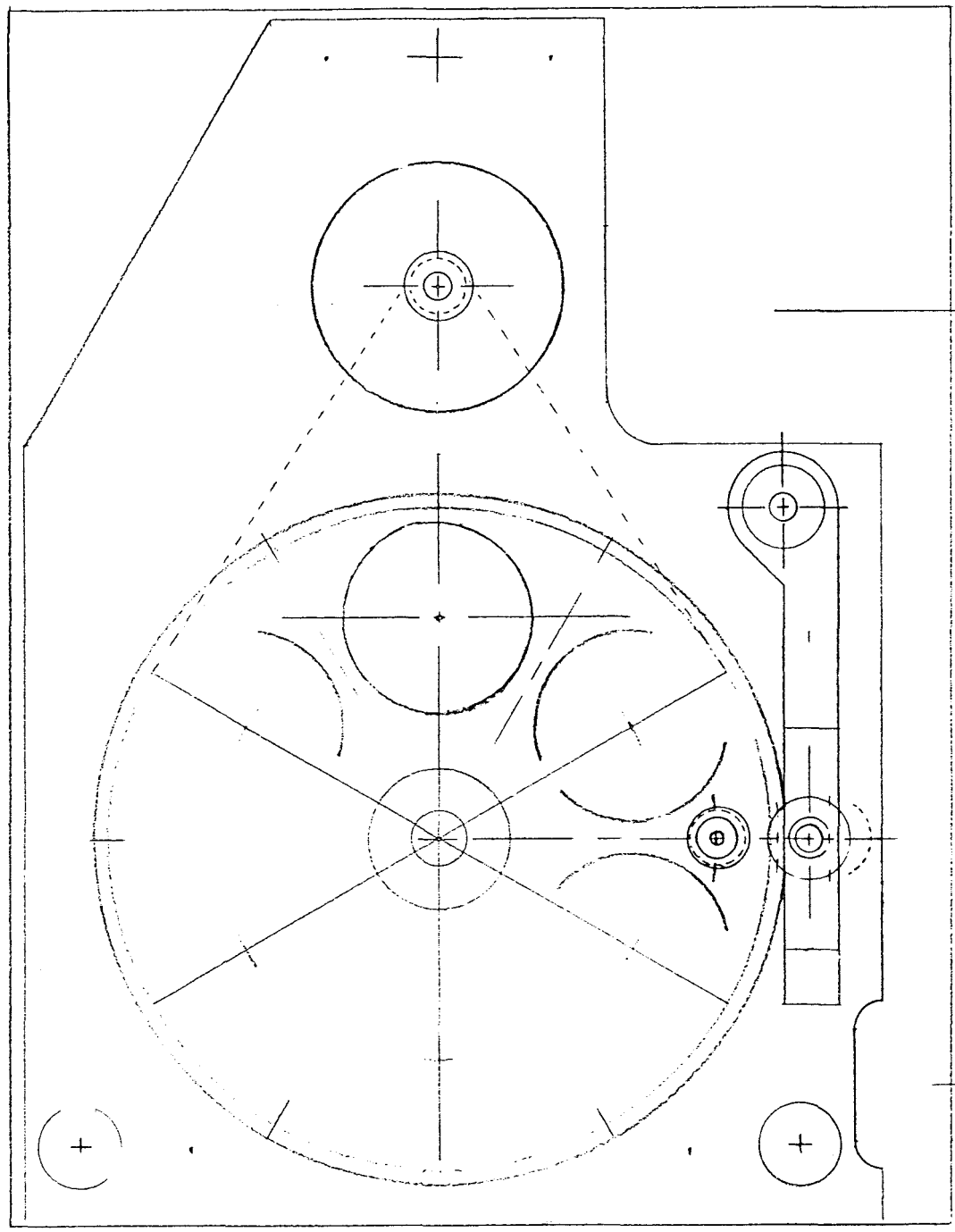

Figure 2-11
(continued)

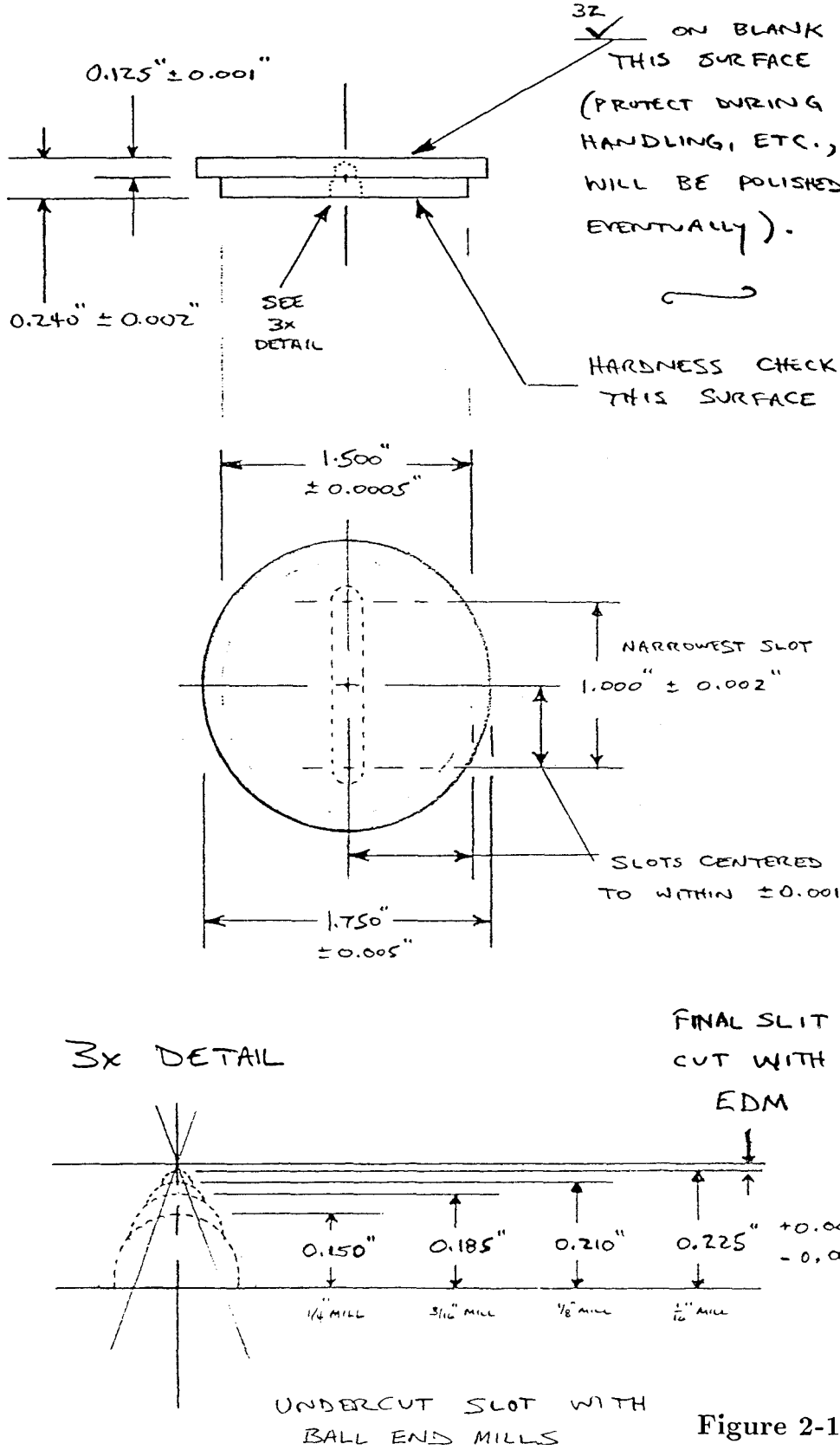
32
ON BLANK THIS SURFACE (PROTECT DURING HANDLING, ETC., WILL BE POLISHED EVENTUALLY).
0.125" ± 0.001"
0.240" ± 0.002"
SEE 3x DETAIL
HARDNESS CHECK THIS SURFACE
1.500" ± 0.0005"
NARROWEST SLOT
1.000" ± 0.002"
SLOTS CENTERED TO WITHIN ±0.001"
1.750" ± 0.005"
3x DETAIL
FINAL SLIT CUT WITH EDM
0.150"
0.185"
0.210"
0.225"
+0.000" -0.002"
1/4" MILL
3/16" MILL
1/8" MILL
1/16" MILL
UNDERCUT SLOT WITH BALL END MILLS

Figure 2-12

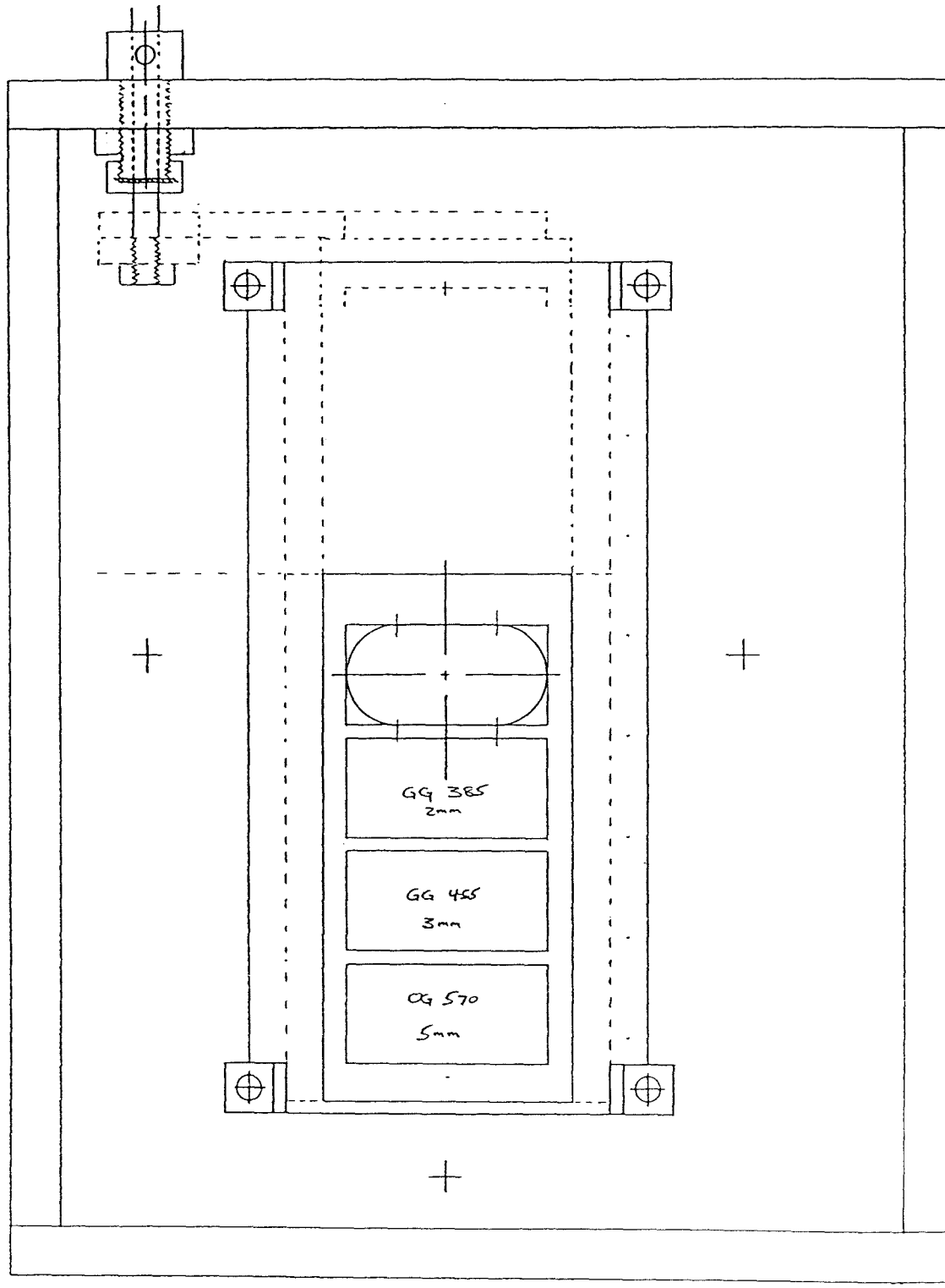

Figure 2-13

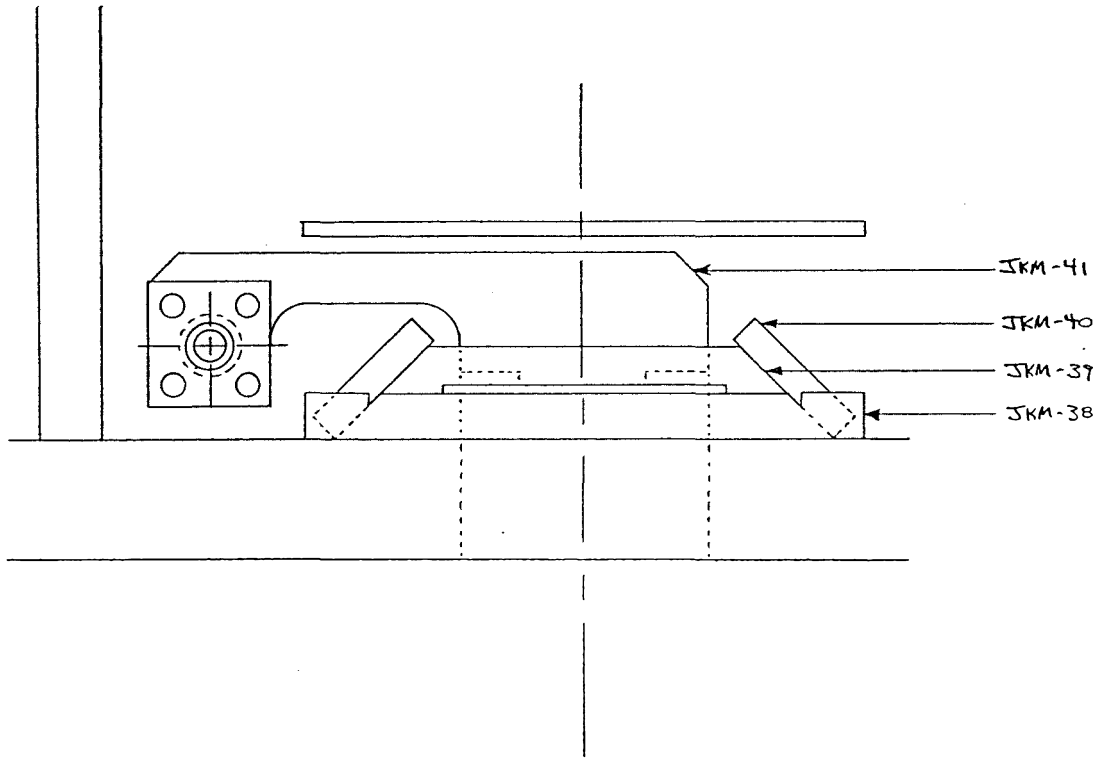

Figure 2-14

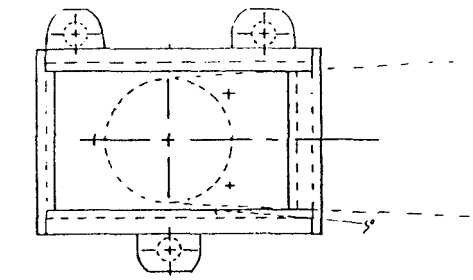

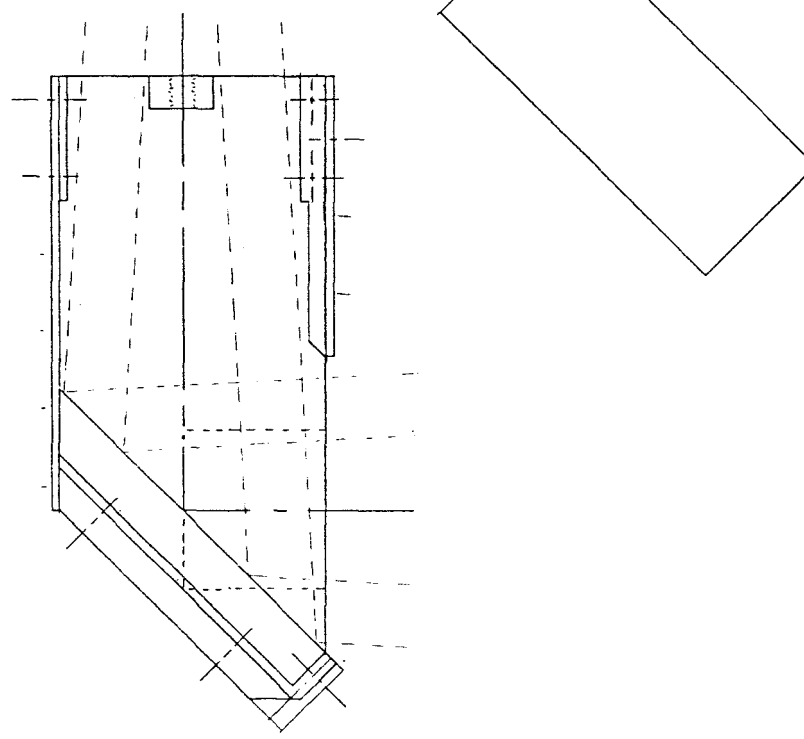

Figure 2-15

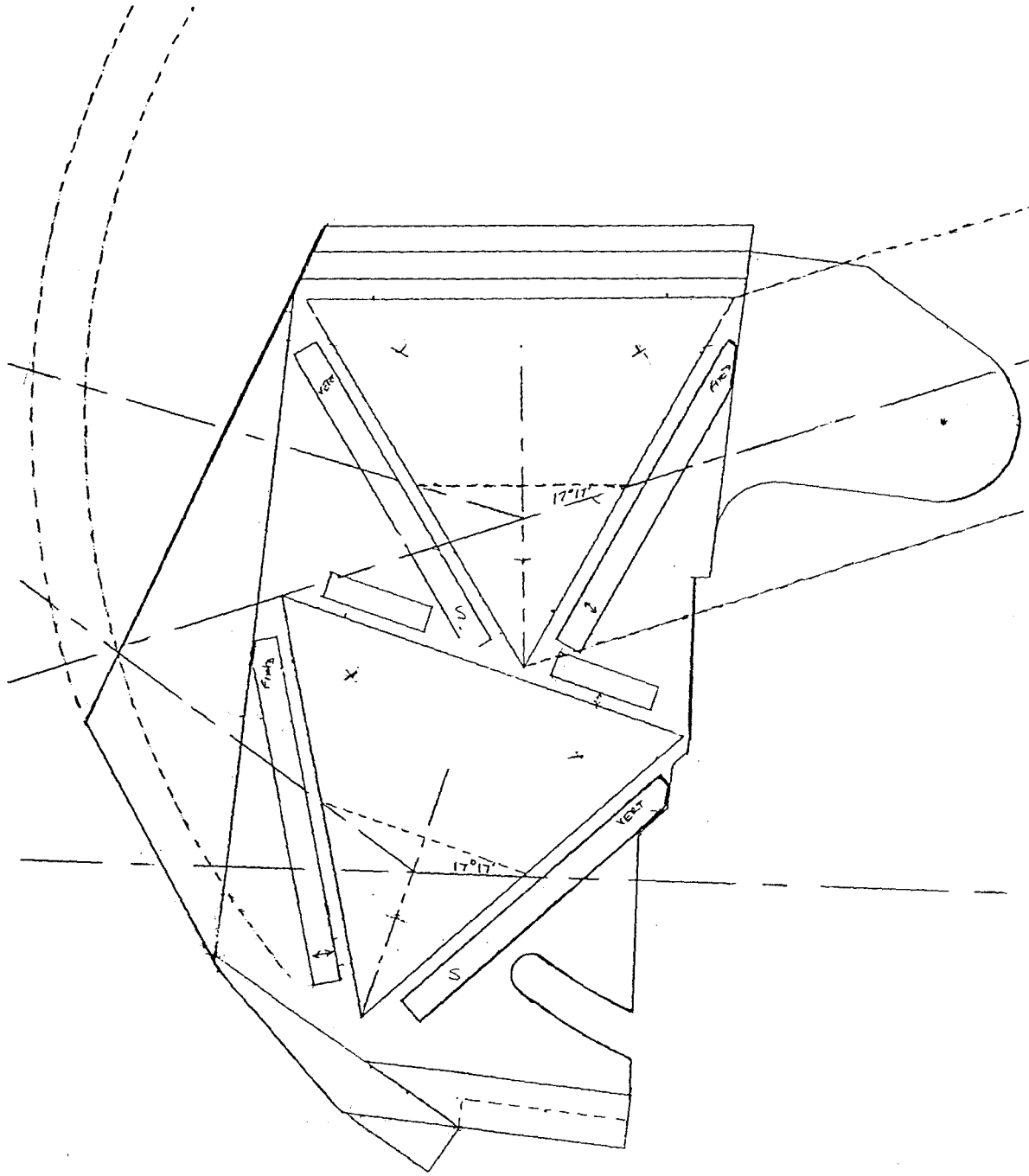

Figure 2-16

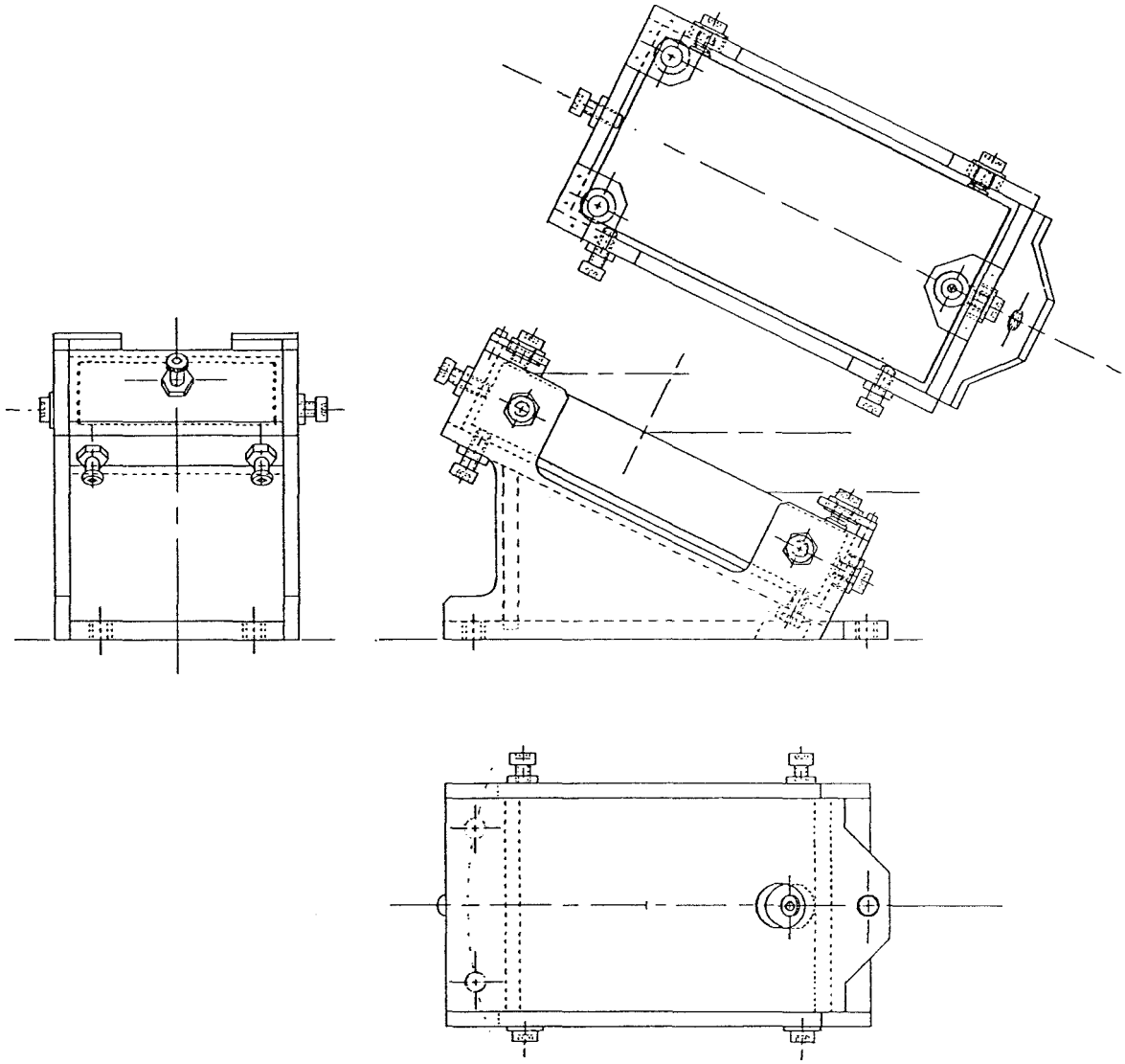

Figure 2-17

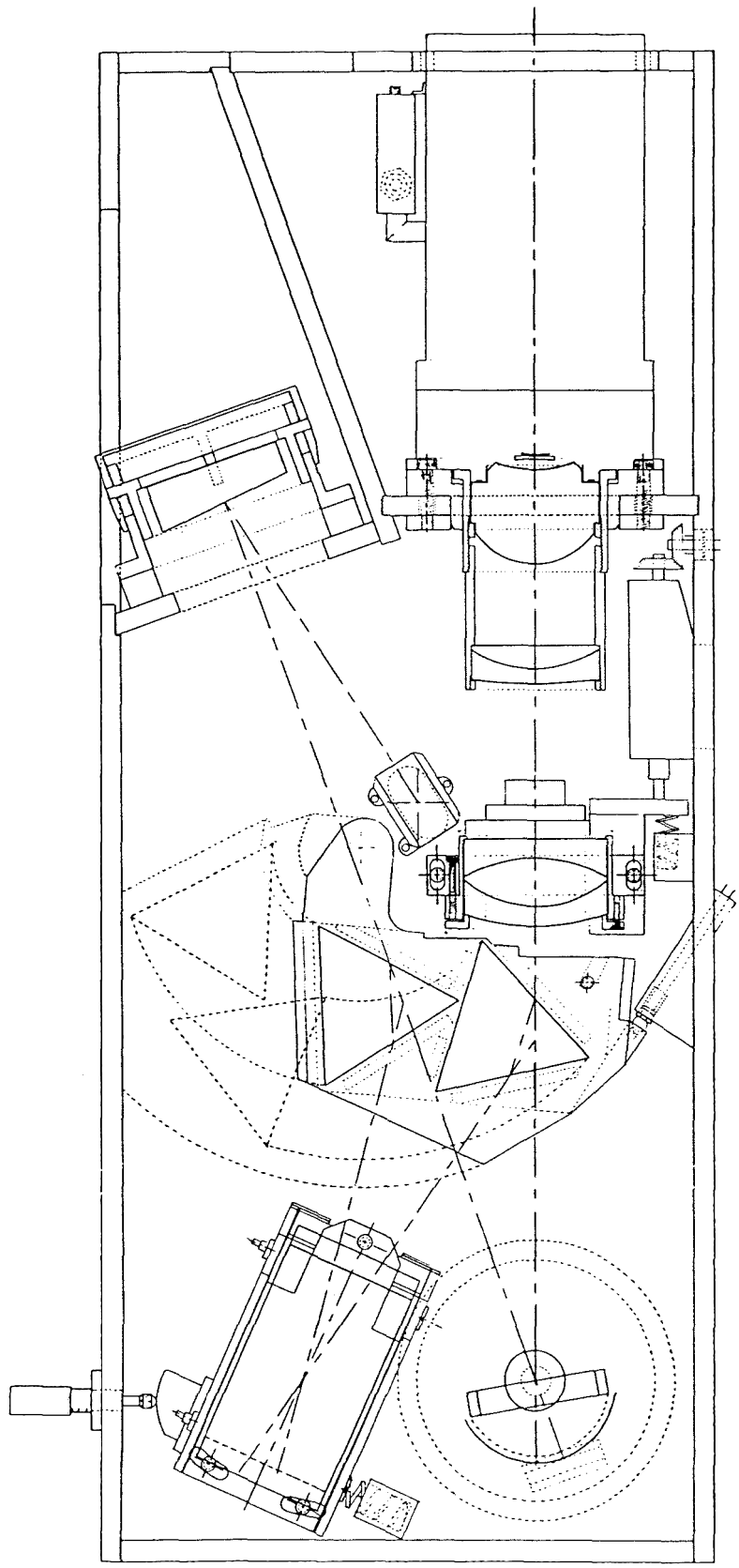

Figure 2-18

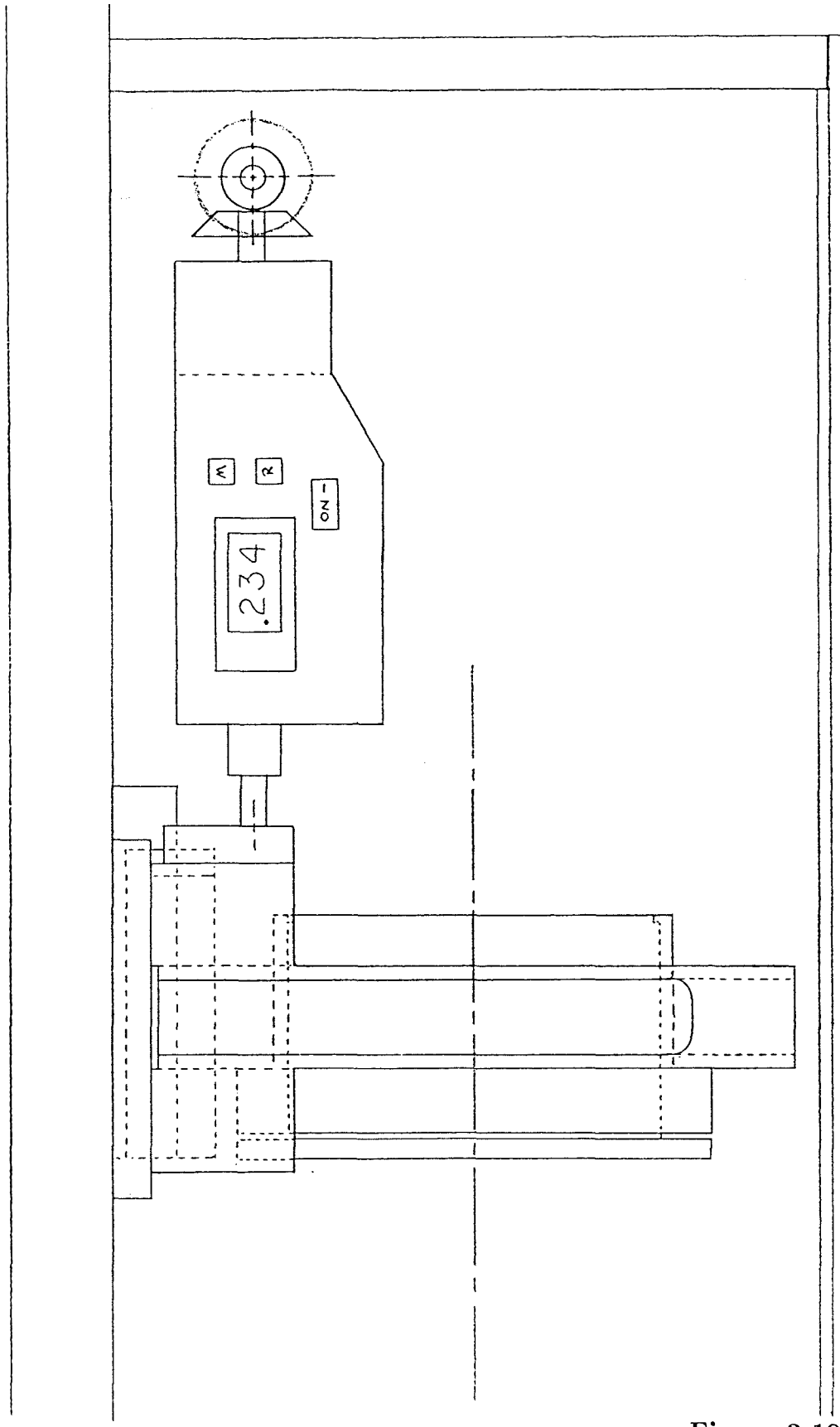

Figure 2-19

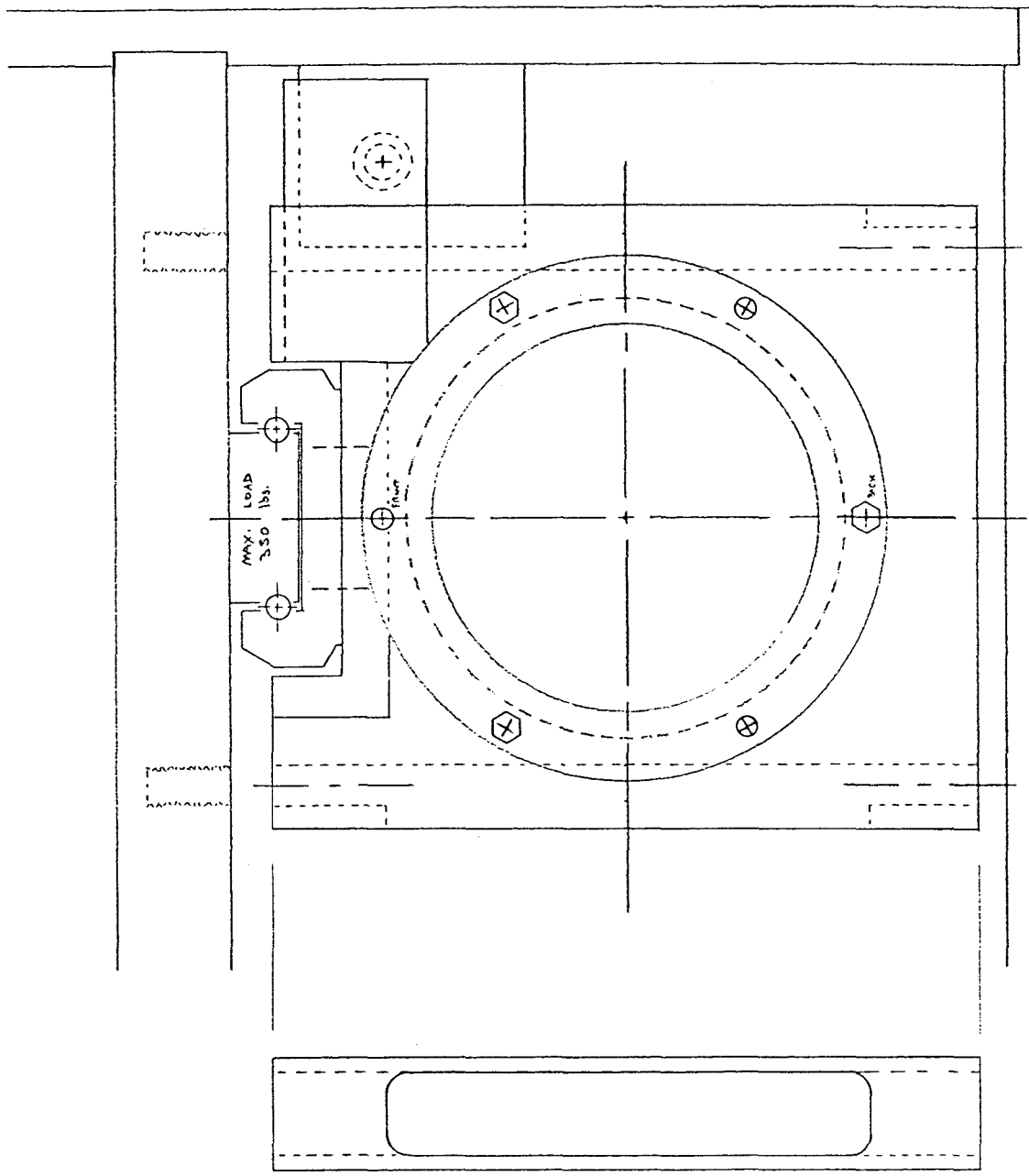

Figure 2-20

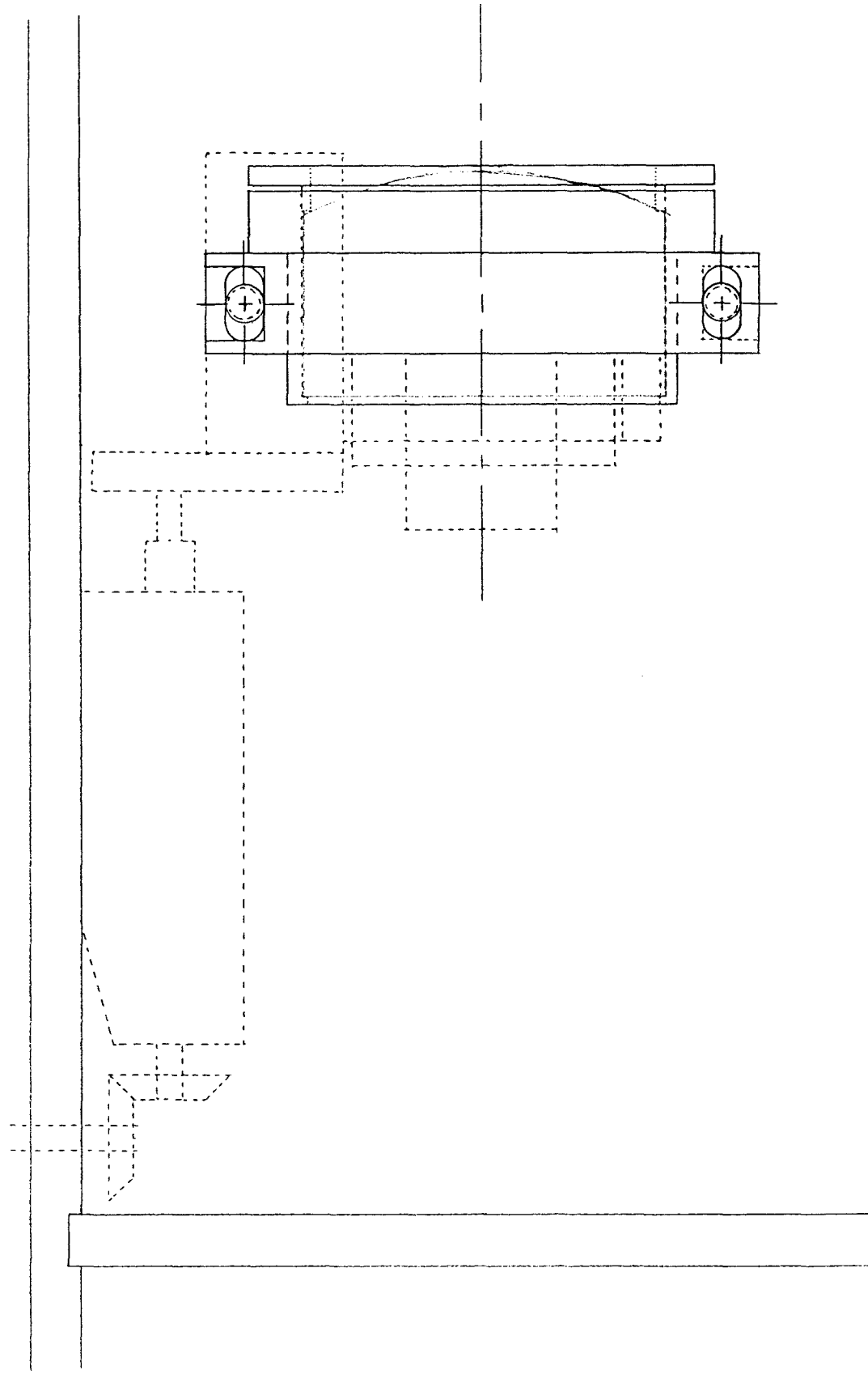

Figure 2-21

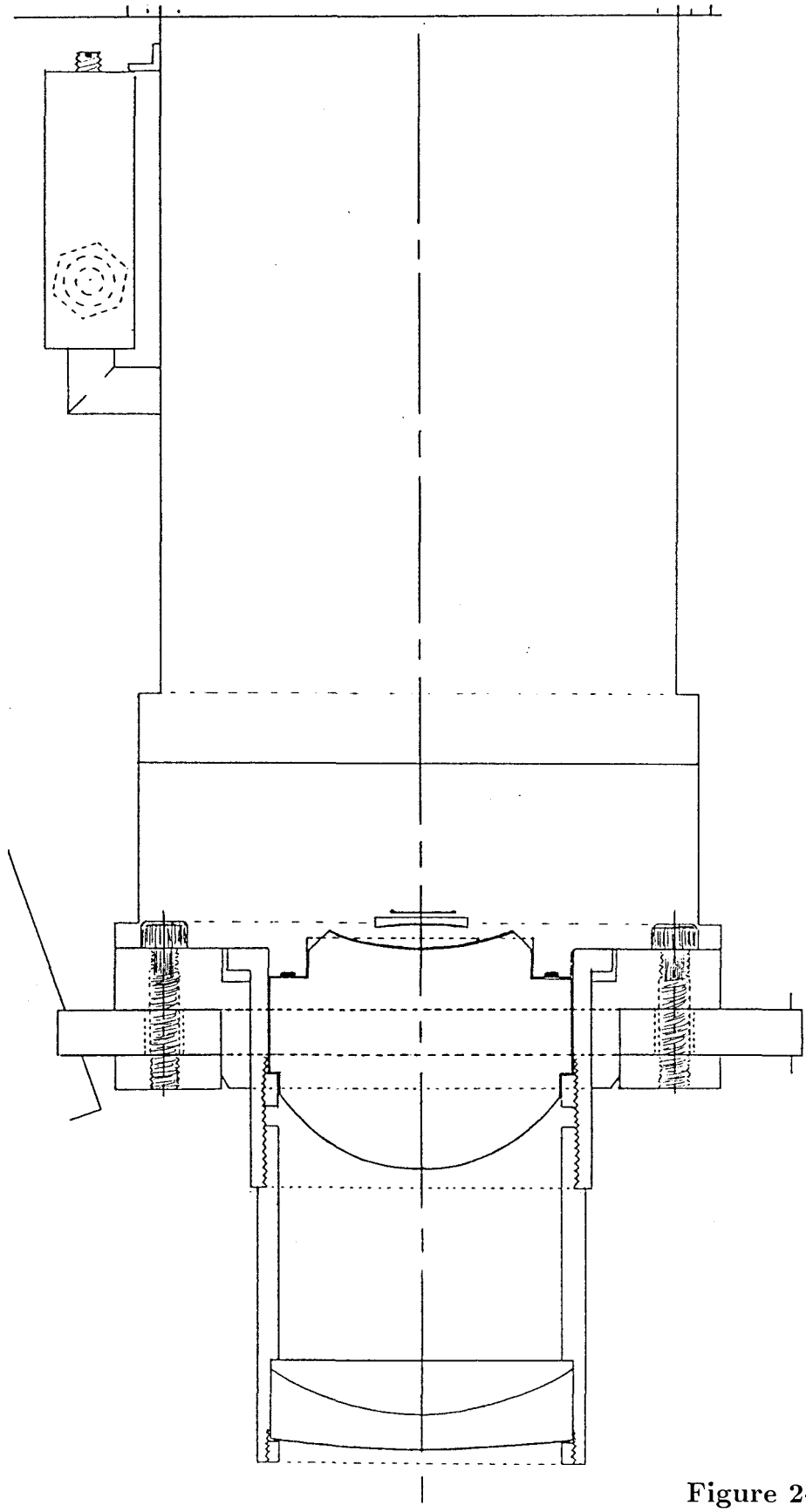

Figure 2-22

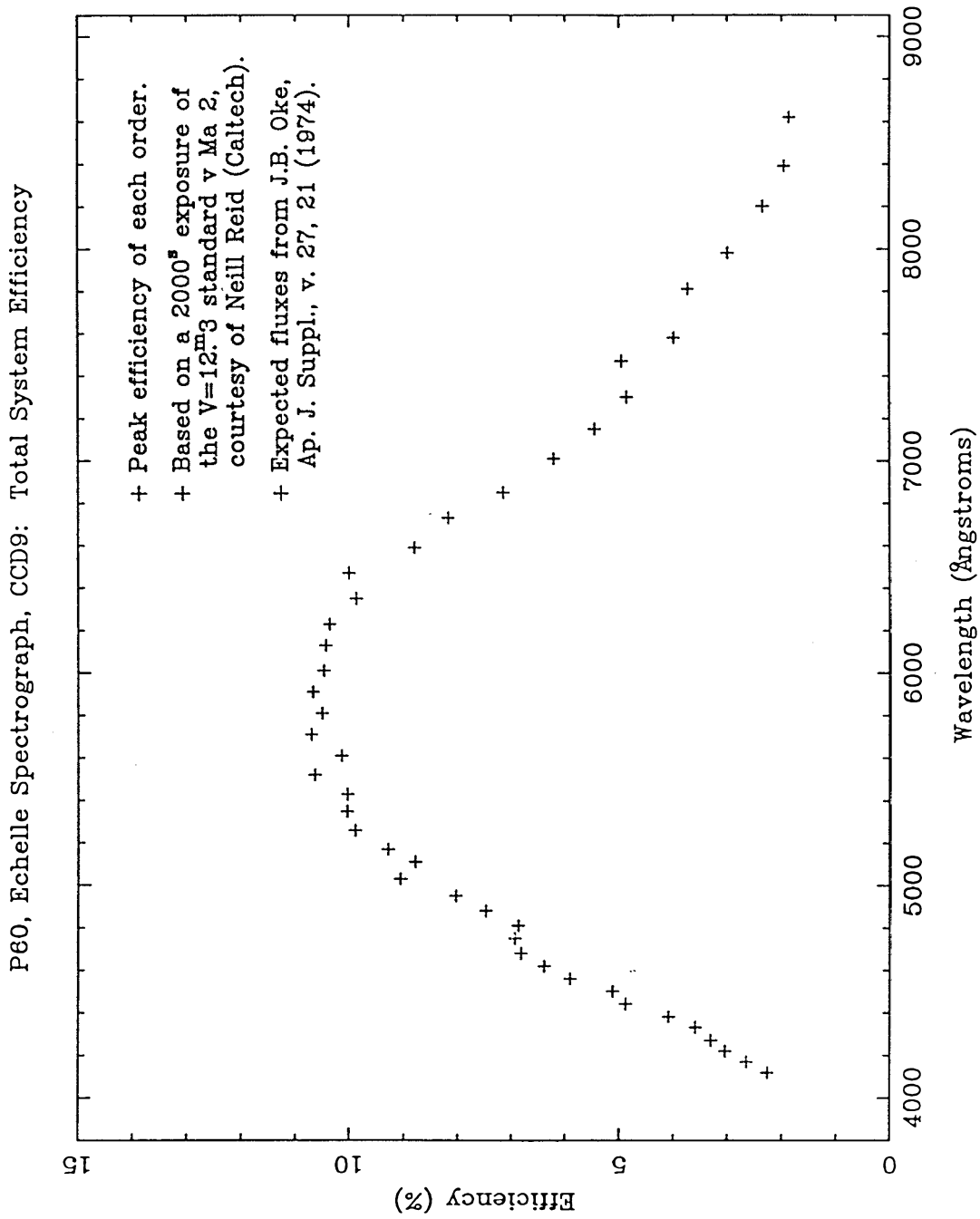
P60, Echelle Spectrograph, CCD9: Total System Efficiency
+ Peak efficiency of each order.
+ Based on a 2000s exposure of the V=12.m3 standard v Ma 2, courtesy of Neill Reid (Caltech).
+ Expected fluxes from J.B. Oke, Ap. J. Suppl., v. 27, 21 (1974).
Efficiency (%)
0
5
10
15
4000
5000
6000
7000
8000
9000
Wavelength (Angstroms)

Figure 2-23

III. Echelle Data Reduction

This chapter describes the set of VAX/VMS Fortran programs written to reduce the CCD data obtained with the P60 echelle spectrograph. These programs were written as subroutines and invoked as part of the FIGARO data reduction package (Shortridge, 1984a). It is beyond the scope of this chapter to provide a detailed account of FIGARO; the reader is instead referred to the document *"FIGARO: An Introduction for Beginners"* (Shortridge, 1984b) which can also be found on-line in the file FIGARO_PROG_S:FIGBASIC.MEM wherever the FIGARO package has been installed. This chapter is also not intended to provide a complete description of each and every command parameter; Appendix C contains for reference purposes the "C+" comment sections from the Fortran source code for each subroutine as well as the "connection files" for each command, which together fully explain to the user of the software what is required for each parameter. Therefore the emphasis in the following sections will be on the philosophy and algorithms employed by the echelle data reduction routines.

A. SDIST and CDIST

The first step in the data reduction process is to rectify the echelle images so that the orders run exactly parallel to the rows of the CCD. This is accomplished with the existing FIGARO routines SDIST and CDIST, which were written to correct S-distortion in data from detectors incorporating image intensifier tubes; by comparison the curvature and tilt of the echelle orders poses a much less difficult challenge for these two commands.

The distortion correction process starts by interactively locating with ICUR the centers of approximately ten orders in a bright B star echelle spectrum, equally spaced over the range of orders visible in the cross-dispersion direction. SDIST

then attempts to follow these orders from the starting cursor position to the left and right edges of the image in X, and fits the order peaks it finds with a polynomial function. The B star is ideal for this purpose as it has many orders without strong lines, which are a potential source of trouble for SDIST. It has been noticed that SDIST has less trouble if the order width, WIDTH, is underestimated when a value for this parameter is input. Since SDIST draws over the orders it locates on the image display, it is easy to verify that the orders have been traced properly, and repeat the ICUR selection changing the orders which SDIST was unable to trace. Note that SDIST writes the polynomial coefficients for each order traced to the file SDIST.DAT; this file may be edited to insert a successfully traced set of coefficients in place of an unsuccessful one. This SDIST.DAT file is next used by CDIST, which corrects the distorted image.

CDIST rebins each column of the original image based on a second polynomial fit to the shifts necessary to bring each traced order location to its average value. Because such a column rebinning process runs counter to the row by row sequence of the original image as it is stored in computer memory, CDIST works very slowly for large images such as those from the 800 × 800 CCD array used in the P60 echelle spectrograph. For this reason, Shortridge (1986) added a ROTATE keyword option to the CDIST command so that for large images CDIST could be instructed to first rotate the image by 90°, then rebin along the rows, and finally rotate the image by −90° in order to restore its original orientation.

The geometrical curvature and tilt of the echelle orders do not change perceptibly over the course of a night. It has therefore been possible to CDIST an entire night's data, including the flat field sum image, using a single SDIST.DAT file, and to postpone flat fielding until the ECHTRACT stage in the reduction process. Ideally, CDIST could be performed at the observatory (Cohen and Lee, 1987) and rectified data only brought back for subsequent reduction.

B. ECHTRACT

Examining a cut through a stellar P60 echelle image in the cross-dispersion direction (e.g., Figure 3-1), one immediately notices that the intensity does not drop to zero between the orders. The inter-order minima are typically less than 3 percent of the intensity of the order peaks and slightly larger than this when the seeing or guiding is poor. Ancient wisdom has always treated the inter-order minima as a measure of the globally distributed scattered light background in the spectrograph, and interpolated between adjacent inter-order minima to determine the background to be subtracted from each order.

However, upon closer examination of Figure 3-1 one notices that when the intensity of an order decreases substantially (e.g., where the atmospheric A-band is located in the red portion of Figure 3-1), the two adjacent inter-order minima also decrease. The implication of this observation is that in addition to a globally scattered light contribution to the inter-order minima rows, there must also be a "local" contribution from the two immediately adjacent orders. Since this local portion is a decreasing function of distance from order maximum, the adjacent order contribution at an inter-order minimum row is likely to be greater than the adjacent order contribution to the next order. Therefore subtracting a background based simply on the intensity of the inter-order minima will in general *over-estimate* the actual background found at each order's position.

The solution adopted for use in ECHTRACT is to correct the inter-order minima rows for the adjacent order contribution and then treat what inter-order light remains as globally scattered background light, which can later be smoothed and subtracted from the orders. To accomplish this correction, ECHTRACT performs a Gaussian fit to each order's cross-sectional profile in several locations along the order. From the fit parameters it determines an appropriate correction to be sub-

tracted not only from the adjacent inter-order minima but from the two adjacent orders as well, although the correction — which attempts to model the wings of the order profile — is most significant at the inter-order minimum and decreases outward from there. Note that this solution only requires an assumption about the functional relationship between the order wings and the Gaussian fit to the order peak; the globally scattered light that remains is not assumed to have any analytic distribution. In this respect this solution has advantages over that developed simultaneously by Gehren and Ponz (1986) for reduction of CASPEC data from the Cassegrain Echelle Spectrograph of the ESO 3.6m telescope. Since their CASPEC data covers a much smaller number of orders (typically only from 4000 Å to 5000 Å), Gehren and Ponz were able to assume that the globally scattered background light was a constant, "a," for each cut in the cross-dispersion direction and deduce its value from the intensity of the inter-order minima, $F_{\mathrm{m,min}}$ as a function of the average intensity of the two adjacent order maxima:

$$F_{\mathrm{m,min}} = a + bX \ , \quad X = \frac{F_{\mathrm{m,max}} + F_{\mathrm{m+1,max}}}{\left(\frac{1}{2}\Delta x_{\mathrm{m}}\right)^2} \tag{3.1}$$

where $F_{\mathrm{m,max}}$ is the peak of order m and Δx_{m} is the order-to-order separation between orders m and m+1. Although computationally much simpler, this approach proved unworkable for P60 echelle data. The linear function in equation (3.1) which Gehren and Ponz extrapolated to zero local contribution ($\Delta x \rightarrow \infty$) in order to find the global contribution a was very far from linear when computed for P60 echelle data (cf. Figures 3-2 and 3-3) due to variations in the global background.

The implementation of the Gaussian fitting approach in the FIGARO command ECHTRACT begins by dividing the input image into a number of sections in the cross-dispersion direction, based on the value of the input parameter *NFITS*. The median value of each row section is then determined to produce a single cross-dispersion cut from each section; note that the use of the median instead of the

mean makes each of the cross-dispersion cuts representative of the continuum profile independent of cosmic rays, bad columns, or strong absorption or emission lines. The higher the signal-to-noise ratio of the input data, the greater the number of *NFITS* sections possible which still maintain smooth order cross-sectional profiles for Gaussian fitting. Values of *NFITS* greater than 8 have in practice proved unnecessary for images containing 800 columns, resulting in more Gaussian fitting than required to adequately correct the inter-order minima rows for order-to-order crosstalk.

ECHTRACT does its Gaussian fitting starting with the center median section, expecting the best signal to be found in the center where the echelle blaze function is a maximum. Starting values for the Gaussian fit parameters for the first two orders are furnished to ECHTRACT by user input; ECHTRACT works best if the starting order is chosen to be the bluest order desired, since the orders are most separated from each other at the blue extreme. The second order to be fit is then one order to the red, in the direction of decreasing order number m. ECHTRACT estimates the location of the third and subsequent orders based on the most recent order-to-order separation found from the Gaussian fits done thus far, then looks for the actual order maximum near the expected position. When the Gaussian fits to the center median section are completed, these centroid values are used as initial estimates of where the orders are to be found in the remaining sections. Note that, for debugging purposes, the *MONITOR* keyword can be specified on the command line used to invoke ECHTRACT; in such cases, plots are sent to the logical device 'PGPLOT' following the Gaussian fit to each order, and it is then a simple matter to determine whether or not these fits are being done successfully or not.

The algorithm used for the Gaussian profile fitting is based on the non-linear least squares fitting by linearization of the fitting function method developed by Marquadt (1963), embodied in the Fortran subroutine CURFIT presented in chap-

ter 11 of Bevington (1969). The actual routine NLFIT used by ECHTRACT is based on a modification of CURFIT by Huenemoerder (1985), which allows upper and lower bounds on the fitting parameters to be specified. NLFIT was further modified for inclusion in ECHTRACT in order to remove restrictions on the array sizes of the input image data, and extensive tests were performed comparing NLFIT results to those obtained by Gaussian fitting with AMINI (Tonry, 1980) as well as to determine the most appropriate set of weights to assign across the profile for rapid convergence. It was found that weights W_j for each pixel j of:

$$W_j = \sqrt{\frac{Z_j}{Z_{max}}}\ , \tag{3.2}$$

where Z_j is the intensity of pixel j and Z_{max} is the peak intensity in the order profile to be fit, gave the most reliable fit results.

In order to determine from the *NFITS* median section Gaussian fit parameters the appropriate parameters to use at any pixel i along a given order, ECHTRACT averages the *NFITS* Gaussian centroid results; since the image has been previously rectified with CDIST, the centroids do not vary by more than 0.05 pixels. The peak Gaussian intensity as a function of i is found by scaling the sum of the three peak rows of the order to match the *NFITS* peak Gaussian intensities as determined from the actual fits. The Gaussian sigma as a function of i is found by a cubic spline interpolation of the *NFITS* Gaussian sigmas of the actual fits, although these are slightly smoothed with a triangular weighting function prior to the spline interpolation, and a linear extrapolation is used between the first and last section centers and the first and last pixels in the order, respectively. Note that ECHTRACT creates output data structures .Z.SFIT, .Y.YFIT, and .X.XFIT in which it saves the Gaussian sigmas, centroids, and the median section centers for future reference; this precaution was taken because in the most recent data from the P60 echelle, the sigma values as determined by the *NFITS* fits across a given order vary by up to 0.5

pixels. Because this is a real effect and not simply an artifact of the non-linear least squares fitting, it has serious implications for the shape of the extracted continuum (see the discussion of ECHXCONT in §**III.C** below).

From the averaged centroids, scaled maxima, and interpolated sigma Gaussian fit parameters, ECHTRACT can now correct the adjacent orders and especially the adjacent inter-order minima rows for contamination by the wings of each order. These wings, however, are broader at low levels than the wings of a true Gaussian, and so ECHTRACT must estimate their shape based on the Gaussian parameters it has as a function of i along the order. This is done most conveniently (Schechter, 1986) by truncating the Taylor expansion for a true Gaussian function:

$$\begin{aligned} G(y) = I_o\, e^{-\frac{1}{2}\left(\frac{y-y_o}{\sigma}\right)^2} &= I_o\, e^{-Y^2}\,, \qquad Y = \frac{y-y_o}{\sqrt{2}\,\sigma} \\ &= I_o\left(1 - Y^2 + \frac{1}{2!}Y^4 - \frac{1}{3!}Y^6 + \frac{1}{4!}Y^8 - \cdots\right). \end{aligned} \tag{3.3}$$

It was found empirically (see Figure 3-4) that the order cross-sectional profiles have wings which decrease approximately as Y^6, and so the Y^8 and higher order terms in the expansion of equation (3.3) are dropped for the best match to the profile wings when correcting for order-to-order crosstalk.

Unfortunately the two wings of the order cross-sectional profiles were not symmetric, and therefore the truncated Gaussian expression for the red and blue wings each had to be multiplied by a different scale factor in order to properly subtract the order-to-order crosstalk. These scale factors were determined experimentally so that the atmospheric A-band feature was removed from the two adjacent inter-order minima rows. Figures 3-5 and 3-6 show the inter-order minima rows adjacent to the A-band before and after correction for order-to-order crosstalk; the undulations which remain are caused by variations in the flat field response of the CCD.

The *MONITOR* mode of ECHTRACT displays a central cross-section before

correction for order-to-order crosstalk on which it overplots the same cross-section after this correction. Figure 3-7 shows such a comparison plot, where the solid line indicates the inter-order minima depths before the correction, and the dashed line afterwards. Note that there is little or no change for the blue orders ($y \gtrsim 400$) and that the maximum change in the red is a $\sim$50% correction to the original inter-order minima intensities.

Note in passing that for data of very poor signal-to-noise, in which the Gaussian fitting process is either not necessary — because the cross-talk correction is small compared to the noise in the inter-order minima rows — or not possible, or for data without continua to be fit (e.g., arc data), the *FIT* keyword can be specified .FALSE. and the orders found by alternate means. The most useful of these is the *TEMPLATE*=.TRUE. mode, in which the same rows are extracted from the present image as were extracted from a template image. The command TEMPLATE is used to define the template file, *TFILE*, whose extraction is to be duplicated. If *SEARCH* is .TRUE., ECHTRACT will look within the template bounds for the order peak and center the new extraction limits on this peak; otherwise the template extraction will be duplicated exactly. It is important when using ECHTRACT for arc data to specify *TEMPLATE NOSEARCH* so that the identical rows will be extracted from the arc as were extracted from the object frame. As was pointed out in §**II.B** above, some slight tilt of the slit image remains due to small variations in the γ angle which incoming light of different wavelengths makes with the echelle grating, since one of the cross-dispersing prisms precedes the grating. This tilt can introduce a wavelength calibration error if different rows are extracted for the arc than were extracted for the object, and for the utmost precision, perhaps one should consider weighting the extracted arc rows according to the relative counts in the corresponding object rows.

Regardless of whether the orders were fit with Gaussians and the inter-order

minima corrected for crosstalk or not, ECHTRACT next considers the value of the keyword *BCKGND*. If *BCKGND*=.TRUE., it proceeds to smooth and subtract the remaining globally scattered light background from the data. The smoothing is preceded by a median filtering of the (corrected or uncorrected, depending upon the keyword *FIT*) inter-order minima rows, in order to guarantee that cosmic rays, bad columns, and emission lines still remaining in these rows are removed and not propagated by smoothing to corrupt the surrounding global background. The amount of median filtering and smoothing is governed by the input parameters *XAVG* and *YAVG* specified by the user; typically values of $XAVG = 15$ pixels and $YAVG = 5$ orders are sufficient. If smoothing and median filtering are not desired, values *XAVG* and *YAVG* of 1 are acceptable.

ECHTRACT then pauses to save the inter-order minima rows, either corrected or uncorrected for order-to-order crosstalk depending upon the value of the keyword *FIT*, for future reference. If the keyword *SAVE*=.TRUE., the background rows are saved in the output data structure .Z.BCKGND; otherwise a second output file is created with the suffix "_B" and the background rows written to its .Z.DATA structure. By inspecting these background rows, it is a simple matter to determine whether the crosstalk correction and/or the median filtering processes were successful in removing features from the inter-order minima rows.

Upon reaching this point, ECHTRACT has applied all the necessary corrections (i.e., order-to-order crosstalk, global background median filtering, smoothing, and subtraction) which were requested by the user. It also knows where the order maxima are, based either on the Gaussian fit centroids or the information contained in the template file, and so it can proceed to extract the desired number of rows (*EXWIDTH*) from each order. However, up until now the data has not been divided by the flat field image, since doing so would have destroyed the information contained in the inter-order minima rows where the flat field intensity

is very small. ECHTRACT therefore combines the actual extraction process with flat field division, applying a scaling factor to each order of the flat field which effectively normalizes it to one at the order center. Algebraically, this combination of operations can be expressed as:

$$S_{i,m} = \sum_{j=j_1(m)}^{j_2(m)} \frac{Z_{i,j}}{N_m^{-1} F_{i,j}}, \qquad N_m = \sum_{j=j_1(m)}^{j_2(m)} F_{i_o,j}$$
$$j_1(m) = j_o(m) - EXWIDTH/2 \tag{3.4}$$
$$j_2(m) = j_o(m) + EXWIDTH/2$$

where S is the extracted sum, Z is the corrected image intensity, F is the flat field image intensity, N_m is the flat field normalization for order number m, i and j are pixel indices in X and Y, respectively, $j_o(m)$ is the value of j in the center of order m, i_o is the value of i in the center column of the image, and $EXWIDTH$ is the extracted width in rows specified by user input. This particular flat field normalization was chosen to preserve the number of net counts in the center of the order, while at the same time removing the curvature in the unflattened net counts caused by the echelle blaze function, the variations in the red due to interference fringing in the CCD membrane, and the pixel-to-pixel variations in CCD quantum efficiency. However, if the number of counts in the center of the unflattened image exceeds N_m, the sum of the counts in the center of the flat field, no flat fielding is done, since doing so would degrade the signal-to-noise ratio of the data. The output data structure .Y.PROC records whether or not flat field processing was performed on each order.

The extracted sum $S_{i,m}$ is written to .Z.DATA in the output file, which is a two-dimensional data structure containing the same number of columns as the input image but having only one row per extracted order. This output format (often referred to as the "collapsed echelle format" below) has been found to be much more

convenient throughout the data reduction process than the more customary — but very long — one-dimensional spectrum resulting from piecing the orders together end-to-end. This is especially true when examining plots of each order from the collapsed echelle format, since any CCD column blemishes are aligned with each other and easy to distinguish from real features. Bright emission lines which saturate and spread along a column are also easily identified when each order is plotted individually. Further advantages will become apparent in the sections to follow which deal with determining the continuum across broad features (ECHYCONT; §**III.D**) and arc fitting (ECHARC; §**III.E**). The major disadvantage is the absence of a two-dimensional X.DATA array for wavelength information; one solution to this problem is the program ECHXREBIN discussed in §**III.F**.

Shown in Table 3-1 is a sample of the full collapsed echelle data structure output by the ECHTRACT command. Since it has .X.DATA, .Y.DATA, and a two-dimensional .Z.DATA array, it looks to most of FIGARO like an ordinary image. For instance, it is possible to display the extracted sum image on an image display using FIGARO's standard IMAGE command (N.B., increasing the *YWIDTH* parameter to the maximum value allowed will make the order rows easier to distinguish from one another). As far as the non-standard FIGARO image data structures of Table 3-1 are concerned, other echelle extraction approaches one may wish to invent, and still make use of the post-extraction echelle reduction routines to follow, should attempt to duplicate this format as much as possible. By way of summary and for future reference, Figure 3-8 presents a flowchart of the ECHTRACT command program.

C. ECHXCONT

The flat field division performed as part of ECHTRACT does not result in a perfectly straight and flat continuum level for several reasons. First of all there

is the difference in color temperature between the incandescent flat field lamp and the stellar continuum, which gives rise to a non-zero slope in the flattened stellar spectrum. Secondly, as was pointed out in §**III.B** above, there is a variation in the order profile width across the length of the order. When a constant number of rows is extracted, the variation in sigma causes an inverse variation in the fraction of the order profile extracted; the undulation in the continuum which results is of the order of several percent. The most serious problem at present, however, is the lack of sufficient blue flat field light in the spectrograph guider base incandescent source (see below, §**V.A**), which causes severe flat fielding problems for wavelengths $\lambda \leq 4500$ Å because the blue light and scattered red light contributions to the flat field in the blue become comparable.

For these reasons and possibly others, it is necessary to further "flatten" the already flat fielded collapsed echelle images. This operation is performed in three stages: the first (ECHXCONT) interpolates across "narrow" features in the spectrum to define a trial continuum; the second (ECHYCONT, see §**III.D** below) replaces the trial continuum in the vicinity of "broad" features with a continuum determined on the basis of the two adjacent order trial continua; and the third step is to divide the original collapsed echelle spectrum by the final continuum image using the IDIV command of FIGARO, thereby normalizing the original spectrum to unity in the continuum. The difference between "narrow" and "broad" features in the spectrum is left up to the discretion of the user. In other words, the distinction is an operational one, depending on over how broad a region the ECHXCONT interpolation in the echelle dispersion (or X) direction is reliable: "broad" features are those wider than this amount, for which the ECHXCONT continuum is not satisfactory. In the particular case of hot stellar spectra, the hydrogen Balmer lines and helium lines have wings at least 50 to 100 pixels wide, across which ECHYCONT produces a more reliable continuum level than ECHXCONT.

The ECHXCONT program incorporates an automatic mode which, for spectra of high signal-to-noise ratio, is capable of distinguishing between "narrow" spectral features and "continuum" regions without the help of the user. This automated decision is based on a comparison between the original data (cleaned up slightly by a running median filter which removes cosmic rays, bad columns, etc.) and its median calculated over a running bandpass *XMED* pixels in width. For disagreement between the two greater than a threshold amount *CFACTOR* (expressed in fractional continuum units), ECHXCONT concludes that a "narrow" feature is present and performs a cubic spline interpolation across all such regions to produce the "narrow" line-free trial continuum. Note that features whose width is of the same order as the median bandpass will only be detected if they have particularly sharp cores which the median filtered comparison will reveal. Figure 3-9 illustrates the use of ECHXCONT's automatic mode on a sample B star order: the smooth narrow line is the median filtered spectrum being compared, the dashed vertical lines indicate the "narrow" line regions masked by ECHXCONT, and the smooth heavy line is the cubic spline interpolation between the points (+) which will be used in place of the data within the dashed boundaries.

ECHXCONT writes the regions masked owing to the presence of "narrow" features into the file XMASK.ECH; alternately, the user can specify the keyword *CONTX*=.TRUE. and the program will write into the file XCONT.ECH the acceptable "continuum" regions between the features it detects. This file can later be edited to add, subtract, or modify either the line or continuum regions, and ECHXCONT run a second time with *PREVIOUS*=.TRUE. and the same *CONTX* keyword value. The program will then read the file as input and use it as the basis for masking "narrow" features to be replaced by cubic spline fits across them.

Unfortunately, a single collapsed echelle input spectrum quite often contains orders covering a very broad range in signal-to-noise, which is typically rather low in

the red and blue extreme orders compared to the more central orders. The result is that a single set of automatic parameters for ECHXCONT (e.g., the median band-pass *XMED*, the threshold parameter *CFACTOR*, etc.) which might be optimum for detecting "narrow" features where the signal-to-noise is best are inappropriate where it is poor, and the automatic detection success rate falls to unacceptable levels. Besides the option of editing the XMASK.ECH or XCONT.ECH file to correct the unsuccessful orders, ECHXCONT also has an interactive mode in which the user indicates the line boundaries in every order with a graphics cursor.

The output from ECHXCONT is collapsed echelle format image whose .Z.DATA is a "narrow" line-free version of the input file. A file called YMASK.ECH is also produced which contains a list of those regions where the ECHXCONT continuum of one order disagrees with the average of the two adjacent ECHXCONT orders by more than another threshold amount, *AFACTOR*. This file can be edited and used as input to ECHYCONT (see below), saving some of the work involved in generating this ECHYCONT input file from scratch. Graphical output from ECHXCONT depends on the choices made for the *MONITOR* and *INTERACT* keywords (see Appendix C for more details).

D. ECHYCONT

As stated above, ECHYCONT is the second stage of the continuum normalization process. It is based on the fact that the curved shape of the continuum is a slowly varying function of order number; the continuum of any order can be very closely approximated by the average of the two adjacent orders. This is clearly demonstrated by Figure 3-10, which shows order 51 of a B star spectrum (containing Hα) compared to the average of orders 50 and 52 (which have not had "narrow" features removed by ECHXCONT).

Note, however, that the smoothly varying change in order intensity is not linear, and so the average intensity does not match that of the intermediate order. Thus it is necessary to properly scale the adjacent order average before using it in place of a broad feature specified by YMASK.ECH; it was decided to perform this normalization independently in two regions just outside the masked region, and to linearly interpolate the normalization factor across the masked region. Shown in the first panel of Figure 3-11 is the result of this normalization for the Hα B star order of Figure 3-10, where the dashed vertical lines indicate the boundaries of the regions used for normalizing the average.

As can be seen from Figure 3-11, the normalization technique adopted does not produce an average which matches the order at the inside set of boundaries to the masked region. However, the technique guarantees that between the edge of the masked region and the normalization region, the average will cross the order at some point. ECHYCONT looks for the crossing points on both sides of the masked region, and replaces the order between these two crossing points by the adjacent order average. The dotted lines in the second panel of Figure 3-11 indicate the boundaries of the continuum region actually replaced by the adjacent order average by ECHYCONT. Finally, to normalize the original collapsed echelle format spectrum to unity in the continuum, it can be divided by the ECHYCONT output using the IDIV command; the third panel of Figure 3-11 shows the result of this division for the sample Hα spectrum of Figure 3-10.

E. ECHARC

The routine ECHARC identifies arc lines in a collapsed echelle format arc image from ECHTRACT (see above, §**III.B**). The approach used initially is identical to that of the FIGARO one-dimensional arc fitting command, ARC, for 3 or more echelle orders which are fit interactively. ECHARC then automatically identifies

arc lines in all the remaining orders. In practice this process requires many arc lines in each order, and so is well suited for use with Thorium-Argon arc spectra.

The one-dimensional arc fitting process is described elsewhere (see Shortridge, 1984c; or type HELP @FIGARO TECHNIQUES ARC when on-line after having invoked the FIGARO system); here it is only necessary to point out that a good Th-Ar line-list exists in the file DEIMOS::IMP:[JKM.FIGARO]ECH_THAR.ARC, which has been compiled from several sources, and this line-list is extensive enough that good use can be made of the one-dimensional automatic line search option "A" once a preliminary interactive fit is achieved. Note that when an interactive fit to a single order is completed, the continue option "C" must be selected to move on to the next order's interactive fit. It is also recommended that the first and last order chosen for interactive arc selection be close to the first and last orders in the input arc image, since ECHARC finds it much easier to interpolate between interactive fits than to extrapolate beyond them (see §**V.B** below).

Given interactive arc fits to at least 3 orders, ECHARC then proceeds to predict λ as a function of order m and pixel number i for all the remaining orders by fitting a polynomial to $\lambda(m)$ for each column i. With this set of predicted wavelengths, ECHARC then attempts to find as many lines in the remaining orders as possible; finally the set of predicted wavelengths is modified based on a fit $\lambda(i)$ to the identified lines in each order. The automatic line search technique differs significantly from that used by ARC in one dimension. ECHARC is able to search for lines much more rapidly since it looks for a line in the data at the expected position of each line in the line-list, whereas ARC looks for a line at each pixel position and tries to match the wavelengths of the lines it finds to wavelengths given in the line-list. Figure 3-12 shows the fit residuals as a function of order number for a typical Th-Ar exposure; in each order the wavelength was fit with a cubic polynomial ($NCOEFF$=4) function of pixel number. The $\gtrsim$ 1200 arc lines in Figure 3-12 were automatically identified

by ECHARC in less than 30 CPU seconds.

The output from ECHARC is a collapsed echelle image (*WAVES*) whose .Z.DATA array contains the fitted wavelengths for each pixel in the arc image. Note that the FIGARO commands ICMULT, ICDIV, and IADD can be used to combine several ECHARC output *WAVES* files that bracket an object exposure into a weighted average wavelength file to be assigned to that object image (see the discussion of ECHXREBIN below). ECHARC writes the pixel number and order number of each identified arc line into the disk file ARLINES.ECH, which can be read back into the program to repeat the fit or edited down to just a few orders and used as the initial guesses for the orders fit interactively. Other forms of output information from ECHARC available as options include a graphical atlas of all the line identifications made in every order, and/or an order by order analysis of each arc line identified, its residual $r = \lambda_{\rm catalog} - \lambda_{\rm fit}$, and the rms residual for the entire order were that line to be removed from the fit.

F. ECHXREBIN

As was pointed out in §**III.B** above, the decision to package the collapsed echelle format into a two-dimensional FIGARO image data structure has several advantages, but one significant disadvantage is that a normal FIGARO two-dimensional image has only a one-dimensional .X.DATA array. While this is all that is needed for typical CCD images, in the collapsed echelle format each row of the image (i.e., each order) has a different set of wavelengths assigned to it (cf., the discussion of ECHARC above). ECHXREBIN is one attempt to solve this conflict by adapting the data to the convenient format; obviously many other solutions are possible which change the format to adapt to the peculiarities of echelle data. Yet the output from the ECHXREBIN solution is believed to be the most consistent with the other software in the FIGARO system, since the .X.DATA array remains

one-dimensional.

This solution is based upon the fact that, as a result of the relation given by equations (2.1a,b), the product of order number times wavelength, $m\lambda$, is approximately constant for a given X value ($\beta \sim$ constant). Therefore the single one-dimensional .X.DATA array could contain the product $m\lambda$ common to all the orders; unfortunately this product is not exactly constant, because the angle γ in equation (2.1a) is not a constant, nor is β strictly constant for constant X. But these are expected to be small variations, and so the solution is in principle sound.

In actual fact what ECHXREBIN does is define an "effective order number," $m_{\rm eff}$, such that the product $m_{\rm eff}\lambda$ is strictly a constant for constant X down the center of the array. ECHXREBIN begins by calculating the average $\langle m\lambda \rangle$ for the center column of the array:

$$\langle m\lambda \rangle = \frac{1}{N_{\rm orders}} \sum_{m=m_1}^{m_2} m\lambda_{i_o,m} \tag{3.5}$$

where m_1 and m_2 are the extreme order numbers and $\lambda_{i_o,m}$ is the wavelength of the center pixel i_o in order m. The definition of the set of $m_{\rm eff}$ values follows from this average $\langle m\lambda \rangle$ as:

$$m_{\rm eff} = \frac{\langle m\lambda \rangle}{\lambda_{i_o,m}} \, . \tag{3.6}$$

Therefore when the data is rebinned onto a common $m_{\rm eff}\lambda$ scale, the central pixel remains nearly centered; the definition of $m_{\rm eff}$ given by equation (3.6) eliminates any large shift of the order centers.

In a manner analogous to equation (3.5), ECHXREBIN next defines average starting and ending $\langle m_{\rm eff}\lambda \rangle$ values, which become the starting and ending .X.DATA

array elements, respectively:

$$\langle m_{\rm eff}\lambda_1\rangle = \frac{1}{N_{\rm orders}}\sum_{m=m_1}^{m_2} m_{\rm eff}\lambda_{1,m} = \text{.X.DATA[1]}$$
$$\langle m_{\rm eff}\lambda_{\rm NX}\rangle = \frac{1}{N_{\rm orders}}\sum_{m=m_1}^{m_2} m_{\rm eff}\lambda_{{\rm NX},m} = \text{.X.DATA[NX]} \qquad (3.7)$$

where λ_1 and $\lambda_{\rm NX}$ are respectively the wavelengths of the first and last columns of data. The output .X.DATA[i] array is determined finally by dividing the range .X.DATA[1] to .X.DATA[NX] into NX intervals according to the value specified for the keyword *LINEAR*: equally spaced in $m_{\rm eff}\lambda$ for *LINEAR*=.TRUE., equally spaced in $\log(m_{\rm eff}\lambda)$ for *LINEAR*=.FALSE. (see Appendix C for more information).

Having determined the desired output .X.DATA array, the input wavelengths from the ECHARC output WAVES image are used to rebin the input data onto the output scale having constant $m_{\rm eff}\lambda$. The existing FIGARO utility routine FIG_REBIN (Ashley, 1983; as modified by Shortridge, 1984d, for use in the commands SCRUNCH, CDIST, etc.) is used to perform the actual rebinning, which can be done either by linear or quadratic interpolation when dividing the data into a fraction of a pixel; the keyword *IQUAD* governs which interpolation mode is employed. Lastly, the rebinning can be done conserving either total flux or mean value when the size of a pixel bin increases or decreases, as specified by the keyword *CFLUX*. Note that for net counts or fluxes, *CFLUX*=.TRUE. should be selected, while for data on a magnitude scale or data normalized to a continuum equals unity scale, *CFLUX*=.FALSE. is appropriate.

The output data structure is virtually identical to that of the input, except that a new array .Y.MEFF has been added to save the set of $m_{\rm eff}$ values, and the .X.LABEL and .X.UNITS have been changed to reflect the changes in .X.DATA, now containing the $m_{\rm eff}\lambda$ product. Both .Y.MEFF and .X.DATA are saved as double precision arrays, since to later compute λ for a single order spectrum, the

FIGARO command EXTRACT (as modified for use with echelle data; see Appendix C) must divide .X.DATA by .Y.MEFF for the row of data desired. The complete ECHXREBIN output data structure is shown in Table 3-2 for future reference.

In order to make it possible to rebin two images having two slightly different *WAVES* files onto the same $m_{\rm eff}\lambda$ scale, a template for the ECHXREBIN process can be specified with the TEMPLATE command, and ECHXREBIN invoked with the *TEMPLATE* keyword .TRUE. In this case, the new output file will have arrays .Y.MEFF and .X.DATA identical to those of the template file instead of ones determined independently by equation (3.7).

Note that as a consequence of maintaining the collapsed echelle format throughout the reduction process, it is now possible to define a two-dimensional analog to the cross-correlation function and to cross-correlate a pair of collapsed echelle format images simultaneously in all orders:

$$R_{\rm 2D}^{(1,2)}(s) = \frac{1}{N_{\rm orders}} \sum_{m=m_1}^{m_2} \left(\frac{1}{\rm NX} \sum_{i=1}^{\rm NX} Z_{i,m}^{(1)} Z_{i+s,m}^{(2)} \right) \tag{3.8}$$

assuming the $Z^{(1)}$ and $Z^{(2)}$ data arrays have been rebinned onto identical .Y.MEFF and .X.DATA scales, the latter having pixels equally spaced in $\log(m_{\rm eff}\lambda)$. Not only does this save bookkeeping effort as compared to $N_{\rm orders}$ one-dimensional cross-correlations performed separately, it is likely that for low signal-to-noise data the two-dimensional cross-correlation peak resulting from equation (3.8) would be sharper than the one-dimensional peaks from the single orders. Radial velocity measurements not being a priority of this work, and the spectrograph mounting base not yet containing a Th-Ar lamp, equation (3.8) has not at present been implemented into an "ECHROSS" command.

G. ECHPLOT and MBPLT

In order to plot echelle spectra in the collapsed echelle format, the standard FIGARO program SPLOT was modified to produce the routine ECHPLOT, which retained most of the standard features of SPLOT (see Shortridge, 1984b,c). In addition, ECHPLOT has two additional input parameters, *YSTART* and *YEND*, which are the first and last order numbers desired for the plot. While soft plots are still supported, ECHPLOT is intended to be used to produce *BUILD* plots, which the routine MBPLT can direct to any desired device plotting multiple orders per page — an important consideration when dealing with $\sim$ 60 echelle orders per echelle spectrum.

There are a few other non-SPLOT features of ECHPLOT specifically geared towards echelle data. The *AUTOSCALE* feature of ECHPLOT is based not on the minimum and maximum values in each order (since these are too frequently corrupted by bad columns, or in the particular case of CSPN, by nebular emission lines) but rather plots from zero intensity to some factor times the median value of each order. For data which has been normalized to unity in the continuum, the *CONTINUUM* keyword is provided which adds a thin line at this 1.00 level. Lastly, this work required spectra plotted with a constant number of Å per cm on the page; the command parameter *WLENGTH* was therefore designed to allow the horizontal length of the plot in Å to be specified. If the actual order length is greater than *WLENGTH*, two or more plots per order will be produced. Further details concerning both ECHPLOT and MBPLT can be found in Appendix C.

TABLE 3-1

Sample Echelle Data Structure Following ECHTRACT

Structure (1)	Type (2)	Contents (Abbreviated where .... appears) (3)
ESUM	Echelle	
.OBS	Struct	
.OBJECT[30]	Char	#216: NGC 6210
.FRAME	Short	94
.NIGHT	Short	2
.DATE[20]	Char	6-JUL-1987
.TELESCOPE	Short	60
.PORT	Short	1
.DEWAR	Short	9
.CHIP[10]	Char	TI204
.ETIME	Short	180
.TIME	Short	180
.RA[4]	Float	16 43 56 9
.DEC[4]	Float	23 48 56 7
.DECS	Char	+
.EPOCH	Float	1987.5
.UT[4]	Float	4 22 14 2
.HA[4]	Float	1 10 42 6
.HAS	Char	-
.LST[4]	Float	15 33 14 3
.AIRMASS	Float	1.052
.TEMP	Float	-123.8
.ERASE	Float	411.8
.FILTER[20]	Char	
.SATURATED	Int	98
.GRATING	Short	53
.ANGLE[2]	Short	63 26
.X	Struct	
.LABEL[20]	Char	COLUMN #
.UNITS[20]	Char	
.DATA[800]	Float	1 2 3 4 5 6 .... 794 795 796 797 798 799 800
.Y	Struct	
.LABEL[20]	Char	ORDER NUMBER
.UNITS[20]	Char	m
.PROC[48]	Float	1 1 1 1 1 1 .... 1 1 1 1 1 1 1 1 1 1 1 1 1
.ROW1[48]	Float	712 697 679 664 648 632 .... 93 85 76 67 58
.ROW2[48]	Float	716 701 683 668 652 636 .... 97 89 80 71 62
.DATA[48]	Float	93 92 91 90 89 88 .... 52 51 50 49 48 47 46
.Z	Struct	
.LABEL[20]	Char	Counts
.UNITS[20]	Char	
.ERASE[801]	Float	413 419 407 414 415 405 .... 423 407 410 417
.DATA[800,48]	Float	37.3 69.8 55.0 94.7 82.6 99.2 .... 95.8 71.5

TABLE 3-2

Sample Echelle Data Structure Following ECHXREBIN

Structure (1)	Type (2)	Contents (Abbreviated where .... appears) (3)
ESUMW	Echelle	
.OBS	Struct	
.OBJECT[30]	Char	#216: NGC 6210
.FRAME	Short	94
.NIGHT	Short	2
.DATE[20]	Char	6-JUL-1987
.TELESCOPE	Short	60
.PORT	Short	1
.DEWAR	Short	9
.CHIP[10]	Char	TI204
.ETIME	Short	180
.TIME	Short	180
.RA[4]	Float	16 43 56 9
.DEC[4]	Float	23 48 56 7
.DECS	Char	+
.EPOCH	Float	1987.5
.UT[4]	Float	4 22 14 2
.HA[4]	Float	1 10 42 6
.HAS	Char	-
.LST[4]	Float	15 33 14 3
.AIRMASS	Float	1.052
.TEMP	Float	-123.8
.ERASE	Float	411.8
.FILTER[20]	Char	
.SATURATED	Int	98
.GRATING	Short	53
.ANGLE[2]	Short	63 26
.X	Struct	
.LABEL[20]	Char	Meff * Lambda
.UNITS[20]	Char	Angstroms
.DATA[800]	Double	332765.8 332774.5 332783.2 332791.8 .... 339762.8 339771.7 339780.6
.Y	Struct	
.LABEL[20]	Char	ORDER NUMBER
.UNITS[20]	Char	m
.PROC[48]	Float	1 1 1 1 1 1 .... 1 1 1 1 1 1 1 1 1 1 1 1 1
.ROW1[48]	Float	712 697 679 664 648 632 .... 93 85 76 67 58
.ROW2[48]	Float	716 701 683 668 652 636 .... 97 89 80 71 62
.DATA[48]	Float	93 92 91 90 89 88 .... 52 51 50 49 48 47 46
.MEFF[48]	Double	92.73 91.75 90.76 89.78 88.79 87.81 .... 50.11 49.11 48.11 47.11 46.12
.Z	Struct	
.LABEL[20]	Char	Counts
.UNITS[20]	Char	
.ERASE[801]	Float	413 419 407 414 415 405 .... 423 407 410 417
.DATA[800,48]	Float	1.17 1.91 1.44 1.07 1.02 .... 0.80 1.32 1.12

Bibliography

Ashley, M., 1983. *Subroutine REBIN for use in LOLITA, Version 1.4.*

Bevington, P.R., 1969. *Data Reduction and Error Analysis for the Physical Sciences* (New York: McGraw-Hill).

Cohen, J.G., and Lee, C.K., 1987. *The OBSERVING Superset of FIGARO, v. 1.0 Release.*

Gehren, T., and Ponz, D., 1986. *Astron. Astrophys.*, v. **168**, p. 386.

Huenemoerder, D., 1985. Private communication.

Marquadt, D., 1963. *J. Soc. Ind. Appl. Math.*, v. **12**, p. 431.

Schechter, P.L., 1986. Private communication.

Shortridge, K.I., 1984a. *"The Figaro Programmer's Guide,"* unpublished.

————, 1984b. *"FIGARO: An Introduction for Beginners,"* unpublished.

————, 1984c. *"FIGARO Manual,"* unpublished.

————, 1984d. *FIGARO Data Reduction Package, Version 1.0 Release.*

————, 1986. *FIGARO Data Reduction Package, Version 2.1 Release.*

Tonry, J., 1980. *Subroutine AMINI for use in PLAY, Version 1.0.*

Figure Captions

Figure 3-1: A cut through a B star echelle spectrum in the cross-dispersion direction, with red orders to the left and blue to the right. Note that the inter-order minima rows reach $\sim 3\%$ of the peak intensity of the adjacent orders, and decrease when the peak intensity in either adjacent order decreases (see text).

Figure 3-2: The linear equation derived by Gehren and Ponz (1986) applied to a column of data from the P60 echelle spectrograph. The size of the plotting symbol increases from blue to red. Note that the points do not fall along a straight line owing to the variations in the global background contribution.

Figure 3-3: The data of Figure 3-2 replotted as a function of Δx.

Figure 3-4: The wings of each order profile fit with a Gaussian function truncated after the Y^6 term (see equation 3.3 of the text).

Figure 3-5: The inter-order minima row to the red of the order containing the atmospheric A-band feature, before (thick line) and after (thin line) correction for adjacent order crosstalk.

Figure 3-6: The inter-order minima row to the blue of the order containing the atmospheric A-band feature, before (thick line) and after (thin line) correction for adjacent order crosstalk.

Figure 3-7: The reduction in the intensity of the inter-order minima rows resulting from the correction of adjacent order crosstalk. The solid line joins the inter-order minima before the correction; the dashed line does the same for those following the correction and so represents the true "global" scattered light. Note that the difference between the solid and dashed lines increases going from blue to red, and reaches a maximum correction of about 50%.

Figure 3-8: A flowchart for the ECHTRACT echelle extraction routine.

Figure 3-9: A sample application of the ECHXCONT command's automatic mode to high signal-to-noise data from a bright B star spectrum.

Figure 3-10: A comparison between a single order (that containing Hα) and the average of the two adjacent orders, not pre-processed by ECHXCONT.

Figure 3-11: The correction to the Hα order of Figure 3-10 determined by the ECHYCONT command.

Figure 3-12: The residuals of an echelle Th-Ar arc image as a function of order number, based on the automatic line identifications performed by the ECHARC command. Four orders were fit interactively in the initial phase of the program (their residuals are indicated by "*" as opposed to the "×" used to plot the residuals for the automatically fit arc lines).

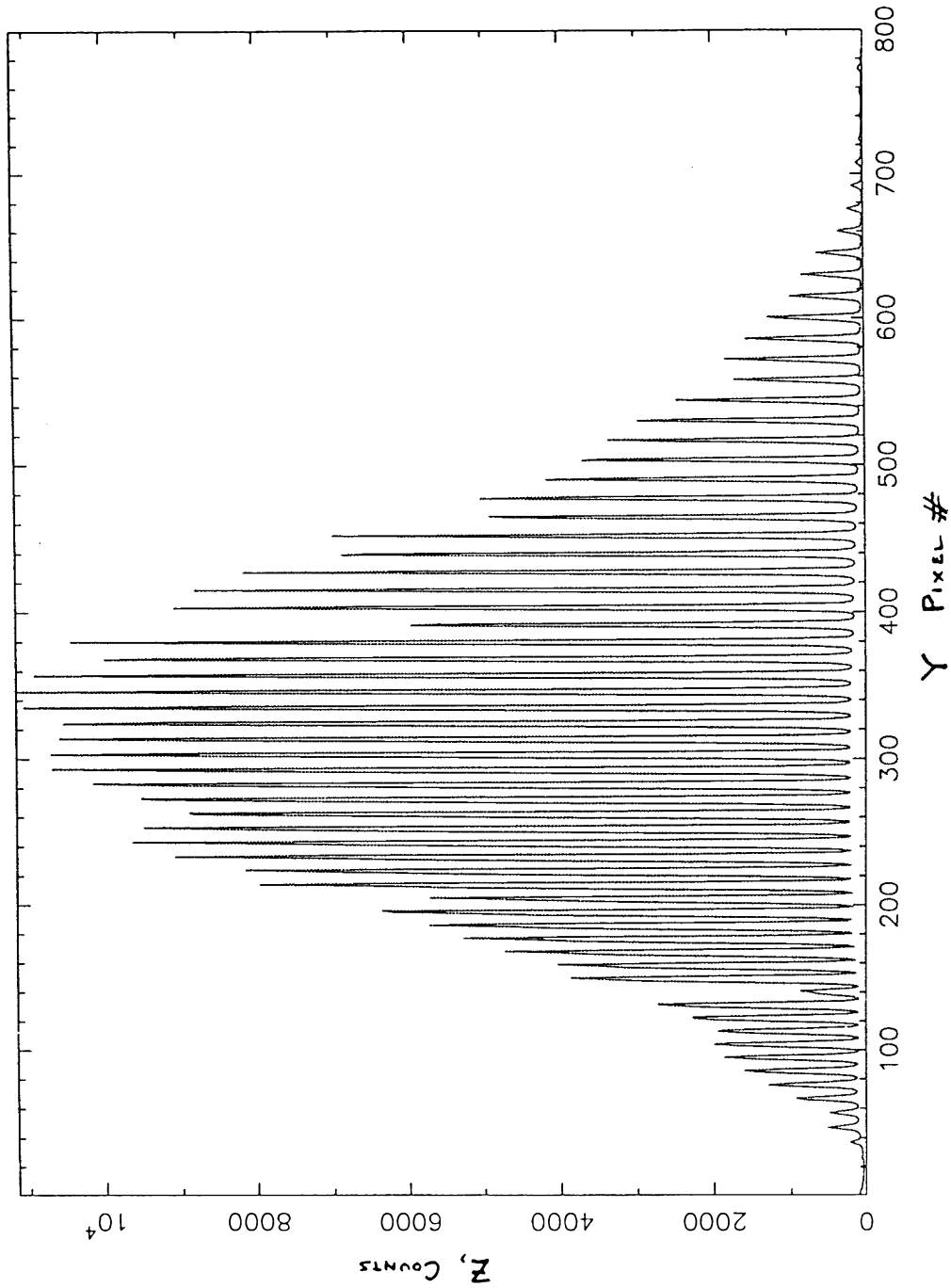
R, Counts
0
2000
4000
6000
8000
10^4
100
200
300
400
500
600
700
800
Y Pixel #

Figure 3-1

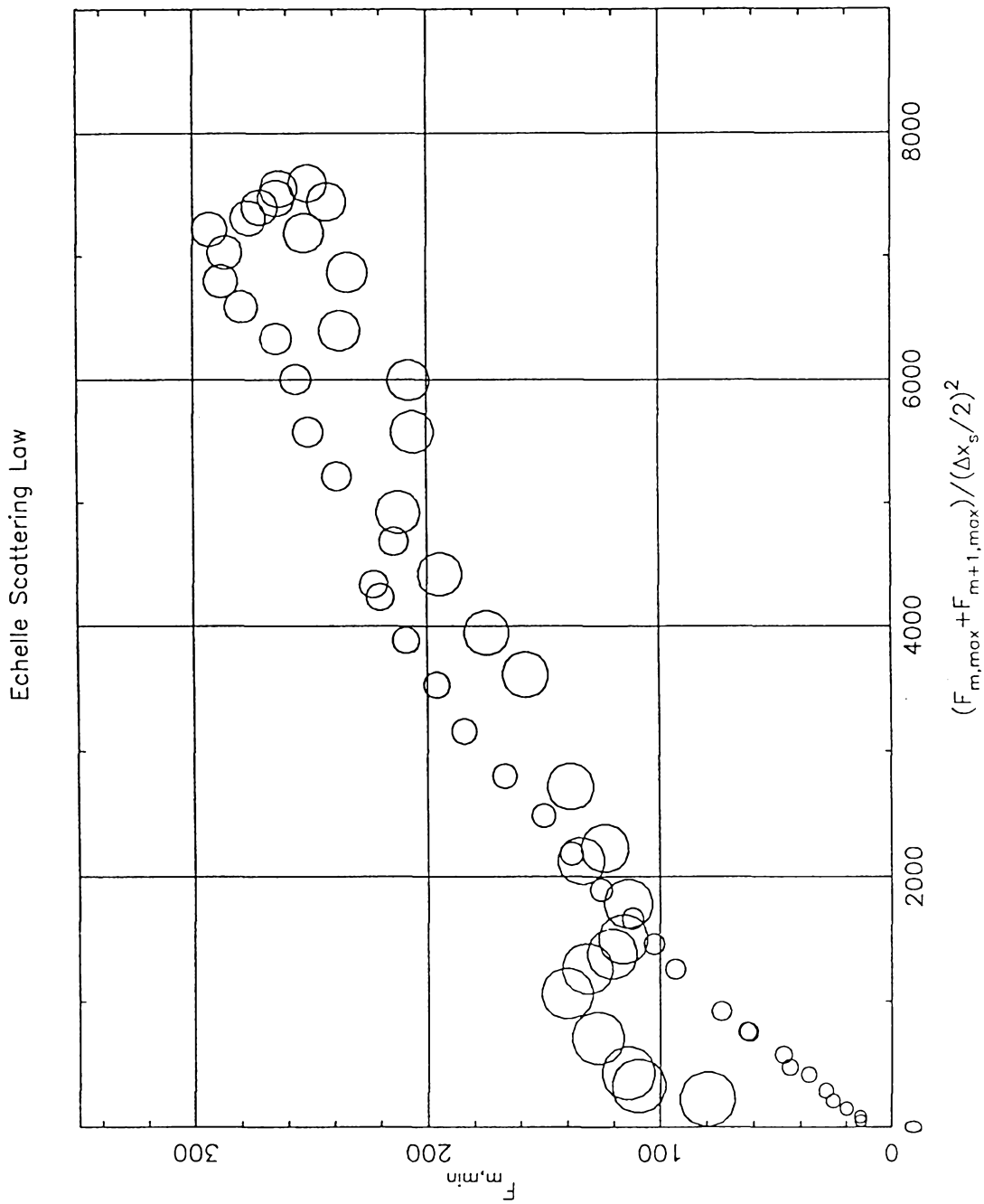
Echelle Scattering Law
$F_{m,min}$
0
100
200
300
0
2000
4000
6000
8000
$(F_{m,max}+F_{m+1,max})/(\Delta x_s/2)^2$

Figure 3-2

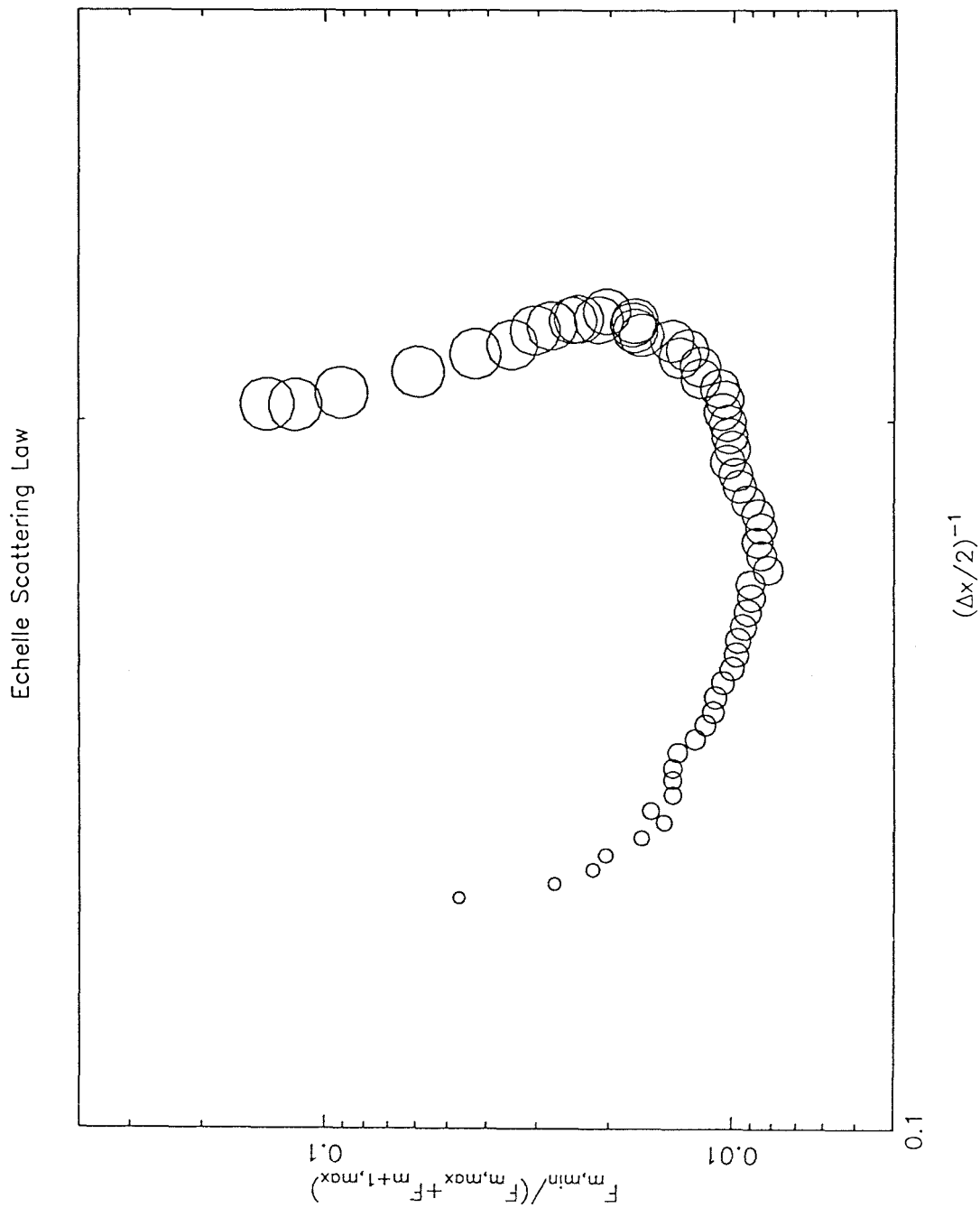
Echelle Scattering Law
$F_{m,min}/(F_{m,max}+F_{m+1,max})$
0.1
0.01
0.1
$(\Delta x/2)^{-1}$

Figure 3-3

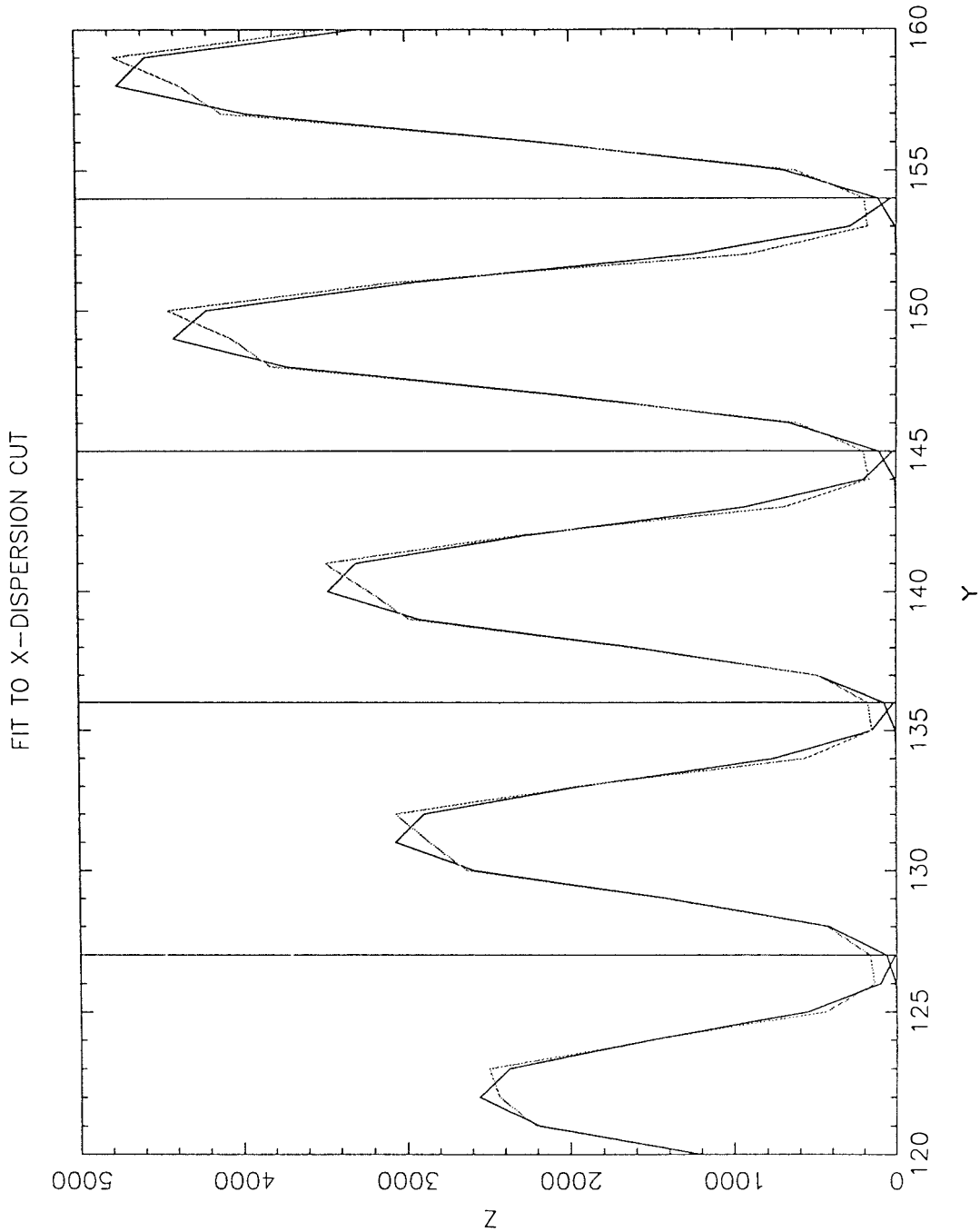
FIT TO X–DISPERSION CUT
Z
0
1000
2000
3000
4000
5000
Y
120
125
130
135
140
145
150
155
160

Figure 3-4

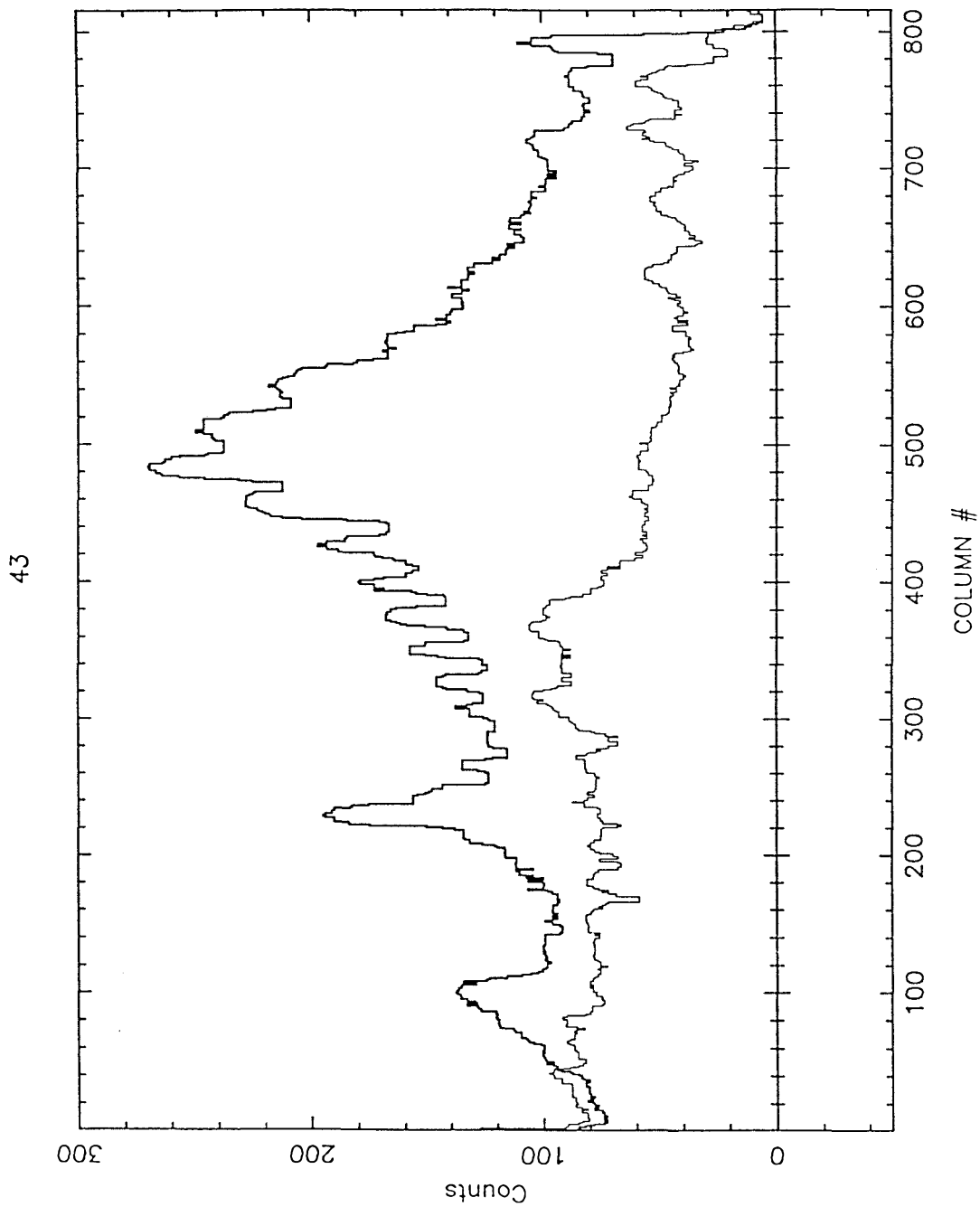

Figure 3-5

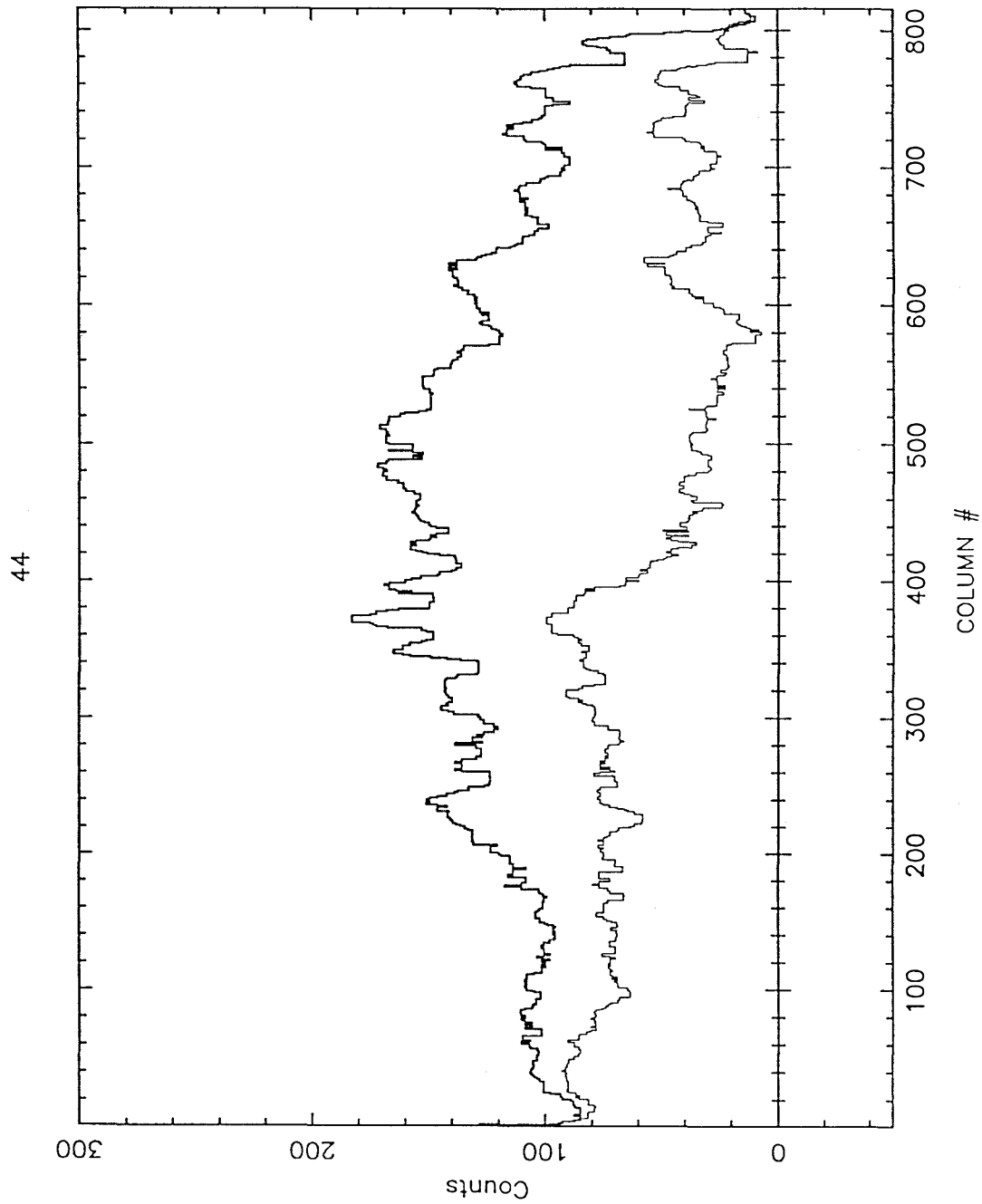

Figure 3-6

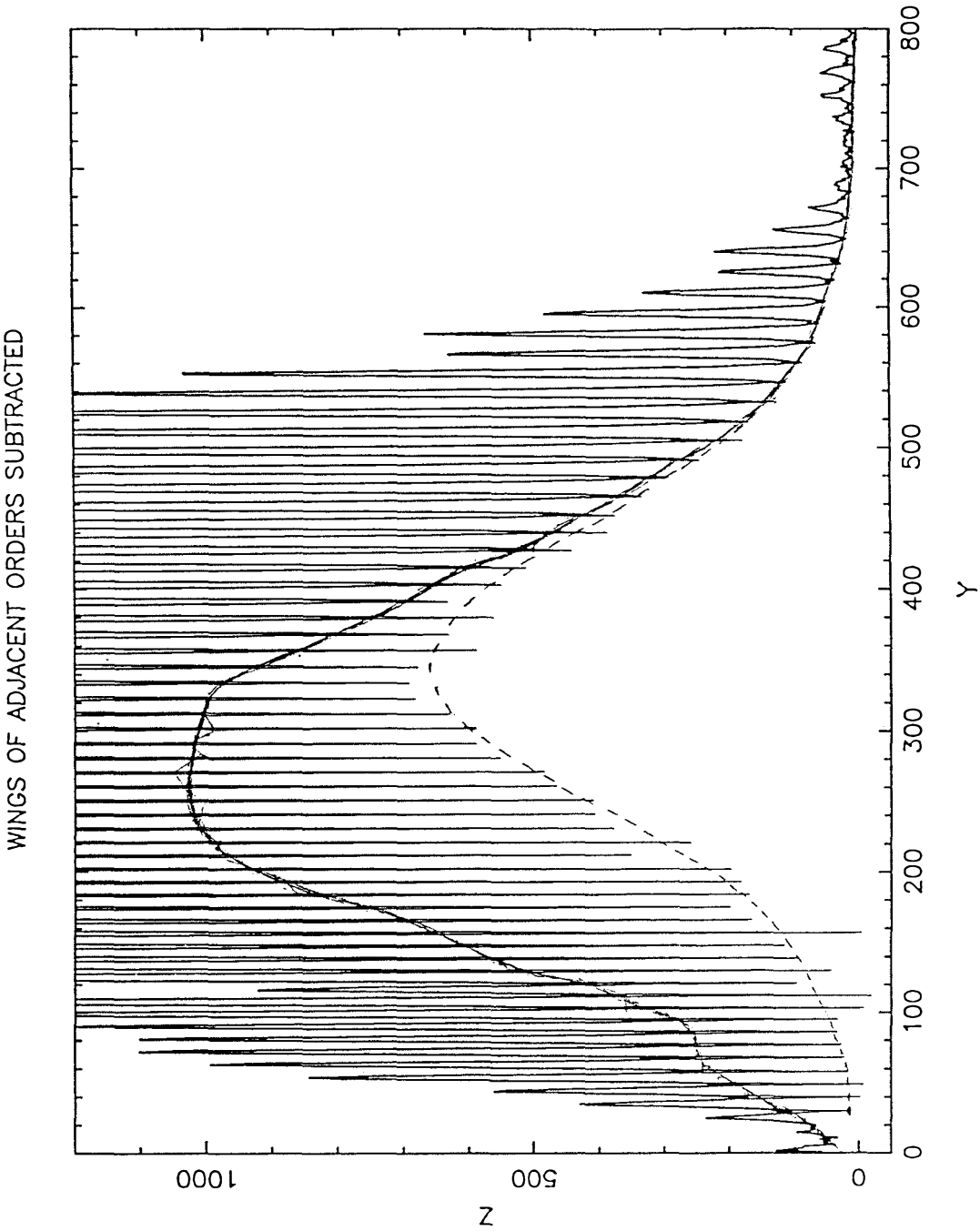
WINGS OF ADJACENT ORDERS SUBTRACTED
Z
1000
500
0
Y
0
100
200
300
400
500
600
700
800

Figure 3-7

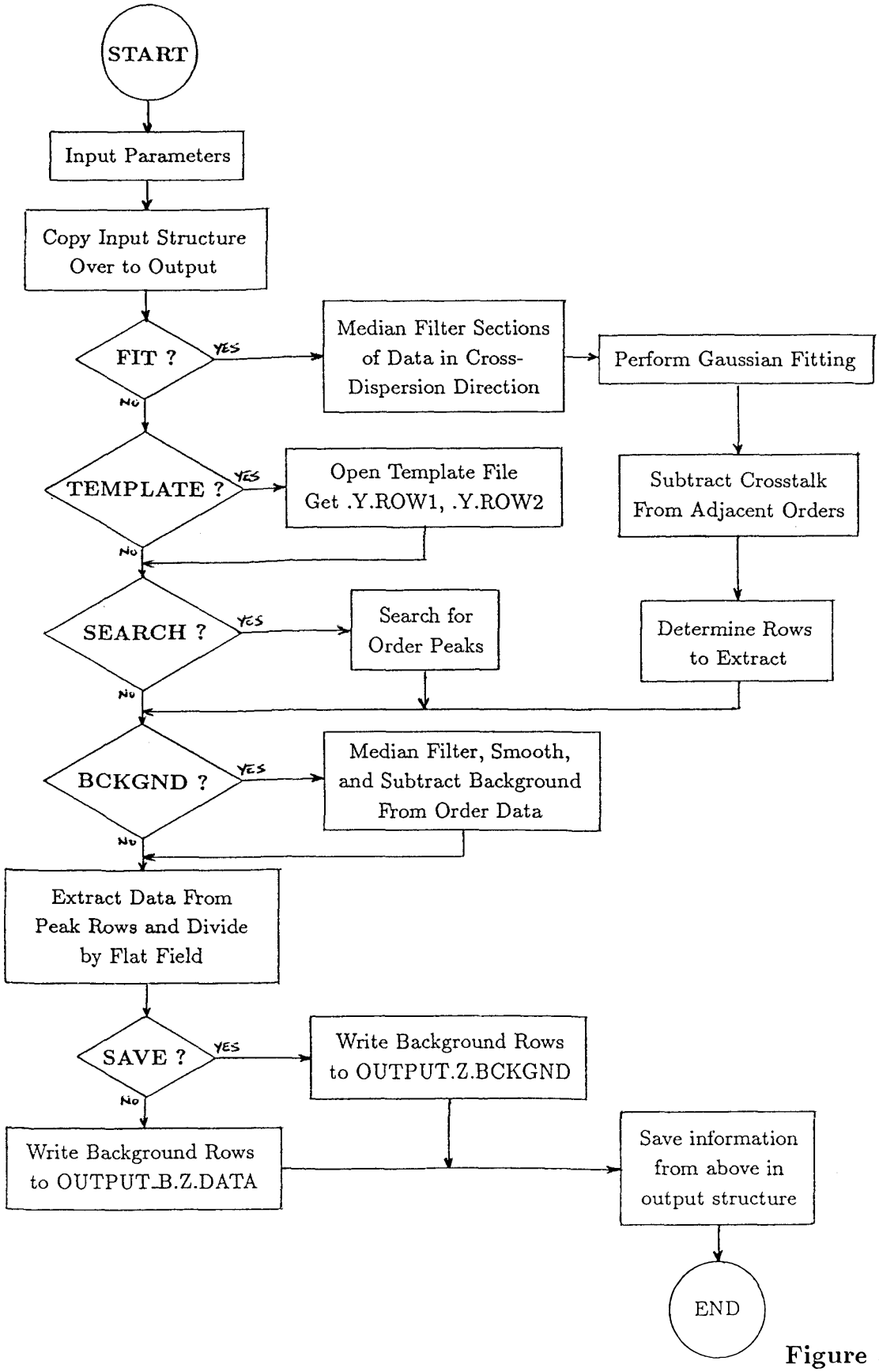
START
Input Parameters
Copy Input Structure Over to Output
FIT ?
YES
No
Median Filter Sections of Data in Cross-Dispersion Direction
Perform Gaussian Fitting
TEMPLATE ?
YES
No
Open Template File Get .Y.ROW1, .Y.ROW2
Subtract Crosstalk From Adjacent Orders
SEARCH ?
YES
No
Search for Order Peaks
Determine Rows to Extract
BCKGND ?
YES
No
Median Filter, Smooth, and Subtract Background From Order Data
Extract Data From Peak Rows and Divide by Flat Field
SAVE ?
YES
No
Write Background Rows to OUTPUT.Z.BCKGND
Write Background Rows to OUTPUT_B.Z.DATA
Save information from above in output structure
END

Figure 3-8

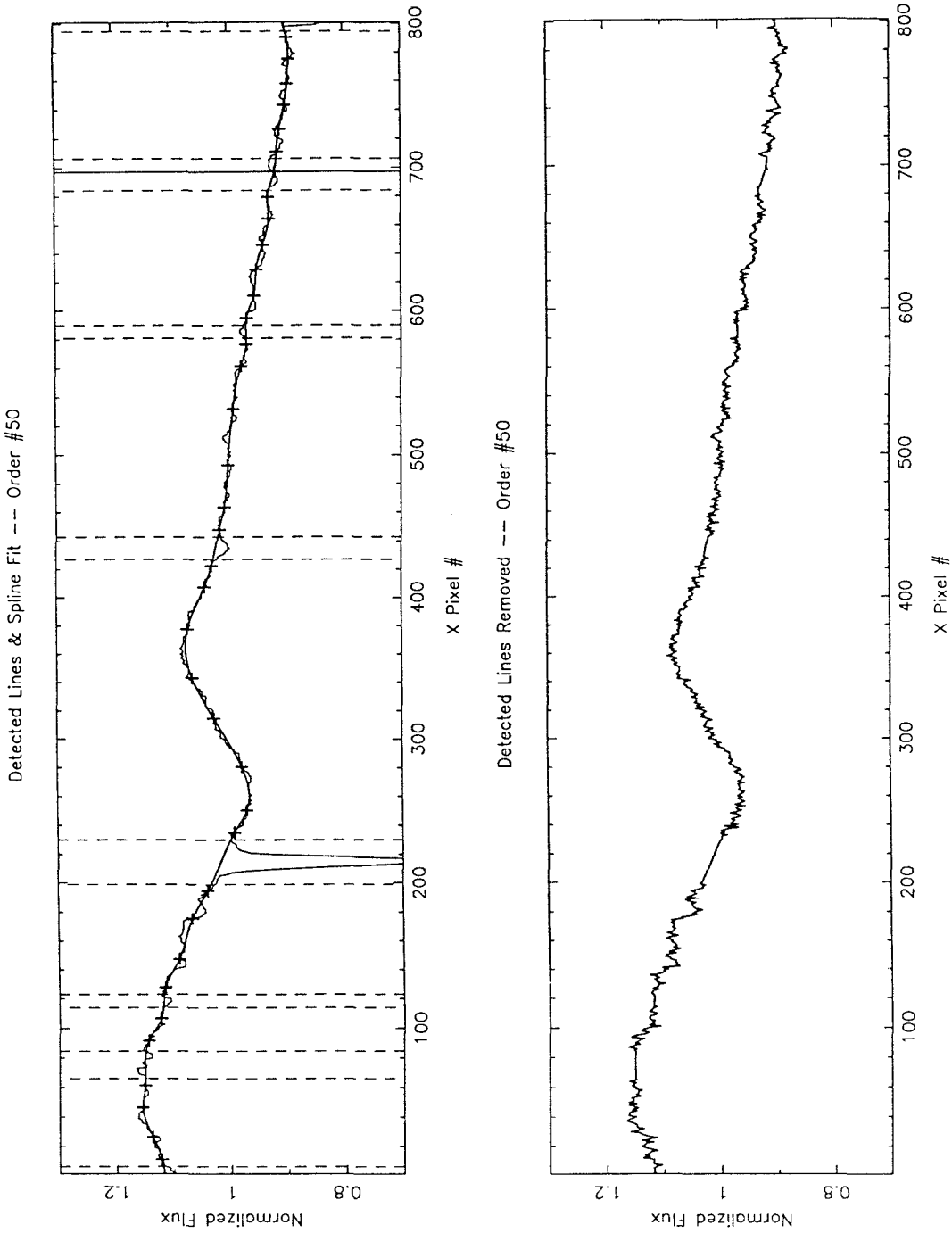
Detected Lines & Spline Fit -- Order #50
Normalized Flux
X Pixel #
Detected Lines Removed -- Order #50
Normalized Flux
X Pixel #

Figure 3-9

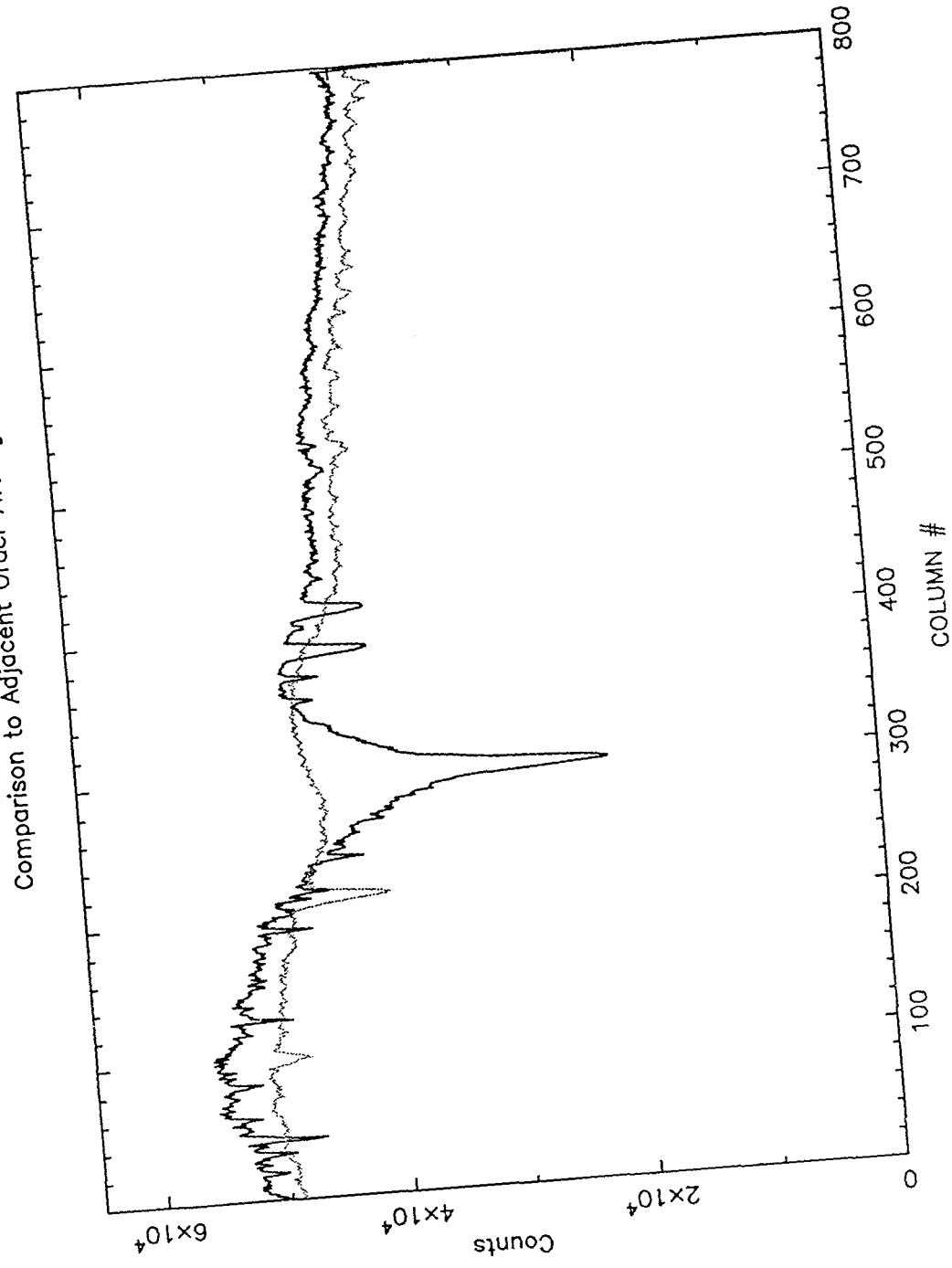
Comparison to Adjacent Order Average
Counts
6x10⁴
4x10⁴
2x10⁴
0
100
200
300
400
500
600
700
800
COLUMN #

Figure 3-10

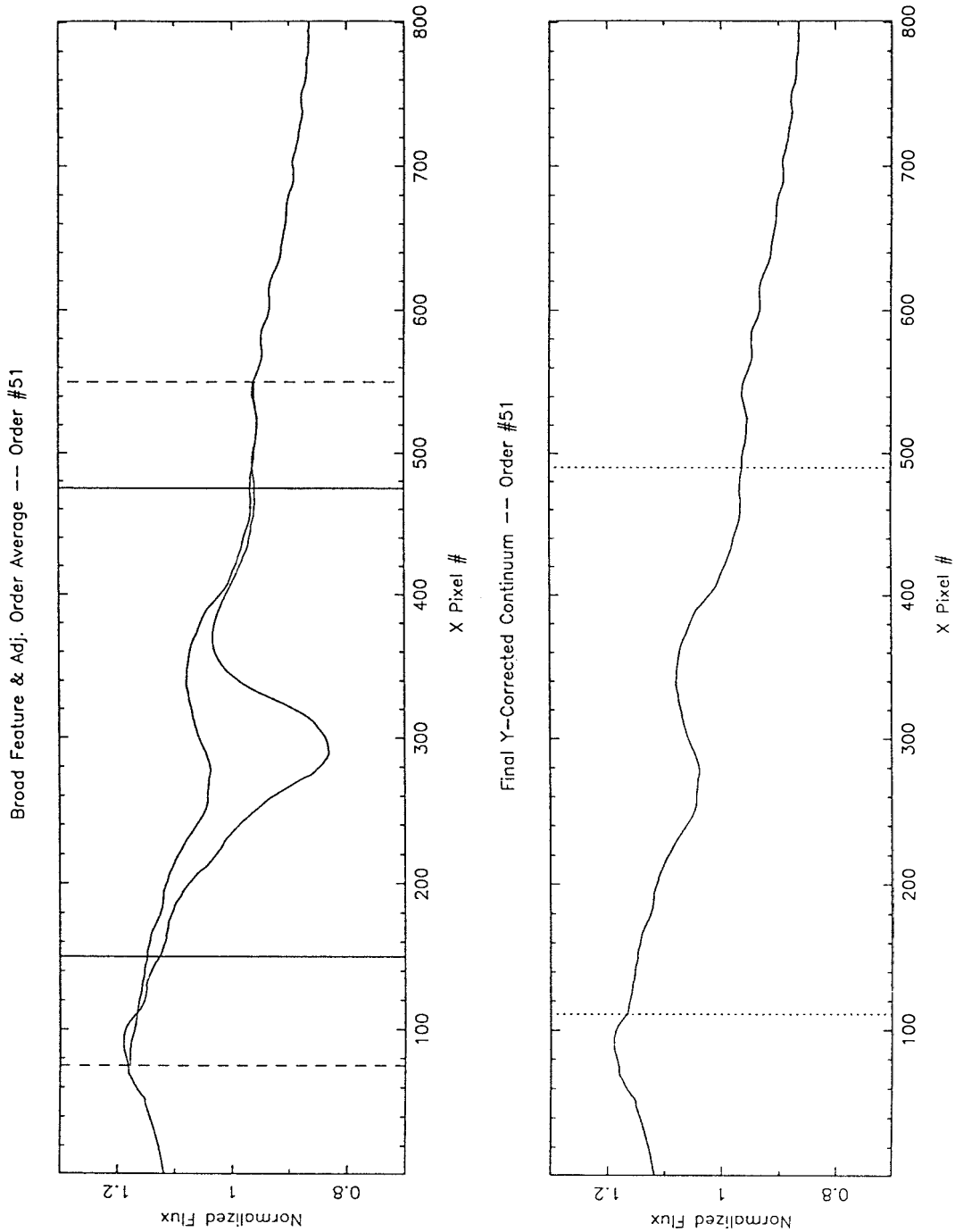
Broad Feature & Adj. Order Average -- Order #51
Normalized Flux
X Pixel #
Final Y-Corrected Continuum -- Order #51
Normalized Flux
X Pixel #

Figure 3-11

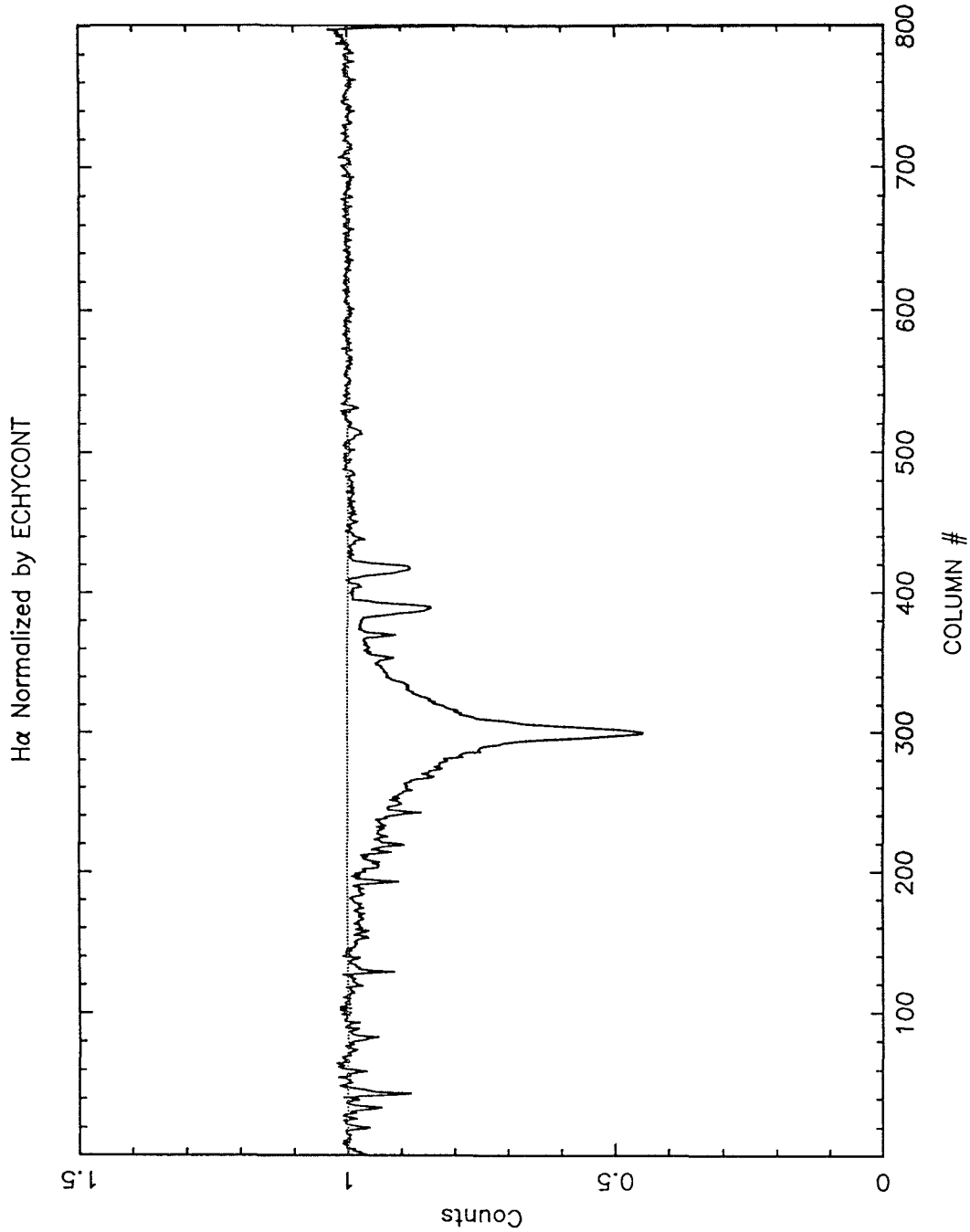

Figure 3-11
(continued)

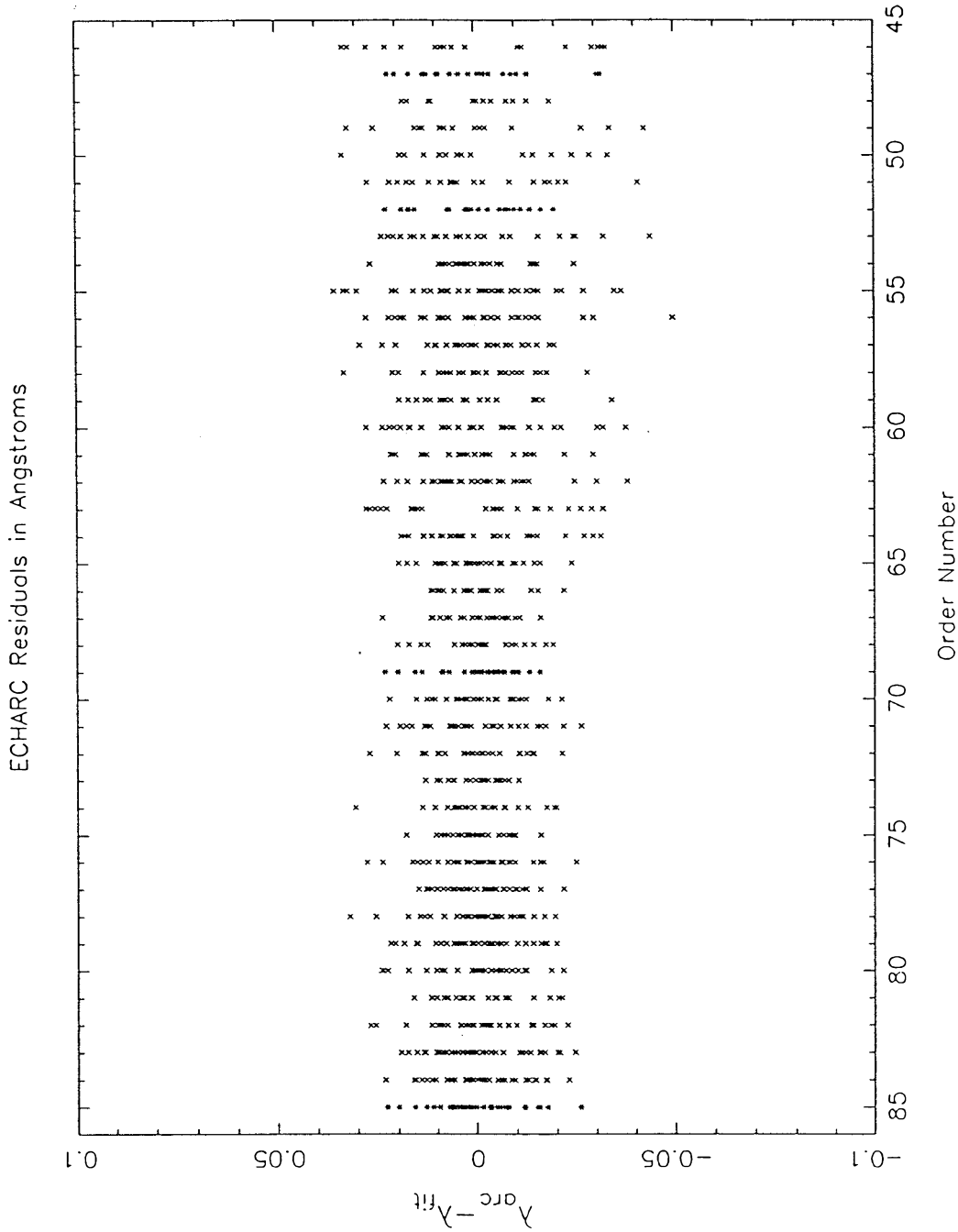
ECHARC Residuals in Angstroms
0.1
0.05
0
−0.05
−0.1
$\lambda_{arc} - \lambda_{fit}$
45
50
55
60
65
70
75
80
85
Order Number

Figure 3-12

IV. Astrophysical Parameters of an Initial CSPN Sample

A. The Observational Material

Returning now to the particular study of the central stars of planetary nebulae that was introduced in Chapter **I**, the P60 echelle spectrograph (see Chapter **II**) was used to obtain high resolution spectra of 21 of the CSPN in the distance limited sample of Table 1-1. These objects and a summary of the P60 echelle observations are listed in Table 4-1. In all cases the slit width used was equal to 1.5 arcseconds; although larger slit widths would have increased the throughput and (in the extreme) permitted spectrophotometry, the narrow slit was necessary in order to maximize the contrast between stellar and nebular emission, as well as to minimize the width of the instrumental profile. For all observations the spectrograph was rotated so that the slit was along the direction of atmospheric dispersion. The exposure times were kept short in cases where the CSPN was imbedded in a nebula of high surface brightness, so as to prevent saturation of the nebular emission lines.

In August and September of 1987, these data were distortion corrected and extracted according to the procedures described in Chapter **III**, with the following precautions taken owing to the unique nature of CSPN spectra and the model atmosphere fitting objectives of this work: (1) No effort was made to interpolate across bad columns, cosmic rays, etc., since the stellar line profiles of interest were broad and corrupted data could be ignored; (2) ECHTRACT was run in *FIT* mode, so that the wings of adjacent orders would be subtracted from the inter-order minima rows before the latter were smoothed and subtracted from the echelle spectral orders, so as to produce the most accurate net continuum counts possible; (3) Smoothing of the global inter-order background rows was preceded by a pair of median filters with $15 \leq XAVG \leq 45$ and $5 \leq YAVG \leq 11$, the exact values chosen so as to guarantee that any evidence of the nebular lines were removed from these rows prior to

smoothing and subtracting from the echelle orders.

The resulting collapsed data structures were taken to Munich, West Germany, in order that the P60 echelle spectra could be compared to the NLTE model atmosphere line profiles of Dr. Rolf Kudritzki and his co-workers at the Universität Sternwarte München. The data to be fit with model profiles were normalized using ECHXCONT and ECHYCONT, under the supervision of Dr. Roberto Mendez and using the VAX computer facilities of the European Southern Observatory's Scientific Center in Garching. Interactively obtaining an accurate fit to the continuum for the ECHXCONT normalization was the most subjective step in the reduction process, and the experience Dr. Mendez has had with CSPN spectra proved very valuable in distinguishing between possible real features and artifacts of incomplete flat fielding, the latter being troublesome only in the blue ($\lambda \leq 4500$ Å). Note, however, that ECHYCONT was used to normalize the echelle spectra in the vicinity of each broad feature of diagnostic importance, and so any subjective decisions only played a role in removing relatively weak and narrow features from those adjacent orders used by ECHYCONT. Therefore there should be no reason to doubt the final normalization of the diagnostic lines, even in the far wings. On the other hand, future work involving CSPN abundances from those "relatively weak and narrow" lines of C, N, and O will need to pay particular attention to how this normalization with ECHXCONT was done.

Finally, the full set of ≤ 60 orders comprising the collapsed echelle data structures were reduced with ISUBSET to only the range of orders containing adequate signal-to-noise data to be useful for model atmosphere analysis, and the same was done to the corresponding Th-Ar arc frames. These were then fit with ECHARC, and the normalized CSPN frames wavelength calibrated with ECHXREBIN, using: (1) a logarithmic as opposed to a linear wavelength scale; (2) quadratic as opposed to linear interpolation; and lastly (3) conserving mean value as opposed to flux,

since the data had already been normalized to unity in the continuum. The data were then in a final form and ready to be compared to the line profiles resulting from the model atmospheres of the Universität Sternwarte group.

B. The Model Atmosphere and Line Formation Codes

These NLTE model atmospheres (Kudritzki, 1973, 1976; Husfeld, et al., 1984; Husfeld, 1986; Groth, 1986) treat the stellar atmosphere as plane parallel, consisting entirely of hydrogen and helium in radiative and hydrostatic equilibrium. As many as 5 levels of HI, 5 levels of HeI, and 10 levels of HeII are permitted to deviate from their respective LTE populations. Herrero (1987a, 1987b) has calculated the line profiles that result from these model atmospheric structures using a technique known as "Accelerated Lambda Iteration" (or ALI, developed by Werner and Husfeld, 1985), which takes into account each transition's Stark profile when calculating radiative transitions between levels to determine occupation numbers and radiation transfer. The 45 line transitions used are to be compared with the standard treatment of Auer and Mihalas (1972), which treated only 6 lines and used for each a pure Doppler profile. As a consequence of the improved accuracy possible with the ALI technique, Herrero's Balmer line profiles are approximately 10% deeper in the line cores than pre-ALI line formation code results (cf., Auer and Heasly, 1976). Herrero (1987a) also reports much better agreement with observations of line profiles in massive O stars (e.g., τ Sco), subdwarf O stars (e.g., Ross 162 in the globular cluster NGC 6397), as well as CSPN (e.g., the central star of NGC 1360 as observed by Mendez, et al., 1985). However, the best fit with these new line profiles are for temperatures 10 to 20% higher because of their deeper line cores.

In addition, the new line profiles for HeII 4686 Å resulting from an improved broadening theory (Schöning and Butler, 1988) were incorporated into the process described below. These new profiles are somewhat narrower than those resulting

from the previous Auer-Mihalas theory (1972), the primary result being a slightly higher temperature together with an increased He abundance for the revised best fit to high temperature CSPN (see note added in proof, Mendez, et al., 1988).

In a recent review paper, Kudritzki (1987) identifies the three most important areas in which the models are currently deficient: (1) The models neglect metal line blanketing. Kudritzki claims that including the effects of metal lines will only change T_{eff} by up to 5 or 10%, and cites the thesis work of Werner (1987) which included carbon with little change in the temperature structure of the atmosphere *in the region of formation of optical H and He lines,* as these lines are formed deeper within the atmosphere than the layers effected most by metal line blanketing. (2) The models also neglect the possible existence of strong stellar winds, which would be expected to heat the atmosphere by backscattering photosheric photons back towards the stellar surface. This "wind blanketing" could be a potential source of error for massive CSPN which exhibit Of-type spectra. (3) Finally, the models are plane-parallel, and sphericity effects from extended atmospheres may alter the line profiles. For sdO stars, the study of extended NLTE models made by Gruschinske and Kudritzki (1979) found only minor effects, and Kudritzki (1987) expects this deficiency in the models to be secondary to assumptions (1) and (2).

Mendez, et al. (1988), and Kudritzki (1987) quote nominal uncertainties associated with the type of model atmosphere analysis to be discussed below of $\pm 10\%$ in T_{eff}, ± 0.2 in log(g), and $\pm 20\%$ in He abundance "y". These estimates are the combined uncertainties from two sources: *both* the likely systematic uncertainties arising from assumptions made in the calculation of the theoretical line profiles (as summarized above) *and* errors in the fitting process itself due to noise in the high resolution echelle spectra; neither Mendez nor Kudritzki provide any estimates of the separate contributions from these two sources to the totals. Following the description of the fitting process in §**IV.C** below, the latter noise contribution to the

total uncertainties will be calculated quantitatively and compared to these estimates of the total uncertainties.

In order to gain greater insight into the behavior of the Balmer line profiles predicted by the models as a function of T_{eff} and log(g), Figure 4-1 was prepared showing contours for Hγ along which $FW(0.025)$, the full width at a fractional continuum depth of 0.025, has the constant values indicated. This figure was produced by measuring this characteristic parameter throughout the grid of models which the Universität Sternwarte München group had calculated as of December, 1987, represented as crosses in Figure 4-1; then the values of $FW(0.025)$ at regularly spaced intermediate points were determined using the IMSL interpolation routine IQHSCV and the contours drawn with the graphics routine for this purpose (PGCONT) from the PGPLOT package (Pearson, 1986).

Note from the contours of Figure 4-1 that, for constant T_{eff}, the Hγ linewidth increases with increasing log(g). This behavior is a consequence of Stark broadening, for which the nearest neighbor treatment (such as that presented in, e.g., Gray, 1976) yields for the wing absorption coefficient per hydrogen atom:

$$\alpha = 3.21 \times 10^2 \; C_2 \frac{P_e}{T} \Delta\lambda^{-5/2} \tag{4.1}$$

which for fixed alpha can be solved for $\Delta\lambda$ and so:

$$\Delta\lambda \propto P_e^{2/5} T_e^{-2/5} \; , \quad P_e \propto g^{1/3} \; , \tag{4.2}$$

where C_2 is a constant for each transition and P_e and T_e are respectively the electron pressure and temperature. Note further that the slope of the contours decreases with increasing T_{eff}; one might conclude from this behavior that, for high effective temperature, the Hγ line is insensitive to T_{eff} and has a shape dependent only upon the value of log(g). This conclusion is incorrect, however, due to the fact that $FW(0.025)$ is a measure of just one characteristic line *width* of the full Hγ line

profile, and therefore is not a complete description of the line's behavior. From additional measurements of $FW(0.100)$ and the maximum line depth, a set of contours similar to Figure 4-1 but representing instead a rough measure of the equivalent width of the Hγ line were produced (Figure 4-2). One finds that the model Hγ line profiles are becoming weaker towards higher T_{eff} (as the ionized fraction of hydrogen increases), and so the Hγ line profile at high T_{eff} is not only a function of log(g). Note lastly that in practice the equivalent width contours of Figure 4-2 have little usefulness, due to the fact that the core of the line profile is typically obscured by nebular emission, and so the fitting process must make use of the set of complete profiles calculated for each model atmosphere.

C. The Model Atmosphere Fitting Process

The model atmosphere fitting process for each planetary nebulae central star began with a visual inspection of the fully reduced echelle spectra. Answers to questions like: (1) Does the star have HeI lines ? (2) HeII lines ? (3) Are the Balmer lines broad or narrow ? (4) Are the nebular lines masking much of the stellar lines ? — and so forth would help guide the fitting process by identifying the most appropriate diagnostic lines to be used, and restricting the search through the grid of model atmosphere line profiles to those grid points expected to lie fairly close to the CSPN in the log(g) – log(T_{eff}) plane.

The next phase of the fitting process was to define a locus of points in the log(g) – log(T_{eff}) plane that match the central star's Balmer line profiles. This was done with the help of the grid of model atmospheres for which diagnostic line profiles had been calculated by the Universität Sternwarte München group (the "+" symbols in Figures 4-1 and 4-2). These profiles exist in the form of transparent overlay line tracings, with a constant intensity scale (10 cm from 0 to 100 percent of the continuum) as well as wavelength scale (5 Ångstroms per cm). At each of several

temperatures for which a series of models exist with differing log(g), the model's Hγ profile is compared to the data, and the best fit log(g) at that temperature is determined visually by interpolation between the pair of model profiles which most closely match the observed profile. The reason for concentrating on the Hγ line at this phase is that Hβ and Hα are more likely than Hγ to be filled in by emission from a stellar wind. Higher upper quantum number lines in the Balmer series are located too far to the blue, where the CCD is not as sensitive, and so these lines are less useful than Hγ because of increased noise.

In the particular case of the central star of NGC 1360, the Hγ line profile in the observed spectrum was matched with the following pairs of (T_{eff}, log(g)) values: (40,000 K, 4.5), (50,000 K, 5.0), and (80,000 K, 5.5); at T_{eff} = 100,000 K all the model Hγ profiles were too shallow to match the observed data. The Hγ fit locus for NGC 1360 obtained in this phase of the fitting process is shown in Figure 4-3. Note the similarity this locus has to the $FW(0.025)$ contours in Figure 4-1, and the decrease in model Hγ line strengths between T_{eff} values of 80,000 K and 100,000 K exhibited by the contours in Figure 4-2.

The next step is of course to determine where along this Hγ locus in the log(T_{eff}) – log(g) plane one obtains the best fit to the other lines in the CSPN spectra. If the spectrum contains both HeI and HeII lines, this step is quite simple as the HeI/HeII ionization equilibrium restricts the best fit to a very narrow range of temperatures. A comparison of the HeI lines at 4471 Å and 5875 Å versus the HeII lines at 4542 Å and 5411 Å is made for a series of temperatures (using a corresponding log(g) value from the Hγ fit locus) until all lines present in the spectra are in agreement with the model profiles, or else all differ in the same sense of being either too weak or too strong. All the HeI and HeII line strengths can then be adjusted by varying the He abundance in the model until a satisfactory fit is derived.

In the particular case of NGC 1360, the situation was more complex at this step because of the absence of the HeI lines 4471 Å and 5875 Å. While this information served to rule out temperatures cooler than about 50,000 K or 60,000 K, to proceed further towards a best fit temperature and gravity determination in such cases of high T_{eff} required another approach.

There are in fact two different HeII series which have lines in the optical spectrum: the series $n \rightarrow 3$ (analogous to the HI Paschen series), which is responsible for the HeII lines at both 4686 Å (4–3) and 3200 Å (5–3), and then the Pickering series $n \rightarrow 4$ responsible for lines at 10,129 Å (5–4), 5411 Å (7–4), 4542 Å (9–4), 4200 Å (11–4), and so on. Note that the even members of this series, (6–4), (8–4), (10–4), etc., have wavelengths that coincide with the Balmer series ($n \rightarrow 2$) of HI and thus are not independently observable (although high temperature Balmer line profiles are asymmetric owing to the presence of HeII). Because the HeII absorption line at 4686 Å originates from $n = 3$, whereas the HeII absorption lines at 4542 Å and 5411 Å originate from $n = 4$, the 4686 Å line behaves differently under NLTE conditions than do the Pickering series lines as temperature and gravity in the stellar atmosphere change.

Some insights into the reasons for this effect can be had by considering how the $n = 3$ and $n = 4$ levels are determined under NLTE conditions: the strongest radiative transitions into and out of these levels are HeII Lyman β (Lβ) and HeII Lyman γ (Lγ), respectively. According to Husfeld (1988), $n = 3$ and $n = 4$ will have the same departure coefficients as the ground state so long as both of the dominant HeII Lyman lines are optically thick. However, HeII Lβ line is formed higher in the atmosphere than the HeII Lγ line, and so the strengths of the two transitions — and hence the populations of the $n = 3$ and $n = 4$ levels — will behave differently as a function of depth under NLTE conditions. Husfeld suspects that HeII 4686 Å is formed in a region of the atmosphere close to where HeII Lγ (and possibly even

HeII Lβ as well for high values of T_{eff}) is formed, while the Pickering series lines are formed much deeper in the atmosphere where most of the HeII Lyman series lines are optically thick. In other words, whereas $n = 4$ is coupled to the ground state by collisions deep in the atmosphere where the HeII Pickering series lines are formed, $n = 3$ is less coupled at the depths of importance for HeII 4686 Å; for this reason one might expect the two lines to behave quite differently as functions of T_{eff} and log(g), with the HeII Pickering series lines exhibiting behavior closer to that predicted by LTE (cf., equations (4.1) and (4.2) above, recalling that HeII is a hydrogenic ion).

Therefore to proceed further with the model fitting of hot CSPN without HeI lines, a simultaneous fit to both HeII 4686 Å and the HeII Pickering series lines 4200 Å, 4542 Å, and 5411 Å must be found at some unique point along the Hγ fit locus. This point determines the final fit parameters log(g) and T_{eff}. Then lastly, if all the HeII lines are too strong or too weak, the model's He abundance can be adjusted to obtain the final result.

In the particular case of NGC 1360, this best fit final result was obtained for a temperature of 75,000 K, a log(g) of 5.5, and a "normal" He abundance y of 0.09 by number. At higher temperatures, the HeII Pickering series lines in the models were too weak relative to HeII 4686 Å, while the reverse was true at lower temperatures.

Recall that Mendez, et al. (1988), and Kudritzki (1987) claim an overall uncertainty of $\pm 10\%$ in T_{eff}, ± 0.2 in log(g), and $\pm 20\%$ in y without substantiating these numbers. Using NGC 1360 as a typical example, the uncertainties due to solely to the noise in the observed spectrum can be calculated as follows. Figure 4-4 shows the Hγ profile of NGC 1360 with a solid line at the continuum = 1.00 level, and a dashed line at a depth 0.025 below the continuum level. The slope of the line profile at its point of intersection with this dotted line is approximately $dy/dw = 0.01 \text{Å}^{-1}$.

The uncertainty in the y-value of each pixel i is the reciprocal of the S/N ratio of the data, since these data have been normalized to a continuum = 1.00 scale:

$$\sigma(i) = [S/N]^{-1} = 0.0125 \tag{4.3}$$

in this example with S/N = 80. However, when normalizing the data locally to unity in the continuum, as well as in the line fitting process, the result is based not on a single pixel but on a group of neighboring pixels. Typically a "local" region of data spans about 2 or 3 Ångstroms of spectrum, and consists of roughly $N_p = 20$ pixels or more. The 1σ uncertainty in the mean of such a group is:

$$\sigma(N_p) = \frac{\sigma(i)}{\sqrt{N_p}} \; . \tag{4.4}$$

Since the line profile depth is uncertain because of both the noise in the line wing and the uncertainty in determining the continuum level, two $\sigma(N_p)$ errors must be added in quadrature for ΔY:

$$\begin{aligned} \Delta Y &= \sqrt{2} \times \sigma(N_p) \\ &= \frac{\sqrt{2}}{\sqrt{N_p} \times [S/N]} \\ &= 0.004 \end{aligned} \tag{4.5}$$

for S/N = 80 and $N_p = 20$. This error in line depth corresponds to an error in the wavelength position of the depth=0.025 point of:

$$\begin{aligned} \Delta W &= \frac{\Delta Y}{dy/dw} \\ &= \frac{\sqrt{2}}{\sqrt{N_p} \times [S/N] \times dy/dw} \; . \end{aligned} \tag{4.6}$$

Note that the full width of the line depends on the location of two such depth = 0.025 points, and so two such ΔW errors should be added in quadrature. Yet it is seldom true that the S/N of the line wing farther from order center is as good

as the S/N at order center, and so in practice the fit is typically determined more on the basis of one wing of the line profile than the other. So rather than adding two ΔW errors in quadrature, the full width error ΔFW is better approximated by twice the individual ΔW error:

$$\begin{aligned} \Delta FW &= 2 \times \Delta W \\ &= \frac{2\sqrt{2}}{\sqrt{N_p} \times [S/N] \times dy/dw} \\ &= 0.8\text{Å} \end{aligned} \tag{4.7}$$

for $N_p = 20$, $S/N = 80$, and $dy/dw = 0.01\text{Å}^{-1}$.

In the contour map of $FW(0.025)$ developed above in §**IV.B** (see Figure 4-1), it is the case that two such $FW(0.025)$ contours spanning a difference of 5 Ångstroms in $FW(0.025)$ are parallel and are separated vertically by 0.8 in log(g). Therefore it follows that a ±0.8 Å uncertainty in the full width at depth = 0.025 translates into an uncertainty in log(g) of:

$$\begin{aligned} \Delta \log(g) &= \frac{\delta \log(g)}{\delta FW(0.025)} \times \Delta FW \\ &= \frac{0.8}{5.0\text{Å}} \times 8.0\text{Å} \\ &= 0.13 \end{aligned} \tag{4.8}$$

which, being a 1σ uncertainty (±0.13 is then a 68% confidence interval), is consistent with the ±0.2 uncertainty quoted by Mendez and Kudritzki.

In order to estimate the errors involved in the next phase of the fitting process using HeII Pickering series lines versus HeII 4686 Å, these line strengths were measured for two models: (T_{eff} = 80,000 K, log(g) = 5.5); and (T_{eff} = 50,000 K, log(g) = 5.0), since these grid points lie along the Hγ fit locus. The HeII 4686 Å line strength remained nearly constant (i.e., the depth remained constant, while the line width at log(g) = 5.5 was only slightly wider). The HeII 4542 Å line strength,

however, changed considerably: the depth at the low temperature point was 15% of the continuum while at the higher temperature grid point the depth was 9%. Linearly interpolating between these measurements implies that a 10,000 K increase in temperature results in a 2% decrease in the central line depth of the HeII 4542 Å line. While such a 2% change would easily be detected on the basis of the Hγ error analysis presented above, note that the line cores are frequently suspect due to the emission often found there, and so the line fitting is in practice based on the region of the profile where the depth is 1/2 to 1/4 of the central depth. The depth of this region is then affected at the 1% to 0.5% level by a 10,000 K change in temperature along the Hγ fit locus. Adopting a 0.5% criteria for discriminating between different HeII 4542 Å line wing profiles, the $\sigma(N_p)$ for a group of 20 pixels (0.004 from equation (4.5) above) satisfies this criteria down to an uncertainty of $\pm$8000 K. This is precisely the $\pm$10% error quoted by Mendez and Kudritzki; however, the situation is often better determined when a simultaneous match to the Pickering series lines 4200 Å and 5411 Å is required in addition to 4542 Å. Thus the Mendez and Kudritzki error quoted is found again to be a conservative one.

D. Comparison with CASPEC results

Three planetary nebulae central stars in the sample observed with the P60 echelle spectrograph overlapped with the southern hemisphere sample of Mendez, et al. (1988), which they observed with the CASPEC echelle spectrograph at the ESO 3.6m telescope. These three objects were NGC 1360, NGC 2392, and NGC 4361, and they were given top priority as objects to be fit in order to first determine whether or not there were serious systematic differences between the P60 echelle and CASPEC spectra and data reduction methods. The line profiles in each of these three CSPN were fit by a process analogous to that described in §**IV.C** above for the particular case of NGC 1360, and the best fit model parameters obtained as a result

are listed in Table 4-2 along with the results of Mendez, et al. (1988). The two sets of results agree remarkably well (that is, much better than the $\pm 1\sigma$ errors derived in §**IV.C**), even though the two instruments and data reduction schemes employed to produce the observational line profiles were very different. Note, however, that because the same model atmosphere and line formation codes were used to fit both data sets, the comparison which follows is insensitive to systematic errors that may exist in the calculation of the theoretical line profiles.

For NGC 1360 Mendez, et al. (1988), found a best fit temperature and log gravity of 72,000 K and 5.3, respectively, from their CASPEC spectra. The fit process to the P60 echelle data described above placed the CSPN on a best fit Hγ locus slightly lower than that used by Mendez, et al., by just over 0.1 in log(g), which was shown above to be only a 1σ uncertainty in the normalized line profile. This difference combined with a slightly deeper line profile observed for HeII 4686 Å (possibly less filled in by emission due to the slightly higher resolution of the P60 echelle) accounts for the small differences in both T_{eff} and log(g). The P60 echelle data offer the opportunity to confirm the fit parameters by comparing the Balmer lines Hϵ, Hδ, Hβ, and Hα, as well as HeII 5411 Å, to theoretical profiles also. No inconsistencies were encountered when these comparisons were performed (see Figure 4-5 for the complete set of observed versus predicted line profiles for the best fit NLTE model parameters).

In the case of NGC 4361, the P60 echelle results differ from those of CASPEC only in that the best fit Hγ fit locus was slightly lower, and so passes through log(g)=5.4 at a slightly lower temperature (75,000 K as opposed to 80,000 K). The Hβ fit is consistent with this lower Hγ fit curve, and HeII 5411 Å confirms the fit to the HeII Pickering series line 4542 Å. The final fit parameters for NGC 4361 are also compared in Table 4-2 to the CASPC results, while the complete set of profiles is presented in Figure 4-6.

The most noteworthy difference between the P60 echelle fit results and those obtained previously by Mendez, et al. (1988), using CASPEC was for the central star of NGC 2392. In the P60 echelle data, the Hγ best fit locus was again lower than that found by CASPEC, but by an amount larger than the previous differences. For this object, the T_{eff} value of 47,000 K was derived from limits imposed by the HeI lines, and is therefore the same for both sets of observations since these lines are identical. Therefore the lower Hγ fit locus results directly in a higher derived value for log(g): 3.8 as opposed to 3.6; the quoted $\pm$0.2 error bars overlap, yet this change has important implications as far as the mass of the CSPN is concerned (to be discussed in §**IV.F** below). Note that a direct comparison between the CASPEC and P60 echelle spectra is complicated by the fact that the stellar wind emission is likely to be intrinsically variable. An alternative but less plausible explanation of the difference in these two Hγ profiles is again the slightly higher resolution of the P60 echelle spectrograph, which would furnish a profile less filled in from the wings of the central emission feature. This is not thought to be a likely explanation because of the much better agreement between the two data sets in all other cases (see Table 4-2); the final NLTE line profiles for the best fit model are compared with the observed profiles in Figure 4-7.

E. New Results

The first new object to be fit with the Kudritzki model atmosphere line profiles was the central star of NGC 6210. The observed Hγ profile placed the object near the $FW(0.025)$ = 15 Ångstrom contour of Figure 4-1, since a match was made at the model grid point (T_{eff}=50,000 K, log(g)=4.0) and at high temperature the model grid point profiles for log(g)=5.0 were too broad by an estimated 0.2 in log(g). The next step in the fitting process was to compare the HeI and HeII lines in the spectrum to the model line profiles, and it was soon apparent that the effective

temperature T_{eff} must be less than 55,000 K since the HeII lines predicted by the models were too strong above this temperature. For values of T_{eff} lower than 50,000 K, the lack of observed HeI 5875 Å wings alongside the nebular emission would be inconsistent with the predicted strength of this line, and so T_{eff} and log(g) parameters of 50,000 K and 4.0 were adopted as a tentative working grid model at this stage.

However, comparison of the observed HeII 4686 Å profile to that predicted by this grid model demonstrated that, because the model profile was stronger than that observed, a slightly higher gravity and/or lower temperature would be required to bring these two into agreement. Because a lower temperature would be inconsistent with the lack of observed HeII 5875 Å, final values T_{eff}=50,000 K and log(g)=3.9 were adopted. This fit was found to be satisfactory without having to modify the helium abundance from its nominal y=0.09 value.

The second new object to be fit with model atmosphere line profiles was the central star of Abell 36. In this case, the Hγ profile was compared to theoretical profiles and found to exhibit little or no evidence of emission at the line center. It was therefore decided that the observed Hβ profile could be used without the risk of contamination by emission, and would offer the advantage of a much improved signal-to-noise ratio. The best fit locus for this Hβ profile compared to the models was found to lie between the model grid points with log(g)=5.0 and 5.5, and temperatures less than 50,000 K were ruled out by the absence of any HeI lines. At 70,000 K along this locus the model's predicted HeII lines were too weak, with HeII 4686 Å in greater disagreement than 4542 Å. This was an indication that a higher gravity (and a correspondingly higher temperature as a consequence of the Hβ fit line) was necessary to bring these two lines into relative agreement with the observations. By 100,000 K the situation had already started to reverse, with the model HeII Pickering series line at 4542 Å now too weak and too broad while HeII

4686 Å was a relatively better match. By comparing models at T_{eff}=90,000 K to those at 100,000 K (with surface gravities 5.0 and 5.5, respectively), a final set of parameters T_{eff}=95,000 K and log(g)=5.3 was adopted.

The final fit parameters for both Abell 36 and NGC 6210 are summarized in Table 4-3. A complete set of observed versus theoretical line profiles can be found in Figures 4-8 and 4-9 for Abell 36 and NGC 6210, respectively. It is interesting to note that NGC 6210 overlaps with the sample of CSPN studied by Preite-Martinez and Pottasch (1983), who derived Stoy temperatures for central stars by comparing the nebular Hβ flux to the total flux in collisionally excited metal lines. As pointed out in §**I.D**, they parametrized their observational constraint on the central star temperature in terms of the dimensionless ratio:

$$\begin{aligned} \rho(T_{eff}) &= \frac{L_{CE}}{L_{H\beta}} \\ &= 27.8 \quad \text{for NGC 6210,} \end{aligned} \tag{4.9}$$

where L_{CE} is the collisionally excited line luminosity and $L_{H\beta}$ is the Hβ luminosity of the nebula. Although Preite-Martinez and Pottasch assumed a blackbody energy distribution for the central stars and derived a value for T_{eff} = 75,000 K on the basis of the $\rho(T_{eff})$ above — a temperature estimate which differs substantially from the T_{eff} = 50,000 K result obtained in this work from the NLTE line profile analysis — it is possible to reconcile these two temperatures based on figure 3 of Preite-Martinez and Pottasch (1983; which is reproduced here as Figure 4-10). In this figure the solid lines represent ρ as a function of T_{eff} based on a blackbody energy distribution, while the points connected by dotted lines are for various NLTE model atmosphere energy distributions. Note that the observational constraint, ρ = 27.8, implies T_{eff} = 75,000 K from the solid blackbody curve while only T_{eff} = 52,000 K from the dashed curve corresponding to the Universität Sternwarte München model atmospheres, owing to the greater far UV flux from the models. This latter value

is entirely consistent with the line profile analysis presented above.

F. Comparison With Evolutionary Tracks

The log(g) and T_{eff} values derived above for the five CSPN allowed the objects to be placed in the log(g) – log(T_{eff}) plane and compared with evolutionary tracks. Figure 4-11 shows these results, along with the evolutionary tracks of Schönberner (1983) for models of mass 0.546, 0.565, 0.598, and 0.644 $M_{\odot}$, and the tracks of Wood and Faulkner (1986) for models of mass 0.70, 0.76 and 0.89 $M_{\odot}$. The tick marks on the evolutionary tracks are indications of each model's "post-AGB" age in units of 10^3 years; zero age corresponds to the model's reaching T_{eff}= 5,000 K, at which point the model begins to move rapidly away from the AGB and towards higher T_{eff}.

The Schönberner (1983) and Wood and Faulkner (1986) evolutionary models as published gave log($L/L_{\odot}$) as a function of log(T_{eff}); these data were converted to log(g) vs. log(T_{eff}) by first noting that:

$$L = 4\pi R^2 \sigma {T_{eff}}^4 \ , \tag{4.10}$$

which when solved for the radius yields:

$$R = \left(\frac{L}{4\pi\sigma {T_{eff}}^4} \right)^{1/2} . \tag{4.11}$$

This can then be substituted for R in the following expression for the surface gravity:

$$\begin{aligned} g &= \frac{GM}{R^2} \\ &= GM \left(\frac{4\pi\sigma {T_{eff}}^4}{L} \right) \end{aligned} \tag{4.12}$$

which when converted into solar units becomes:

$$g = 2.471 \times 10^{-11} \left(\frac{M}{M_{\odot}} \right) \left(\frac{L}{L_{\odot}} \right)^{-1} {T_{eff}}^4 \tag{4.13}$$

for g in cgs units of dyne/gm and T_{eff} in Kelvin.

Defining $K(M)$ as the mass-dependent terms above (which are constant along the evolutionary track of an object whose mass M is fixed), equation (4.13) can be rewritten:

$$\log(g) = \log(K) - \log\left(\frac{L}{L_\odot}\right) + 4\log(T_{eff}) \ , \tag{4.14}$$

where:

$$\log(K) = \log\left(\frac{M}{M_\odot}\right) - 10.234 \ .$$

For $M = 0.6\ M_\odot$, $\log(K) = -10.83$ and therefore a model with $\log(T_{eff}) = 4.5$ and $\log(L/L_\odot) = 4.5$ has a surface gravity $\log(g) = 3.4$ in cgs units.

The central star masses and post-AGB ages determined from the log(g) – log(T_{eff}) diagram derived in this way are summarized in Table 4-4, along with the corresponding results from Mendez, et al. (1988), where the two samples overlap. Note that the agreement overall is excellent, confirming the reliability of echelle data for this type of analysis. The asymmetric error bars in Table 4-4 were derived by considering the implications of ±10% uncertainty in T_{eff} and ±0.2 uncertainty in log(g) for the mass and post-AGB derived from Figure 4-11; the errors are not symmetric owing to the uneven spacing of the evolutionary tracks, and the rate of evolution along those tracks, as functions of the mass of the CSPN.

Because the evolutionary tracks are more closely spaced for higher CSPN masses, the difference in log(g) between the two NGC 2392 results translates into a larger mass difference than elsewhere in the log(g) – log(T_{eff}) plane. Whereas Mendez, et al. (1988), derive a mass of 0.9 $M_\odot$ for the central star of NGC 2392, the P60 echelle best fit results imply a mass of 0.77 $M_\odot$. The expected errors in each case are on the order of ±0.10 $M_\odot$.

Combining the masses determined in the present work with the larger sample of Mendez, et al. (1988), and setting aside the Mendez, et al., results for the objects

the two studies have in common, the distribution of CSPN masses shown in Figure 4-12 is derived for 22 central stars. Note the predominance of CSPN having masses greater than 0.65 $M_{\odot}$, which is in sharp contrast to the narrow distribution of low mass objects derived by Schönberner (1981). Note, however, that the preliminary distribution of Figure 4-12 may be biased towards high masses owing to selection effects in favor of CSPN with higher luminosities and consequently higher expected core masses (Paczyński, 1971), and includes only those CSPN with sdO and Of-type spectra suitable for NLTE model atmosphere analysis. As discussed in §**V.C** below, a larger and more complete sample will be required before further discussion of the mass distribution becomes warranted.

Kudritzki (1987) has compared the evolutionary post-AGB ages derived for the CASPEC southern hemisphere sample of CSPN to the helium abundance "y" derived for each object from the model atmosphere fits, and found an inverse correlation between the two. The present work supports this trend, although the number of objects is small; note that the two CSPN with greater than normal helium abundances (NGC 2392 and Abell 36) both have young post-AGB ages (~1000 years and ~5000 years, respectively). While absence of old, helium rich CSPN is exactly what one would expect as a consequence of the gravitational settling of He as the CSPN ages, the competing effects of gravitational settling and mass loss would seem to complicate the situation enormously compared to the white dwarf case outlined in §**I.C**, for example.

These post-AGB evolutionary ages will be compared in §**IV.H** below to dynamical ages derived from the nebular radii and expansion velocities. But first the central star radii and model atmosphere fluxes will be determined and used to derive the spectroscopic distance to each of the objects, as these are required to convert the nebular angular radii into linear dimensions.

G. Other Derived Parameters

The radius of each PN central star follows directly from the value derived for log(g) and the mass, since equation (4.11) for surface gravity can be solved for R yielding:

$$R = \sqrt{\frac{GM}{g}} \tag{4.15}$$

and so:

$$\left(\frac{R}{\mathrm{R}_\odot}\right) = 165.5 \sqrt{\frac{M/\mathrm{M}_\odot}{g}} \ . \tag{4.16}$$

The values for each CSPN radius in units of the solar radius are listed in column (2) of Table 4-5. Note the radii of NGC 2392 and NGC 6210 are considerably larger than the other three CSPN, as one expects from their separate location on the right portion of the evolutionary tracks in Figure 4-11. These leftward-moving evolutionary tracks have essentially constant luminosity (cf., equation (4.10) above), and therefore a lower temperature object would require a larger radius to maintain a constant luminosity. A fourfold difference in radius can be accounted for by an inverse 2x temperature difference.

The model atmosphere for the best fit values of log(g) and $\mathrm{T_{eff}}$ can be used to determine the total flux F_ν radiated by the star. When compared to the observed flux f_ν, this yields a spectroscopic distance estimate which, unlike a distance derived by the Shklovskiĭ method (see above, §**I.D**), is independent of assumed properties of the surrounding nebula. Since the observed flux f_ν is most commonly expressed in terms of a visual magnitude V, the emitted flux F_ν is required over the V bandpass also. Figure 4-13 shows the continuum flux of each of the five best fit model atmospheres along with the relative response of the V bandpass as a function of ν. Note that the model continua are shown as Eddington fluxes, H_ν, which are related to the emitted fluxes, F_ν, by the factor 4π, such that:

$$F_\nu = 4\pi H_\nu \tag{4.17}$$

and the units of both are erg/sec/cm^2/Hz.

A numerical integration of H_ν weighted by the relative response of the V bandpass (V_ν) was performed to define the V band weighted mean flux $\langle F_\nu \rangle_V$ where:

$$\begin{aligned} \langle F_\nu \rangle_V &= 4\pi \langle H_\nu \rangle_V \\ &= 4\pi \frac{\int H_\nu V_\nu \, d\nu}{\int V_\nu \, d\nu} \ . \end{aligned} \tag{4.18}$$

For smoothly varying H_ν, this simplifies to:

$$\langle F_\nu \rangle_V = 4\pi H_\nu(\lambda 5480) \ , \tag{4.19}$$

$\lambda = 5480$ Å being the weighted mean center of the V bandpass.

Similarly, at $\lambda = 5480$ Å the apparent visual magnitude V is identical to the magnitude $AB_\nu(\lambda 5480)$, where the AB magnitude scale is defined by Oke and Gunn (1983, and references therein) in terms of f_ν by the equation:

$$AB_\nu = -2.5 \log_{10}(f_\nu) - 48.6 \tag{4.20}$$

with f_ν expressed in units of erg/sec/cm^2/Hz. Substituting a V band weighted mean $\langle f_\nu \rangle_V$ for f_ν and the visual magnitude V for AB_ν above, equation (4.20) can be solved for the flux resulting in:

$$\langle f_\nu \rangle_V = 3.6308 \times 10^{-20} \, \mathrm{erg/sec/cm^2/Hz} \times 10^{-0.4V} \tag{4.21}$$

as an expression for the observed flux.

The spectroscopic distance can now be derived by equating the emitted and observed mean fluxes over the V bandpass:

$$4\pi \left(\frac{R}{\mathrm{R}_\odot} \right)^2 \mathrm{R}_\odot^2 \langle F_\nu \rangle_V = 4\pi \left(\frac{d}{\mathrm{kpc}} \right)^2 \mathrm{kpc}^2 \langle f_\nu \rangle_V \ , \tag{4.22}$$

which when solved for the distance d to the object in kpc with substitutions from equation (4.21) becomes:

$$\begin{aligned}\left(\frac{d}{\mathrm{kpc}}\right)^2 &= \left(3.6308\times10^{-20}\right)^{-1}\left(\frac{\mathrm{R}_\odot}{\mathrm{kpc}}\right)^2\langle F_\nu\rangle_V\left(\frac{R}{\mathrm{R}_\odot}\right)^2 10^{+0.4V_o} \\ &= 1.4012\times10^{-2}\langle F_\nu\rangle_V\left(\frac{R}{\mathrm{R}_\odot}\right)^2 10^{+0.4V_o}\end{aligned} \tag{4.23}$$

where V_o is the apparent magnitude V following correction for interstellar extinction. Upon substituting for $R/\mathrm{R}_\odot$ the surface gravity and mass from equation (4.16) and for $\langle F_\nu\rangle_V$ the Eddington flux from equation (4.19), the spectroscopic distance can be expressed finally as:

$$\left(\frac{d}{\mathrm{kpc}}\right)^2 = 3.838\times10^2\ 4\pi\langle H_\nu\rangle_V\left(\frac{M/\mathrm{M}_\odot}{g}\right)10^{+0.4V_o}\ . \tag{4.24}$$

The spectroscopic distances so determined are given in column (7) of Table 4-5 for each of the five objects in the initial sample, along with the magnitudes V, extinctions c, and Eddington fluxes $\langle H_\nu\rangle_V$ from which they were calculated using equation (4.24). The errors in the spectroscopic distance estimates are between 20 and 30 percent, and are dominated by the log(g) errors in the NLTE line profile fitting (owing to the strong dependence of the luminosity on CSPN mass, and hence log(g) value). Husfeld (1988) expects that the errors in $\langle H_\nu\rangle_V$ are likely dominated by the $\pm10\%$ uncertainty in $\mathrm{T_{eff}}$.

Shown in Table 4-6 are comparisons between the spectroscopic distances derived as above and other distance estimates derived on the basis of: the Shklovskiĭ method (Cahn and Kaler, 1971); radio continuum fluxes (Daub, 1982; see also §**I.F**); CSPN proper motions (Cudworth, 1974); and finally the synthetic statistical method of Acker (1978). The limited size of this initial sample prevents any firm conclusions from being drawn; note, however, the large scatter in distance estimates for any individual object which arises when one bases a distance scale on the "statistical" properties of planetary nebulae in general. From their larger sample of

spectroscopic distances, Mendez, et al. (1988), find better agreement with the Cudworth distance scale than they do with the Daub scale, and they disagree with the distance estimate of Gathier (1984; based on the interstellar extinction law along the line of sight to the PN) for the one object the two studies have in common.

On the basis of the spectroscopic distances, the angular radii of the planetary nebulae shells can be converted into linear radii, according to the relation:

$$\left(\frac{r}{\mathrm{pc}}\right) = (206.265)^{-1} \left(\frac{\theta_r}{\mathrm{arcsec}}\right)\left(\frac{d}{\mathrm{kpc}}\right) , \tag{4.25}$$

where θ_r is the angular radius and r is the linear radius of each of the nebular shells. Assuming spherical symmetry and a constant expansion velocity for the nebular shell over time, the dynamical age of the planetary nebula can be calculated from its linear radius r and its expansion velocity, v_{exp}, along the line of sight as follows:

$$\begin{aligned} t_{\mathrm{dyn}} &= r \times v_{\mathrm{exp}}^{-1} \\ &= 4740.6 \text{ years } \left(\frac{v_{\mathrm{exp}}}{\mathrm{km/s}}\right)^{-1}\left(\frac{\theta_r}{\mathrm{arcsec}}\right)\left(\frac{d}{\mathrm{kpc}}\right) . \end{aligned} \tag{4.26}$$

If the expansion velocity increases with time over the history of the nebula, then the above expression for t_{dyn} will be an underestimate of the true dynamical lifetime. Table 4-7 contains the values of θ_r and v_{exp}, along with the derived estimates for r in parsecs and t_{dyn} in years. For comparison purposes, the post-AGB age for the central star of each planetary nebula is also shown in Table 4-7, which was derived in §**IV.F** above by comparing the location of the CSPN in the log(g) – log(T_{eff}) diagram with evolutionary models (see Figure 4-11).

From a comparison between the evolutionary post-AGB ages and the nebular dynamical ages given in Table 4-7, it is clear that very little relationship exists between these two timescales. The disagreement between such ages has been pointed out already by Mendez, et al. (1988), for their sample of southern hemisphere

CSPN, who found that in almost all cases the dynamical ages were greater than or equal to the evolutionary ages (i.e., a predominance of "old" planetary nebulae around "young" central stars), with only NGC 7293 being a possible exception. Table 4-8 contains two more possible exceptions, NGC 1360 and NGC 4361, both of which this sample has in common with the Mendez, et al., sample, and so some explanation is in order.

It was noted above in §**IV.C** that the uncertainties of the NLTE line profile analysis were typically ±0.2 in log(g). This influenced most the mass determined for NGC 2392, since the evolutionary tracks in the log(g) – log(T_{eff}) plane for different mass objects are more closely spaced at higher masses (see the comparison made to CASPEC results in §**IV.D**). An analogous situation exists when deriving evolutionary ages at low masses; the same value of Δlog (g) translates into a greater age difference as the mass decreases, due to the ever decreasing rate at which CSPN evolve through the log(g) – log(T_{eff}) diagram. Recall from §**IV.D** that the P60 echelle best fit Hγ loci for NGC 1360 and NGC 4361 were each approximately 0.1 in log(g) lower than the corresponding CASPEC results; while this made little or no significant difference in the mass determination, its impact on the evolutionary ages of each object is much greater (cf., the error estimates derived in Tables 4-4 and 4-7). Thus while it is suggested that NGC 1360 and NGC 4361 are possible cases in which the evolutionary age of the CSPN could be several times greater than the expansion age of the surrounding nebula, the uncertainties in the former are large (for low mass objects with $M \leq 0.55M_{\odot}$). It has already been pointed out that the uncertainties in the spectroscopic distances are expected to be approximately ±25%, and this translates into an equal or greater uncertainty in the expansion ages derived according to equation (4.24); see Table 4-7. Lastly, it is noted that there is an unusually large discrepancy in the values of the expansion velocity adopted by various workers in the case of NGC 4361. Mendez, et al. (1988), find a value

of 21 km/s from the nebular emission linewidth in their CASPEC spectra, whereas Bohuski and Smith (1974) quote a lower limit of 23 km/s and Robinson, et al. (1982), quote 38 km/s, both on the basis of Fabry-Parot spectroscopy of the [OIII] nebular emission. Since a lower value of $v_{\rm exp}$ will result in a higher value of $t_{\rm dyn}$, the nebular lines in the P60 echelle spectra of NGC 4361 were examined in an attempt to settle this disagreement, and a mean value of 27.7 km/s was derived for the expansion velocity based on the separation between *resolved* redshifted and blueshifted nebular emission line components; see the nebular line profiles shown in Figure 4-14. This was the value adopted for use in Table 4-7. For his sample of CSPN which overall have lower masses than those of this work and that of Mendez, et al. (1988), Gathier (1984) also found a systematic disagreement with $t_{\rm evol} \geq t_{\rm dyn}$.

These uncertainties for the lowest mass objects aside, the poor agreement between the evolutionary and expansion ages demonstrated in Table 4-7 remains a strong argument *against* the use of $t_{\rm dyn}$ determined from the nebula as a measure of the evolutionary status of the central star, as pointed out again recently by Mendez, et al. (1988). Note that this equality is tacitly assumed when evolutionary tracks are plotted through $M_V - t_{\rm dyn}$ diagrams; see Schönberner (1981) and Heap and Augensen (1987) for two recent examples of this practice.

H. Evolutionary vs. Dynamical Timescales

Is it possible to account for the observed difference between the CSPN evolutionary ages and nebular expansion ages in the context of the post-AGB star evolution ? In order to investigate this question, Figure 4-15 was produced comparing $t_{\rm dyn}$ and $t_{\rm evol}$ for the CSPN in Table 4-7 of this work (those plotted with error bars in Figure 4-15) combined with the sample of Mendez, et al. (1988), which are plotted as points in the figure but are understood to have similar uncertainties. The straight line in Figure 4-15 represents $t_{\rm dyn} = t_{\rm evol}$; from this figure it is clear that

a trend exists towards "old" nebulae surrounding "young" central stars (i.e., those CSPN with $t_{\rm evol} \leq 5000$ years). Based on his observations of planetary nebular shells at radio frequencies as well as on three-dimensional models of their present expansion, Masson (1988a,b) concludes that estimates of $t_{\rm dyn}$ such as those in Table 4-7 are uncertain by much less than a factor of two due to geometrical projection effects, and perhaps by up to a factor of two when uncertainties in the distances are taken into account as well. This would not remove the disagreement from Figure 4-15, nor would replacing θ_r with the inner radius of the nebular shell settle the disagreement, although this would be a much more appropriate characterization of the expansion of the nebular material outward from the central star.

There are in general three ways in which the disagreement between dynamical ages and evolutionary ages for the young CSPN shown in Figure 4-15 can be reconciled: (1) the ionized nebulae could have reached their present sizes in much shorter times than those derived on the basis of the present radii of the ionized nebulae and their respective expansion velocities along the line of sight; (2) the actual evolutionary ages could be much longer than those calculated on the basis of evolutionary models for CSPN evolution; or (3) the two timescales may not share the same zero point. These three possibilities will be discussed in order below, beginning with the rate of expansion of the ionized nebulae.

Given that "young" CSPN are thought to be surrounded by the neutral material ejected during the prior OH/IR star phase of evolution — which ought to extend out to large distances from the central star — one is led to ask the question whether the expansion of the ionized nebulae must be restricted to only the $v_{\rm exp}$ measured radially along the line of sight (i.e., the bulk motion of the ionized gas) ? Note that the size of the visible nebula is determined by the radius of an *ionization front*, and it is conceivable that during the early evolution of the nebula, this ionization front could have expanded into the surrounding neutral material at a much more rapid

pace than the material itself was expanding. A numerical experiment conducted to answer this question is the subject of §**IV.I** below.

Regarding the alternate possibility (2) that the predicted evolutionary times are in error, Iben and Renzini (1983) compare the evolutionary timescales for a variety of 0.6 $M_\odot$ models and conclude that the differences which do exist — differences of less than a factor of two in the times required by the models to fade by a factor of 10 in luminosity from T_{eff} = 30,000 K — can be accounted for in light of the different assumptions made regarding chemical composition, whether the CSPN burns hydrogen, helium, or both, and lastly the phase in the helium shell flash cycle at which the model leaves the AGB (see also Wood and Faulkner, 1986). While such uncertainties are far from sufficient to explain the large differences between the evolutionary and dynamcial ages for the CSPN in Figure 4-15, Iben, et al. (1983), and Iben (1984) have suggested that, as a result of a late helium shell flash experienced during the planetary nebula phase, it is possible for CSPN to evolve back towards the AGB.

Since the time span between helium shell flashes is known to be a strongly decreasing function of core mass, roughly proportional to M_c^{-4} (see for example, Paczyński, 1975; Schönberner, 1979), one test of Iben's hypothesis would be to compute the difference $t_{dyn} - t_{evol}$ as a function of core mass and look for an increased frequency of "born-again" CSPN towards higher M_c. Opposing such a trend is the decrease in the fading time towards higher masses, which according to Iben and Renzini (1983) is an even stronger function of core mass, estimated as proportional to $M_c^{-9.6}$. If this is indeed the case, the situation regarding the "born-again" phenomenon is actually reversed, and one should expect a greater likelihood of a late helium shell flash towards smaller core masses. However, selection effects would work against this latter situation, since short-lived high mass objects would live longer if they were to experience a late helium shell flash and long-lived low mass

objects have finite lifetimes due to dissipation of the surrounding nebulae, which remove them from the sample regardless of any late helium shell flash. Therefore it is perhaps more correct to compare the interflash periods with the nebular dynamical times and not the CSPN fading times.

The results of plotting $(t_{\rm dyn} - t_{\rm evol})$ as a function of core mass are shown in the top panel of Figure 4-16; although it is hard to draw any conclusions from this distribution of points in light of the above caveats, the lower panel should help to clarify the situation somewhat. It presents the ratio of the interflash period to the dynamical age of the nebula as a function of core mass. The dashed horizontal line through the diagram corresponds to a dynamical age equal to half of the evolutionary time period between helium shell flashes. Since none of the CSPN in this sample lie above this line, there do not exist any obvious candidates for "born-again" evolution, especially in light of the suggestion by some theorists that PN ejection is more likely at the luminosity peak of the shell flash period (e.g., Schönberner, 1983); were this the case, the next such flash would occur at $t_{\rm dyn} = \Delta t_{\rm flash}$, and ratios near unity in the lower panel of Figure 4-16 would be expected. No such objects appear in the present sample, although it is perhaps too small and contains too few low mass CSPN to draw any definite conclusions. Future work (see §**V.C** below) should nevertheless investigate in greater detail the uppermost objects in this plot for additional evidence for or against the "born-again" hypothesis; such an investigation is outside the scope of the present discussion.

Note especially the large number of objects with very small values of the $t_{\rm dyn}/\Delta t_{\rm flash}$ ratio. Since these objects also have $t_{\rm dyn} > t_{\rm evol}$, the possible "born-again" experience is very unlikely for the majority of CSPN in this sample. Furthermore, Mendez, et al. (1988), point out that the predominance of "old" nebulae around "young" central stars is observed regardless of the temperature of the central star; according to the timescales calculated by Iben (1984) for such "born-again"

CSPN, they would tend to be observed predominantly at high T_{eff}. Hence while helium shell flashes may alter the evolution of a small fraction of CSPN — Iben (1984) estimates 25% — the majority of the "old" nebulae around "young" central stars in Figure 4-15 must have some other explanation.

Turning finally to the evolutionary timescale for $T_{eff} \leq 30{,}000$ K, as well as the remaining possibility (3) that the zero point of the evolutionary timescale might not correspond to $t_{dyn} = 0$, our understanding is limited by the difficulty of observing CSPN in this transition phase. Note that it will be assumed here that $t_{dyn} = 0$ corresponds to the end of the "superwind" mass loss phase thought to occur at the tip of the AGB and produce an expanding planetary nebula (see §**IV.I** below for an alternate view); the evolutionary timescale meanwhile is governed by the assumed behavior of this mass loss mechanism, which is only poorly understood. In particular, the transition time t_{tr} from the end of the PN ejection to the point at which $T_{eff} = 30{,}000$ K and the central star begins to ionize the nebula can be expressed as:

$$t_{tr} = (M_{eR} - M_{eN})/\dot{M} \tag{4.27}$$

(Schönberner, 1979; Iben and Renzini, 1983). Here M_{eR} is the envelope mass remaining after the ejection of the PN, M_{eN} is the envelope mass when $T_{eff} = 30{,}000$ K is reached and the nebula first appears, and $\dot{M}$ is the combined rate at which the CSPN envelope mass decreases from nuclear burning and/or continued mass loss. The suspected cause of a long transition time (Renzini, 1981; Iben and Renzini, 1983) is a high value of M_{eR} due to a premature end to the superwind PN ejection process, although Schönberner (1983) argues against treating M_{eR} as a completely free parameter, citing the hydrodymical pulsation studies of Härm and Schwarzchild (1975) and Tuchman, et al. (1979), which indicate that the pulsational instability thought to feed the mass loss process dies out when M_e falls below $\sim 10^{-3}\,M_\odot$. Note however, that Schönberner's own criteria for defining $t_{evol} = 0$ is based on a

specific T_{eff} and not on a critical M_{eR} as a function of core mass. In a later §**IV.J** below, the exact amount of residual mass M'_{eR} required to reconcile the evolutionary ages of the models of Schönberner (1983) and Wood and Faulkner (1986) with the observed dynamical ages will be derived for each CSPN, and the results compared with those assumed by these authors in the evolutionary model computations.

I. Photo-Ionization of an AGB Envelope

In order to investigate further the apparent contradiction between the evolutionary and dynamical ages presented in §**IV.H** above, a computer program was written to model the photo-ionization of material surrounding a hot star. Strömgren (1939) first calculated the radius of the HII region on the basis of the luminosity and effective temperature of the ionizing source; hence the photo-ionized region is referred to as a "Strömgren sphere." In the discussion that follows, the time rate of change of the radius of the Strömgren sphere (hereafter the Strömgren radius) will be of particular importance, since the central star of a planetary nebula evolves quickly to high T_{eff}, especially for $M_* \geq 0.6$ $M_\odot$. As outlined in §**I.B** above, the ancestors of CSPN are thought to be OH/IR stars, losing mass on the AGB at rates on the order of 10^{-5} $M_\odot$ per year with ejection velocities $V_{ej} \lesssim 20$ km/s. Therefore when the CSPN evolves to a temperture $T_{eff} \sim 30{,}000$ K, it is surrounded by neutral material out to very large distances, and were it able to quickly photo-ionize this material, a large planetary nebula would appear around a young central star. Note that in this case the *ionization front* is expanding rapidly, while the bulk v_{exp} of the ionized material itself remains the same order of magnitude as before ionization occurs ($v_{exp} \gtrsim V_{ej}$). The dynamical age derived by dividing the PN ionized radius by v_{exp} would therefore be expected to exceed the evolutionary age of the central star, as has been observed to be the case for the very young CSPN in this sample.

The AGB mass loss will be treated as a constant $\dot{M}$ over time, and the ejected

material constrained to obey the following velocity law with radius r away from the surface of the star with radius R_o:

$$V_{ej}(r) = V_o \left(\frac{r}{R_o}\right)^{\beta} . \tag{4.28}$$

Assuming conservation of mass, this leads to a density distribution with radius of:

$$\rho(r) = \rho_o \left(\frac{r}{R_o}\right)^{-(\beta+2)} , \tag{4.29}$$

where

$$\rho_o = \frac{\dot{M}}{4\pi R_o^2 V_o} . \tag{4.30}$$

Analogously one can define the number density distribution of hydrogen atoms as:

$$n(r) = n_o \left(\frac{r}{R_o}\right)^{-(\beta+2)} , \tag{4.31}$$

where

$$\begin{aligned} n_o &= \frac{\dot{M}}{4\pi R_o^2 m_H V_o} \\ &= 6.187 \times 10^{21}\,\mathrm{cm}^{-3} \left(\frac{\dot{M}}{\mathrm{M}_\odot/\mathrm{yr}}\right) \left(\frac{V_o}{\mathrm{km/s}}\right)^{-1} \left(\frac{R_o}{\mathrm{R}_\odot}\right)^{-2} \end{aligned} \tag{4.32}$$

in convenient units.

The time rate of change of the Strömgren radius, dr_s/dt, can be now derived by considering the fate of a number of Lyman continuum photons ($\lambda \leq 911$ Å), dN_L, emitted by an ionizing source. Ignoring any absorption of these photons by dust grains, some fraction of the photons will be absorbed in the surrounding HII material to compensate for recombinations that have occurred within the Strömgren sphere. The remainder of the ionizing photons will penetrate into neutral HI material and ionize it, increasing the Strömgren radius by an amount dr_s. Therefore per unit time dt the following equation must be satisfied:

$$\begin{array}{ccc} \#\text{ ionizing photons} \\ \text{emitted per unit time} \end{array} = \begin{array}{c} \#\text{ of new ionizations} \\ \text{into HI per unit time} \end{array} + \begin{array}{c} \#\text{ of recombinations} \\ \text{in HII per unit time} \end{array}$$

$$\frac{dN_L}{dt} = 4\pi r_s^2 n(r_s) \frac{dr_s}{dt} + \int_{R_i}^{r_s} 4\pi r^2 n_e n_i \alpha^{(2)}\, dr \tag{4.33}$$

where R_i is the inner radius of the ionized region, n_e and n_i are respectively the number density of electrons and ions as functions of r, and $\alpha^{(2)}$ is the recombination coefficient to all energy levels of hydrogen above the second (i.e., recombinations directly to the n=1 state will emit Lyman continuum photons which are capable of ionizing another hydrogen atom nearby in the nebula). Spitzer (1978) expresses $\alpha^{(2)}$ in the form:

$$\alpha^{(2)} = \frac{2.569 \times 10^{-11} Z^2}{T_{\rm HII}^{1/2}} \, {\rm cm}^3 {\rm s}^{-1} \tag{4.34}$$

where the atomic weight $Z = 1$ for hydrogen and typically the HII region has a temperature $T_{\rm HII} = 10,000\,{\rm K}$ nearly independent of location within the ionized sphere. Substituting into equation (4.33) with $n_e = n_i = n(r)$ from equation (4.31) one finds:

$$\begin{aligned}
\frac{dN_L}{dt} &= 4\pi r_s^2 n_\circ \left(\frac{r_s}{R_\circ}\right)^{-(\beta+2)} \frac{dr_s}{dt} + 4\pi n_\circ^2 \alpha^{(2)} \int_{R_i}^{r_s} r^2 \left(\frac{r}{R_\circ}\right)^{-2(\beta+2)} dr \\
&= 4\pi r_s^2 n_\circ \left(\frac{r_s}{R_\circ}\right)^{-(\beta+2)} \frac{dr_s}{dt} + 4\pi n_\circ^2 \alpha^{(2)} R_\circ^3 \int_{R_i/R_\circ}^{r_s/R_\circ} x^{-2\beta-2} \, dx \\
&= 4\pi r_s^2 n_\circ \left(\frac{r_s}{R_\circ}\right)^{-(\beta+2)} \frac{dr_s}{dt} \\
&\qquad + \frac{4\pi}{(2\beta+1)} n_\circ^2 \alpha^{(2)} R_\circ^3 \left[\left(\frac{R_i}{R_\circ}\right)^{-(2\beta+1)} - \left(\frac{r_s}{R_\circ}\right)^{-(2\beta+1)}\right],
\end{aligned} \tag{4.35}$$

for values of $\beta \neq -1/2$. This last can be solved for dr_s/dt, yielding finally:

$$\begin{aligned}
\frac{dr_s}{dt} = \frac{1}{4\pi r_s^2 n_\circ} \left(\frac{r_s}{R_\circ}\right)^{\beta+2} \Bigg\{ &\frac{dN_L}{dt} \\
&- \frac{4\pi}{(2\beta+1)} n_\circ^2 \alpha^{(2)} R_\circ^3 \left[\left(\frac{R_i}{R_\circ}\right)^{-(2\beta+1)} - \left(\frac{r_s}{R_\circ}\right)^{-(2\beta+1)}\right] \Bigg\},
\end{aligned} \tag{4.36}$$

where $n_\circ$ is given by equation (4.32), $\alpha^{(2)}$ is given by equation (4.34), and dN_L/dt has yet to be derived.

Assuming that the central ionizing source radiates like a blackbody, the number of ionizing photons it emits per unit time per unit area is just the Planck function divided by $h\nu$, the energy per photon, and integrated over all frequencies higher than ν_L, the frequency of the Lyman limit. The total number of such photons is then the surface area of the star, $4\pi R_*^2$, times this integral:

$$\frac{dN_L}{dt} = 4\pi R_*^2 \left(\frac{2\pi}{c^2} \int_{\nu_L}^{\infty} \frac{\nu^2}{e^{h\nu/kT_*} - 1} \, d\nu \right) , \tag{4.37}$$

which cannot be solved analytically. However, for temperatures such that $h\nu_L \gg kT_*$ (i.e., $T \ll 160,000$ K), the -1 term is small compared to $e^{h\nu/kT_*}$ and the integrand becomes $\nu^2 e^{-h\nu/kT_*}$, which can be solved analytically so that:

$$\begin{aligned} \frac{dN_L}{dt} &= 4\pi R_*^2 \left(\frac{2\pi}{c^2} \int_{\nu_L}^{\infty} \nu^2 e^{-h\nu/kT_*} \, d\nu \right) \\ &= 4\pi R_*^2 \left(\frac{2\pi}{c^2} \left(\frac{kT_*}{h} \right)^3 \int_{\frac{h\nu_L}{kT_*}}^{\infty} x^2 e^{-x} \, dx \right) \\ &= 4\pi R_*^2 \, \frac{2\pi}{c^2} \left(\frac{kT_*}{h} \right)^3 \left[-x^2 - 2x - 2 \right] e^{-x} \Big|_{x=h\nu_L/kT_*}^{x=\infty} \\ &= 4\pi R_*^2 \, \frac{2\pi kT_*}{hc^2} \, \nu_L^2 \, e^{-h\nu_L/kT_*} , \quad h\nu_L \gg kT_* , \end{aligned} \tag{4.38}$$

where the additional assumption has been made that $2x + 2$ is small compared to x^2 for $x \gg 1$. The number of photons predicted by equation (4.38) has been compared to that given by equation VII-9 and Table VII-4 of Pottasch (1984), which are based on a numerical integration of equation (4.37), and the results are nearly identical for $20,000\,\mathrm{K} \leq T_* \leq 50,000\,\mathrm{K}$. Upon substitution into equation (4.36), the velocity of the ionization front is then:

$$\begin{aligned} \frac{dr_s}{dt} = \frac{1}{4\pi r_s^2 n_\circ} \left(\frac{r_s}{R_\circ} \right)^{\beta+2} \Bigg\{ & 4\pi R_*^2 \, \frac{2\pi kT_*}{hc^2} \, \nu_L^2 \, e^{-h\nu_L/kT_*} \\ & - \frac{4\pi}{(2\beta+1)} n_\circ^2 \alpha^{(2)} R_\circ^3 \left[\left(\frac{R_i}{R_\circ} \right)^{-(2\beta+1)} - \left(\frac{r_s}{R_\circ} \right)^{-(2\beta+1)} \right] \Bigg\} . \end{aligned} \tag{4.39}$$

Note that in addition to r_s, the parameters R_i, R_*, and T_* in equation (4.39) are functions of time. The CSPN evolutionary models of Schönberner (1983) and Wood and Faulkner (1986) were used to determine R_* and T_* (=$T_{\rm eff}$) as functions of evolutionary time, the radius following from the model CSPN luminosity L_*:

$$R_* = R_\odot \times \left(\frac{L_*}{L_\odot}\right)^{0.5} \left(\frac{T_{\rm eff,*}}{T_{\rm eff,\odot}}\right)^{-2} . \qquad (4.40)$$

Given the input data $\dot{M}$, $V_\circ$, β, and $R_\circ$ regarding the properties of the AGB precursor mass loss, the input functions $T_*(t)$ and $L_*(t)$ for the evolution of the central star, and the temperature $T_{\rm HII}$ appropriate to the Strömgren sphere that will arise, it was possible to solve the differential equation (4.39) for the Strömgren radius as a function of time via the Runge-Kutta method.

The results for a 0.6 $M_\odot$ CSPN are shown in Figure 4-17, where $\dot{M} = 3 \times 10^{-5}\,M_\odot$/yr, $V_\circ = 15$ km/s, $\beta = 0$, and $R_\circ = 100\,R_\odot$ (the radius the 0.6 $M_\odot$ Schönberner CSPN model has at $t_{\rm evol} = 0$). Notice that the Strömgren radius, given in pc as a function of time by the solid line in Figure 4-17, increases linearly at first for $t_{\rm evol} \geq 0$. During this phase the ionized mass, given in $M_\odot$ by the dotted line in Figure 4-17, remains very small; the Strömgren radius is merely following the linear growth of R_i with time as the AGB envelope expands with $V_\circ = V_{\rm ej}$. But then when $T_{\rm eff}$ for the central star, given in units of 10^5 K by the dashed line in Figure 4-17, reaches roughly 30,000 K at $t_{\rm evol} \sim 3000$ years, it emits enough ionizing photons to increase $r_s > R_i$, causing the Strömgren radius to increase at a rate larger than $V_{\rm ej}$ and the ionized mass to increase as well. The very rapid rate at which the ionized radius expands (i.e., the large dr_s/dt) can be attributed to the $1/r^2$ density distribution surrounding the CSPN, since both constant mass loss and ejection velocity ($\beta = 0$) have been assumed. Figures 4-18, 4-19, and 4-20 show the results of increasing the mass loss rate to $\dot{M} = 5 \times 10^{-5}$, 1×10^{-4}, and $2 \times 10^{-4}\,M_\odot$/year, respectively; according to Knapp, et al. (1982), these values are

representative of the high density range of OH/IR star mass loss rates observed, whereas Figure 4-17 is useful as a low density range example. As expected the ionization of the AGB envelope is delayed as the density increases, but dr_s/dt still greatly surpasses V_{ej} for $t_{evol} \geq 3000$ years and $\dot{M} \leq 1 \times 10^{-4}\,M_\odot$/year. In the two highest density cases, the recombination rate is actually large enough that the decrease in the number of ionizing photons for $t_{evol} \geq 6000$ years causes the Strömgren radius (e.g., the solid line in Figure 4-19) and ionized mass (e.g., the dotted line in Figure 4-20) to decrease significantly as well.

Note, however, that the rapid increase of the Strömgren radius shown in these figures will continue only until reaching the outer radius of the material lost by the AGB star (not shown); for a main sequence progenitor mass of 1.2 $M_\odot$ and a CSPN core mass of 0.6 $M_\odot$, the ionized mass M_{is} obviously cannot exceed 0.6 $M_\odot$. The model Strömgren radius presented in Figure 4-17 has already surpassed 1 pc before this amount of AGB envelope material is ionized (recall that it was the lowest density example). For the model in Figure 4-19, however, the finite envelope mass will cause the Strömgren radius to stop increasing rapidly upon reaching a radius $r_s \sim 0.15$ pc (for $M_{is} = 0.6\,M_\odot$); for later t_{evol}, the Strömgren radius will continue to expand linearly with time at a rate $\sim V_{ej}$.

Analogous envelope ionization calculations were also performed for CSPN masses of 0.565, 0.70, 0.76, and 0.89 $M_\odot$ over similar ranges of $\dot{M}$ (see Figures 4-21 through 4-29 for complete details). The 0.565 and 0.70 $M_\odot$ cases were qualitatively similar to the 0.6 $M_\odot$ results discussed above; the less rapid increase in T_* as a function of time in the 0.565 $M_\odot$ case delayed somewhat the ionization of the surrounding envelope, especially at high values of $\dot{M}$, while the reverse is true in the 0.70 $M_\odot$ case. Note that each of the three more massive CSPN evolve to higher effective temperatures at higher luminosities — enabling them to ionize the surrounding envelope sooner than the 0.6 $M_\odot$ CSPN — but the decline in the

number of ionizing photons also occurs more rapidly. In the most extreme of the calculations performed (CSPN mass 0.89 $M_\odot$, $\dot{M} = 5 \times 10^{-5}\,M_\odot$/year; see Figure 4-29), the nebular ionization only lasts from $t_{\rm evol} = 500$ years to $t_{\rm evol} = 700$ years, although it was possible in this brief period to ionize over 0.7 $M_\odot$ of the envelope.

The possible absorption of Lyman continuum photons by dust was ignored in the above calculations; Spergel, et al. (1983), calculated the photo-ionization of AGB envelopes with and without dust using the CSPN models of Paczyński (1971; N.B., the questionable evolutionary timescales of these models owing to an early helium shell flash, as pointed out by Iben and Renzini, 1983). They found differences of at most a factor of 2 in the time required to completely ionize a surrounding envelope of a specific mass (selected based on the CO emission results of Knapp, et al., 1982) and hence also a specific outer radius. The results presented here based on equation (4.39) are in general agreement with their "no dust" results, apart from the CSPN evolutionary timescale issue noted above.

Although the derivation of equation (4.39) considered only photo-ionization and neglected compression of the AGB envelope into a shell by the expansion of the $T_e \sim 10^4$ K ionized volume and/or a fast wind from the CSPN, these simple numerical experiments do succeed in demonstrating how it is possible to produce large, low bulk $v_{\rm exp} \sim V_{\rm ej}$ ionized shells — for which one would calculate "old" $t_{\rm dyn} = r_s/v_{\rm exp}$ — around young planetary nebulae central stars. More detailed calculations will be required in order to determine if in fact these ionized AGB envelopes bear any relationship at all to real planetary nebulae. The conclusion to be drawn from the above discussion is that it is not necessary to immediately reject the derived evolutionary timescales on the basis of the disagreement with the nebular dynamical timescales. The latter measure the bulk expansion of the nebular material and not the expansion of the ionization front, and as demonstrated above it is possible for these to be vastly different during the early $T_{\rm eff} \sim 30{,}000$ K history of the central

star. In the next section, variations in the evolutionary transition time caused by slight changes to the residual envelope mass $M_{\rm eR}$ remaining at the end of the superwind mass loss phase will be quantitatively investigated as a possible alternate means of reconciling the evolutionary and dynamical timescales. This independent explanation will be examined working under the assumption that the PN dynamical ages $t_{\rm dyn} = r_s/v_{\rm exp}$ do approximately measure the time since the superwind mass loss phase ended, contrary to the results of the numerical experiments presented above.

J. Residual Envelope Masses and Transition Timescales

The conclusion reached in the discussion of §**IV.H** above was that two extreme possible explanations exist concerning the disagreement between evolutionary and dynamical timescales. The previous §**IV.I** presented the first of these, namely that model evolutionary times could be correct and the dynamical ages too large due to expansion of the nebular ionization front at a rate larger than the bulk motion of the nebular material itself. This section focusses on the opposite extreme, assuming that the dynamical ages are correct and the evolutionary timescales in error owing to our lack of knowledge of the AGB to CSPN transition times given by equation (4.27). Whereas the argument in the previous section was theoretical, the approach here is a strictly empirical one: given that the values adopted for the transition time for each mass are uncertain due to the unknown residual envelope mass, $M_{\rm eR}$, which remains following the superwind phase, does one derive reasonable *empirical* residual envelope masses (here denoted $M'_{\rm eR}$) by requiring that the transition times be such that the $t_{\rm evol}$ match the observed $t_{\rm dyn}$ of the surrounding nebulae ?

The empirical residual envelope mass estimates $M'_{\rm eR}$ necessary to answer this question are derived without repeating the model calculations themselves by adopting a series of simplifying assumptions. First, the envelope mass at $\log(T_{\rm eff}) =$

3.8 (here denoted $M_{\rm eR_o}$) as a function of core mass is determined by interpolating between data published along with the evolutionary models of Schönberner (1983) and Wood and Faulkner (1986). Although Schönberner defines $t_{\rm evol} = 0$ corresponding to $\log(T_{\rm eff}) = 3.7$, the slightly hotter $\log(T_{\rm eff}) = 3.8$ is the first temperature at which Wood and Faulkner publish model information, and it corresponds to the end of the superwind phase in their "Case A" models.† The timescale along each track can then be shifted by a constant to transform it to a new evolutionary timescale having $t'_{\rm evol} = 0$ at $\log(T_{\rm eff}) = 3.8$, and the time $t'_{\rm evol}$ elapsed since this zero point temperature determined for each CSPN. The empirical residual envelope mass estimate can then be calculated from the expression:

$$M'_{\rm eR} = M_{\rm eR_o} + \dot{M}_{\rm o}\,(t_{\rm dyn} - t'_{\rm evol}) \ , \tag{4.41}$$

where $\dot{M}_{\rm o}$ is the net rate at which the envelope mass is decreasing at $\log(T_{\rm eff}) = 3.8$ due to both nuclear burning and mass loss from the stellar surface, and is a function of core mass. Equation (4.41) assumes that $\dot{M}_{\rm o}$ is a constant for all $t'_{\rm evol} < 0$ while the empirically deduced "additional" residual envelope mass $(M'_{\rm eR} - M_{\rm eR_o})$ required to enforce $t'_{\rm evol} = t_{\rm dyn}$ is being consumed.

Following Schönberner (1983), values of $\dot{M}_{\rm o}$ were calculated assuming that the mass loss from the stellar surface *after* the superwind ceases is given by the Reimers' rate:

$$\dot{M}_w = 4 \times 10^{-13}\,{\rm M_\odot/yr}\;\eta \left(\frac{L_*}{gR_*}\right) \tag{4.42}$$

(Reimers, 1975), with the parameter $\eta \sim 1$ and the remaining parameters in solar units. Substituting for g from equation (4.12) and for R_* from equation (4.40),

† In the Wood and Faulkner "Case B" models, the superwind phase continues until all of the hydrogen envelope is removed; as a result, "Case B" models evolve very quickly and so are not applicable to the present attempts to delay CSPN evolution by increasing $M'_{\rm eR}$.

equation (4.42) can be rewritten:

$$\dot{M}_w = 4 \times 10^{-13}\,\mathrm{M}_\odot/\mathrm{yr}\;\eta\left(\frac{L_*^{3/2}}{M_*\mathrm{T}_{\mathrm{eff}}^2}\right) \quad . \tag{4.43}$$

Meanwhile, the rate $\dot{M}_n$ at which the envelope mass decreases due to nuclear burning follows from the value of L_* for each CSPN model and the conversion factor 6×10^{18} erg per gram of hydrogen consumed given by Iben and Renzini (1983). When converted into appropriate units this implies:

$$\dot{M}_n = 1 \times 10^{-11}\,\mathrm{M}_\odot/\mathrm{yr}\;X_e\left(\frac{L_*}{L_\odot}\right) \quad , \tag{4.44}$$

where X_e is the mass fraction of hydrogen in the CSPN envelope (here set equal to 0.72 based on the nominal value y = 0.09 found in §**IV.D** and §**IV.E** above). The net rate of envelope mass decline, $\dot{M}_\circ$, then follows from the sum of $\dot{M}_w$ and $\dot{M}_n$, both evaluated at $t'_{\mathrm{evol}} = 0$. Figure 4-30 plots this $\dot{M}_\circ$ sum as a thick line along each of the model tracks used here (cf., Figure 1 of Schönberner, 1983); the thin straight lines in Figure 4-30 show $\dot{M}_w$ for each of the CSPN models based on equation (4.43), in which L_* and M_* are essentially constant during the horizontal phase of evolution in the HR diagram, leaving $\dot{M}_w$ with only a $\mathrm{T}_{\mathrm{eff}}^{-2}$ dependence; lastly, the dashed lines represent $\dot{M}_n$ for each model based on equation (4.44), and hence these behave exactly as does L_* as a function of $\mathrm{T}_{\mathrm{eff}}$.

Some insights may be gained into the relative importance of the two mechanisms — nuclear burning and surface mass loss — which combine to determine $\dot{M}_\circ$ by examining Figure 4-30 in both the low and high temperature limits. Note that for young CSPN at low temperatures, the rate at which mass is lost from the surface (i.e., the Reimers' rate) dominates the rate at which envelope mass is consumed by nuclear burning. This situation, which persists so long as $\mathrm{T}_{\mathrm{eff}} < 10^4$ K, is due to the low surface gravity of the still large extended atmosphere of the CSPN; for example,

it was pointed out in §**IV.I** above that the 0.6 $M_\odot$ Schönberner CSPN model has a radius of 100 $R_\odot$ at $\log(T_{eff}) = 3.7$, when the superwind mass loss rate is replaced by the Reimers' mass loss rate in Schönberner's models. It should therefore come as no surprise that the mass loss from the surface should initially continue to dominate the nuclear burning rate. Conversely, at high effective temperatures, the Reimers' mass loss rate is small owing to the high surface gravity, and so the rate at which the envelope mass decreases is governed by the nuclear burning rate. As the CSPN then cools and the luminosity falls, both the Reimers' rate and the nuclear burning rate will decrease in proportion to L_*, and the latter will continue to dominate as far as the envelope mass is concerned.

Returning now to the empirical residual envelope mass calculation of equation (4.41), note from Figure 4-30 that the $\dot{M}_w$ component of $\dot{M}_o$ increases with decreasing T_{eff} backwards in time along the model tracks. Were the simplifying assumption of constant $\dot{M}_o$ for $t'_{evol} \leq 0$ to be dropped in favor of a detailed evolutionary calculation progressing backwards in time from $t'_{evol} = 0$, the residual envelope mass required to account for $(t_{dyn} - t'_{evol})$ would therefore be greater than the simple empirical estimate M'_{eR} derived on the basis of equation (4.41), which assumes $\dot{M}_o$ is a constant.

Figure 4-31 shows the results of this residual envelope mass calculation for each CSPN in the combined samples of this work and Mendez, et al. (1988). The points in this figure — which are lower limits to M'_{eR} as pointed out above — fall below $10^{-2}\,M_\odot$ over the entire range of CSPN masses spanned by this sample and do not differ from the M_{eR} values assumed by Schönberner (1983) and Wood and Faulkner (1986), which together constitute the solid line in Figure 4-31, by a significant amount. Therefore it would seem entirely plausible that the poorly understood superwind mass loss phase ends with a residual envelope mass M'_{eR} *instead of* M_{eR} as adopted by the evolutionary theorists on the basis of their $t_{evol} = 0$ at $\log(T_{eff})$

= 3.8 (or 3.7) constraint on this transition phase.

The implications of Figure 4-31 for the timescale discussion which began in §**IV.H** is the following: the slight additional residual envelope mass inferred for most CSPN from the difference $(M'_{\rm eR} - M_{\rm eR})$ is all that is required to reconcile the evolutionary and dynamical timescales, assuming for the moment that $t_{\rm dyn}$ is correct. By this view, the "old" planetary nebulae are indeed old, and the "young" central stars are older than the Schönberner (1983) and Wood and Faulkner (1986) evolutionary ages suggest, owing to the extra transition time required to consume the additional residual envelope mass $(M'_{\rm eR} - M_{\rm eR})$ shown in Figure 4-31. Note that for the few low mass central stars for which originally $t_{\rm evol} > t_{\rm dyn}$, equation (4.41) and Figure 4-31 suggest that the residual envelope mass at the end of the super-wind mass loss phase is actually less than the value of $M_{\rm eR}$ assumed in the model calculations, and these low mass central stars evolve more rapidly than previously believed towards higher temperatures.

In conclusion, both possibilities (i.e., the rapid photo-ionization of the AGB envelope demonstrated in §**IV.I** above *and* the effect on the transition time of the empirical residual envelope mass investigated in this section) are at present thought to be viable alternatives, either of which is independently able to account for the observed differences between $t_{\rm evol}$ and $t_{\rm dyn}$; it is also possible that a combination of the two effects is responsible for the predominance of "old" nebulae around "young" central stars seen in Figure 4-15 above. Clearly these possibilities are very important for an adequate understanding of the *simultaneous* evolution of planetary nebulae and their central stars, deserving of much in the way of future study. Some thoughts on the course of such future work will be discussed in §**V.C** below.

TABLE 4-1

Central Stars of Planetary Nebulae (Acker, et al., 1982) Observed '87
Distances by Daub (1982) less than 1.3 kpc

Number (1)	Name (2)	l(II) (3)	b(II) (4)	R.A. 1985.0 (5)	Decl. (6)	P.N. Dia. (7)	U (8)	B (9)	V (10)	R (11)	Spectrum (12)	Dist(kpc) (13)
2	NGC 40	120 + 9 1		0 12 11.3	72 26 20	> 37 "	11.1	11.8	11.8	0.0	WC8	1.070
8	NGC 246	118 - 74 1		0 46 20.9	-11 57 35	250 "	10.4	11.6	12.0	11.9	OIV+K	0.460
21	NGC 1360	220 - 53 1		3 32 36.0	-25 55 10	390 "	9.7	11.0	11.3	11.8	sd O	0.257
28	NGC 1514	165 - 15 1		4 8 20.3	30 44 14	>114 "	9.9	10.0	9.4	0.0	AIII+sdO	0.671
43	IC 418	215 - 24 1		5 26 46.6	-12 42 31	12 "	7.9	9.2	9.4	0.0	O7f,WC7	0.412
51	IC 2149	166 + 10 1		5 55 17.1	46 6 11	> 8 "	10.0	11.0	11.0	0.0	O7 fp	1.120
74	NGC 2346	215 + 3 1		7 8 36.7	0 46 54	> 54 "	11.3	11.1	11.3	0.0	A5 V	1.300
81	NGC 2392	197 + 17 1		7 28 17.5	20 56 36	> 13 "	9.1	10.2	10.5	0.0	O7 f	1.220
86	VV 1-7	235 + 1 1		7 40 34.0	-18 57 30	250 "	9.8	8.2	8.4	8.2	A-0 IV	0.575
127	NGC 3242	261 + 32 1		10 24 2.7	-18 34 4	> 15 "	10.5	11.8	12.0	0.0	Cont. ?	0.730
145	NGC 4361	294 + 43 1		12 23 44.1	-18 42 10	> 45 "	11.7	13.0	13.4	0.0	O6	0.908
148	A 35	303 + 40 1		12 52 44.9	-22 47 30	800 "	10.8	10.5	9.6	10.4	G8III+sd	0.207
156	A 36	318 + 41 1		13 39 52.4	-19 48 10	293 "	10.0	11.4	11.6	12.0	sd O7	0.312
216	NGC 6210	43 + 37 1		16 43 51.7	23 49 38	> 16 "	10.1	10.5	9.9	0.0	O7f,WC7	1.190
279	NGC 6543	96 + 29 1		17 58 33.6	66 38 1	> 18 "	10.1	11.3	11.1	0.0	O7f+WR	0.640
296	NGC 6572	34 + 11 1		18 11 22.5	6 50 58	8 "	10.3	10.2	9.1	0.0	Of+WR	0.474
330	Hu 2-1	51 + 9 1		18 49 9.4	20 49 39	3 "	11.3	12.6	12.6	0.0	Of+WN b	1.180
350	M 1-67	50 + 3 1		19 10 50.8	16 50 0	82 "	12.1	12.2	11.1	0.0	WR-N8	0.836
376	VV 503	64 + 5 1		19 34 9.9	30 28 59	8 "	9.1	10.1	9.9	0.0	WC 9	0.733
417	NGC 7008	93 + 5 2		21 0 6.4	54 28 56	83 "	12.9	13.7	13.6	0.0	O7	0.793
451	NGC 7662	106 - 17 1		23 25 10.4	42 27 9	> 20 "	11.7	12.7	11.7	0.0	Cont.	0.837

TABLE 4-2

Model Fit Parameters for CSPN in Common with CASPEC sample[a]

Object (1)	Teff, K (2)	log(g) (3)	y (4)	Instrument; ref.[b] (5)
NGC 1360	75,000	5.5	0.09	P60 echelle; this work
	72,000	5.3	0.07	CASPEC; Mendez, et al.
NGC 2392	47,000	3.8	0.35	P60 echelle; this work
	47,000	3.6	0.35	CASPEC; Mendez, et al.
NGC 4361	80,000	5.4	0.09	P60 echelle; this work
	75,000	5.4	0.05	CASPEC; Mendez, et al.

[a] Errors in the model fit parameters are: +/- 10% in Teff, +/- 0.2 in log(g), and +/- 20% in y.

[b] Mendez, et al., refers to Mendez, R.H., Kudritzki, R.P., Herrero, A., Husfeld, D., and Groth, H.G., 1988. Astron. Astrophys., v. 190, p. 113.

TABLE 4-3

Model Fit Parameters for New CSPN [a]

Object (1)	Teff, K (2)	log(g) (3)	y (4)
Abell 36	95,000	5.3	0.13
NGC 6210	50,000	3.9	0.09

[a] Errors in model fit parameters are: +/- 10% in Teff, +/- 0.2 in log(g), and +/- 20% in y.

TABLE 4-4

Masses and Post-AGB ages for CSPN

Object (1)	M / Mo (2)	$t(evol)/10^3$ y (3)	Instrument; ref.[a,b] (4)
Abell 36	0.613 + 0.042 - 0.029	5.0 + 1.7 - 0.4	P60 echelle; this work.
NGC 1360	0.547 + 0.002 - 0.001	140 + 120 - 80	P60 echelle; this work.
	0.55 + 0.01 - 0.01	. . . . .	CASPEC; Kudritzki 1987.
NGC 2392	0.767 + 0.104 - 0.033	0.79 + 0.90 - 0.38	P60 echelle; this work.
	0.90 + 0.13 - 0.13	. . . . .	CASPEC; Mendez, et al.
NGC 4361	0.553 + 0.010 - 0.004	38 + 51 - 23	P60 echelle; this work.
	0.55 + 0.01 - 0.01	. . . . .	CASPEC; Mendez, et al.
NGC 6210	0.768 + 0.100 - 0.036	0.79 + 0.90 - 0.36	P60 echelle, this work.

[a] Mendez, et al., refers to Mendez, R.H., Kudritzki, R.P., Herrero, A., Husfeld, D., and Groth, H.G., 1988. Astron. Astrophys., v. 190, p. 113.

[b] Kudritzki, R.P., 1987. in IAU Symp. No. 131, Planetary Nebulae, ed. S. Torres-Peimbert, in press.

TABLE 4-5

Radii, Model Fluxes, Adopted Magnitudes & Extinctions, and Spectroscopic Distances Derived for CSPN

Object (1)	R / Ro (2)	[a] <H > erg/sec/cm^2/Hz (3)	[b,c] V (4)	[d] c (5)	[e] Vo (6)	d/kpc (7)	[f] d/kpc [MK] (8)
Abell 36	0.29 + 0.08 - 0.06	1.393×10^{-3}	11.51 + 0.01 - 0.01	0.00	11.51 + 0.01 - 0.01	0.91 + 0.26 - 0.20	....
NGC 1360	0.22 + 0.06 - 0.04	1.019×10^{-3}	11.35 + 0.01 - 0.01	0.00	11.35 + 0.01 - 0.01	0.54 + 0.14 - 0.11	0.67
NGC 2392	1.8 + 0.6 - 0.4	6.060×10^{-4}	10.53 + 0.02 - 0.02	0.16	10.18 + 0.02 - 0.02	2.05 + 0.68 - 0.45	2.7
NGC 4361	0.25 + 0.07 - 0.05	1.128×10^{-3}	13.04 + 0.1 - 0.1	0.04	12.95 + 0.1 - 0.1	1.35 + 0.40 - 0.31	1.3
NGC 6210	1.6 + 0.5 - 0.4	6.439×10^{-4}	12.90 + 0.33 - 0.5	0.09	12.70 + 0.33 - 0.5	6.0 + 2.4 - 2.1	....

a
The model fluxes were kindly provided by D. Husfeld; their errors are dominated by the 10% error in Teff.

b
Shaw, R., and Kaler, J.B., 1985. Ap. J., v. 295, p. 537. The V=12.4 lower limit on the magnitude of NGC 6210 was derived from the count rate of the P60 echelle spectra, neglecting slit losses.

c
The spectrophotometry of Mendez, et al. [note 6 below] was adopted for NGC 4361.

d
Kaler, J.B., 1983. Ap. J., v. 264, p. 594.

e
Vo = V - 2.175 c.

f
Mendez, R.H., Kudritzki, R.P., Herrero, A., Husfeld, D., Groth, H., 1988. Astron. Astrophys., v 190, p 113.

TABLE 4-6

Comparison Between Spectroscopic Distances and Other Distance Determinations

Object (1)	Spectroscopic[a] (2)	Radio Fluxes[b] (3)	Statistical[c] (4)	Shklovskii[d] (5)	Proper Motion[e] (6)	Other[f,g] (7)
Abell 36	0.91 + 0.26 - 0.20	0.312 + 0.15 - 0.15	0.4 + 0.1 - 0.1	0.47 + 0.50 - 0.25	....	0.59 + 0.3 - 0.3
NGC 1360	0.54 + 0.14 - 0.11	0.257 + 0.13 - 0.13	0.26 + 0.05 - 0.05	0.34 + 0.35 - 0.17	....	0.55 + 0.3 - 0.3
NGC 2392	2.05 + 0.68 - 0.45	1.220 + 0.61 - 0.61	0.94 + 0.05 - 0.05	1.09 + 1.10 - 0.55	1.98 + 0.50 - 0.50	1.6 + 0.13 - 0.13
NGC 4361	1.35 + 0.40 - 0.31	0.908 + 0.45 - 0.45	0.78 + 0.05 - 0.05	0.98 + 1.00 - 0.50	1.46 + 0.37 - 0.37	1.4 + 0.7 - 0.7
NGC 6210	6.0 + 2.4 - 2.1	1.190 + 0.60 - 0.60	1.05 + 0.2 - 0.2	2.04 + 2.00 - 1.00	1.66 + 0.41 - 0.41	....

[a] This work (see Table 4-5).

[b] Daub, C.T., 1982. Ap. J., v. 260, p. 612.

[c] Acker, A., 1978. Astron. Astrophys. Suppl. Ser., v. 33, p. 367.

[d] Cahn, J.H., and Kaler, J.B., 1971. Ap. J. Suppl. Ser., v. 22, p. 319.

[e] Cudworth, K.M., 1974. A. J., v. 79, p. 1384.

[f] Sabbadin, F., 1986. Astron. Astrophys. Suppl. Ser., v. 64, p. 579.

[g] For NGC 2392: Liller, M.H., and Liller, W., 1967. IAU Symposium No. 34, (Dordrecht: Reidel), p. 38.

TABLE 4-7

Nebular Radii, Ionized Masses, Expansion Velocities, & Dynamical Timescales
Derived from Spectroscopic Distances and Compared to Stellar Evolutionary Timescales

Object (1)	Theta(R)/ " [a] (2)	r / pc [b] (3)	Mi / Mo [c,d] (4)	Vexp/(km/s) [e] (5)	t(dyn)/1000y (6)	t(evol)/1000y [f] (7)
Abell 36	190.	0.84 + 0.24 - 0.18		36.0	22.8 + 6.6 - 5.0	5.0 + 1.7 - 0.4
NGC 1360	195.	0.51 + 0.13 - 0.10	0.44 + 0.18 - 0.16	28.0	17.8 + 4.6 - 3.6	140 + 120 - 80
NGC 2392	6.5	0.065 + 0.021 - 0.014	0.20 + 0.15 - 0.08	54.0	1.2 + 0.4 - 0.3	0.79 + 0.90 - 0.38
NGC 4361	55.	0.36 + 0.09 - 0.07	0.35 + 0.25 - 0.12	27.7	12.7 + 3.4 - 2.7	38 + 51 - 23
NGC 6210	6.5	0.19 + 0.08 - 0.07	4.83 + 6.39 - 3.18	21.0	8.8 + 3.5 - 3.1	0.79 + 0.90 - 0.36

a
Wilson, O.C., 1950. Ap. J., v. 111, p. 279.
b
This is the outer radius of the brightest shell; cf. column (2).
c
Based on H-beta fluxes and Te given by Shaw, R., and Kaler, J.B., 1985. Ap. J., v. 295, p. 537.
d
Data for NGC 4361 from Perek, L., and Kouhoutek, L., 1967. Catalog of Galactic Planetary Nebulae (Prague).
e
Data from ref. [a] above along with Bohuski, T.J., & Smith, M.G., 1974. Ap. J., v. 193, p. 197. Expansion velocity of NGC 4361 was determined in this work from P60 echelle spectra of the CSPN (see Figure 4-14).
6
This work; see Table 4-2.

Bibliography

Acker, A., 1978. *Astron. Astrophys. Suppl. Ser.*, v. **33**, p. 367.

Auer, L.H., and Mihalas, D., 1972. *Ap. J. Suppl. Ser.*, v. **24**, p. 193.

Auer, L.H., and Heasly, J.H., 1976. *Ap. J.*, v. **205**, p. 165.

Baud, B., and Habing, H.J., 1983. *Astron. Astrophys.*, v. **127**, p. 73.

Bedijn, P.J., 1987. *Astron. Astrophys.*, v. **186**, p. 136.

Bohuski, T.J., and Smith, M.G., 1974. *Ap. J.*, v. **193**, p. 197.

Cahn, J.H., and Kaler, J.B., 1971. *Ap. J. Suppl. Ser.*, v. **22**, p. 319.

Cudworth, K.M., 1974. *A. J.*, v. **79**, p. 1384.

Daub, C.T., 1982. *Ap. J.*, v. **260**, p. 612.

Gathier, R., 1984. *Ph.D. Thesis*, University of Gronigen, Netherlands.

Gray, D. F., 1976. *The Observation and Analysis of Stellar Photospheres*, (New York: Wiley).

Groth, H.G., 1986. Unpublished work, reported in Kudritzki (1987).

Gruschinske, J., and Kudritzki, R.P., 1979. *Astron. Astrophys.*, v. **77**, p. 341.

Härm, R., and Schwarzchild, M., 1975. *Ap. J.*, v. **200**, p. 324.

Heap, S.R., and Augensen, H.J., 1987. *Ap. J.*, v. **313**, p. 268.

Herrero, A., 1987a. *Astron. Astrophys.*, v. **171**, p. 189.

Herrero, A., 1987b. *Astron. Astrophys.*, v. **186**, p. 231.

Husfeld, D., Kudritzki, R.P., Simon, K.P., and Clegg, R.E.S., 1984. *Astron. Astrophys.*, v. **134**, p. 139.

Husfeld, D., 1986. *Ph.D. Thesis*, Universität München, B.R.D.

Husfeld, D., 1988. Private communication.

Iben, I., Kaler, J.B., Truran, J.W., and Renzini, A., 1983. *Ap. J.*, v. **364**, p. 605.

Iben, I., and Renzini, A., 1983. *Ann. Rev. Astron. Astrophys.*, v. **21**, p. 271.

Iben, I., 1984. *Ap. J.*, v. **277**, p. 333.

Knapp, G.R., Phillips, T.G., Leighton, R.B., Lo, K.-Y., Wannier, P.G., Wootten, H.A., and Huggins, P.J., 1982. *Ap. J.*, v. **252**, p. 616.

Knapp, G.R., 1985. *Ap. J.*, v. **293**, p. 273.

Kudritzki, R.P., 1973. *Astron. Astrophys.*, v. **28**, p. 108.

Kudritzki, R.P., 1976. *Astron. Astrophys.*, v. **52**, p. 11.

Kudritzki, R.P., 1987. In *I.A.U. Symp. No. 131, Planetary Nebulae*, ed. S. Torres-Peimbert, in press.

Kwok, S., Purton, C.R., and FitzGerald, P.M., 1978. *Ap. J. (Letters)*, v. **219**, p. L125.

Kwok, S., 1983. *Ap. J.*, v. **258**, p. 280.

Masson, C.R., 1988a. Preprint.

————, 1988b. Private communication.

Mendez, R.H., Kudritzki, R.P., Herrero, A., Husfeld, D., and Groth, H.G., 1988. *Astron. Astrophys.*, v. **190**, p. 113.

Oke, J.B., and Gunn, J.E., 1984. *Ap. J.*, v. **266**, p. 713.

Paczyński, B.E., 1971. *Acta Astr.*, v. **21**, p. 47.

————, 1975. *Ap. J.*, v. **202**, p. 558.

Pearson, T.J., 1986. *The PGPLOT Graphics Subroutine Library*, unpublished.

Pottasch, S.R., 1984. *Planetary Nebulae*, (Dordrecht: Reidel).

Preite-Martinez, A., and Pottasch, S.R., 1983. *Astron. Astrophys.*, v. **126**, p. 31.

Reimers, D., 1975. *Mem. Soc. R. Sci. Liege*, 6^e *Ser.*, v. **8**, p. 369.

Renzini, A., 1981. In *Physical Processes in Red Giants*, eds. I. Iben and A. Renzini (Dordrecht: Reidel), p. 431.

Robinson, G.J., Reay, N.K., and Atherton, P.D., 1982. *MNRAS*, v. **199**, p. 649.

Schönberner, D., 1979. *Astron. Astrophys.*, v. **79**, p. 108.

————, 1981. *Astron. Astrophys.*, v. **103**, p. 119.

————, 1983. *Ap. J.*, v. **272**, p. 708.

Schöning, S., and Butler, K., 1988. *Astron. Astrophys.*, in preparation.

Spergel, D.N., Giuliani, J.L., and Knapp, G.R., 1983. *Ap. J.*, v. **275**, p. 330.

Strömgren, B., 1939. *Ap. J.*, v. **89**, p. 526.

Tuchman, Y., Sack, N., and Barkat, Z., 1979. *Ap. J.*, v. **234**, p. 217.

Van der Veen, W.E.C.J., Habing, H.J., and Geballe, T., 1987. In *Planetary and Proto Planetary Nebulae: From IRAS to ISO*, ed. A. Preite-Martinez (Dordrecht: Reidel), p. 69.

Werner, K., and Husfeld, D., 1985. *Astron. Astrophys.*, v. **148**, p. 417.

Werner, K., 1986. *Astron. Astrophys.*, v. **161**, p. 177.

Werner, K., 1987. *Ph.D. Thesis*, Universität München, B.R.D.

Wood, P.R., and Faulkner, D.J., 1986. *Ap. J.*, v. **307**, p. 659.

Figure Captions

Figure 4-1: A contour plot of the Hγ line profile width at the fractional continuum depth of 0.025 as a function of T_{eff} and log(g), based on the NLTE model atmosphere calculations (indicated by "+") of the Universität Sternwarte München group.

Figure 4-2: The equivalent width approximations from the same grid of models, calculated on the basis of FW(0.025), FW(0.100), and the depth at line center. Note that in practice nebular emission in the line cores prevents the equivalent width from being accurately determined and so the main purpose of this contour plot is illustrative.

Figure 4-3: The best-fit Hγ locus for the central star of NGC 1360. Steps 1-6 outline the model atmosphere fitting process.

Figure 4-4: The observed Hγ line profile (S/N = 80) for the central star of NGC 1360. The dashed line has been drawn at a depth of 0.025.

Figure 4-5: The complete set of theoretical line profile fits to the P60 echelle spectra of the central star of NGC 1360. The lines shown are Hϵ, Hδ, Hγ, HeII 4542 Å, HeII 4686 Å, Hβ, HeII 5411 Å, and Hα.

Figure 4-6: The complete set of theoretical line profile fits to the P60 echelle spectra of the central star of NGC 4361. The lines shown are Hγ, HeII 4542 Å, HeII 4686 Å, Hβ, HeII 5411 Å, and Hα.

Figure 4-7: The complete set of theoretical line profile fits to the P60 echelle spectra of the central star of NGC 2392. The lines shown are HeII 4200 Å, Hγ, HeI 4471 Å, HeII 4542 Å, HeII 4686 Å, Hβ, and HeII 5411 Å.

Figure 4-8: The complete set of theoretical line profile fits to the P60 echelle spectra of the central star of Abell 36. The lines shown are Hϵ, Hδ, Hγ, HeII 4542 Å, HeII 4686 Å, Hβ, HeII 5411 Å, and Hα.

Figure 4-9: The complete set of theoretical line profile fits to the P60 echelle spectra of the central star of NGC 6210. The lines shown are Hγ, HeII 4542 Å, HeII 4686 Å, Hβ, HeII 5411 Å, and HeI 5876 Å.

Figure 4-10: A reproduction of Figure 3 of Preite-Martinez and Pottasch (1985)

on which is illustrated the difference between the blackbody (solid lines) and model atmosphere (dashed lines) values of T_{eff} derived for NGC 6210 by the energy balance method. Note that the difference between the model atmosphere T_{eff} derived by the method of §**IV.B** and the higher T_{eff} derived by the Stoy method can be accounted for by the non-blackbody ultraviolet flux of the more realistic model atmospheres.

Figure 4-11: The location of the five CSPN studied as part of this work in the log(g) - log(T_{eff}) plane, compared with the theoretical evolutionary tracks of Schönberner (1979) for 0.546, 0.565, 0.598, and 0.644 $M_{\odot}$, and the tracks of Wood and Faulkner (1986) for 0.70, 0.76, and 0.89 $M_{\odot}$ CSPN.

Figure 4-12: The number distribution of CSPN as a function of mass for the combined samples of this work (shaded) and Mendez, et al. (1988). Objects the two samples have in common have been removed from the Mendez list.

Figure 4-13: The best-fit NLTE model fluxes for each of the five CSPN in the visible part of the spectrum. Overplotted on these data is the relative response of the V bandpass.

Figure 4-14: The resolved nebular emission lines from NGC 4361, which have been used to re-evaluate the expansion velocity of the nebula.

Figure 4-15: A comparison of evolutionary and dynamical timescales for the five objects studied in this work ("+" signs with error bars) along with the analogous data computed for the sample of Mendez, et al., 1988 (plotted as " • "). The straight line indicates $t_{\rm dyn} = t_{\rm evol}$; note that most of the objects lie above this line and so constitute "old" nebulae around "young" central stars.

Figure 4-16: *top):* The difference between the dynamical and evolutionary ages as a function of core mass. *bottom):* The ratio of the dynamical age to the helium interflash period as a function of core mass. The horizontal line indicates the 0.5 value of this ratio.

Figure 4-17: The predicted growth of a Strömgren sphere into the neutral AGB envelope surrounding a young 0.6 $M_{\odot}$ CSPN as the CSPN evolves towards higher T_{eff}. The parameters for this model calculation were $\dot{M} = 3 \times 10^{-5}$ $M_{\odot}$/year, $v_{\rm exp}$ = 15 km/s, and the CSPN evolution was taken from Schönberner (1983) for the 0.6 $M_{\odot}$ track. The solid line is the Strömgren radius in pc, the dotted line is the ionized mass of the nebula in solar masses, and the dashed line is the T_{eff} value of the CSPN in units of 10^5 K.

Figure 4-18: Same as Figure 4-17 above, except $\dot{M} = 5 \times 10^{-5}$ $M_\odot$/year.

Figure 4-19: Same as Figure 4-17 above, except $\dot{M} = 1 \times 10^{-4}$ $M_\odot$/year.

Figure 4-20: Same as Figure 4-17 above, except $\dot{M} = 2 \times 10^{-4}$ $M_\odot$/year.

Figure 4-21: Same as Figure 4-17 above, except $\dot{M} = 1 \times 10^{-5}$ $M_\odot$/year and $M_* = 0.565\,M_\odot$.

Figure 4-22: Same as Figure 4-17 above, except $\dot{M} = 3 \times 10^{-5}$ $M_\odot$/year and $M_* = 0.565\,M_\odot$.

Figure 4-23: Same as Figure 4-17 above, except $\dot{M} = 1 \times 10^{-4}$ $M_\odot$/year and $M_* = 0.565\,M_\odot$.

Figure 4-24: Same as Figure 4-17 above, except $\dot{M} = 5 \times 10^{-5}$ $M_\odot$/year and $M_* = 0.70\,M_\odot$.

Figure 4-25: Same as Figure 4-17 above, except $\dot{M} = 7.5 \times 10^{-5}$ $M_\odot$/year and $M_* = 0.70\,M_\odot$.

Figure 4-26: Same as Figure 4-17 above, except $\dot{M} = 1 \times 10^{-4}$ $M_\odot$/year and $M_* = 0.70\,M_\odot$.

Figure 4-27: Same as Figure 4-17 above, except $\dot{M} = 1 \times 10^{-5}$ $M_\odot$/year and $M_* = 0.89\,M_\odot$.

Figure 4-28: Same as Figure 4-17 above, except $\dot{M} = 3 \times 10^{-5}$ $M_\odot$/year and $M_* = 0.89\,M_\odot$.

Figure 4-29: Same as Figure 4-17 above, except $\dot{M} = 5 \times 10^{-5}$ $M_\odot$/year and $M_* = 0.89\,M_\odot$.

Figure 4-30: The rate at which envelope mass decreases (heavy lines) along each of the evolutionary tracks. This rate is the sum of two contributing rates: the rate at which mass is lost from the surface due to a Reimers wind (thin lines; Reimers, 1975, with $\eta = 1$), and the rate at which the envelope is consumed by nuclear burning (dashed lines). See text for details.

Figure 4-31: The empirical residual envelope masses, $M'_{\rm eR}$, required to reconcile the dynamical and evolutionary timescales as a function of core mass. The

solid line represents the envelope masses assumed by Schönberner (1983) and Wood and Faulkner (1986) when computing evolutionary models.

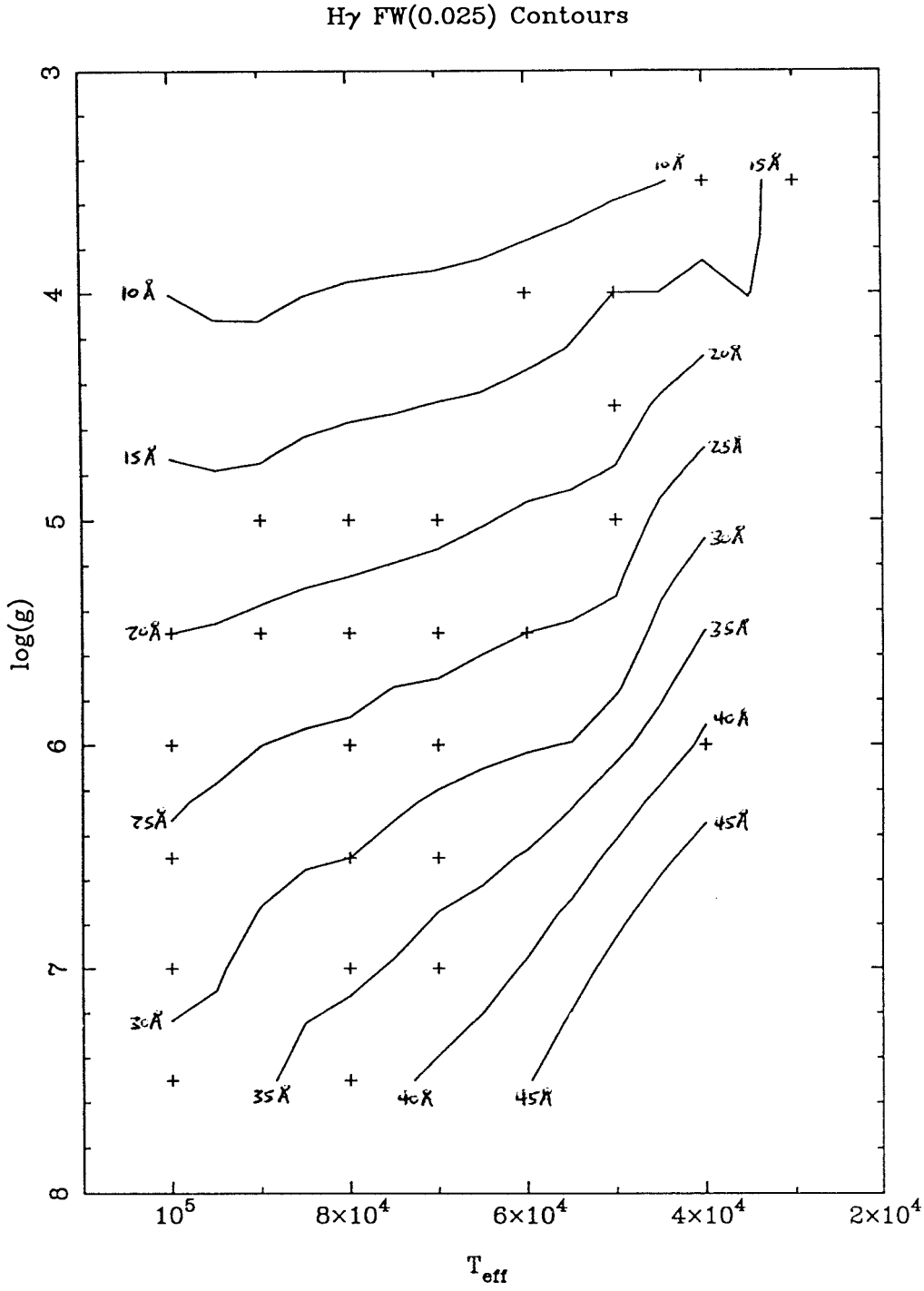
Hγ FW(0.025) Contours
log(g)
T_eff
3
4
5
6
7
8
10^5
8×10^4
6×10^4
4×10^4
2×10^4
10Å
15Å
20Å
25Å
30Å
35Å
40Å
45Å

Figure 4-1

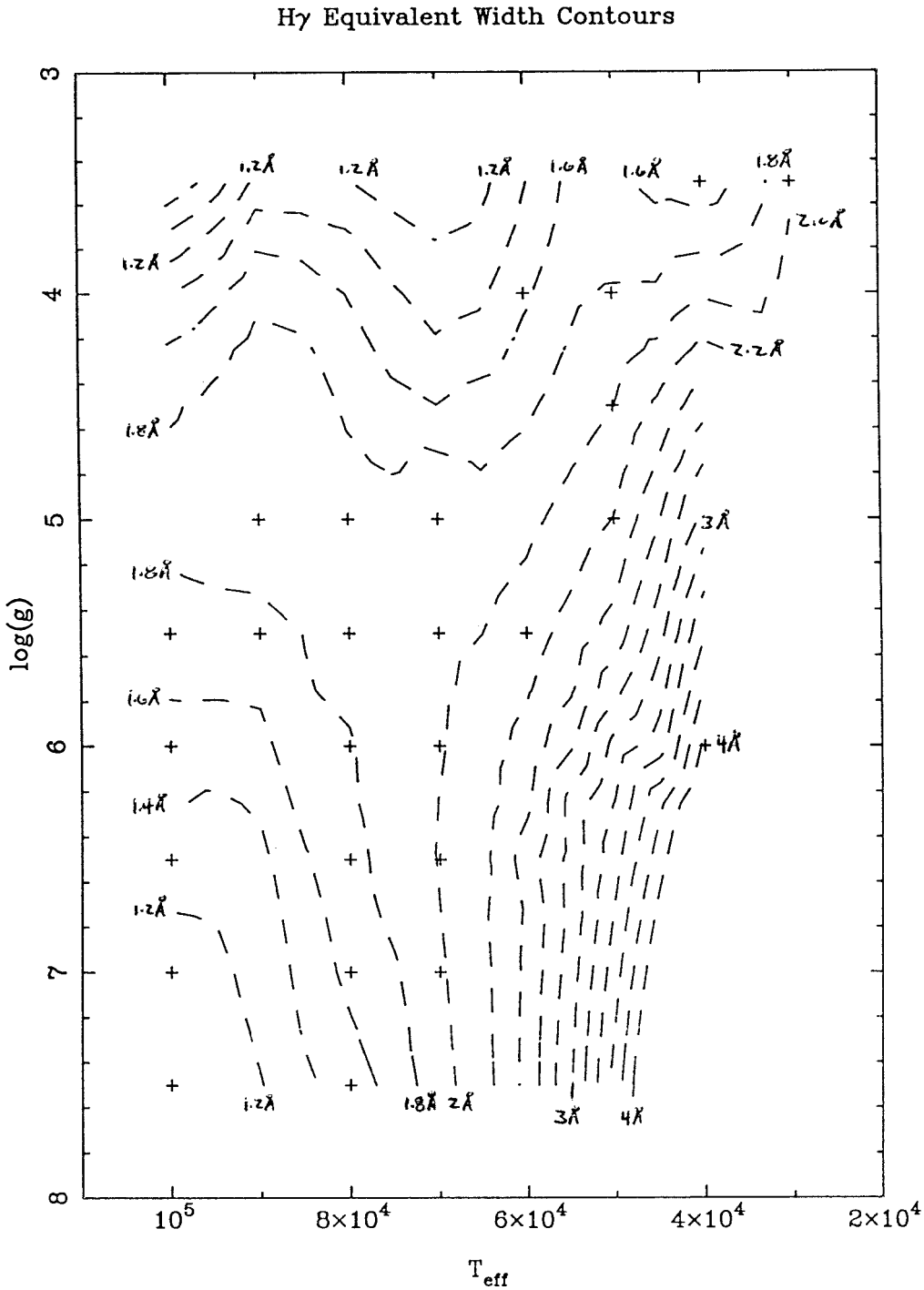
Hγ Equivalent Width Contours
log(g)
T_eff
10^5
8×10^4
6×10^4
4×10^4
2×10^4
3
4
5
6
7
8
1.2Å
1.4Å
1.6Å
1.8Å
2Å
2.2Å
3Å
4Å

Figure 4-2

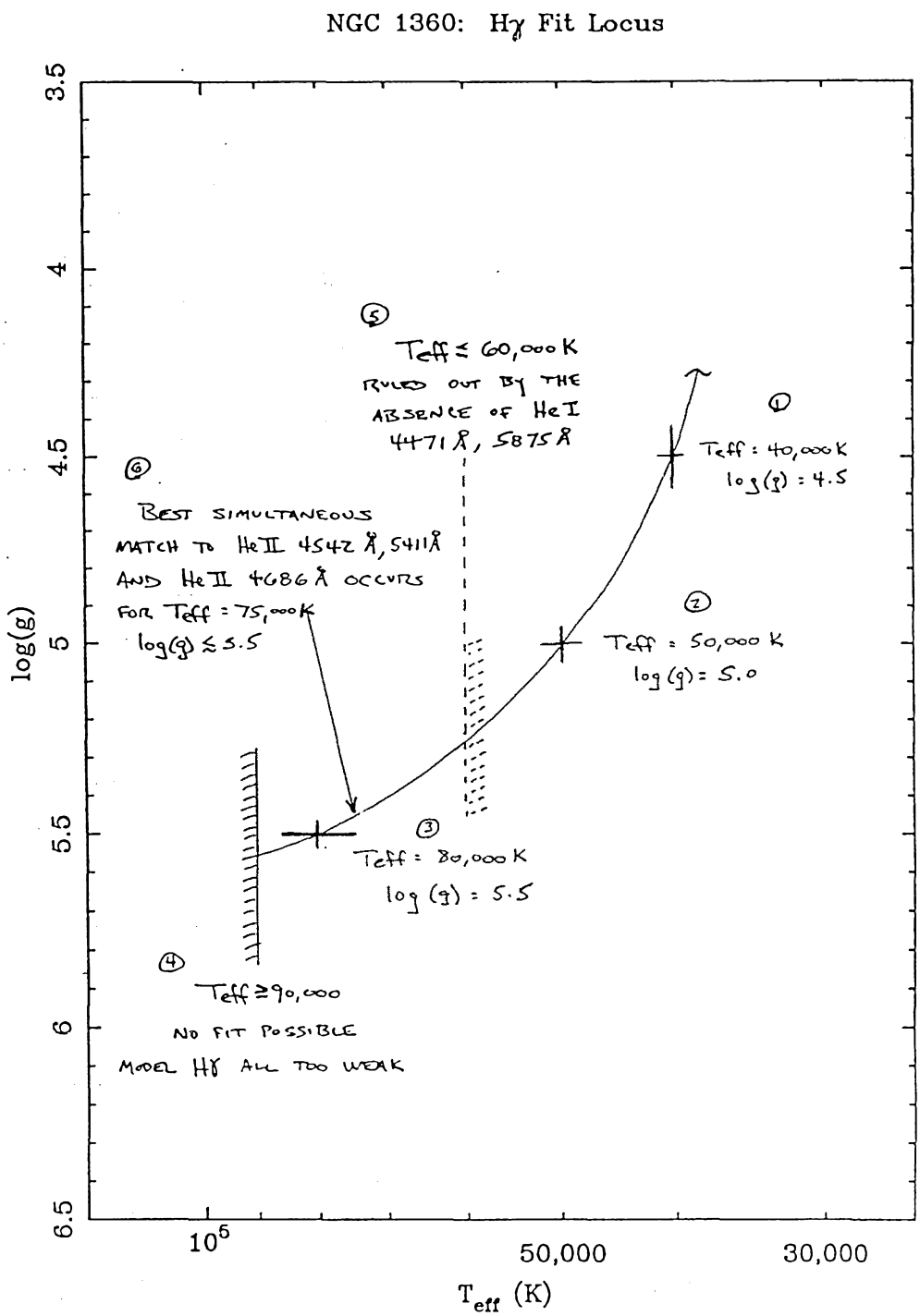
NGC 1360: Hγ Fit Locus
log(g)
3.5
4
4.5
5
5.5
6
6.5
10^5
50,000
30,000
T_{eff} (K)
⑤
Teff ≤ 60,000 K
RULED OUT BY THE
ABSENCE OF HeI
4471 Å, 5875 Å
⑥
BEST SIMULTANEOUS
MATCH TO HeII 4542 Å, 5411 Å
AND HeII 4686 Å OCCURS
FOR Teff = 75,000 K
log(g) ≲ 5.5
①
Teff = 40,000 K
log(g) = 4.5
②
Teff = 50,000 K
log(g) = 5.0
③
Teff = 80,000 K
log(g) = 5.5
④
Teff ≥ 90,000
NO FIT POSSIBLE
MODEL Hδ ALL TOO WEAK

Figure 4-3

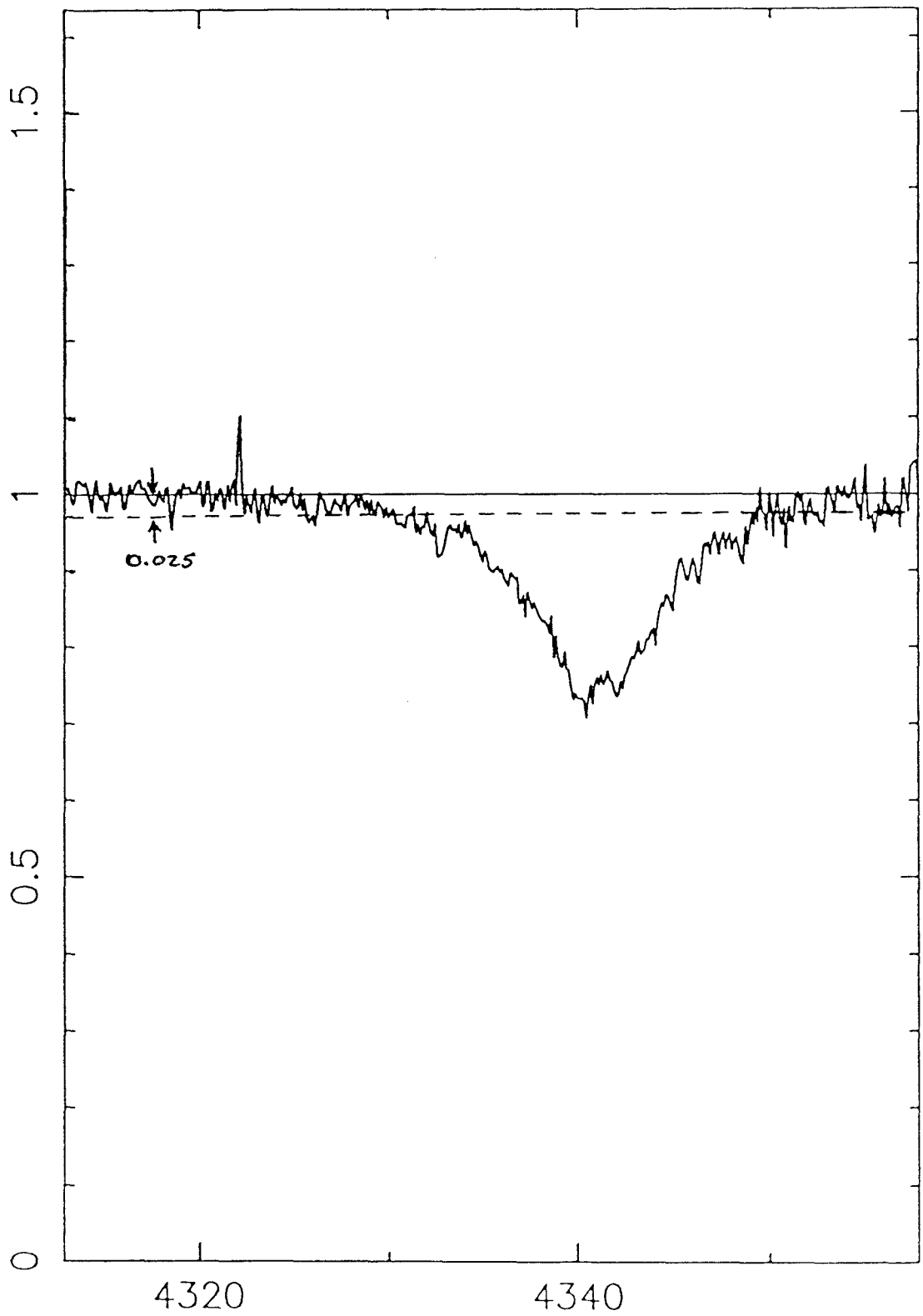

Figure 4-4

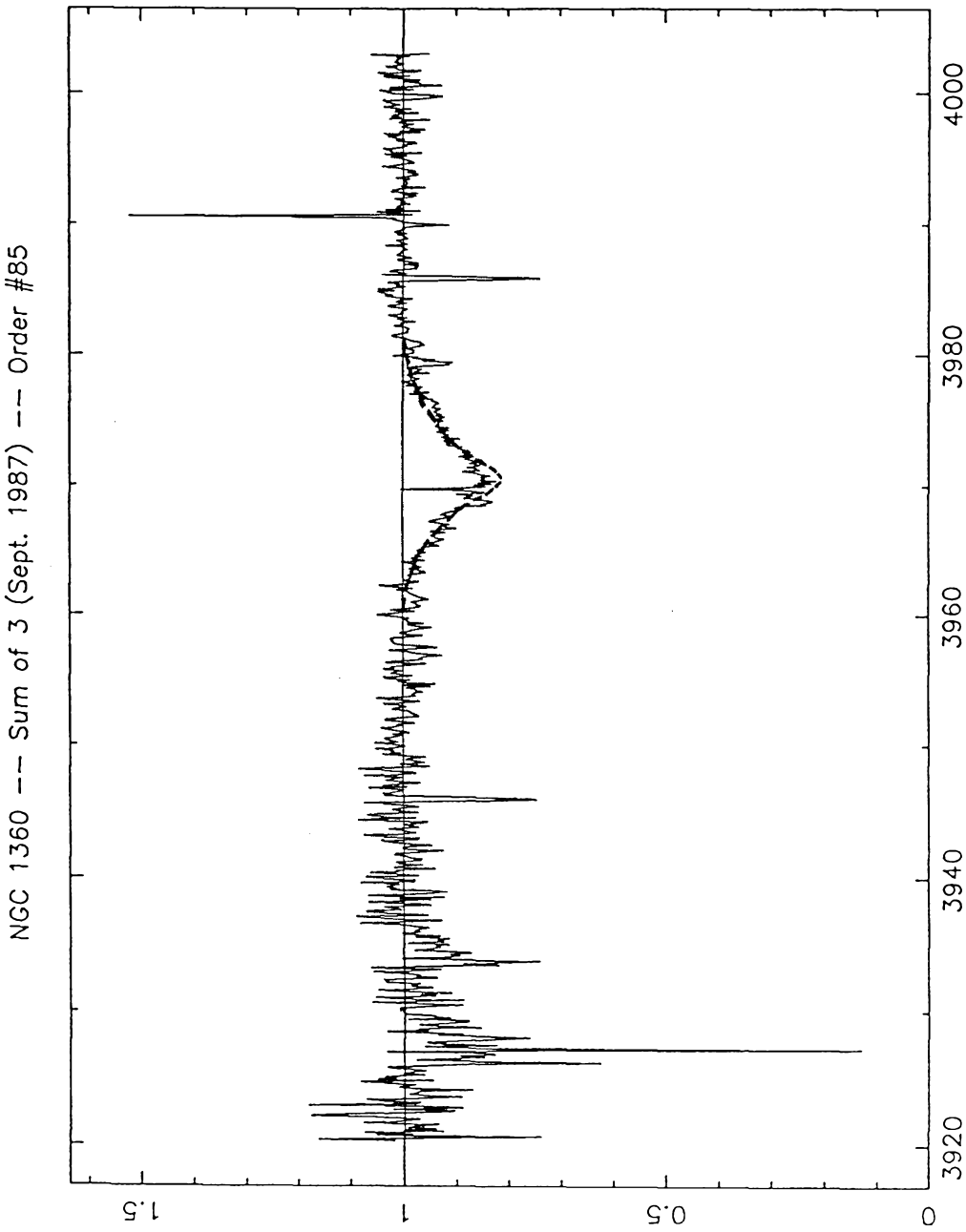
NGC 1360 -- Sum of 3 (Sept. 1987) -- Order #85
1.5
1
0.5
0
3920
3940
3960
3980
4000

Figure 4-5

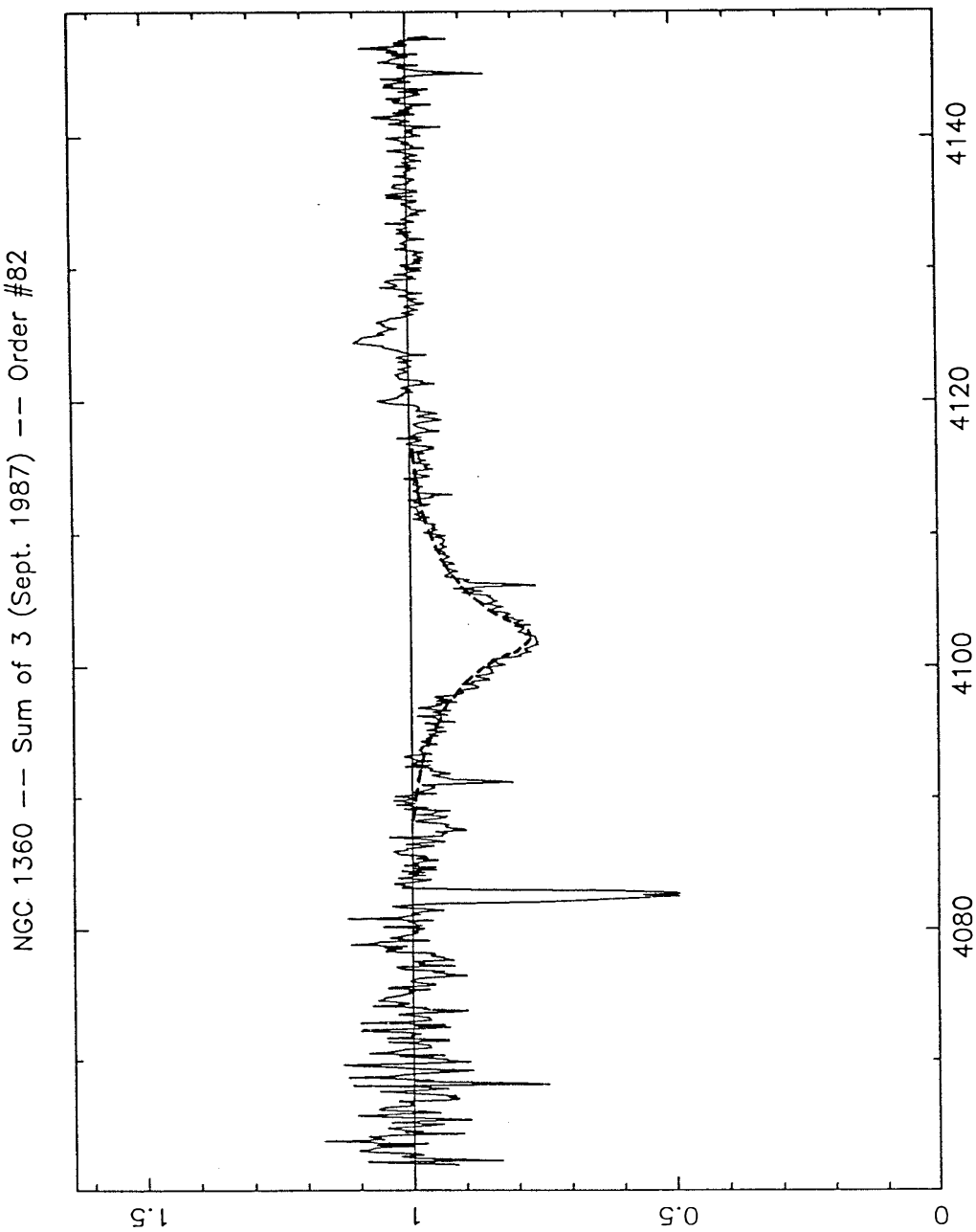

Figure 4-5
(continued)

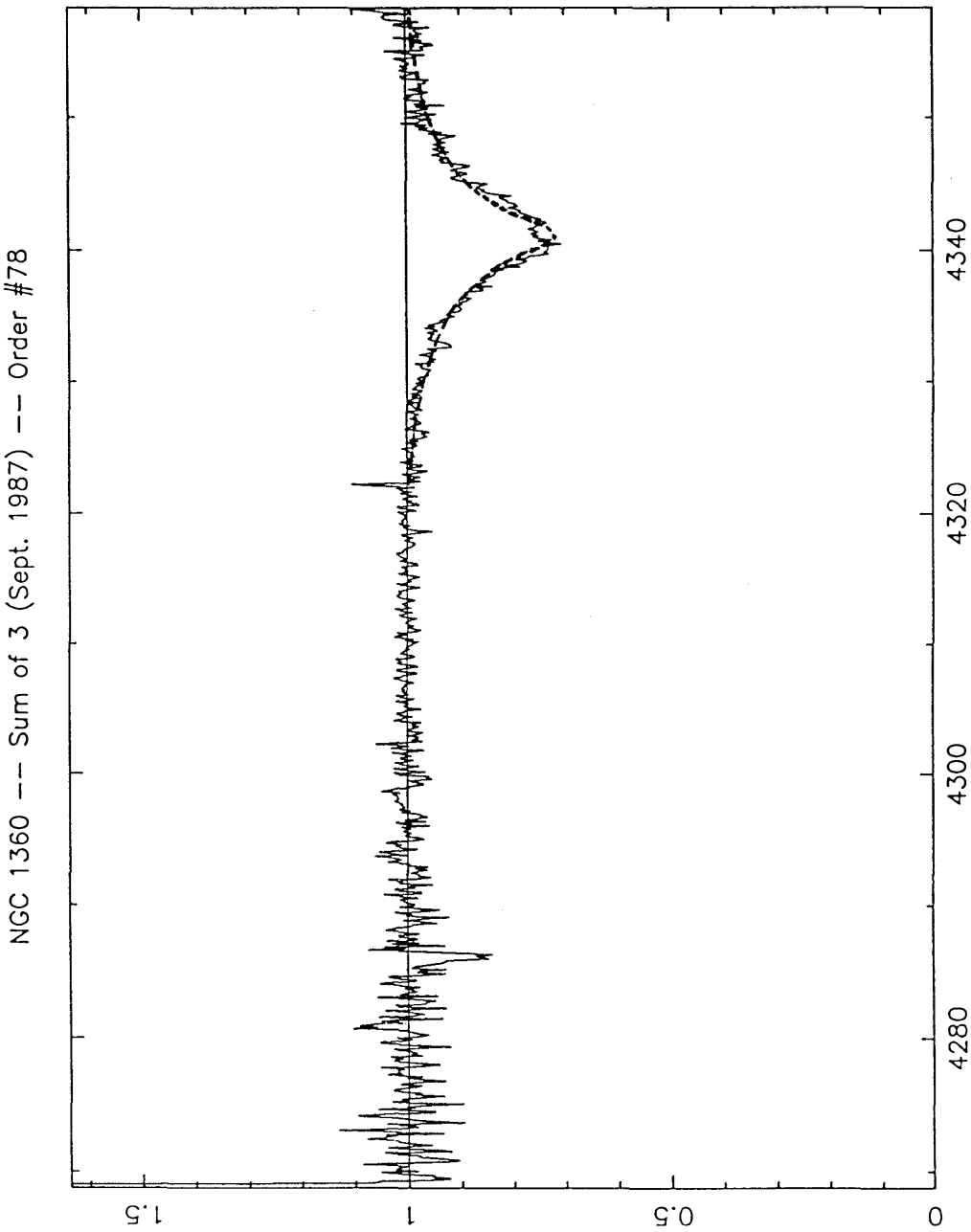

Figure 4-5
(continued)

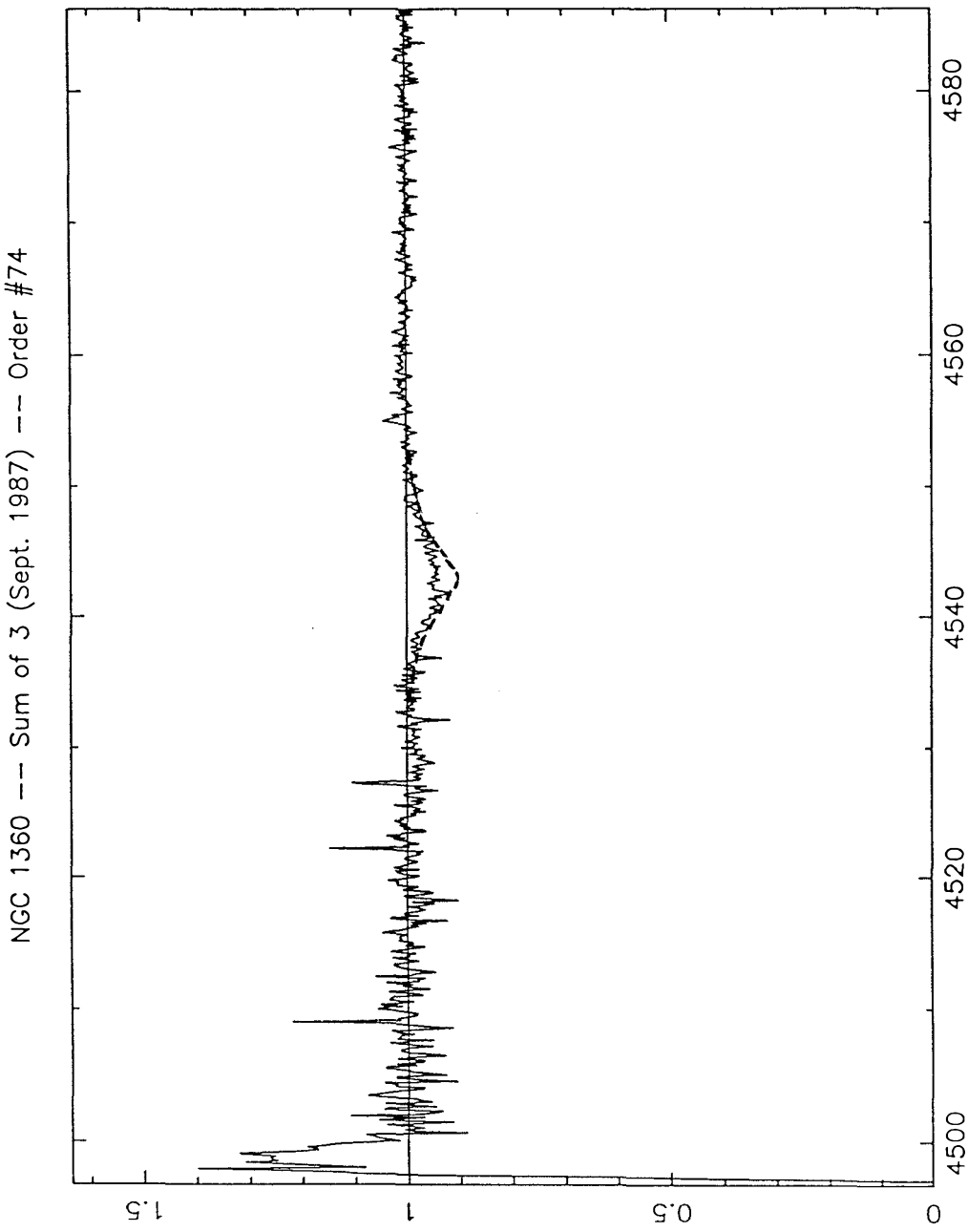

Figure 4-5
(continued)

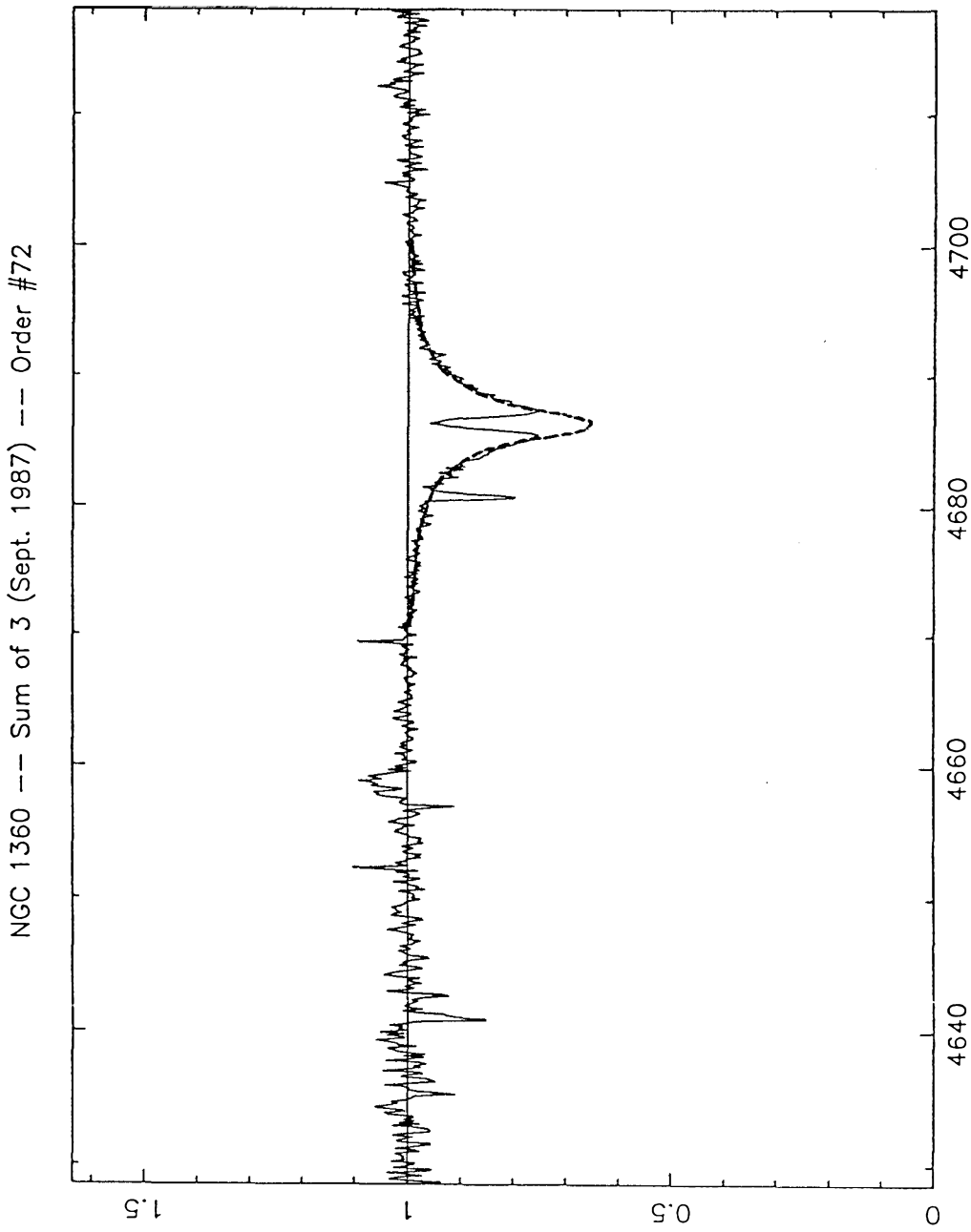

Figure 4-5
(continued)

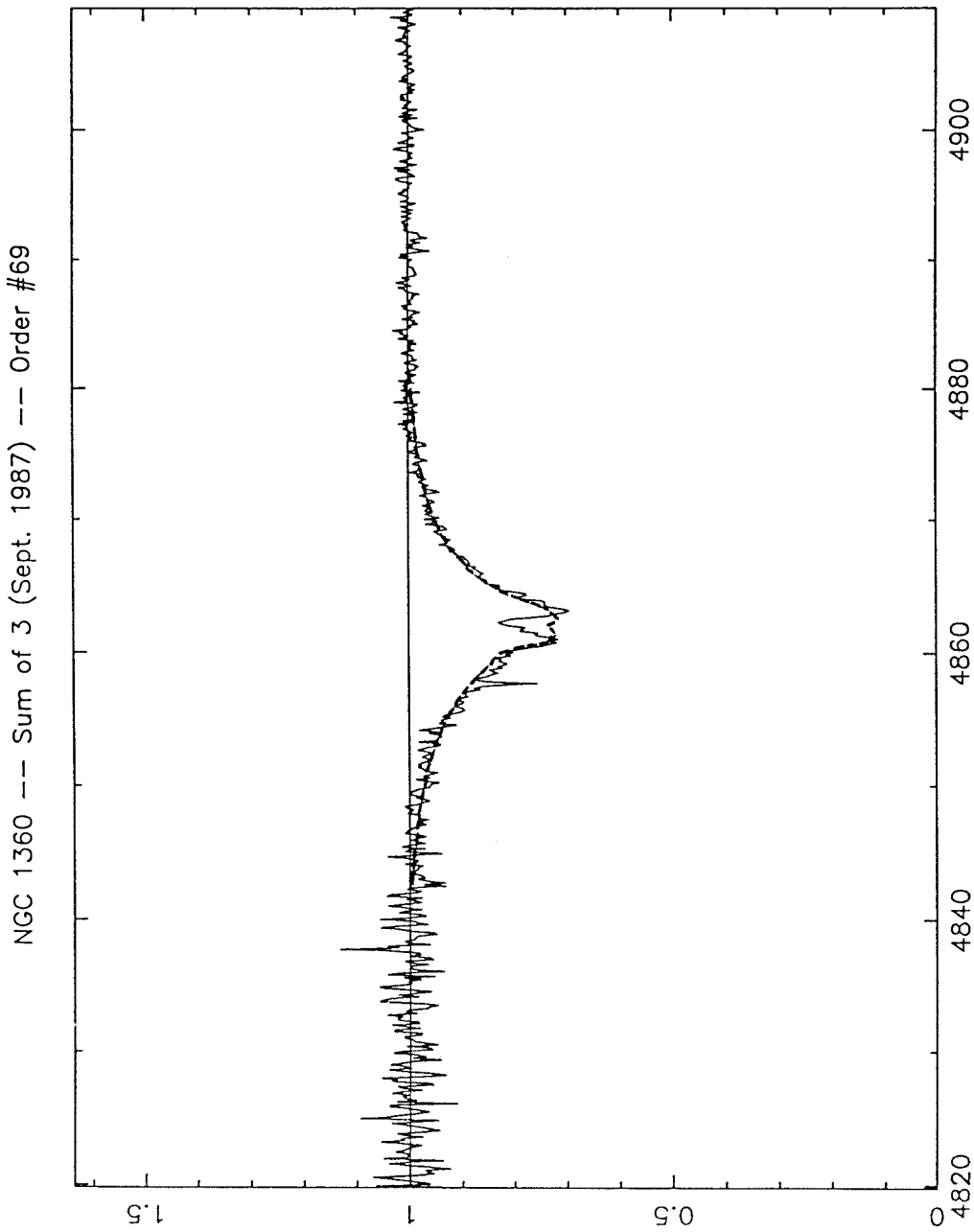

Figure 4-5
(continued)

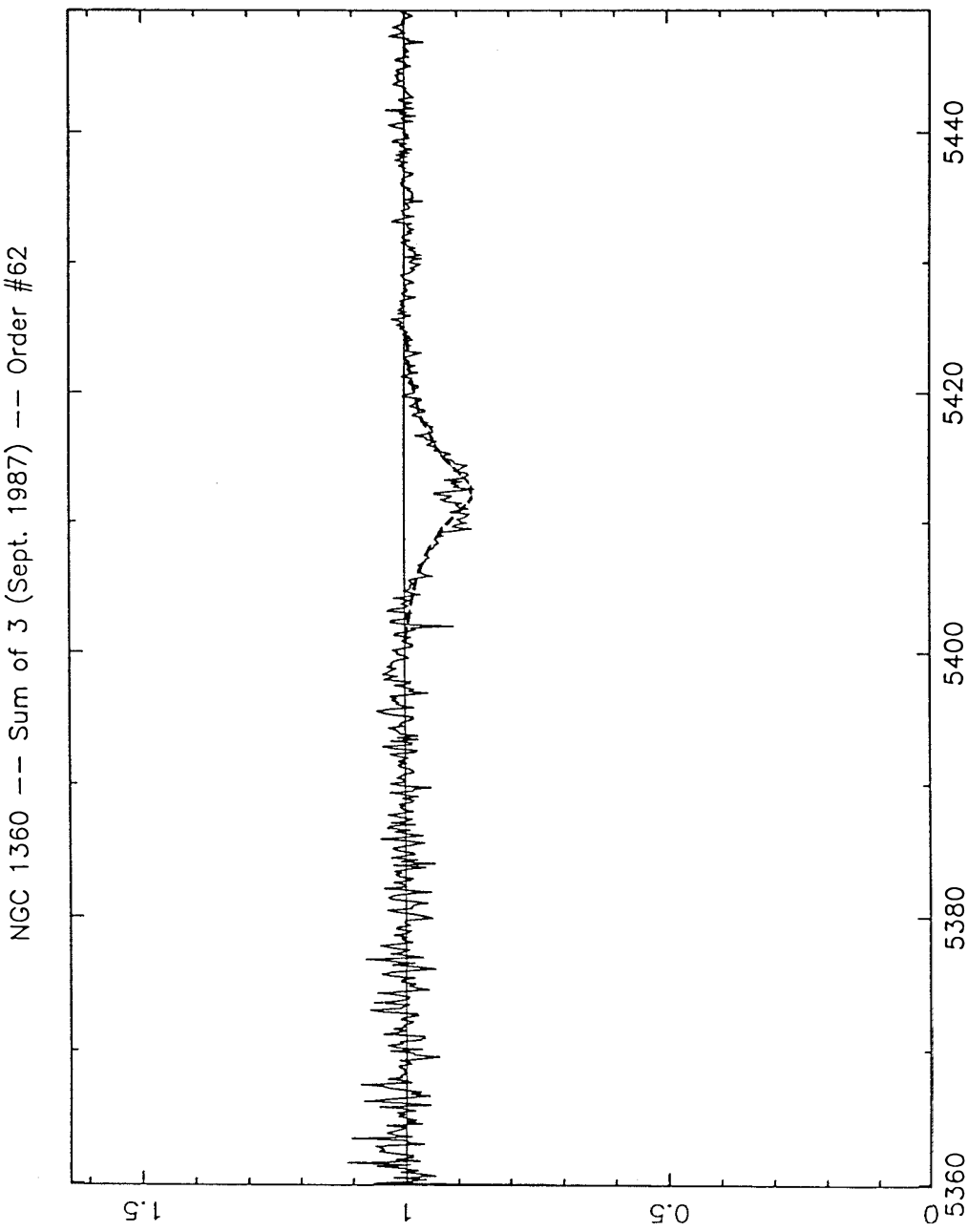

Figure 4-5
(continued)

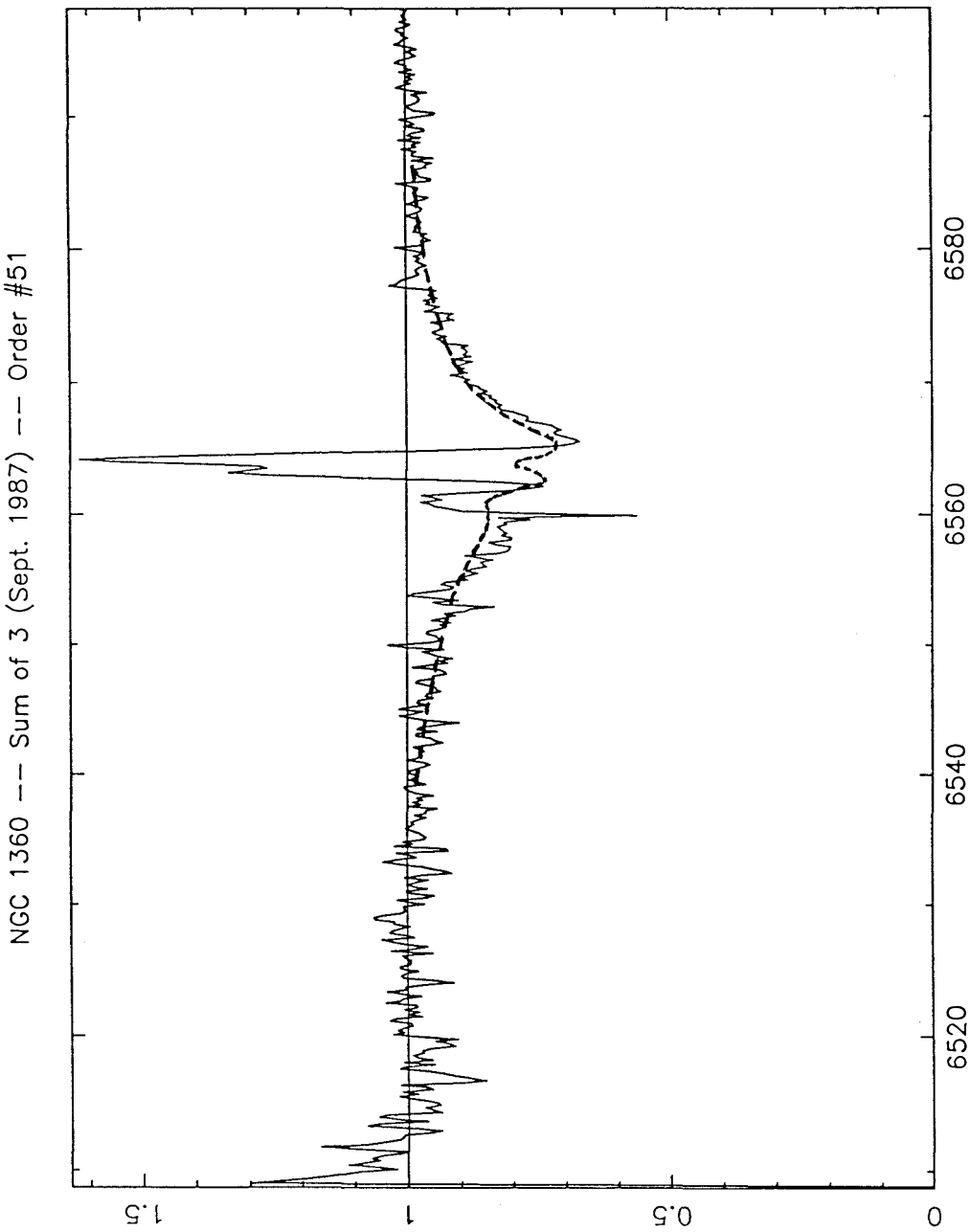

Figure 4-5
(continued)

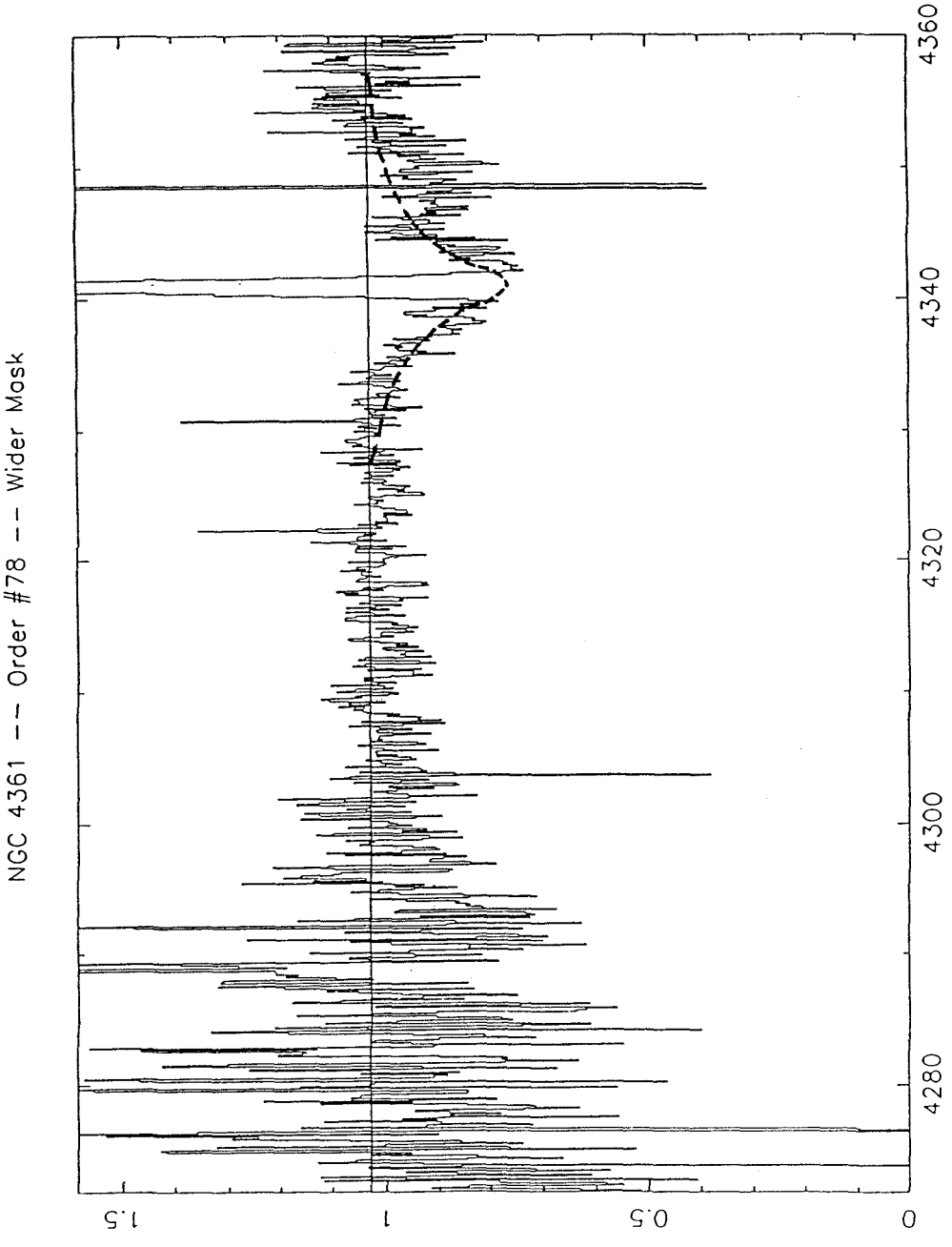

Figure 4-6

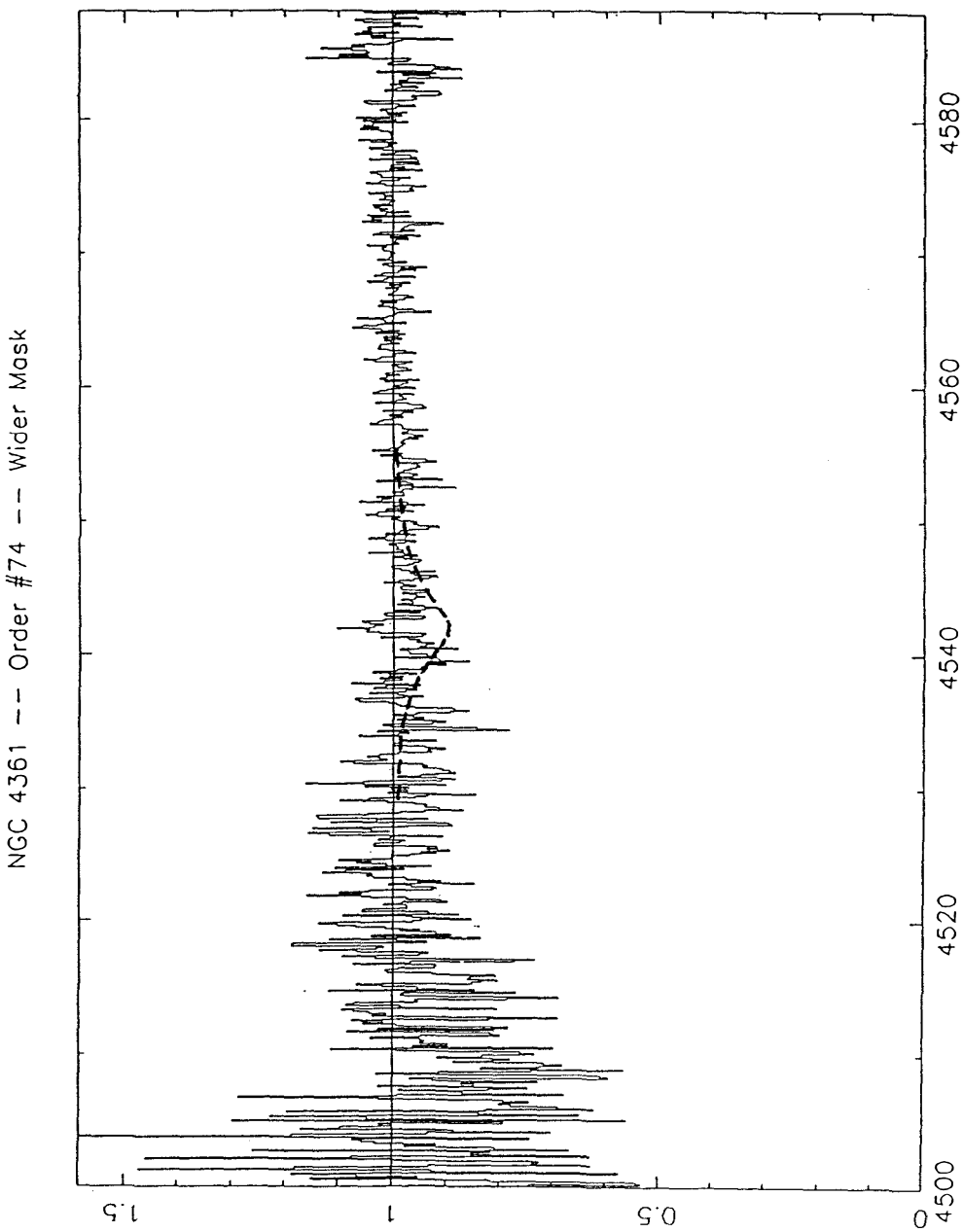

Figure 4-6
(continued)

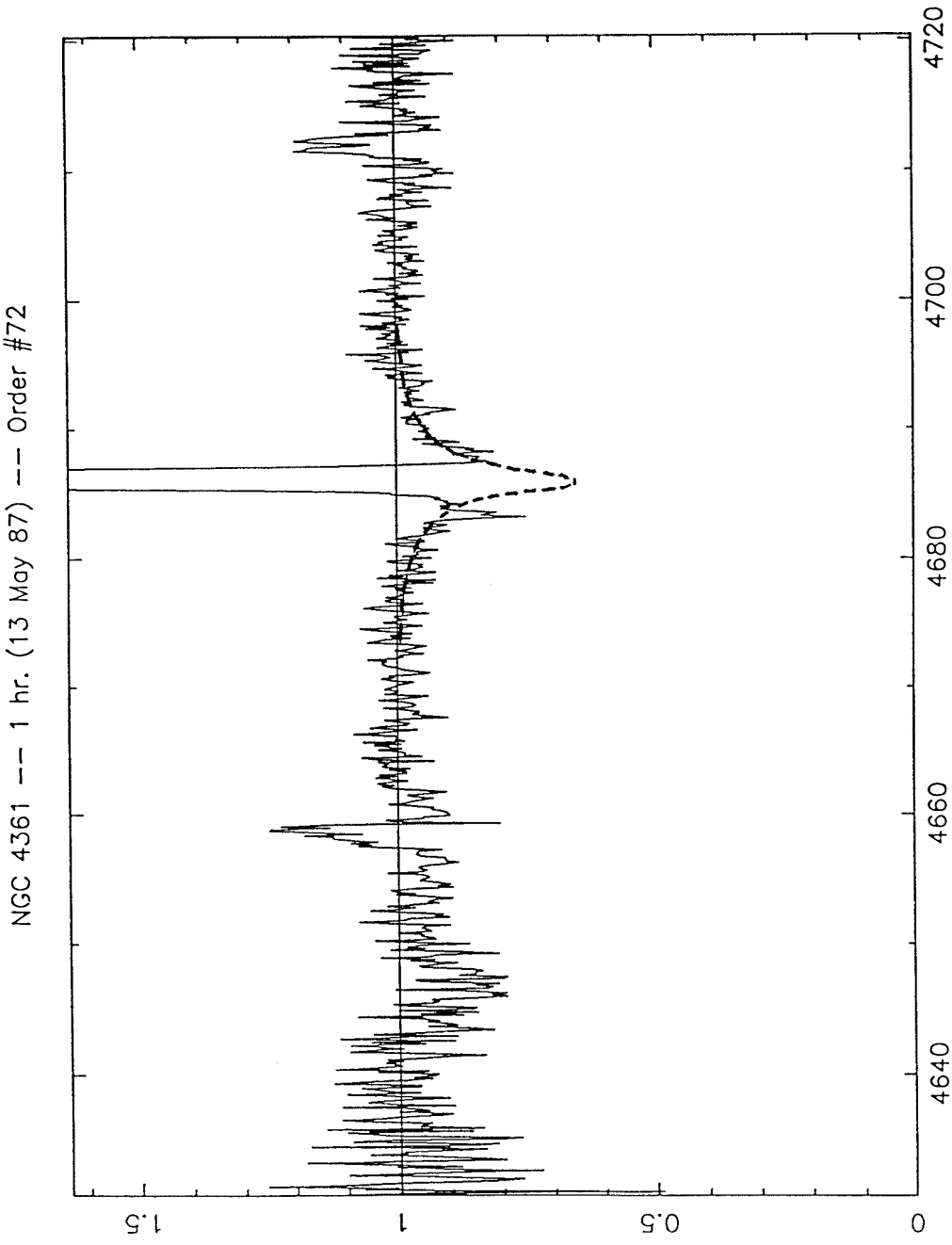

Figure 4-6
(continued)

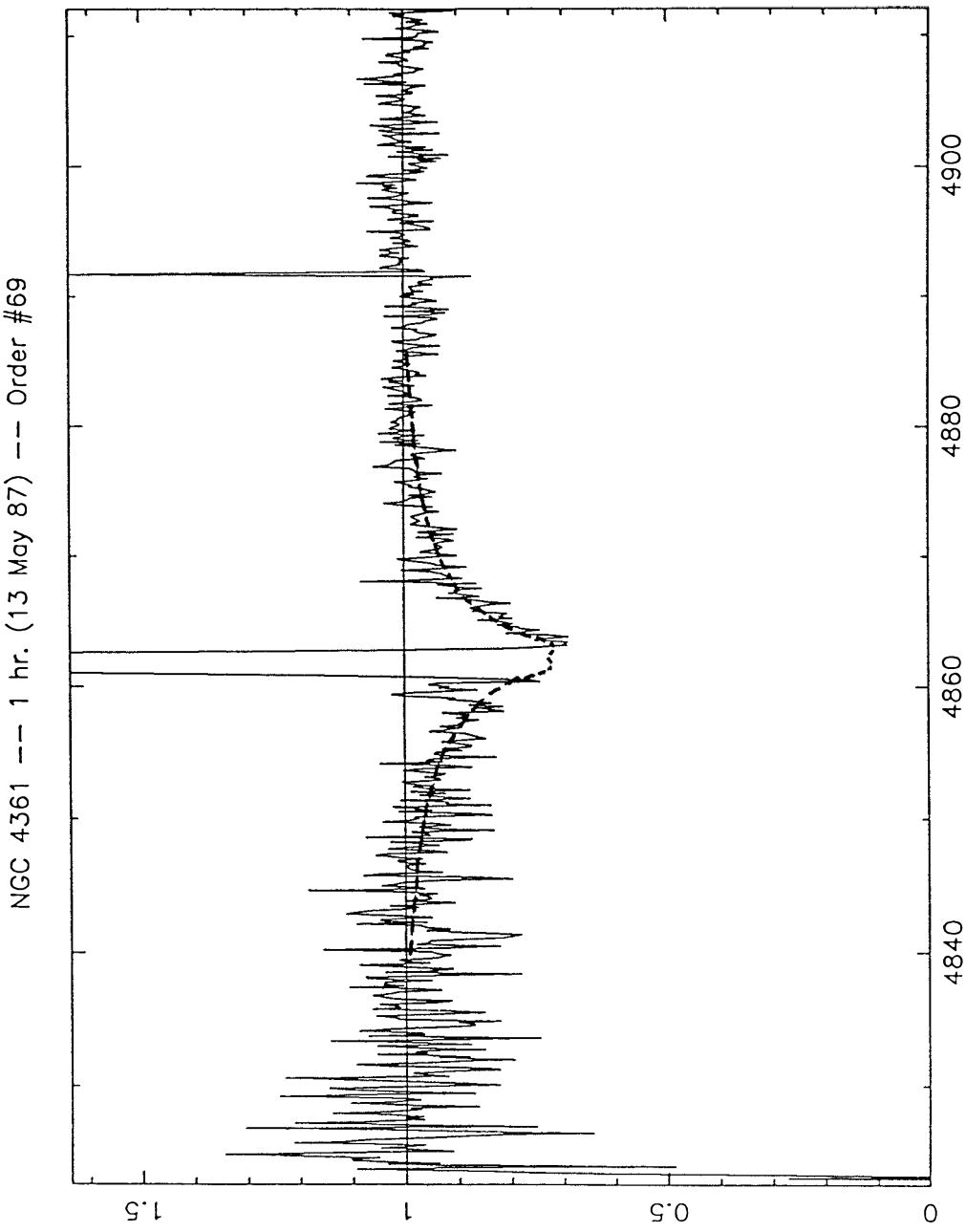

Figure 4-6
(continued)

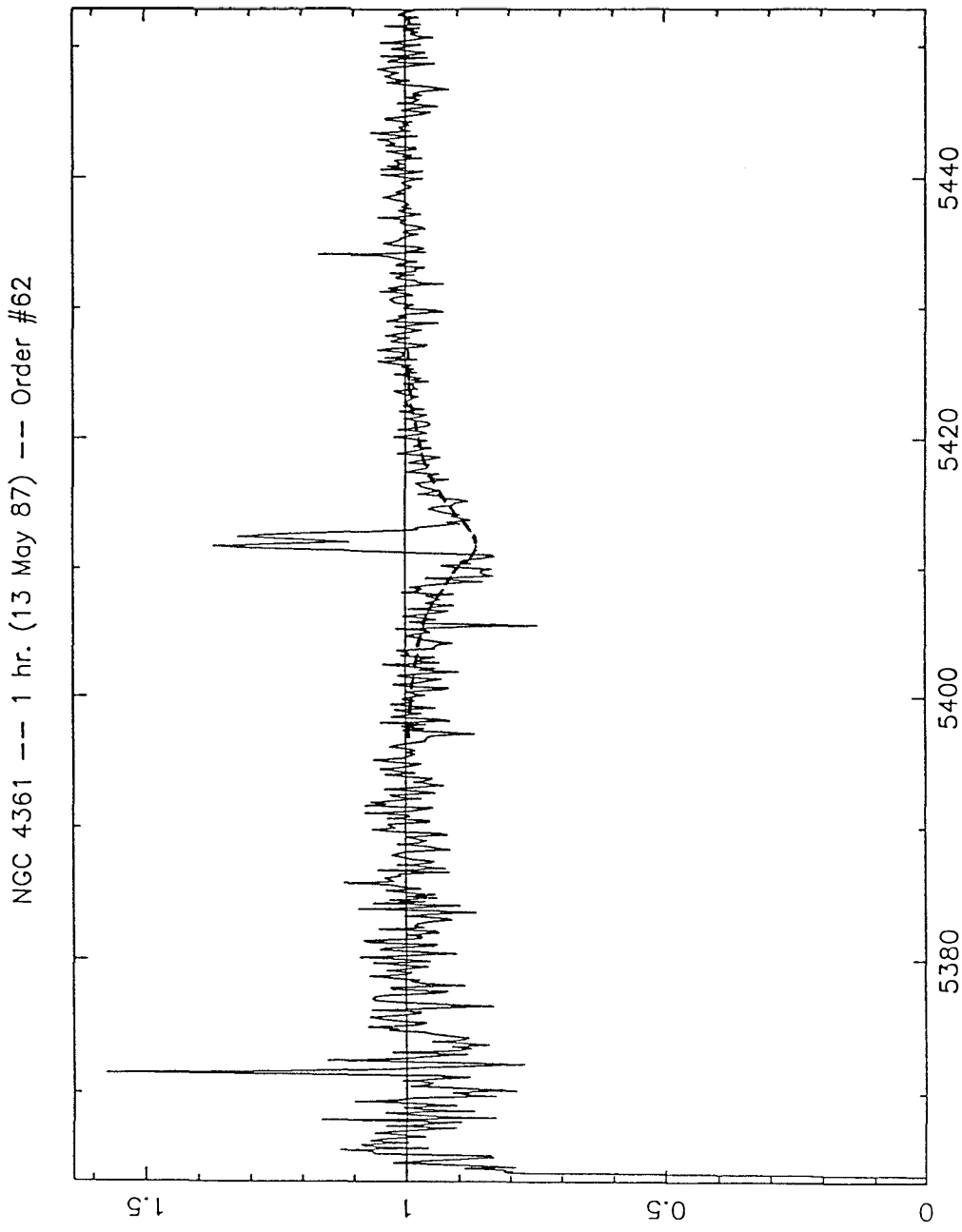

Figure 4-6
(continued)

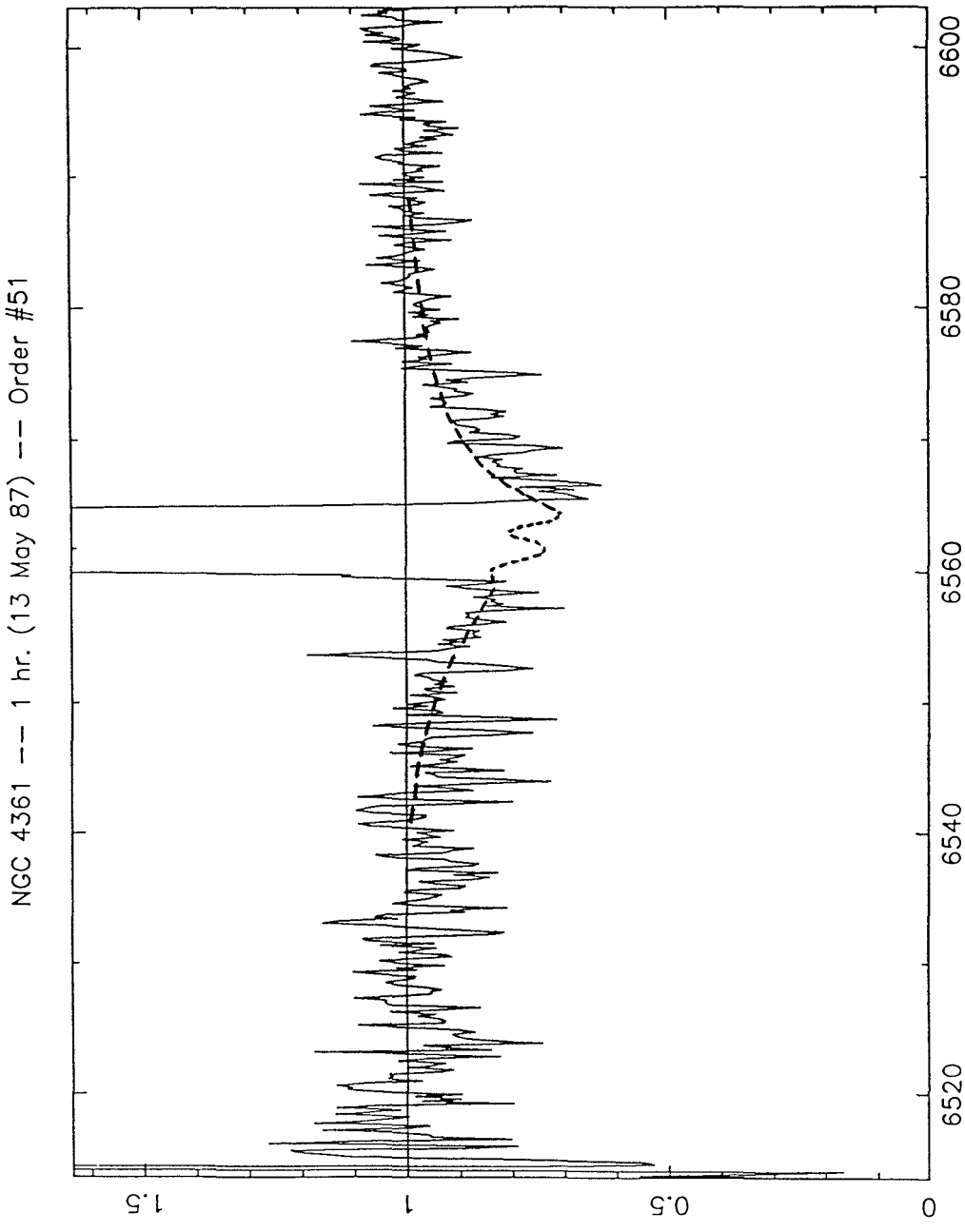

Figure 4-6
(continued)

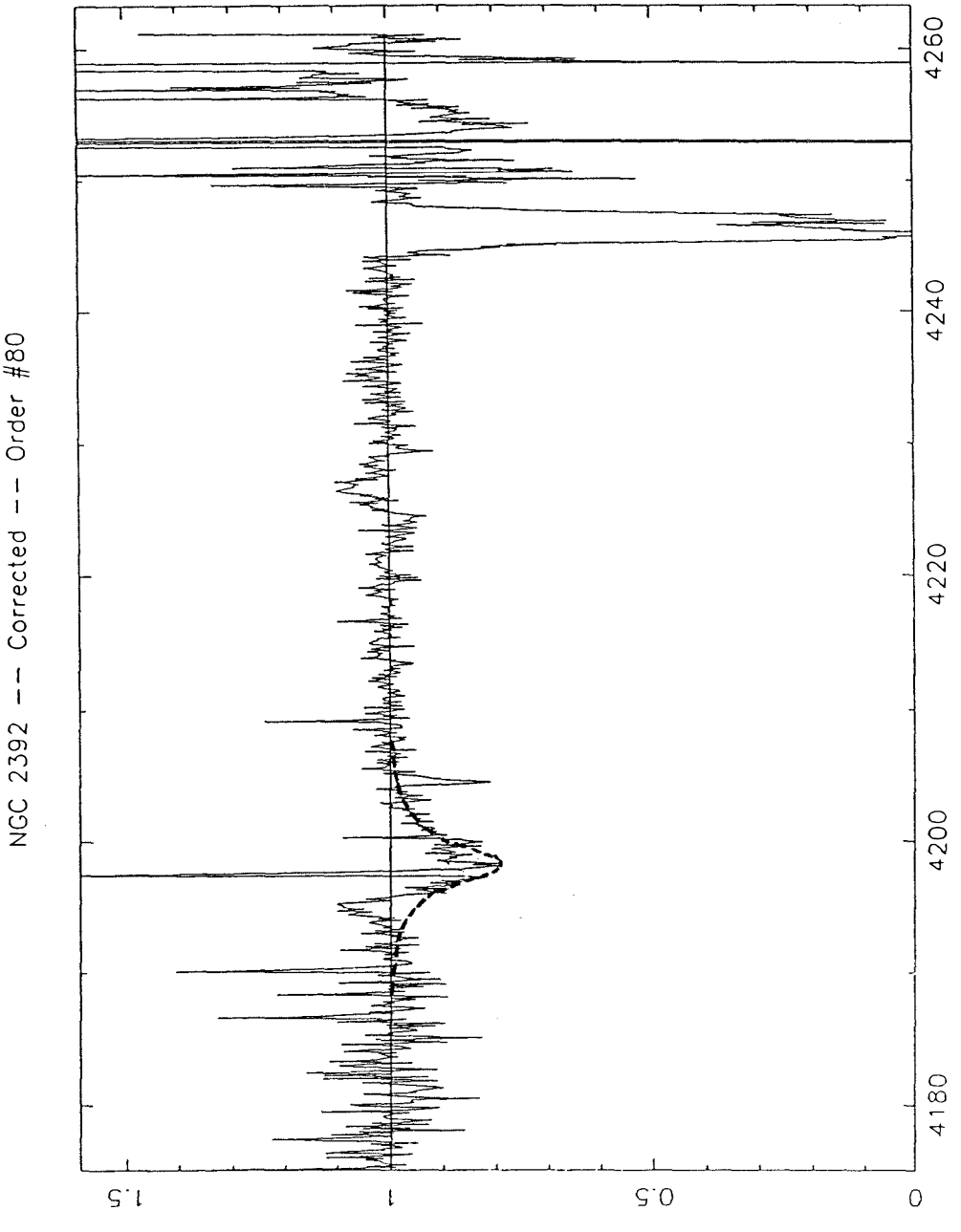

Figure 4-7

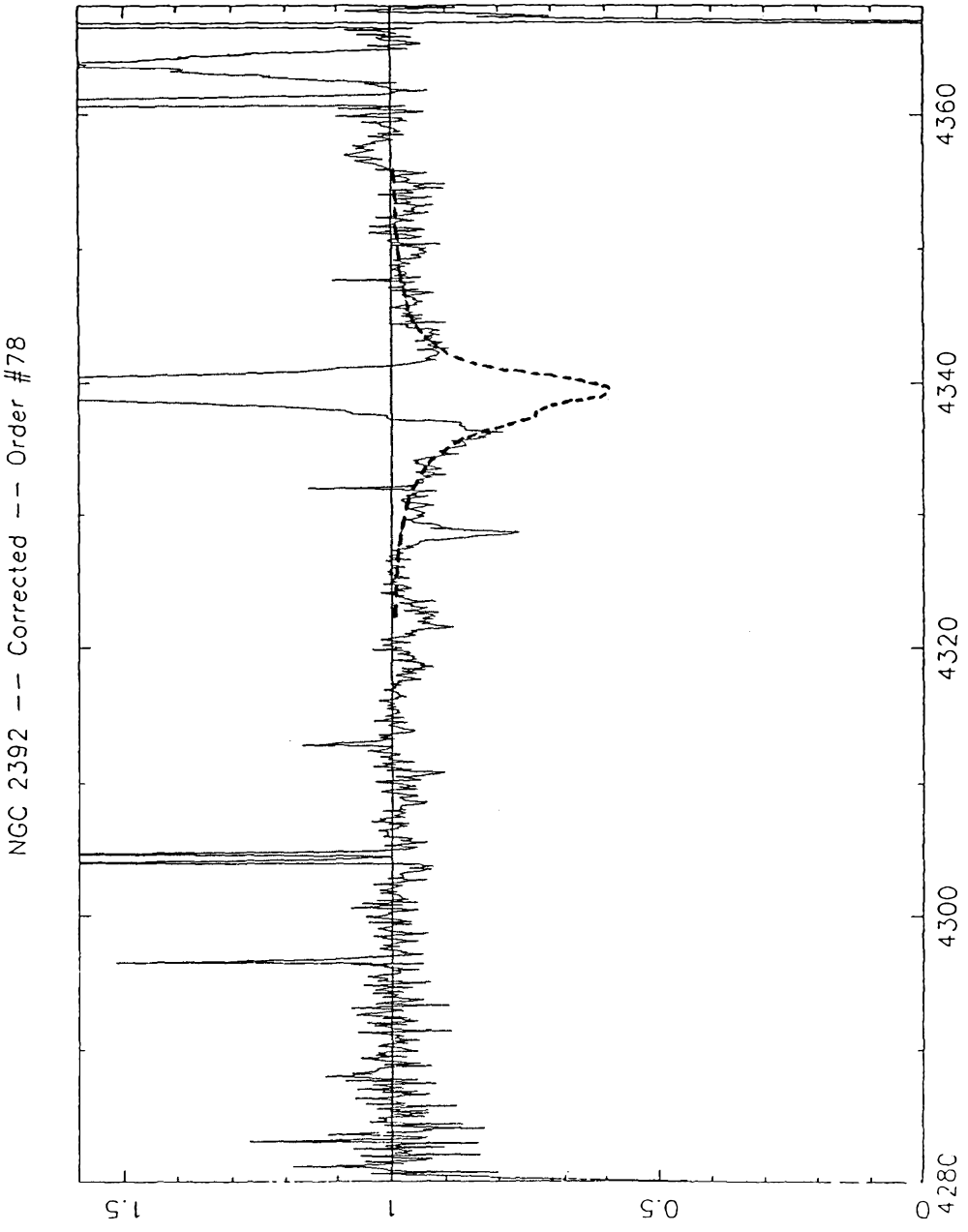

Figure 4-7
(continued)

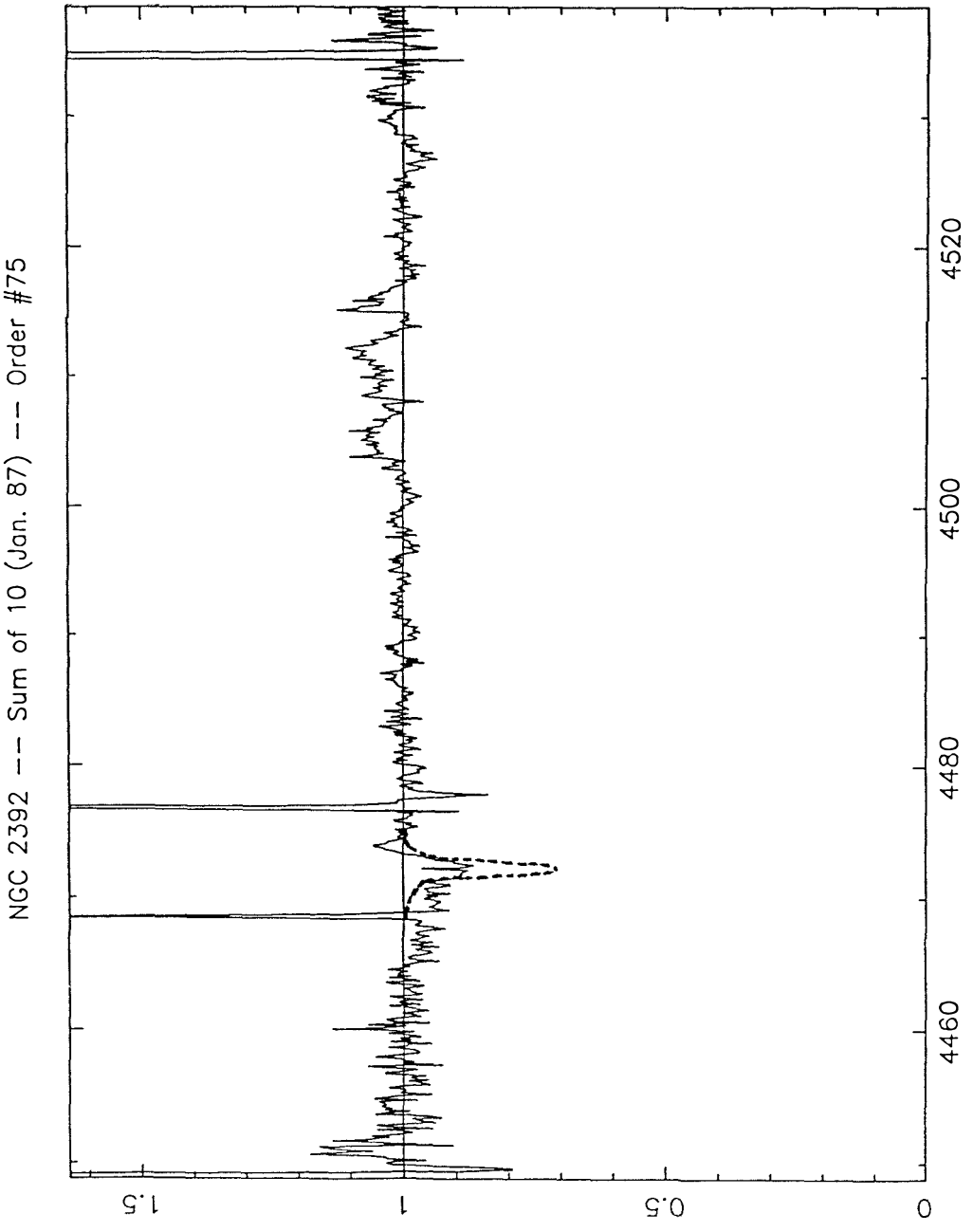

Figure 4-7
(continued)

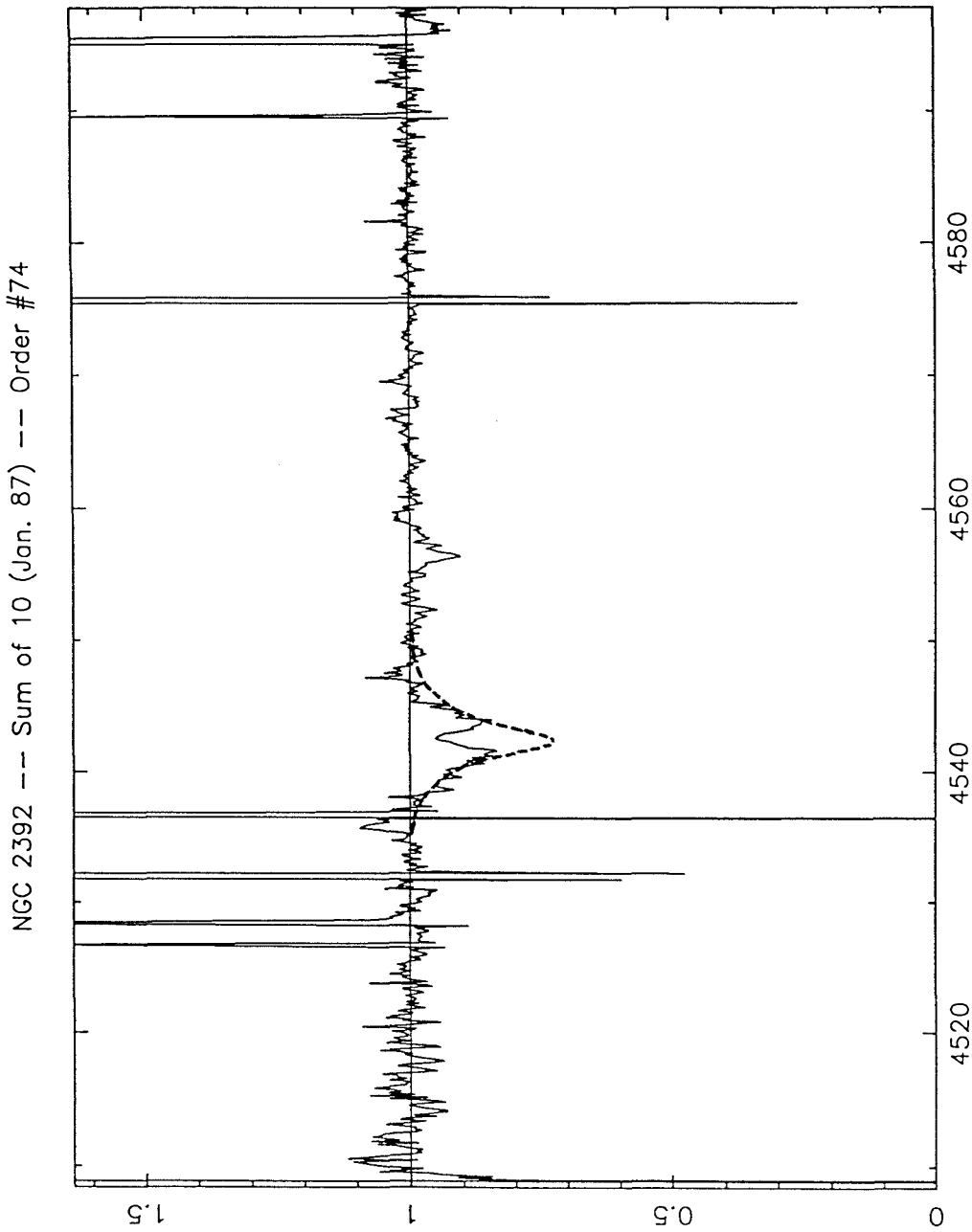

Figure 4-7
(continued)

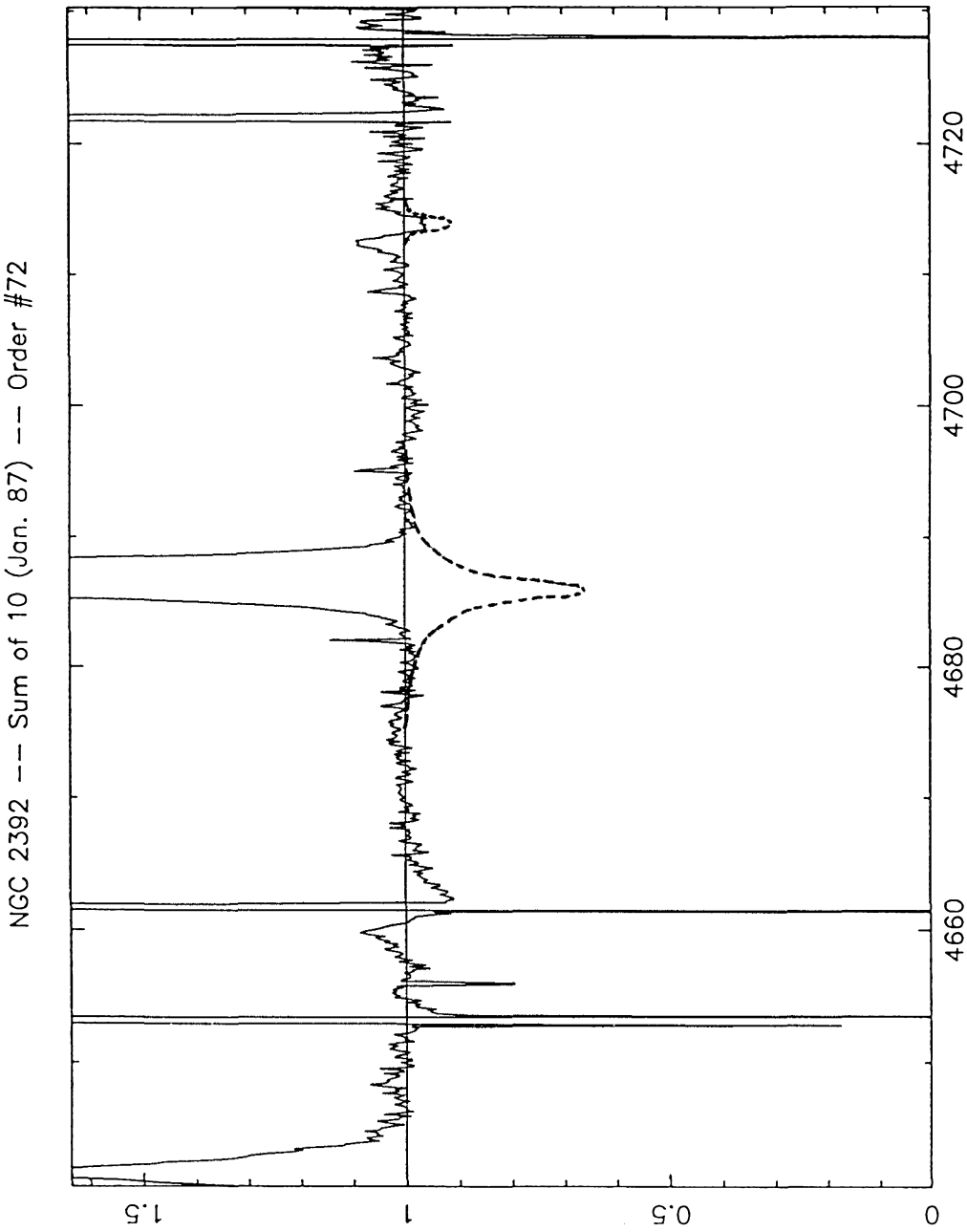

Figure 4-7
(continued)

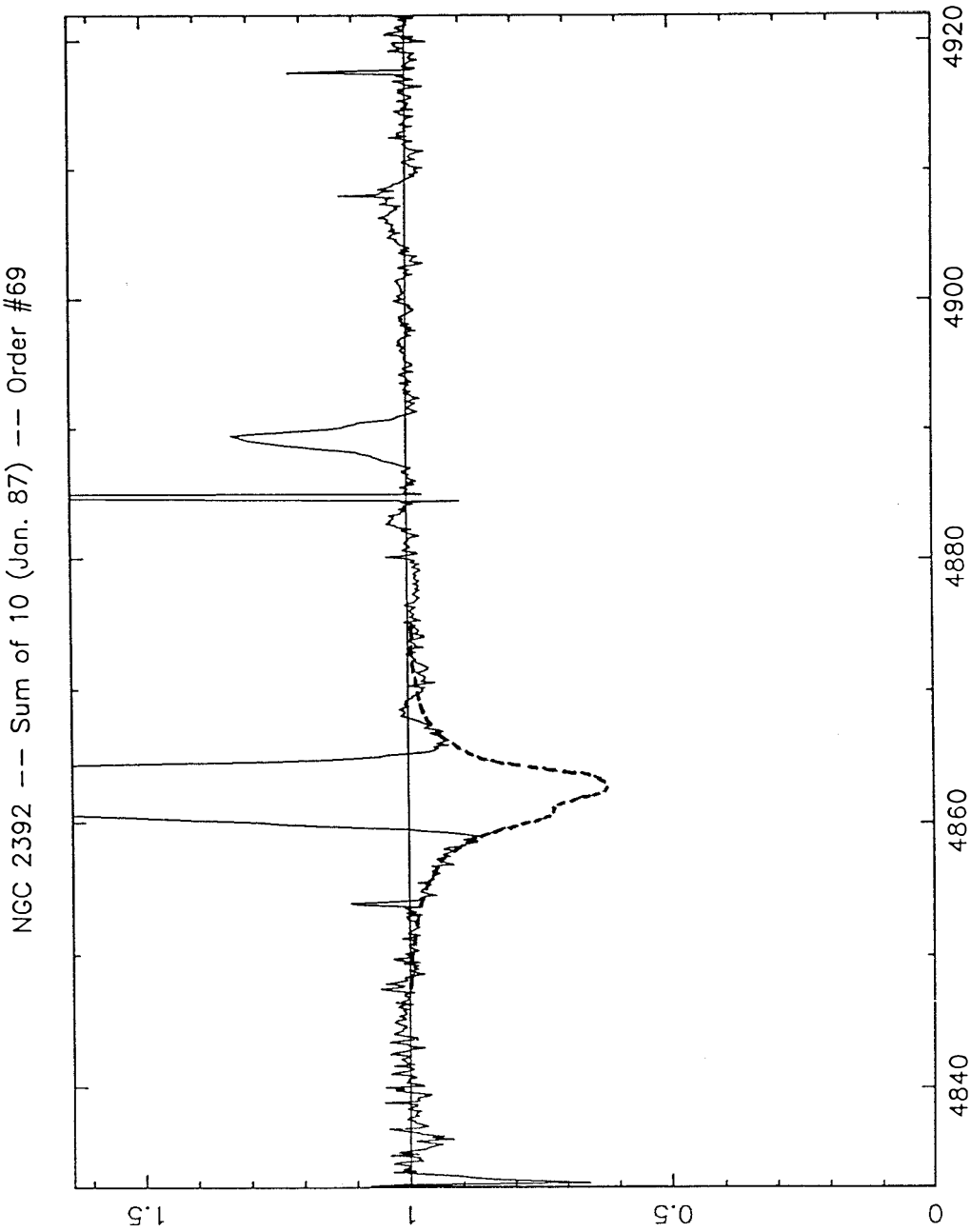

Figure 4-7
(continued)

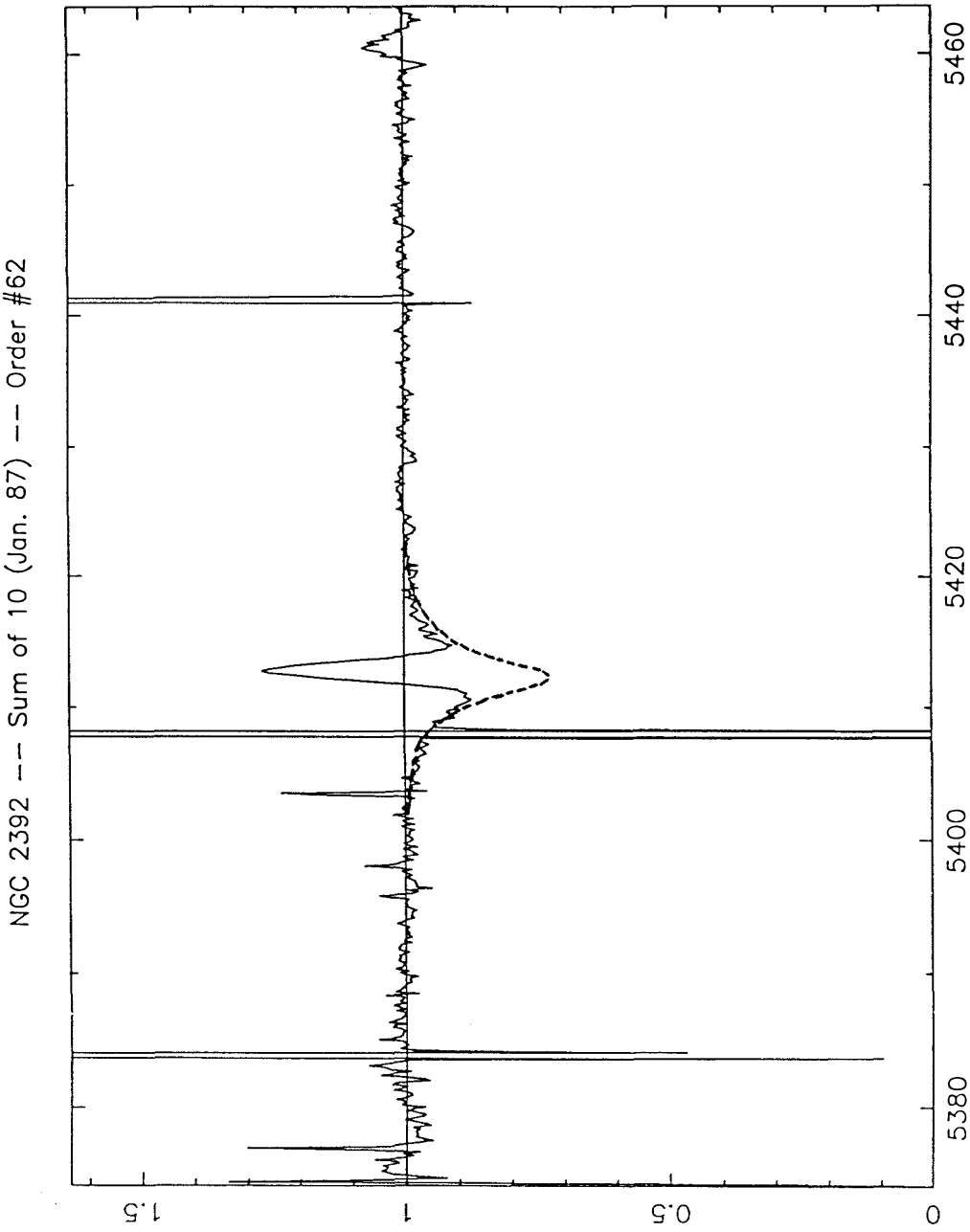

Figure 4-7
(continued)

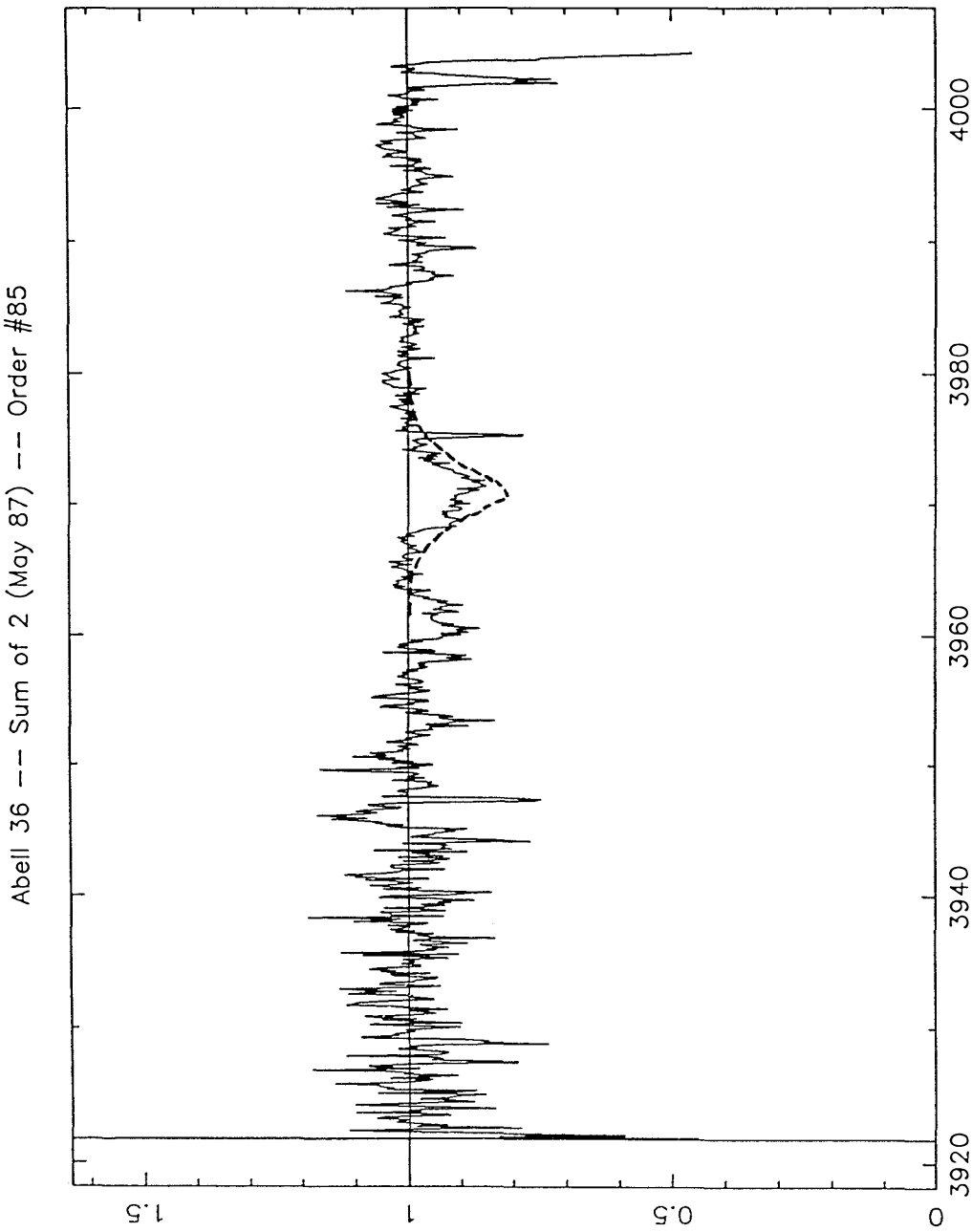
Abell 36 -- Sum of 2 (May 87) -- Order #85
1.5
1
0.5
0
3920
3940
3960
3980
4000

Figure 4-8

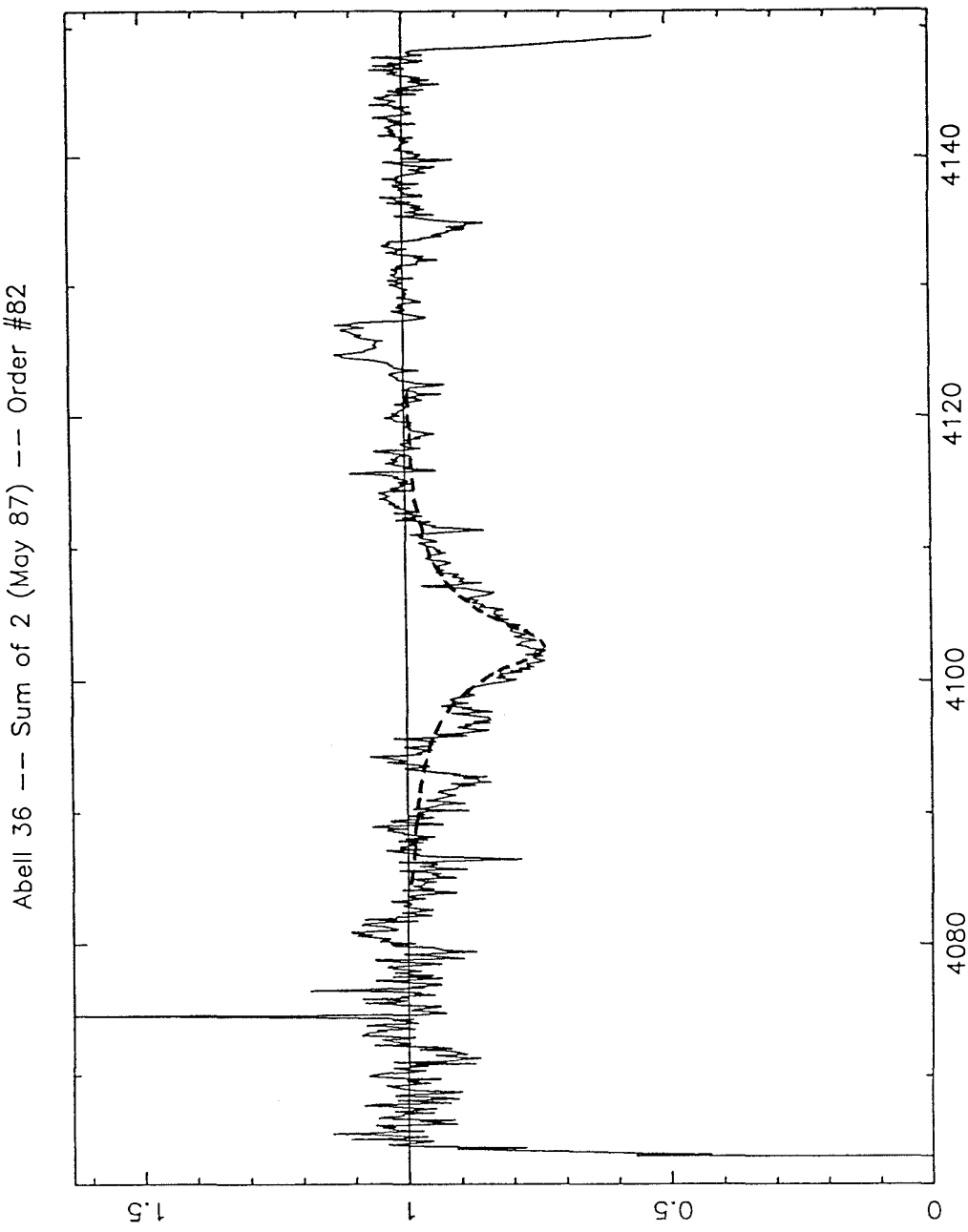

Figure 4-8
(continued)

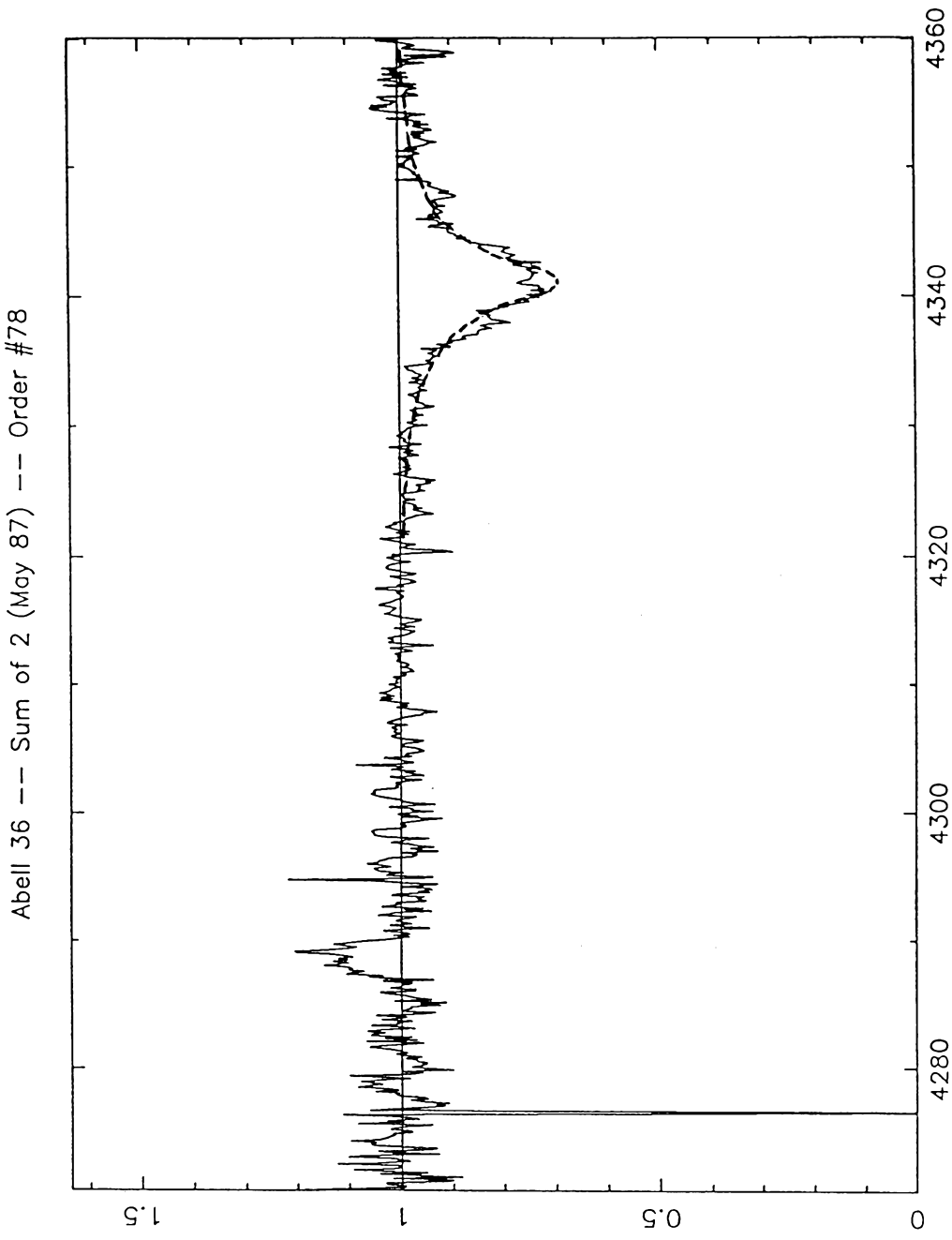

Figure 4-8
(continued)

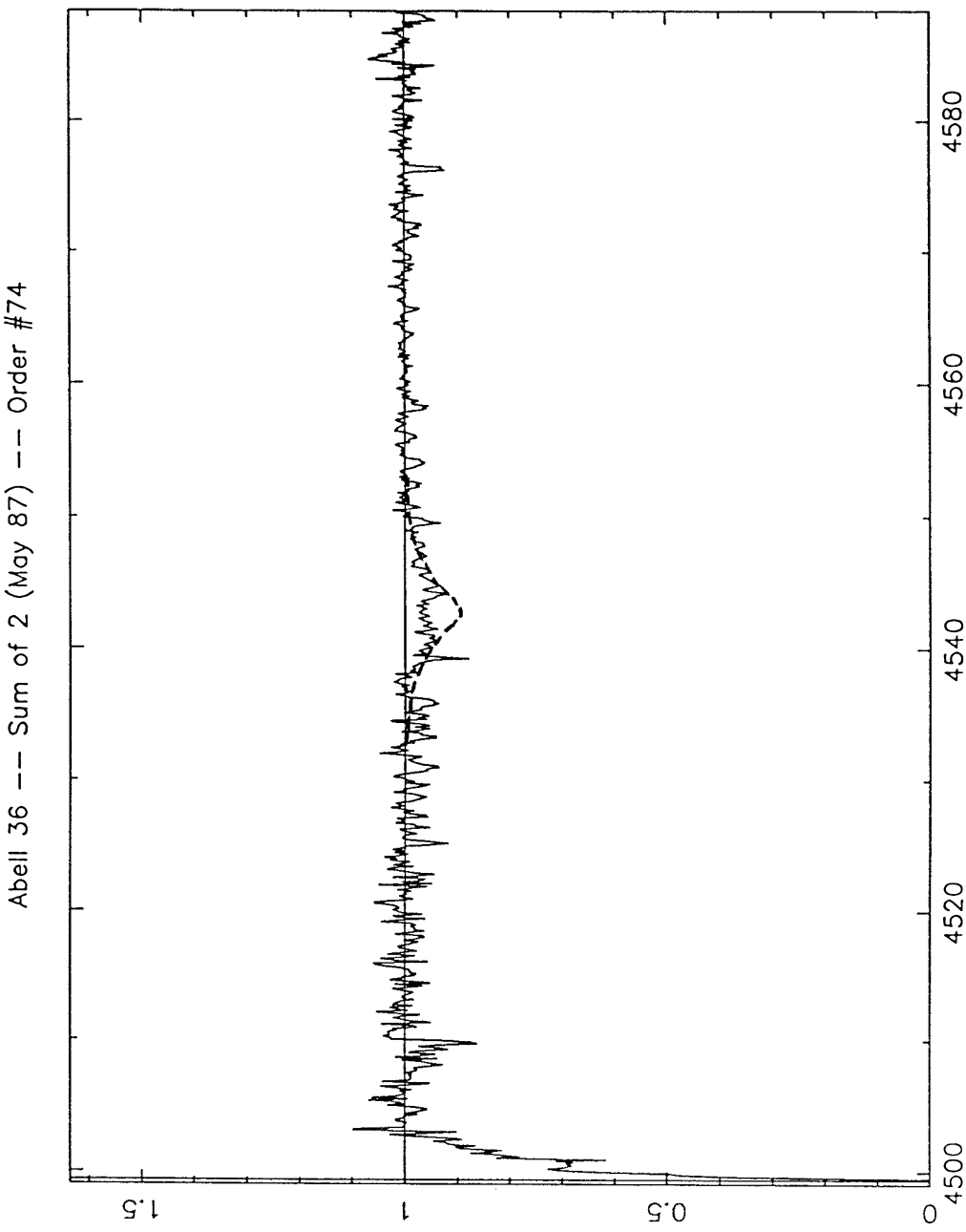

Figure 4-8
(continued)

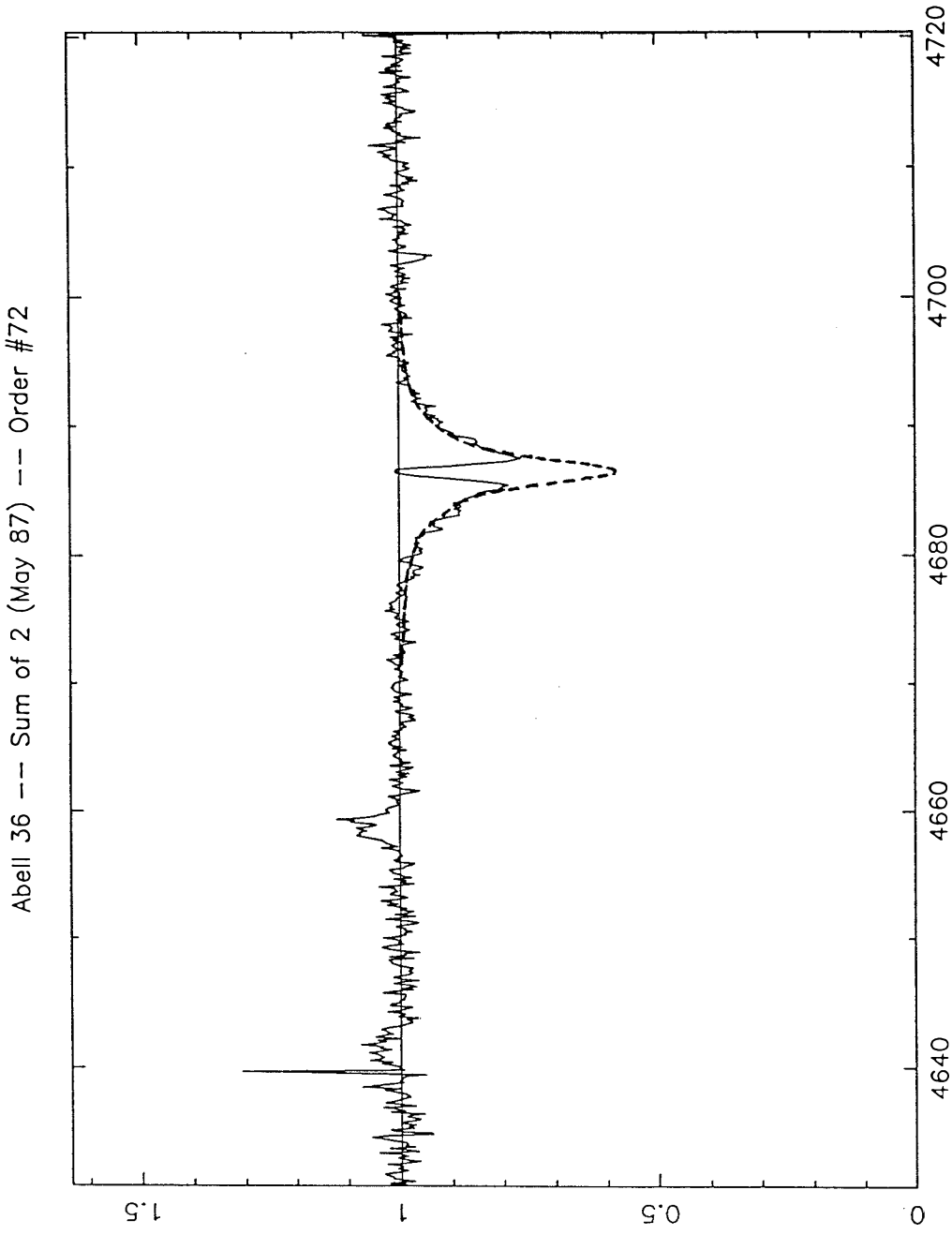

Figure 4-8
(continued)

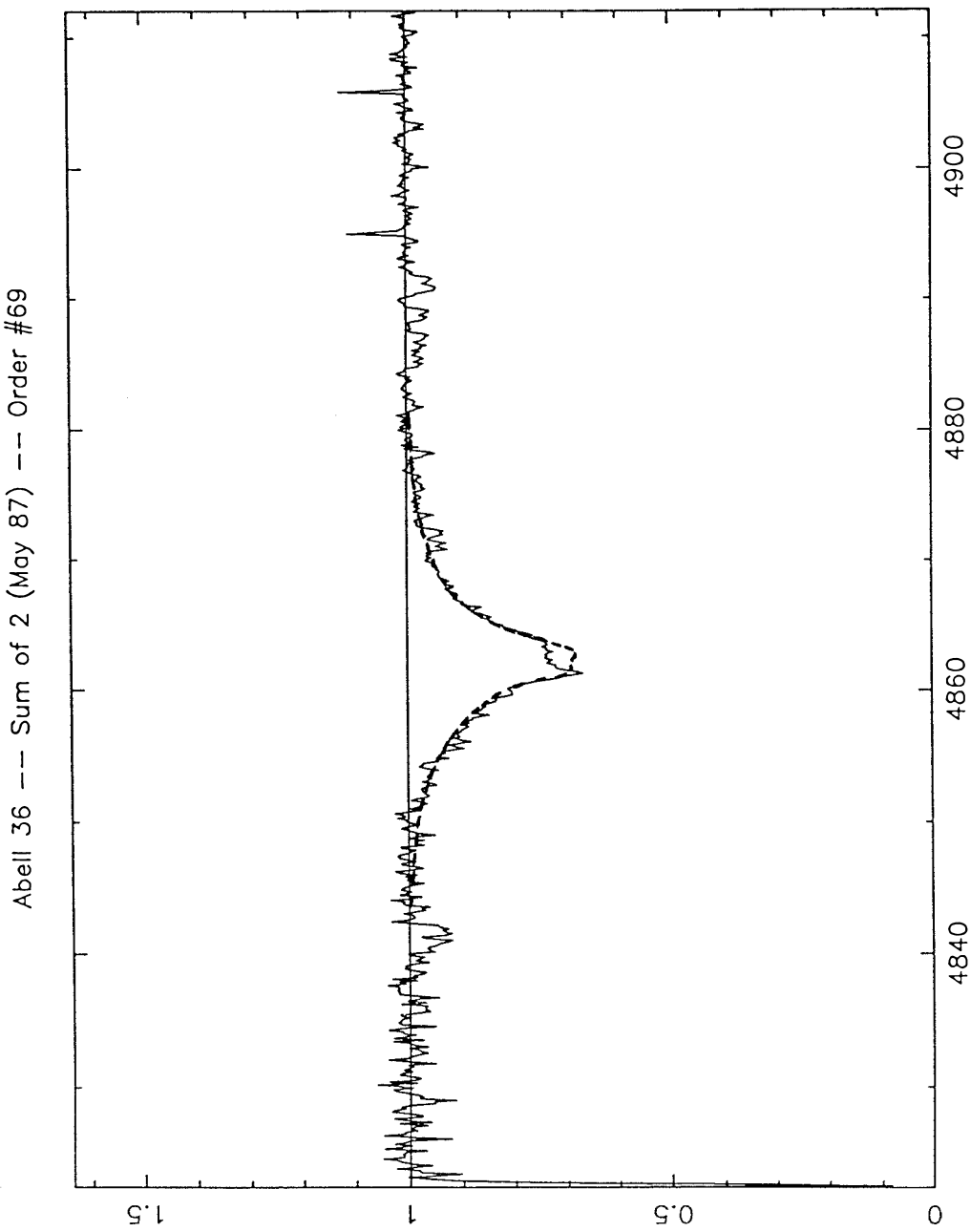

Figure 4-8
(continued)

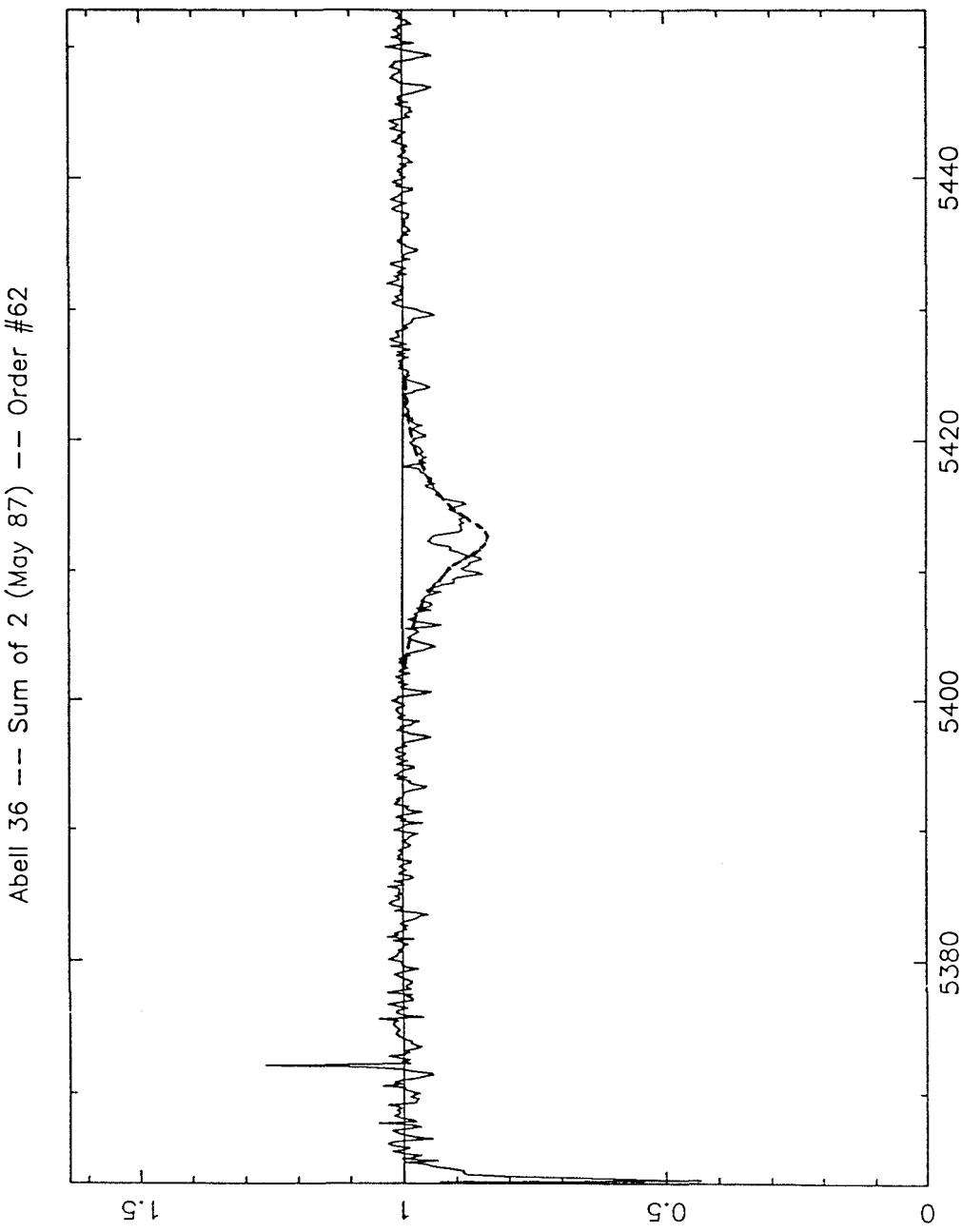

Figure 4-8
(continued)

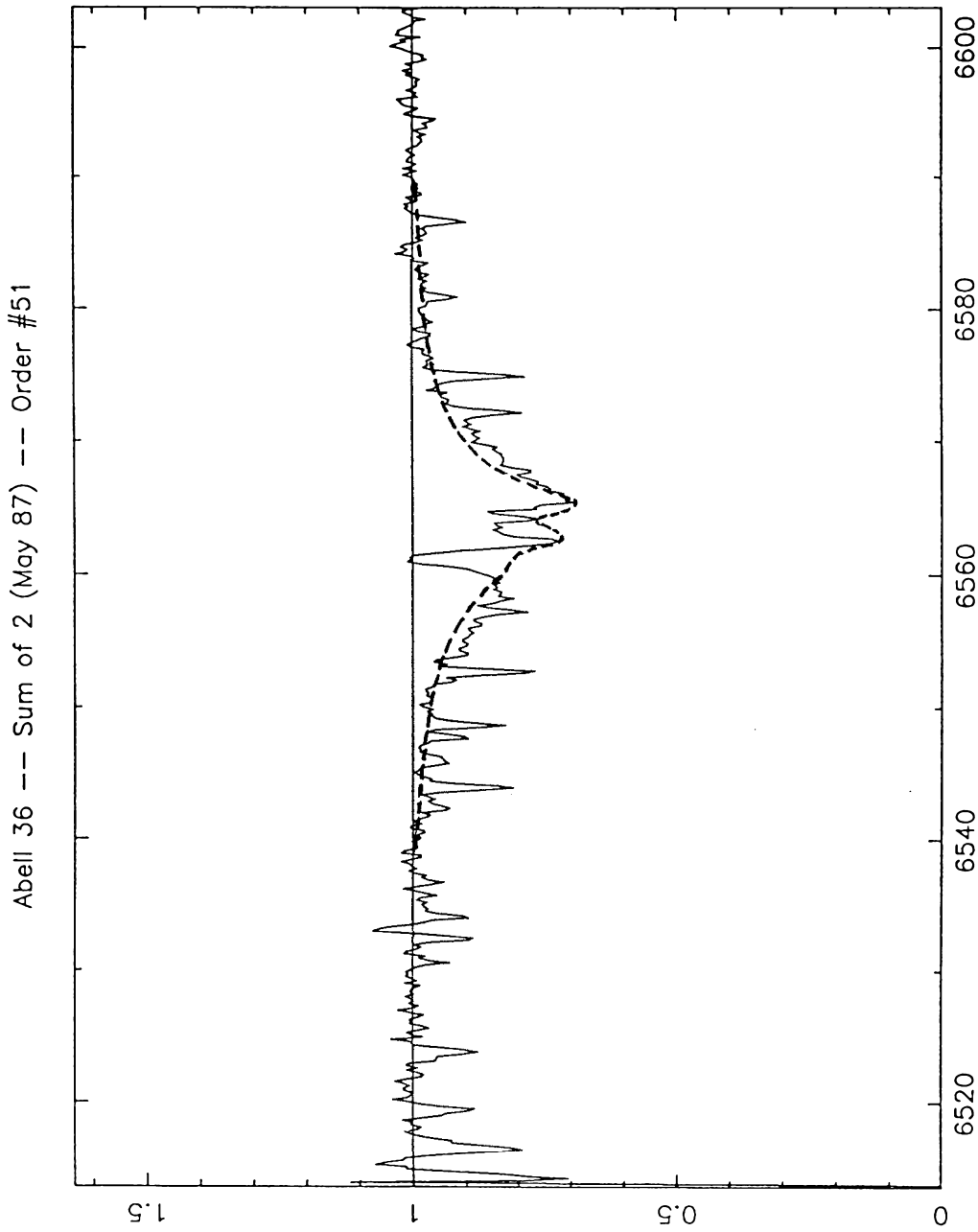

Figure 4-8
(continued)

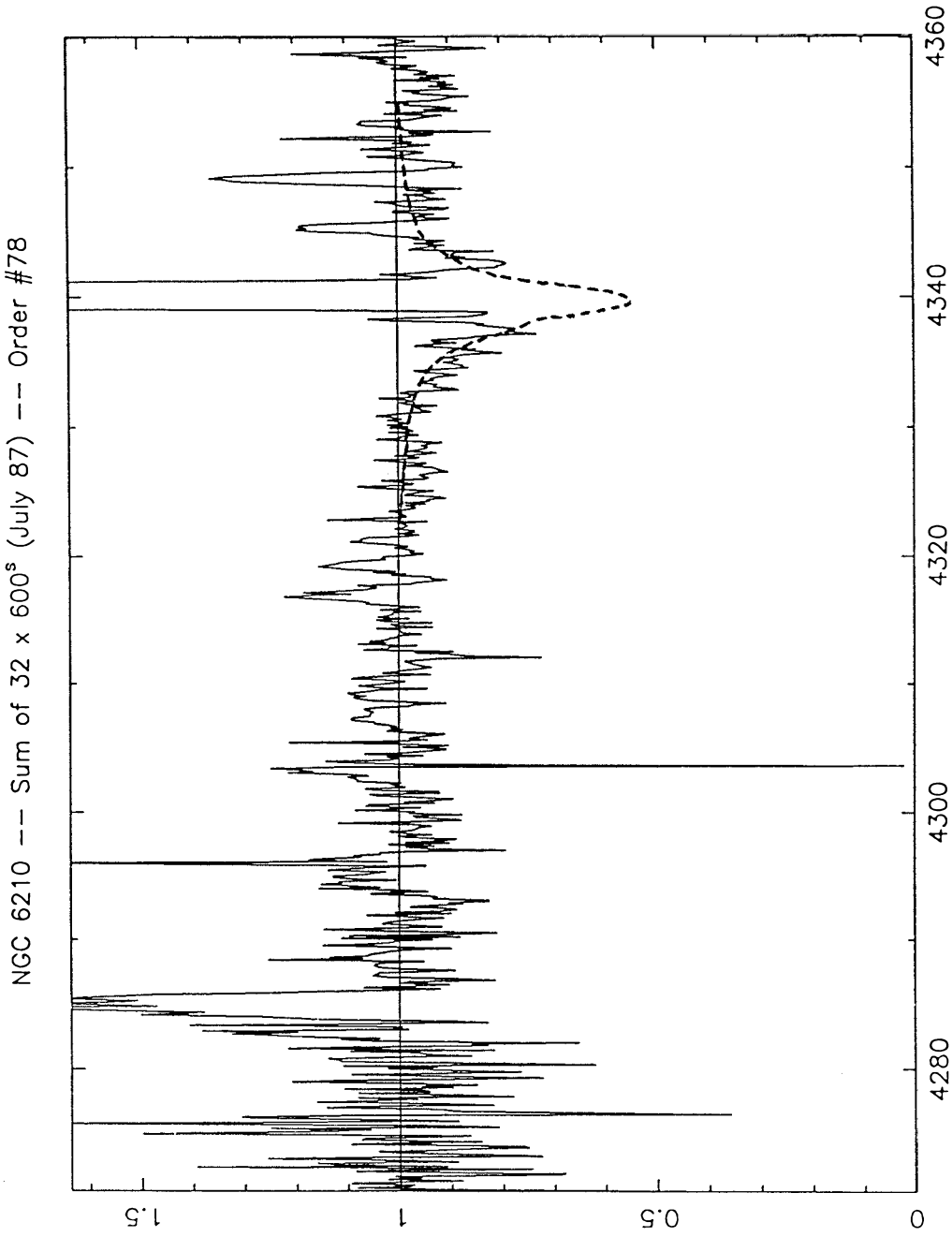
NGC 6210 -- Sum of 32 x 600s (July 87) -- Order #78
4360
4340
4320
4300
4280
0
0.5
1
1.5

Figure 4-9

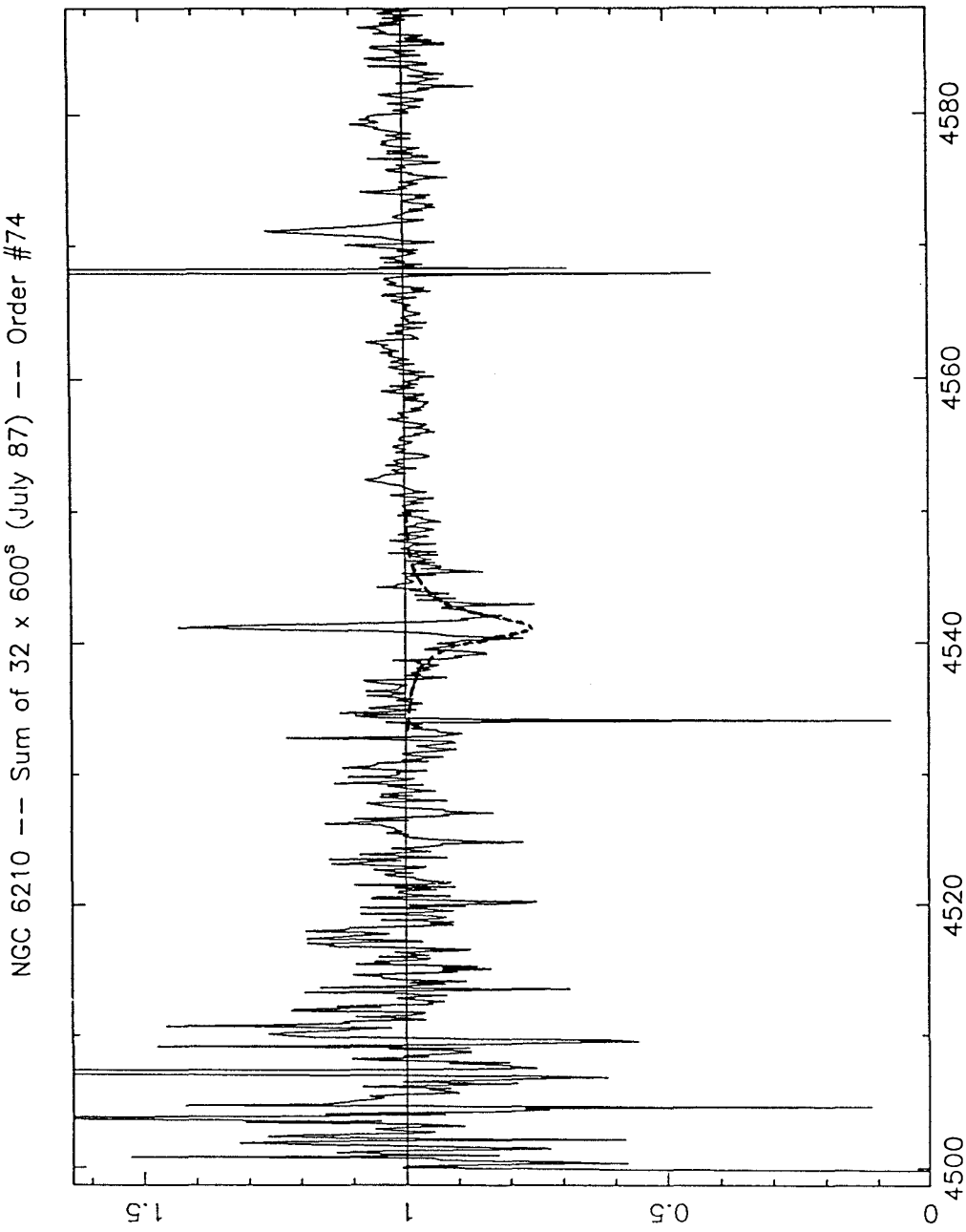

Figure 4-9
(continued)

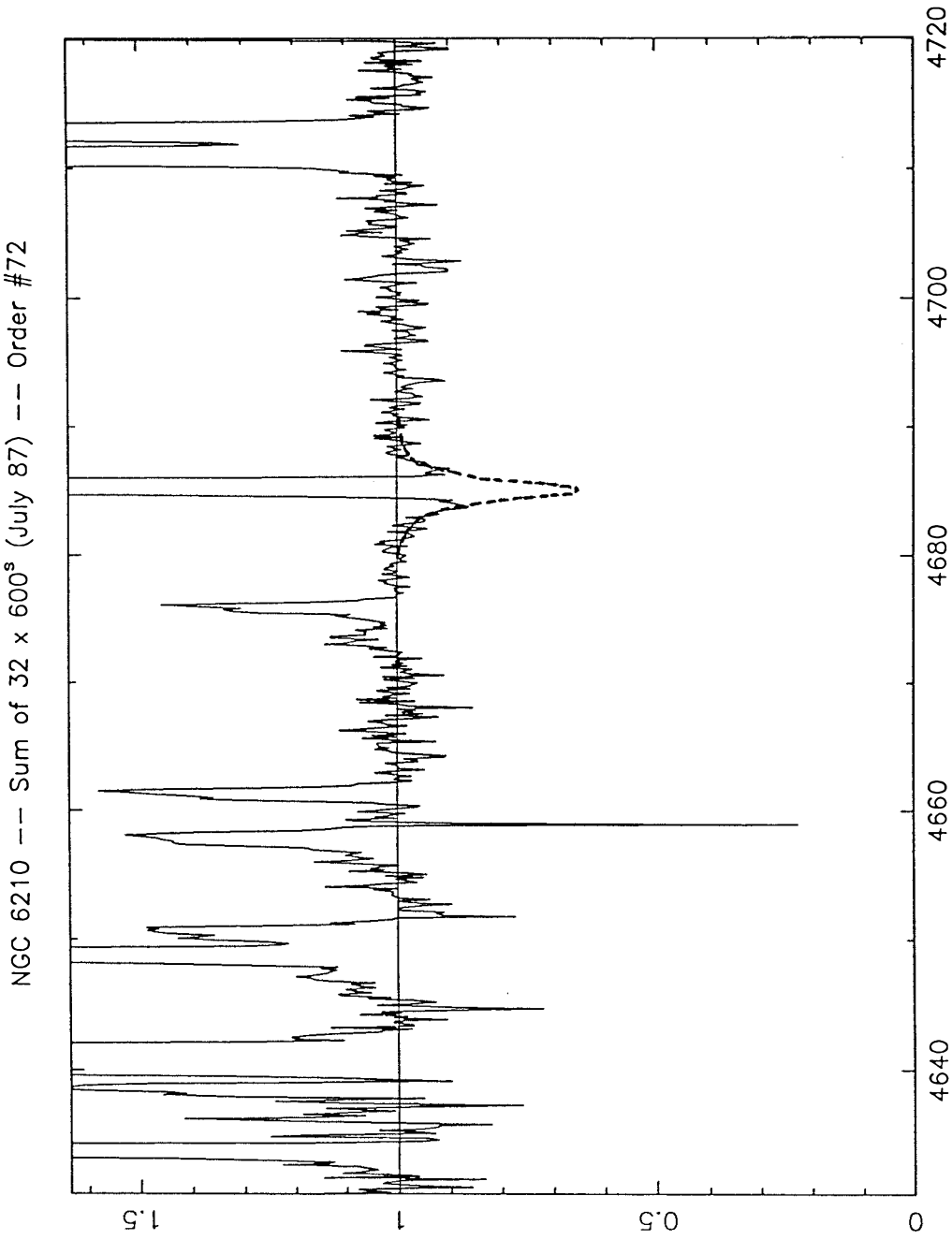

Figure 4-9
(continued)

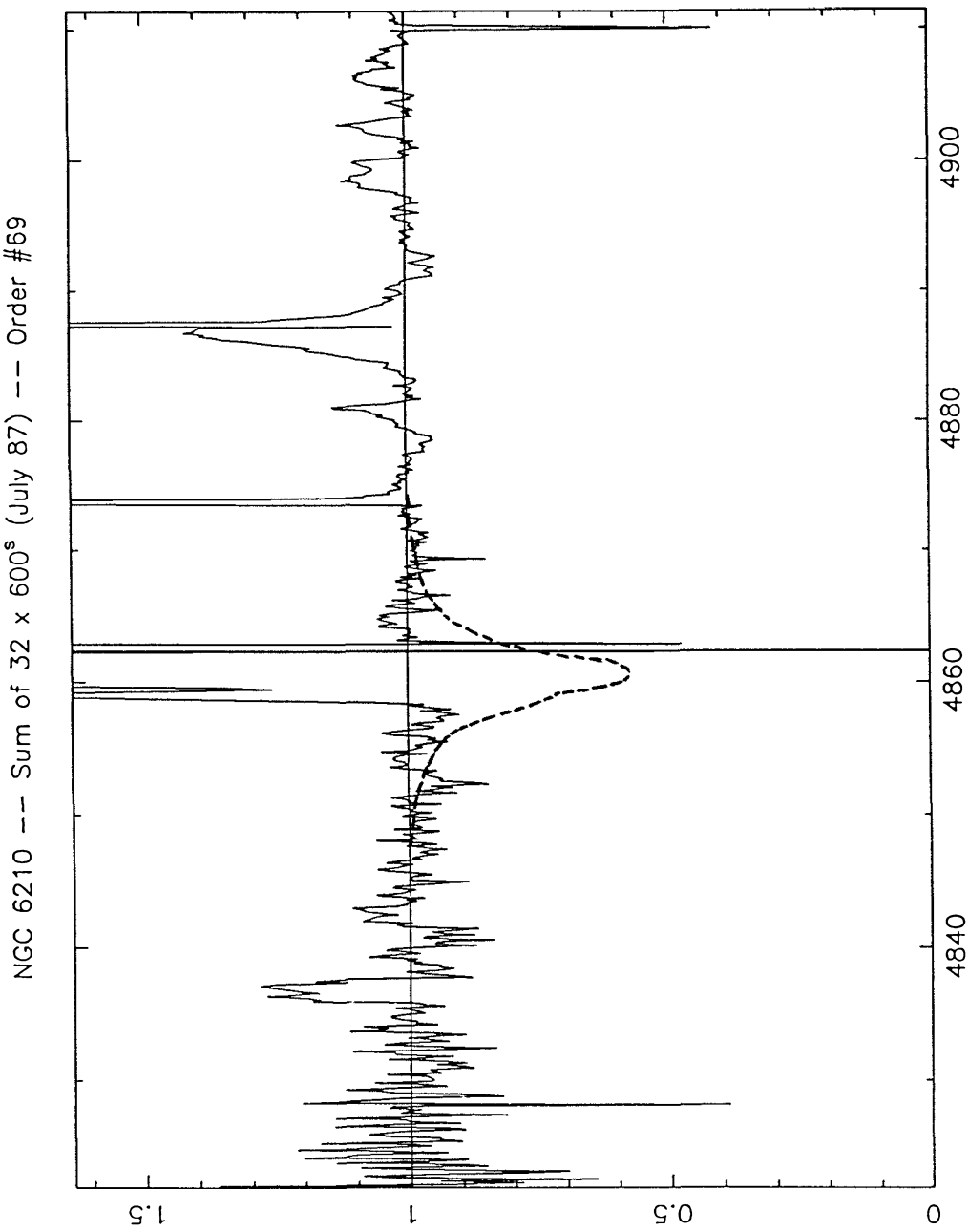

Figure 4-9
(continued)

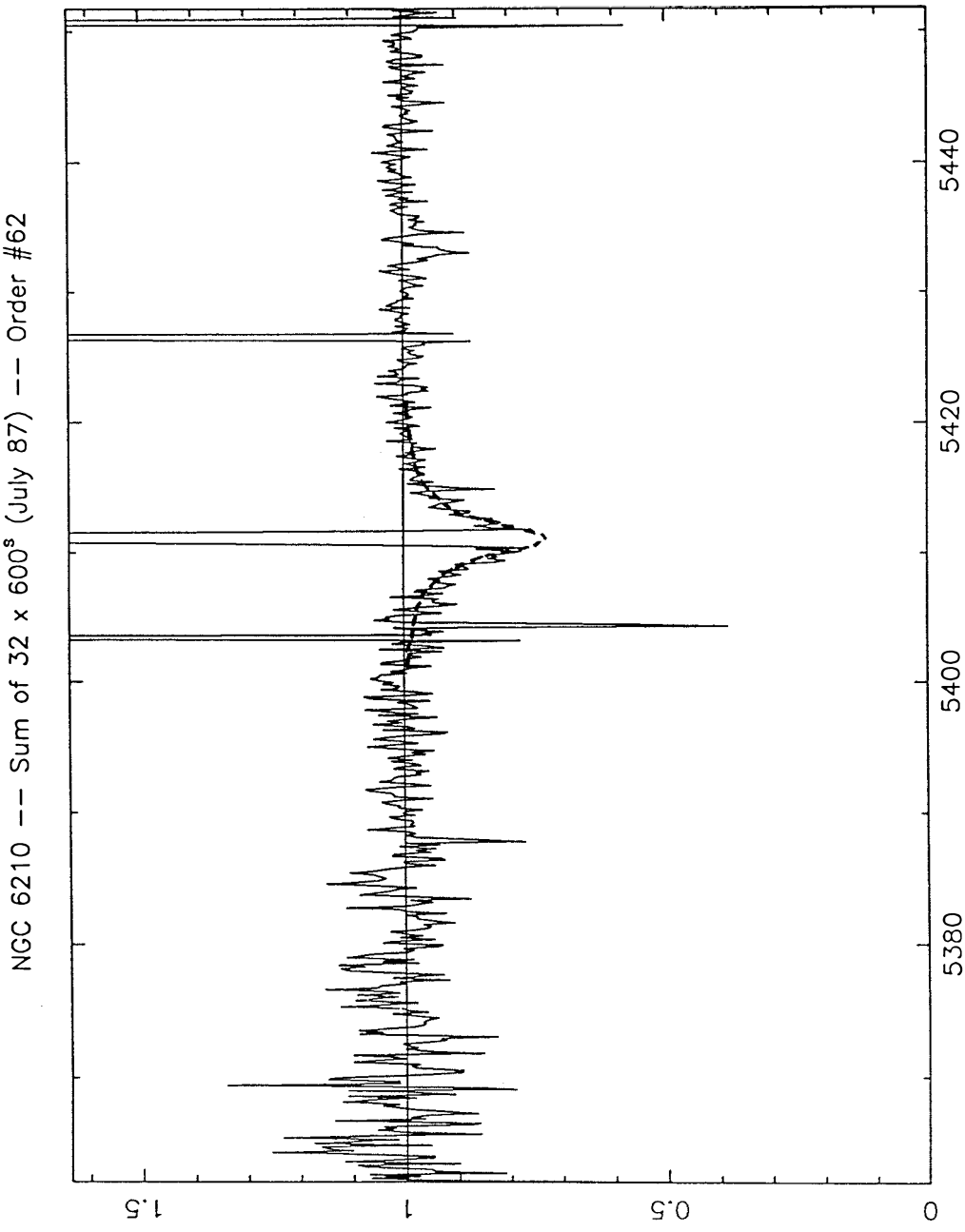

Figure 4-9
(continued)

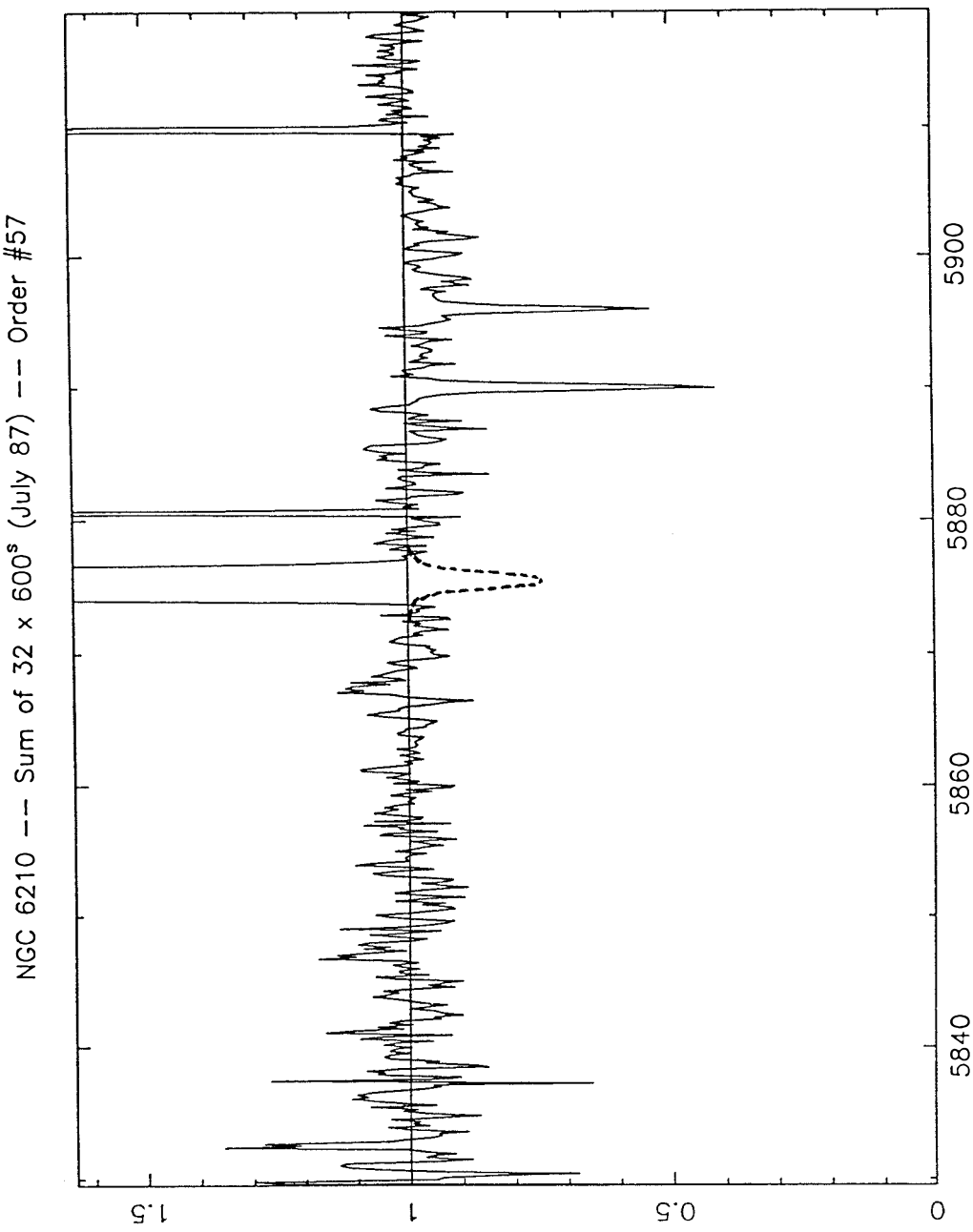

Figure 4-9
(continued)

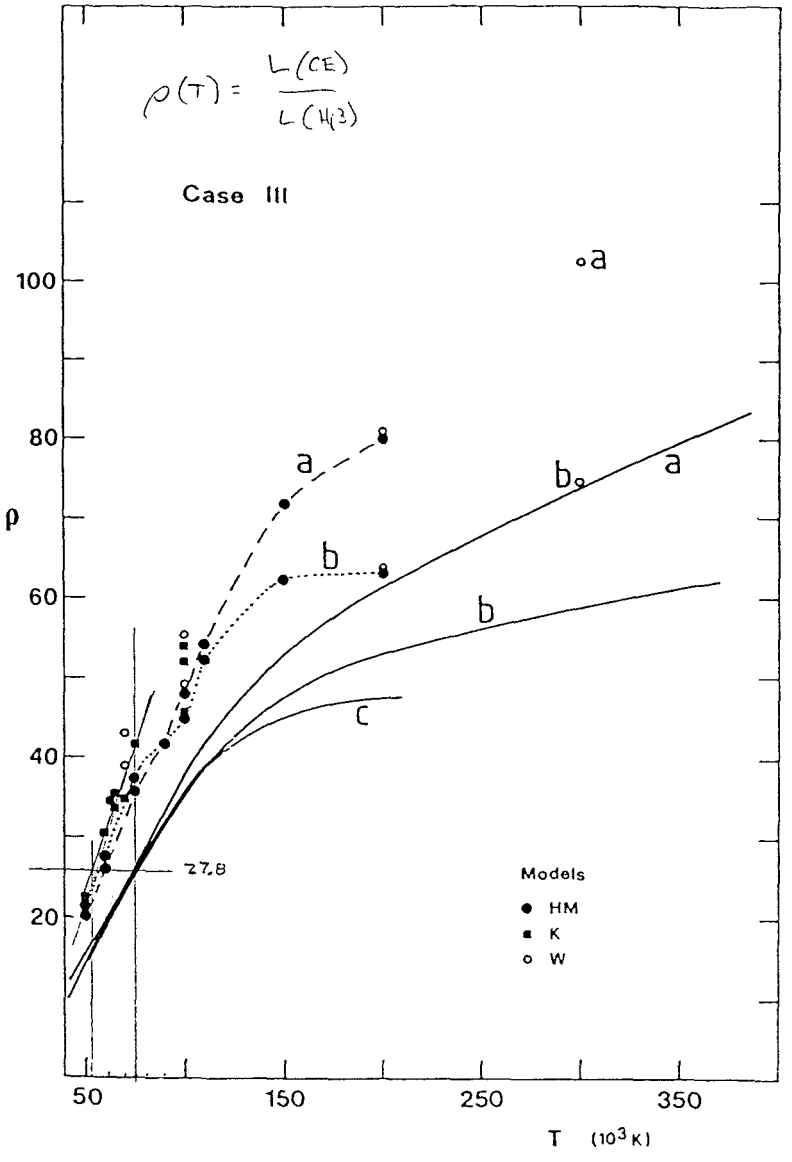

Fig. 3. Same as Fig. 1, with $\varrho(T)$ computed under case III assumptions. Filled circles indicate Hummer and Mihalas (1970) model atmospheres, filled squares Kudritzki (1981) models, open circles Wasemaels (1980) models. The dashed and the dotted lines connect the values of $\varrho(T)$ computed with Hummer and Mihalas models for the sample nebulae (*a*) and (*b*), respectively

Figure 4-10

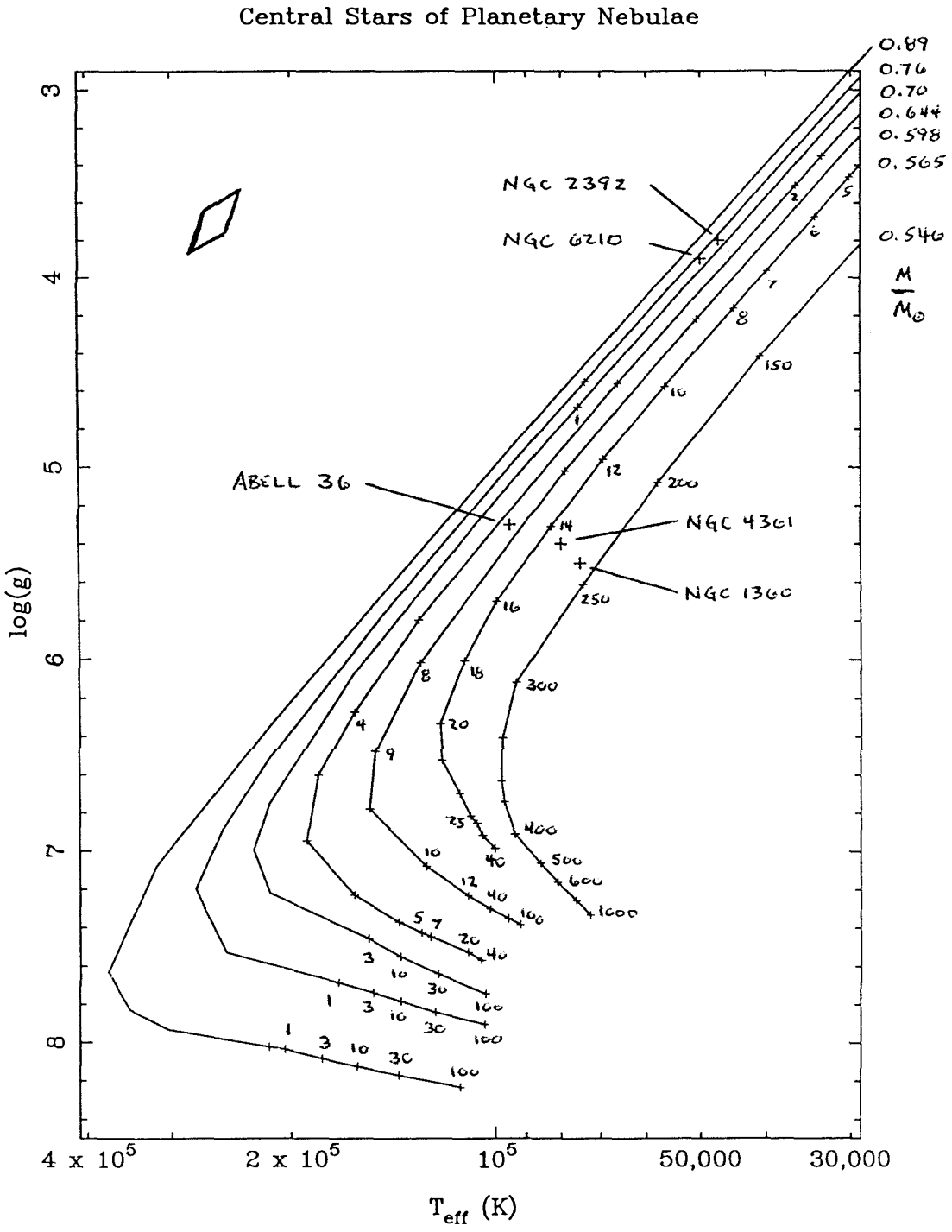
Central Stars of Planetary Nebulae
0.89
0.76
0.70
0.644
0.598
0.565
0.546
M/M⊙
NGC 2392
NGC 6210
ABELL 36
NGC 4361
NGC 1360
log(g)
3
4
5
6
7
8
4 x 10^5
2 x 10^5
10^5
50,000
30,000
T_eff (K)

Figure 4-11

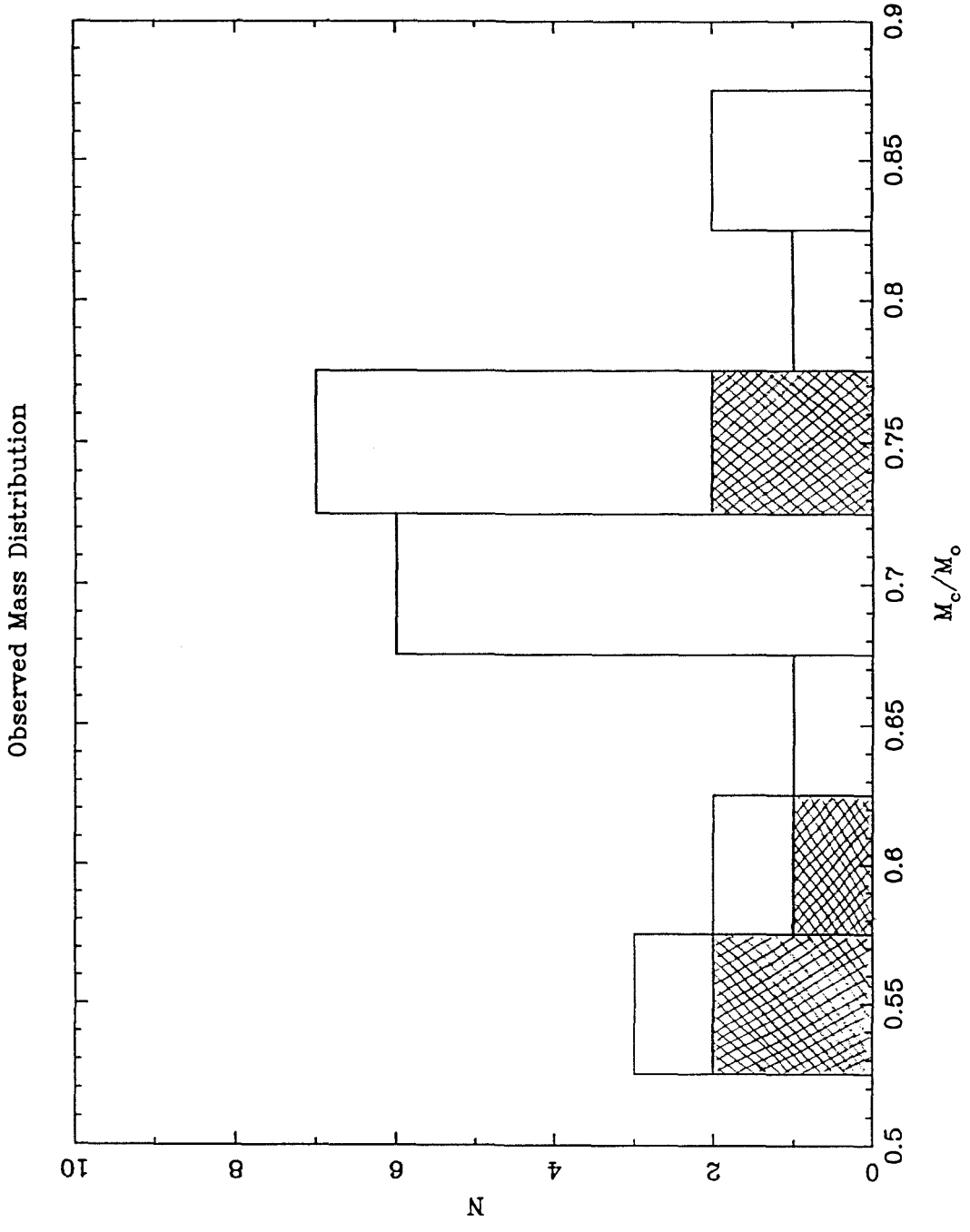
Observed Mass Distribution
N
0
2
4
6
8
10
0.5
0.55
0.6
0.65
0.7
0.75
0.8
0.85
0.9
M_c/M_o

Figure 4-12

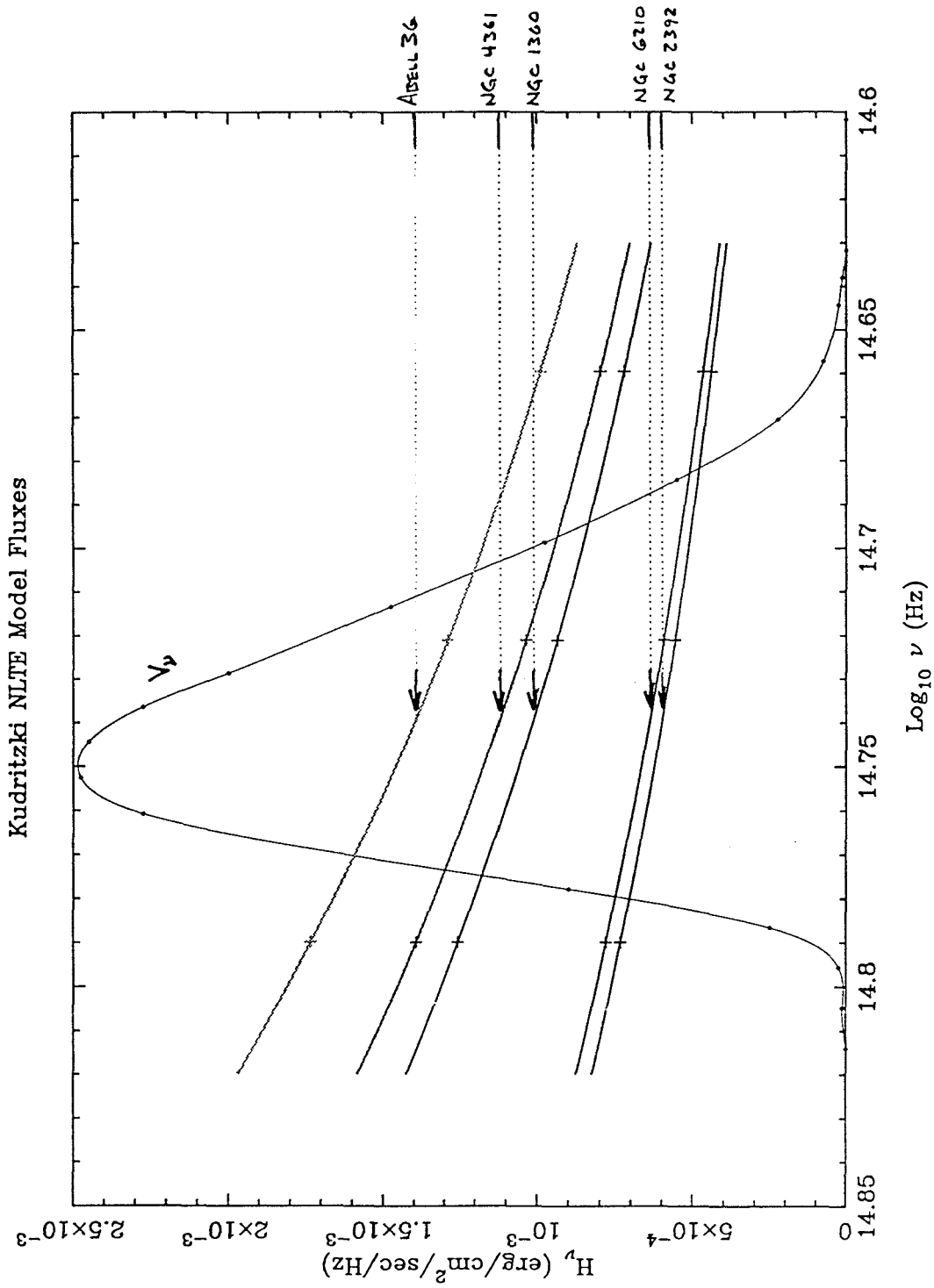
Kudritzki NLTE Model Fluxes
Abell 36
NGC 4361
NGC 1360
NGC 6210
NGC 2392
V_ν
H_ν (erg/cm^2/sec/Hz)
5×10^{-4}
10^{-3}
1.5×10^{-3}
2×10^{-3}
2.5×10^{-3}
0
14.85
14.8
14.75
14.7
14.65
14.6
$\mathrm{Log}_{10}\ \nu$ (Hz)

Figure 4-13

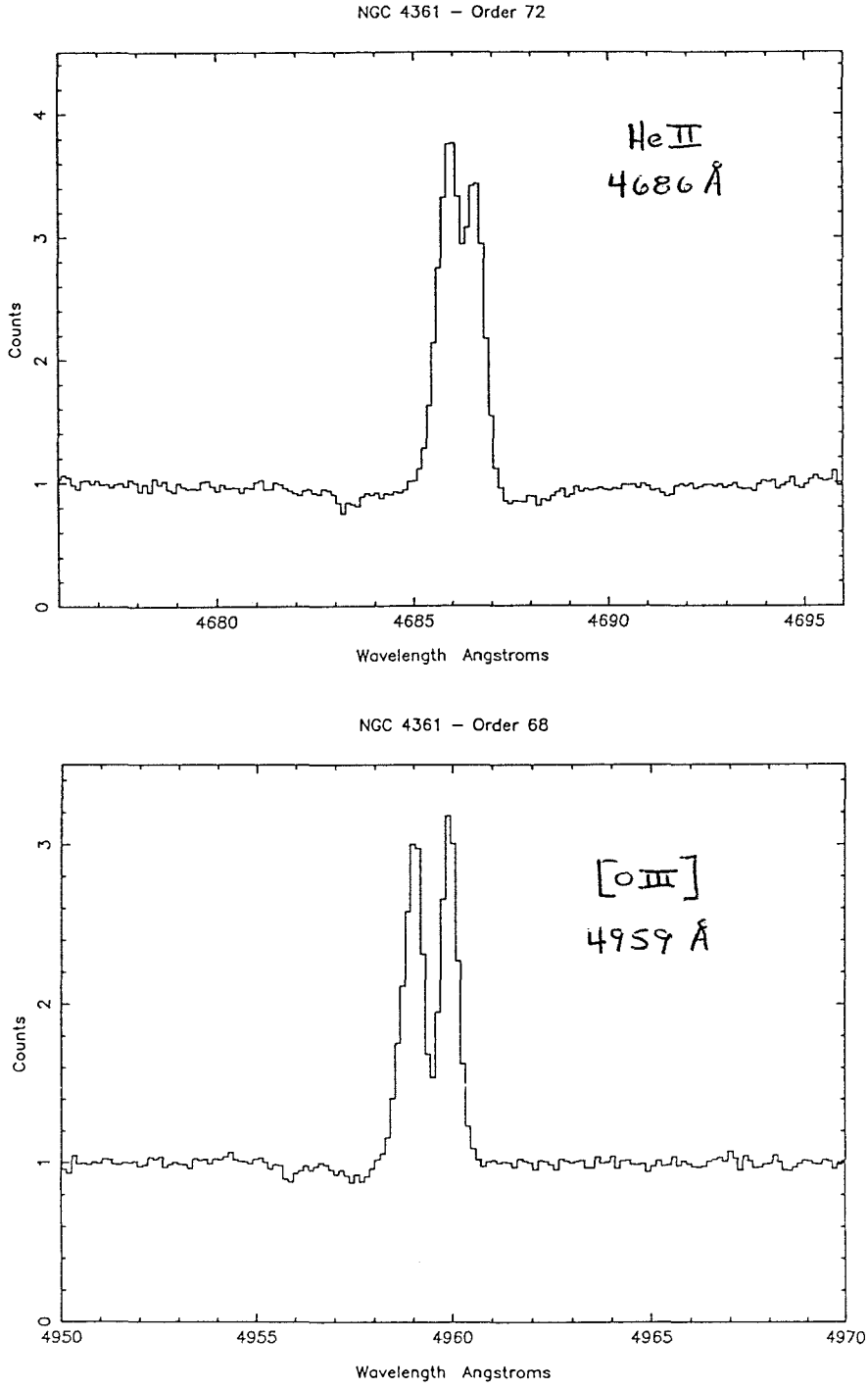
NGC 4361 – Order 72
HeII
4686 Å
Counts
0
1
2
3
4
4680
4685
4690
4695
Wavelength Angstroms
NGC 4361 – Order 68
[OIII]
4959 Å
Counts
0
1
2
3
4950
4955
4960
4965
4970
Wavelength Angstroms

Figure 4-14

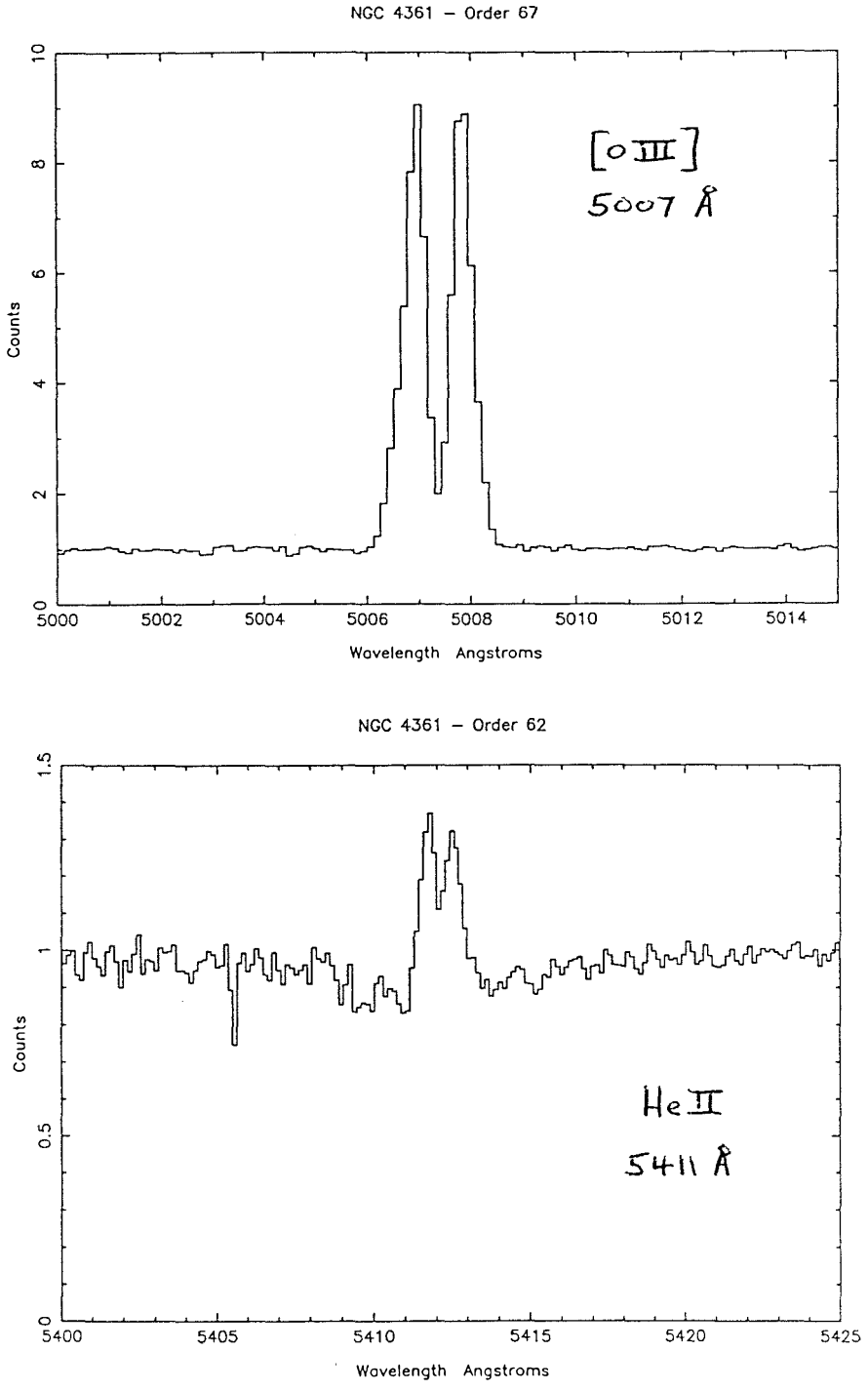

Figure 4-14
(continued)

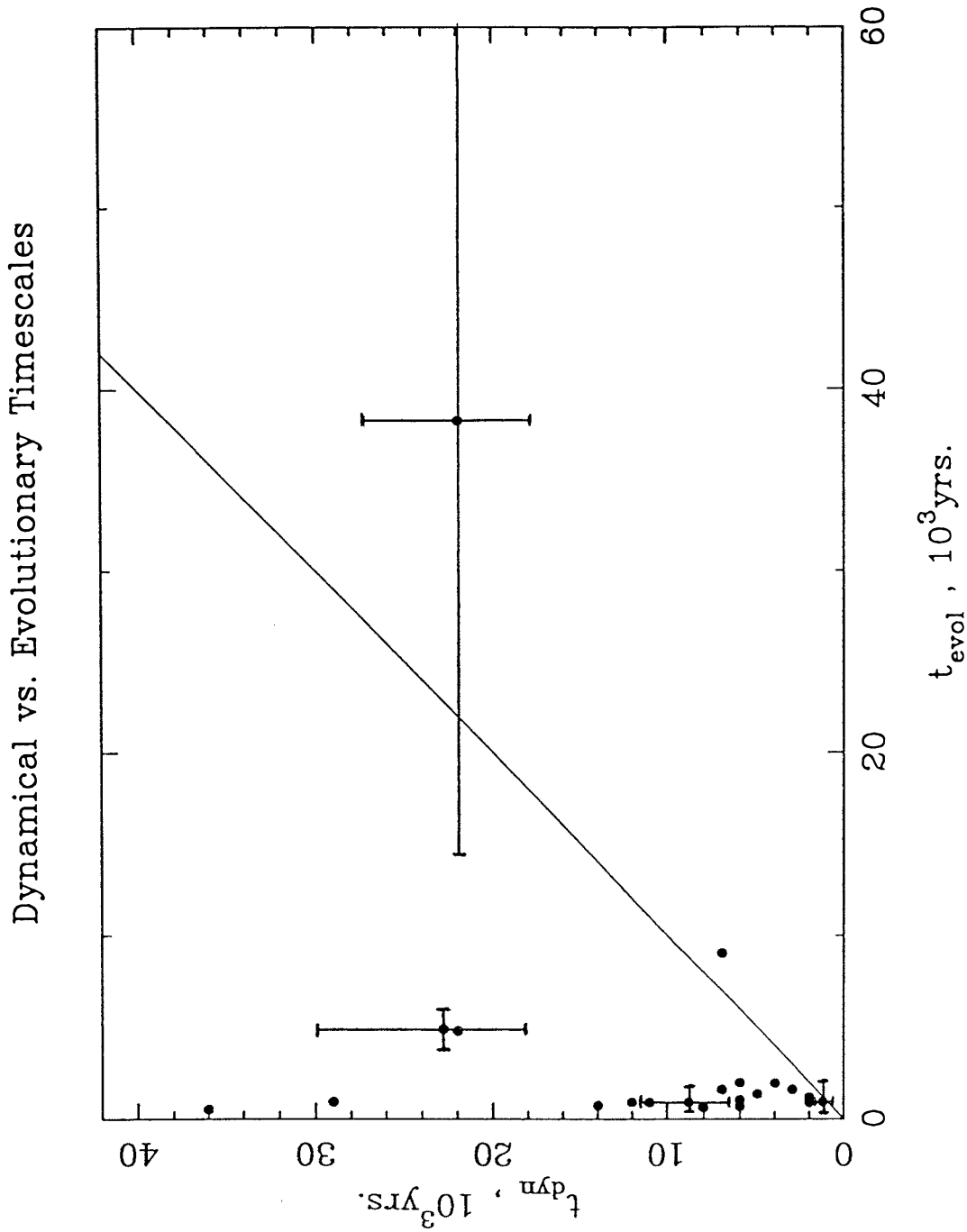
Dynamical vs. Evolutionary Timescales
t_{dyn} , 10^3yrs.
t_{evol} , 10^3yrs.
0
10
20
30
40
0
20
40
60

Figure 4-15

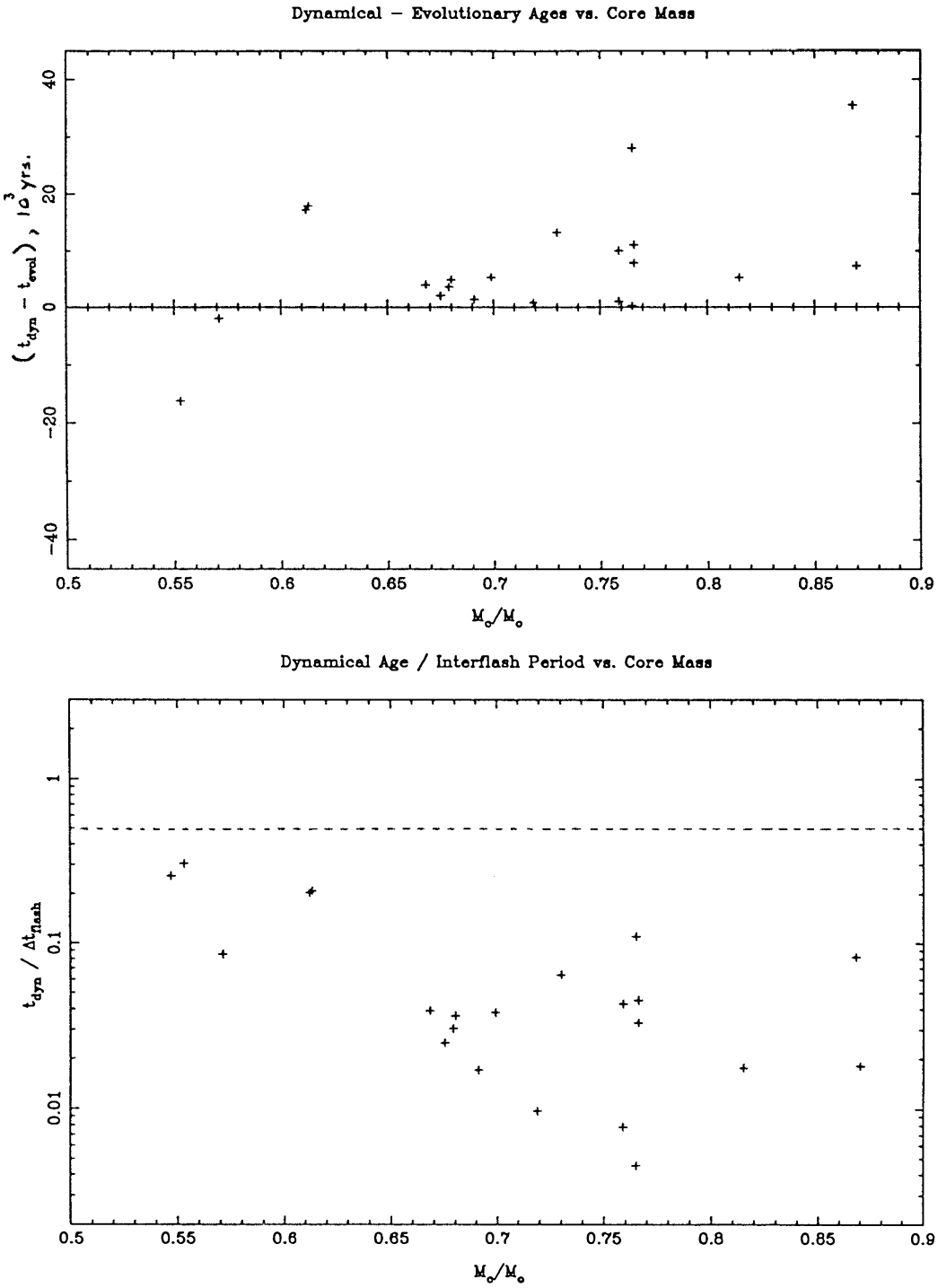
Dynamical – Evolutionary Ages vs. Core Mass
$(t_{dyn} - t_{evol}) \times 10^3$ yrs.
40
20
0
−20
−40
0.5
0.55
0.6
0.65
0.7
0.75
0.8
0.85
0.9
$M_c/M_\odot$
Dynamical Age / Interflash Period vs. Core Mass
$t_{dyn} / \Delta t_{flash}$
1
0.1
0.01
0.5
0.55
0.6
0.65
0.7
0.75
0.8
0.85
0.9
$M_c/M_\odot$

Figure 4-16

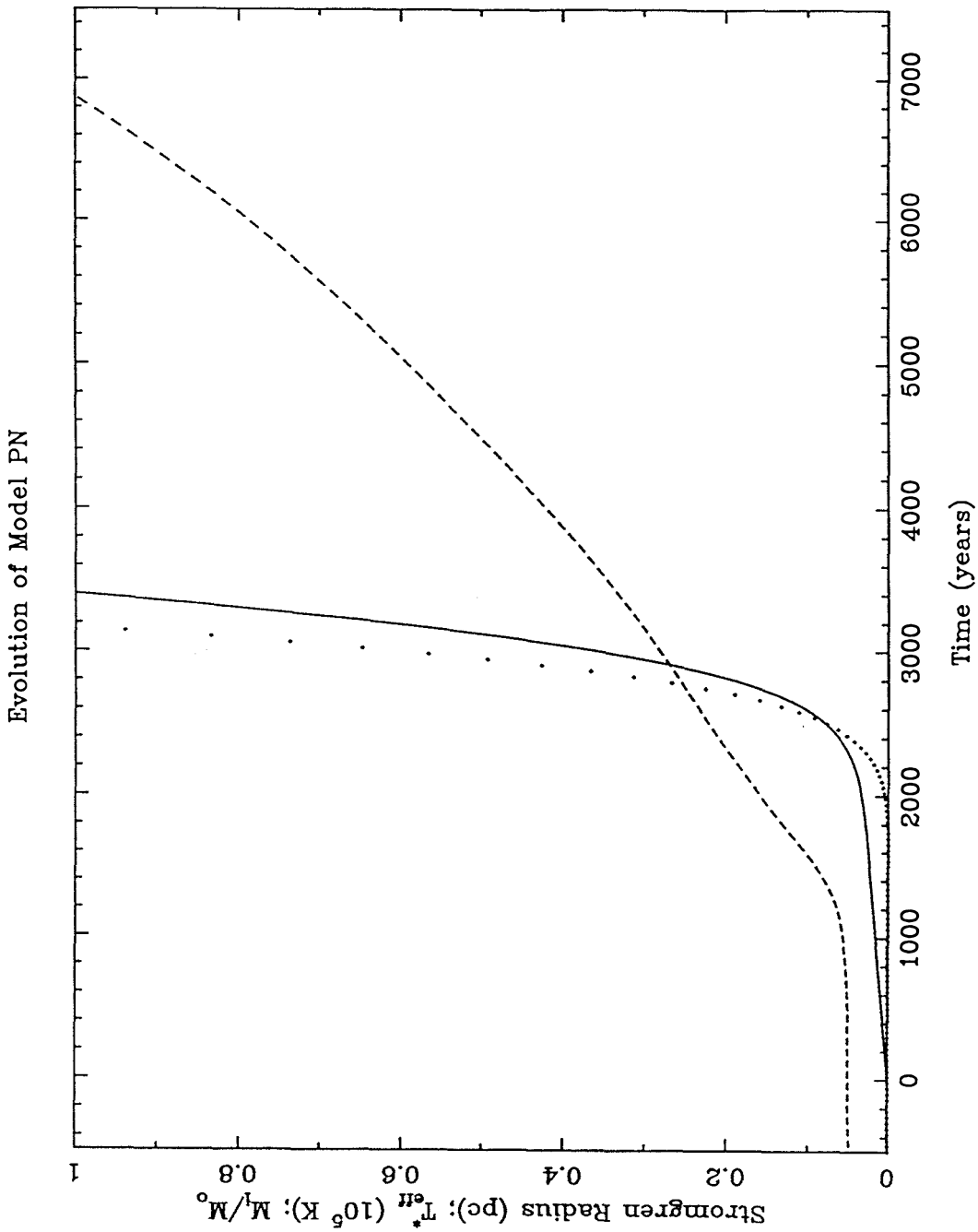
Evolution of Model PN
Time (years)
0
1000
2000
3000
4000
5000
6000
7000
0
0.2
0.4
0.6
0.8
1
Stromgren Radius (pc): T* eff (10^5 K): M_f/M_o

Figure 4-17

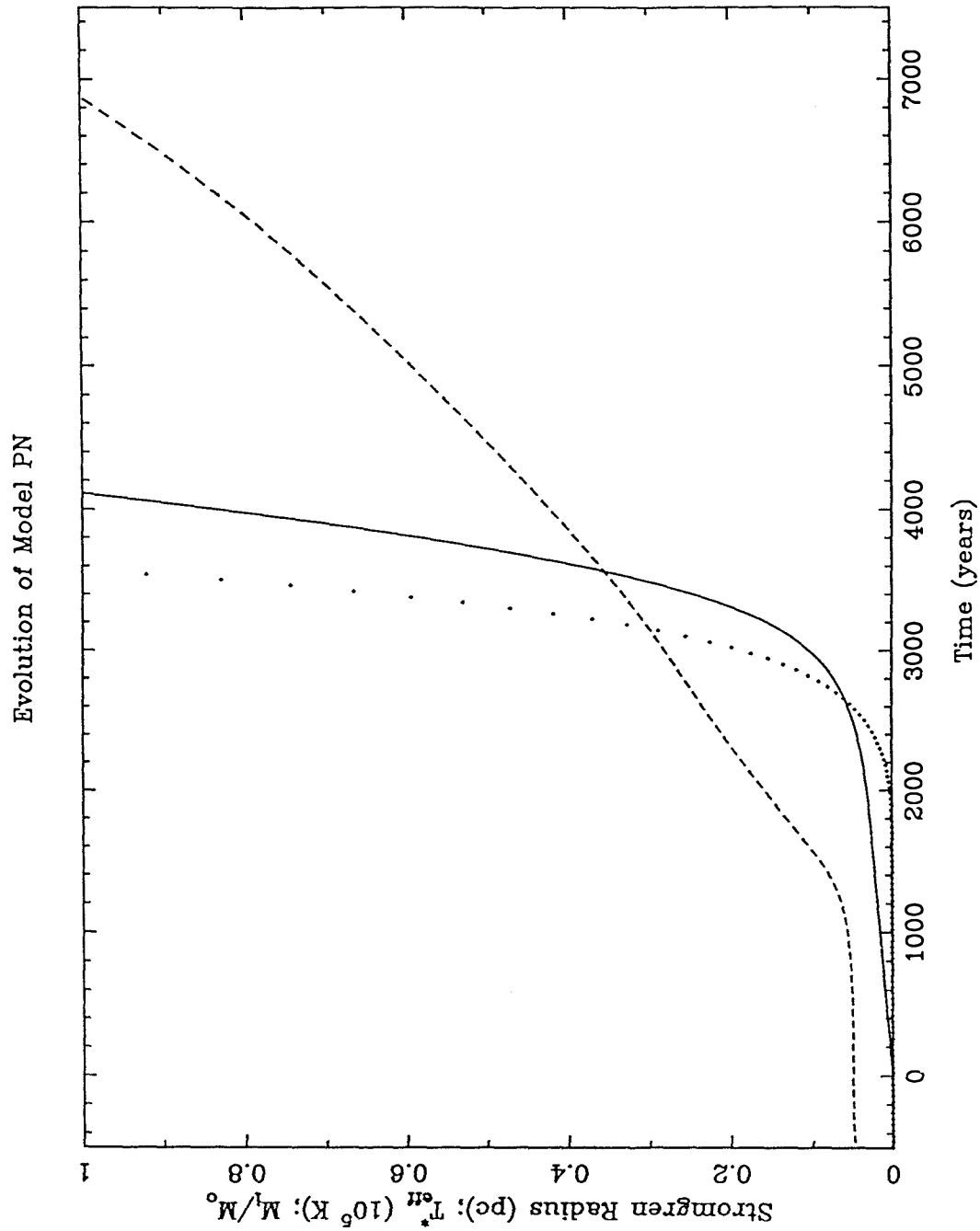
Evolution of Model PN
Time (years)
0
1000
2000
3000
4000
5000
6000
7000
0
0.2
0.4
0.6
0.8
1
Stromgren Radius (pc); T*eff (10^5 K); M1/M⊙

Figure 4-18

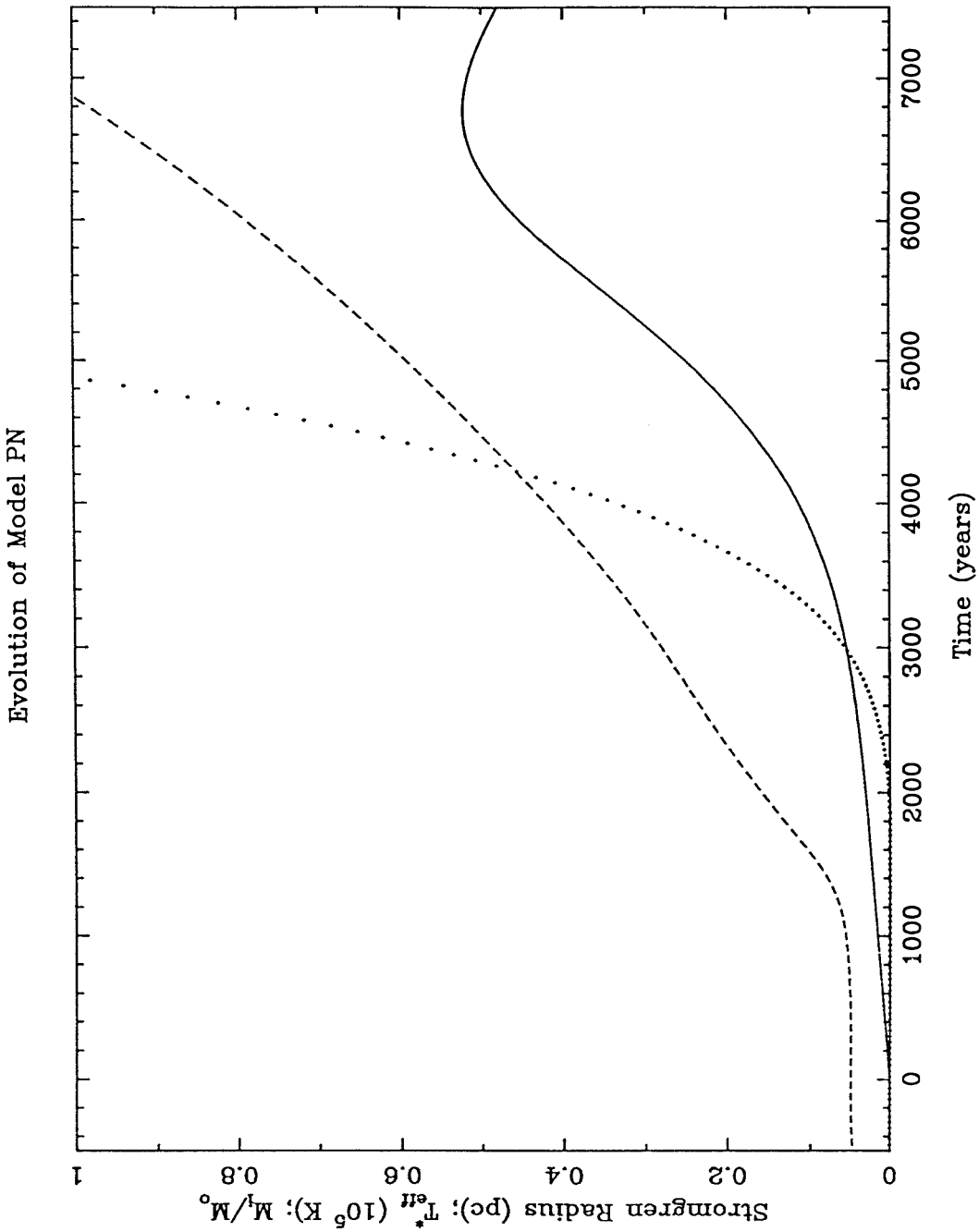
Evolution of Model PN
Stromgren Radius (pc); T^*_{eff} (10^5 K); M_f/M_o
Time (years)
0
0.2
0.4
0.6
0.8
1
0
1000
2000
3000
4000
5000
6000
7000

Figure 4-19

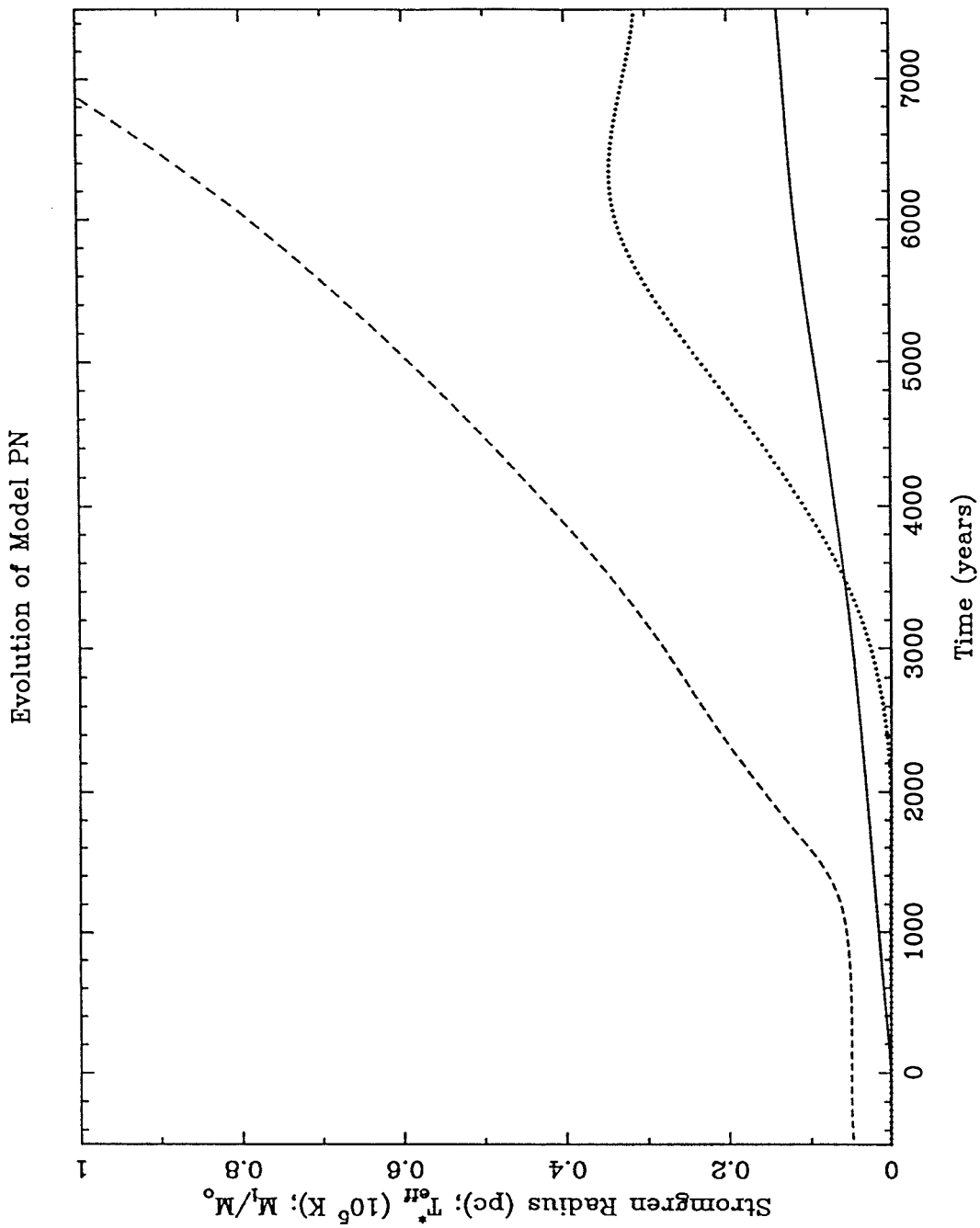
Evolution of Model PN
Stromgren Radius (pc); T*eff (10^5 K); M1/M⊙
0
0.2
0.4
0.6
0.8
1
0
1000
2000
3000
4000
5000
6000
7000
Time (years)

Figure 4-20

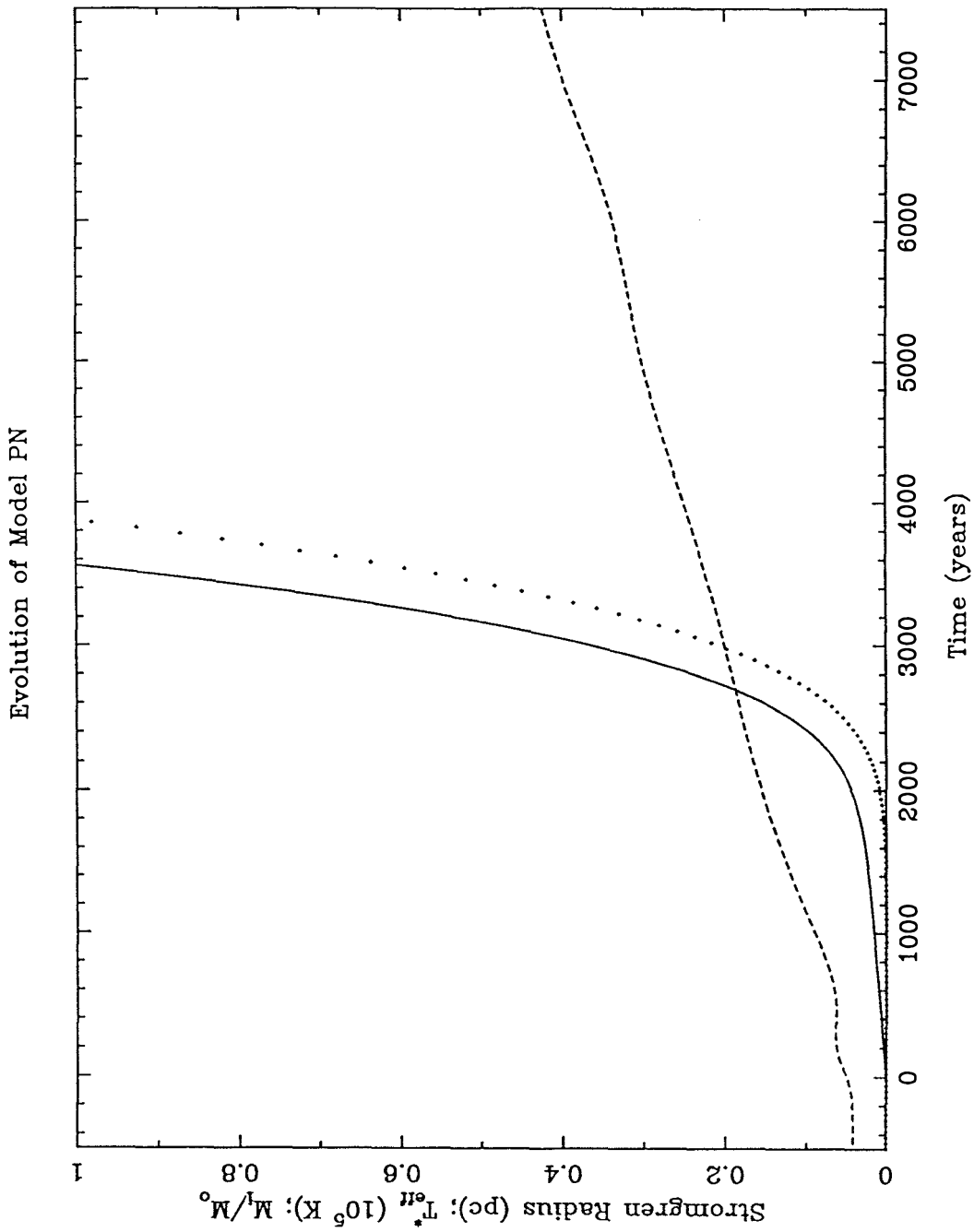
Evolution of Model PN
Stromgren Radius (pc): T^*_{eff} (10^5 K): M_f/M_o
Time (years)
0
0.2
0.4
0.6
0.8
1
0
1000
2000
3000
4000
5000
6000
7000

Figure 4-21

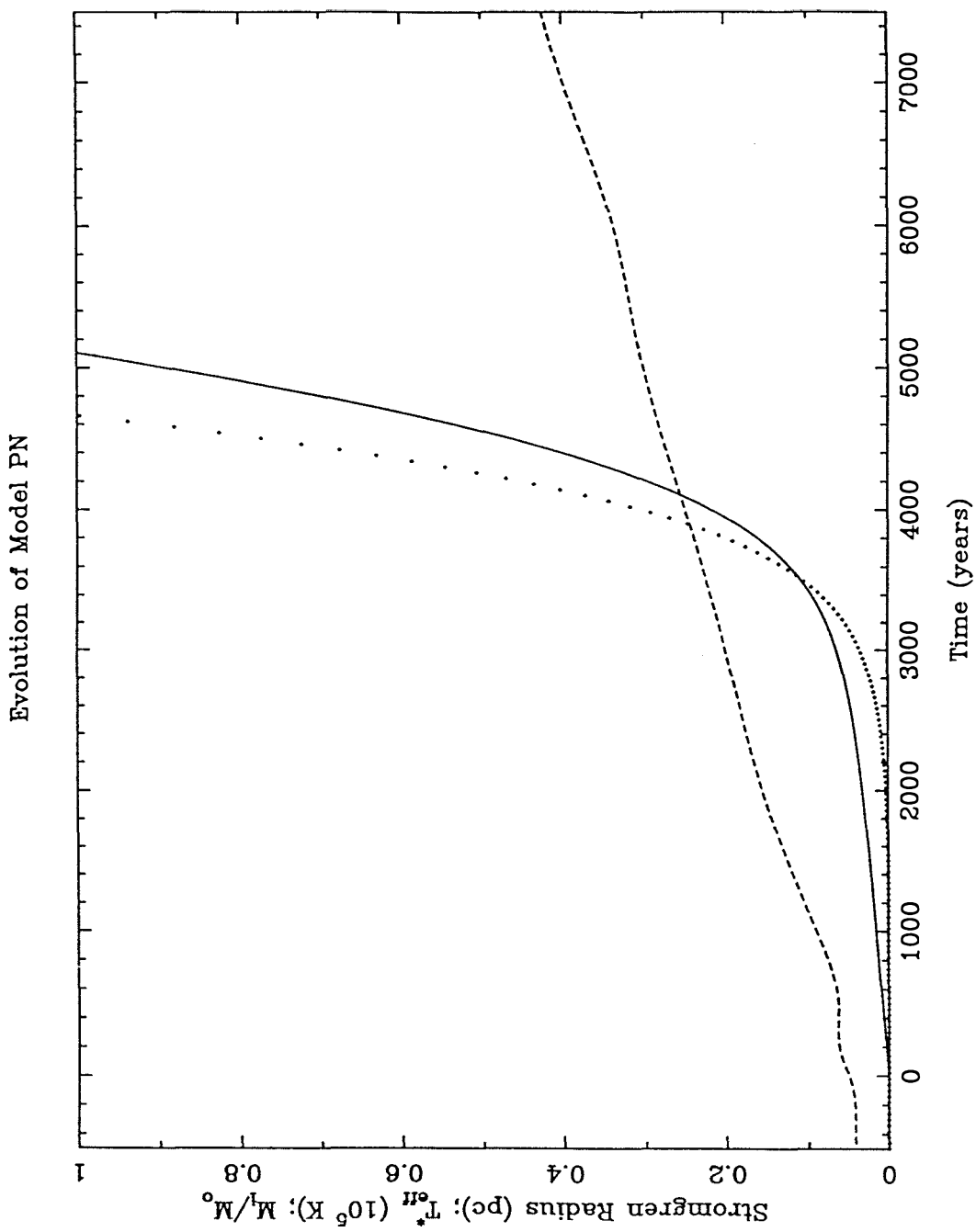
Evolution of Model PN
Stromgren Radius (pc); T^*_{eff} (10^5 K); $M_1/M_\odot$
Time (years)
0
0.2
0.4
0.6
0.8
1
0
1000
2000
3000
4000
5000
6000
7000

Figure 4-22

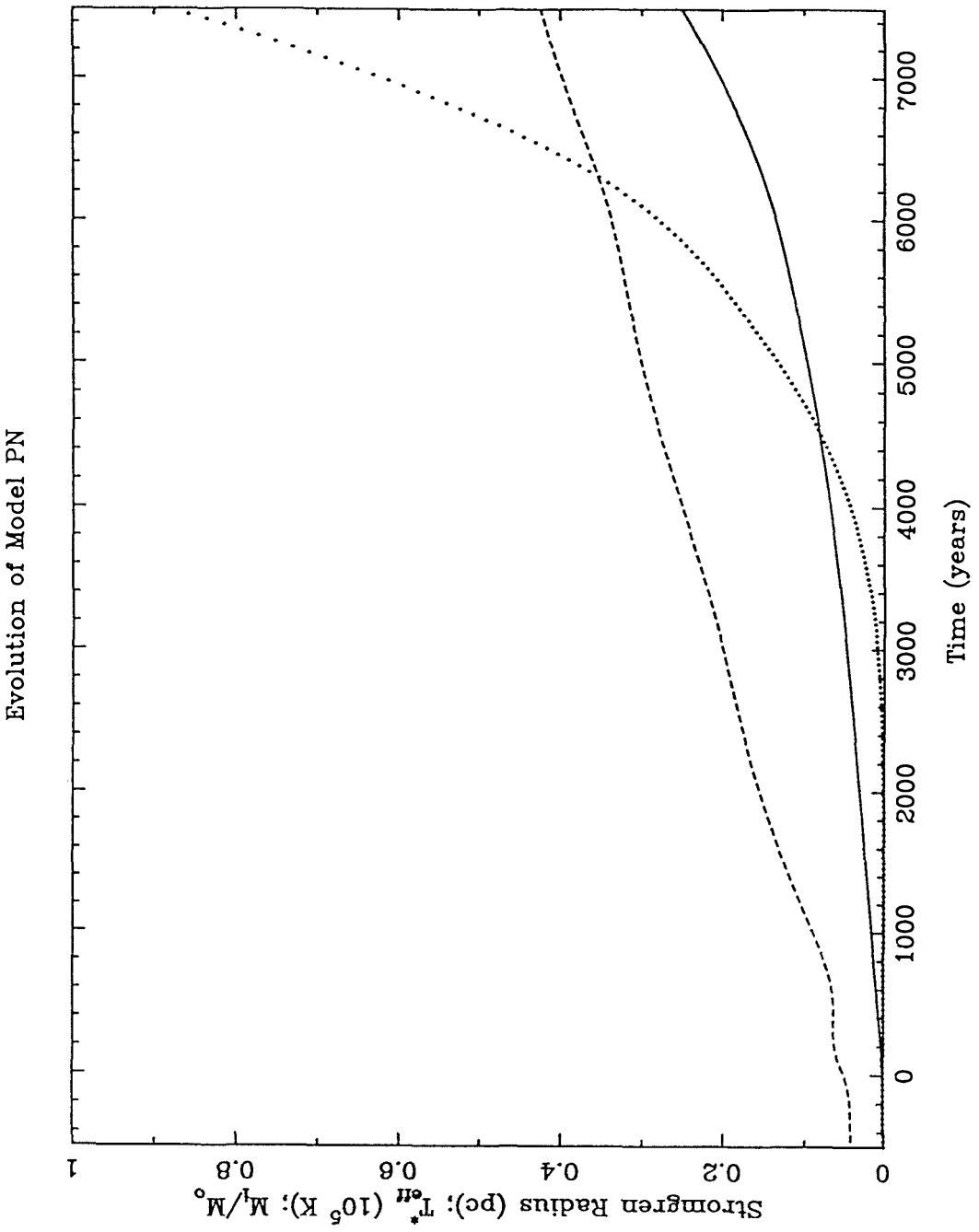
Evolution of Model PN
Time (years)
0
1000
2000
3000
4000
5000
6000
7000
Stromgren Radius (pc); T*eff (10^5 K); M_f/M_o
0
0.2
0.4
0.6
0.8
1

Figure 4-23

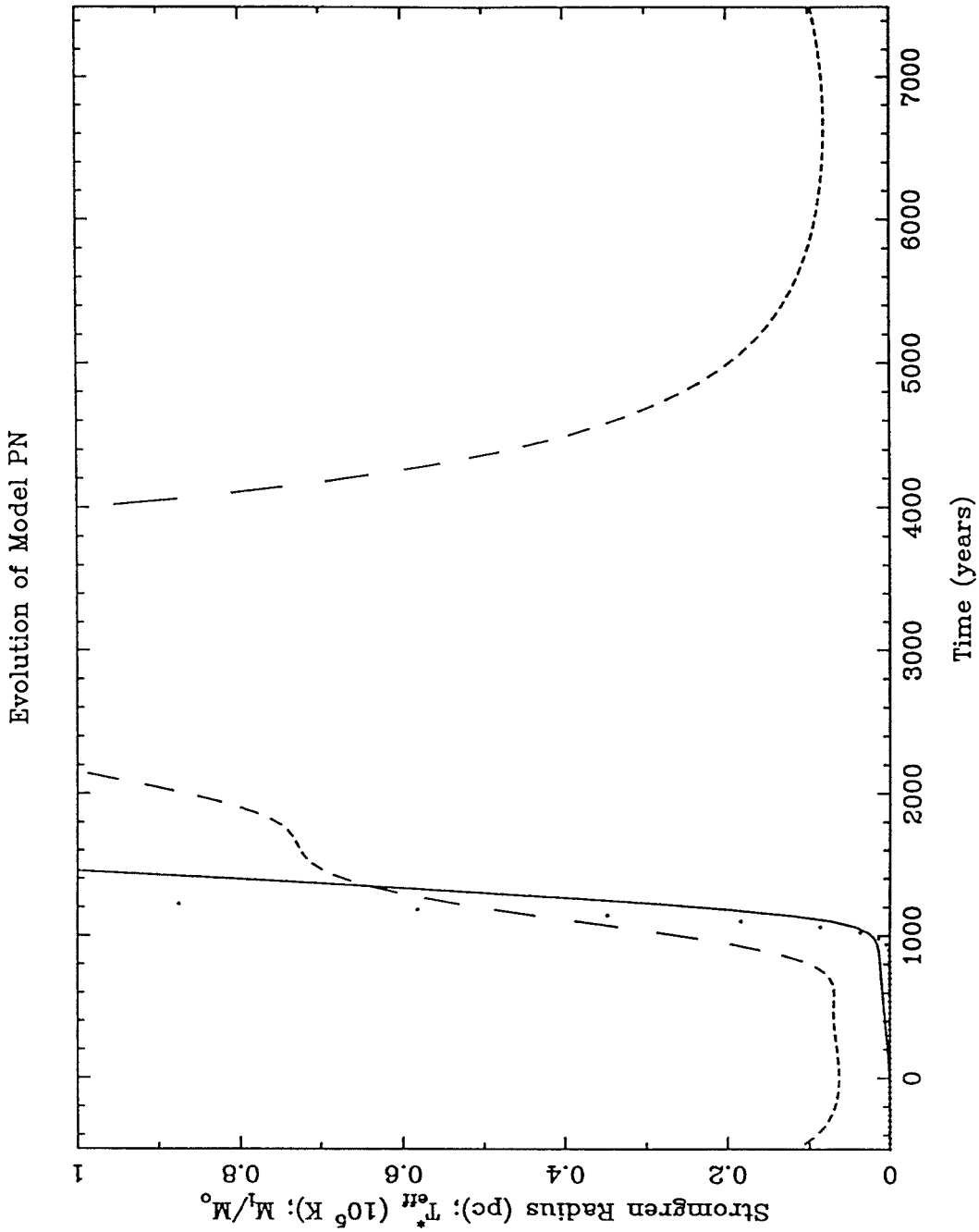
Evolution of Model PN
Time (years)
0
1000
2000
3000
4000
5000
6000
7000
Stromgren Radius (pc): T*eff (10^5 K): Mf/Mo
0
0.2
0.4
0.6
0.8
1

Figure 4-24

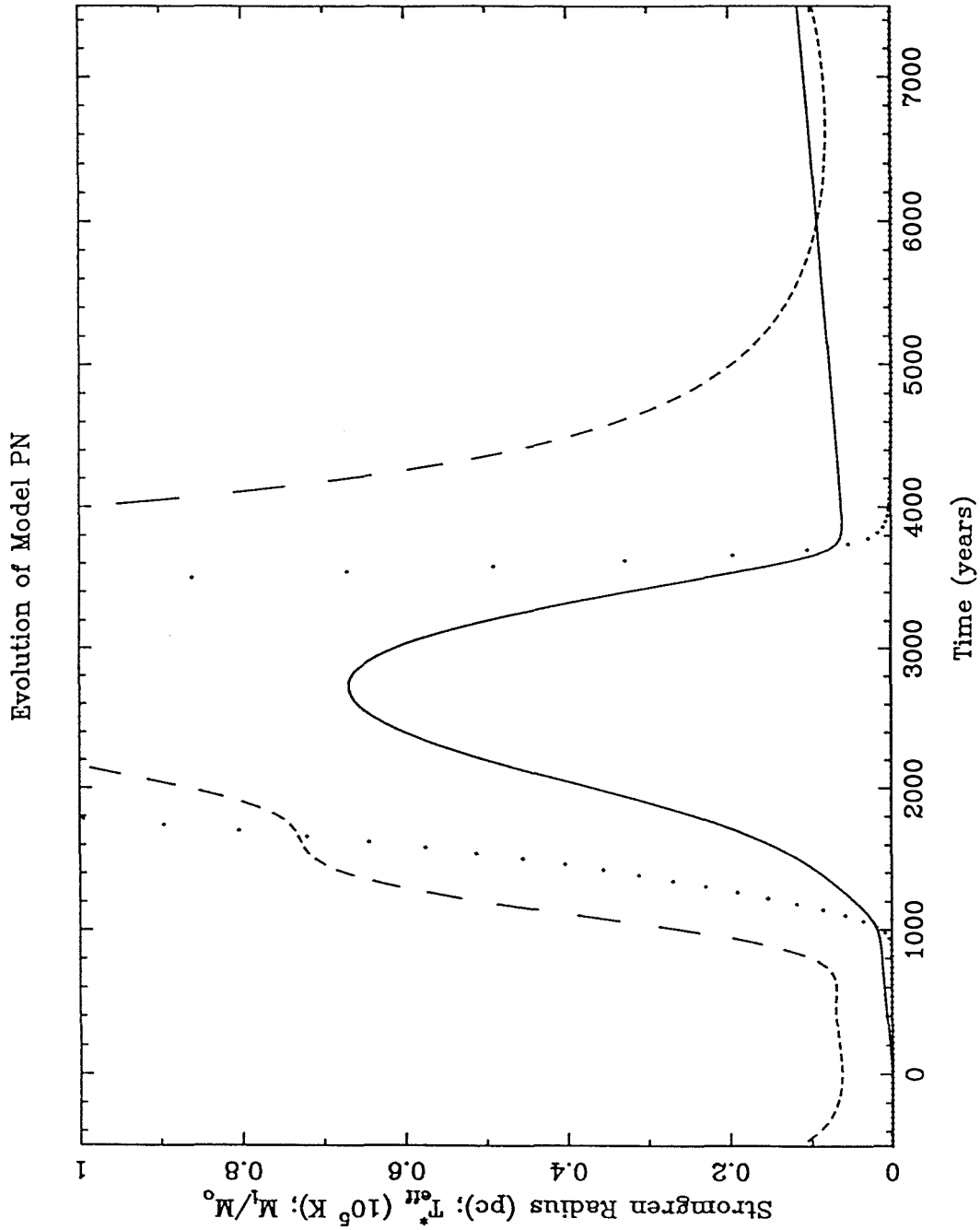
Evolution of Model PN
Stromgren Radius (pc); T^*_{eff} (10^5 K); $M_i/M_\odot$
Time (years)
0
0.2
0.4
0.6
0.8
1
0
1000
2000
3000
4000
5000
6000
7000

Figure 4-25

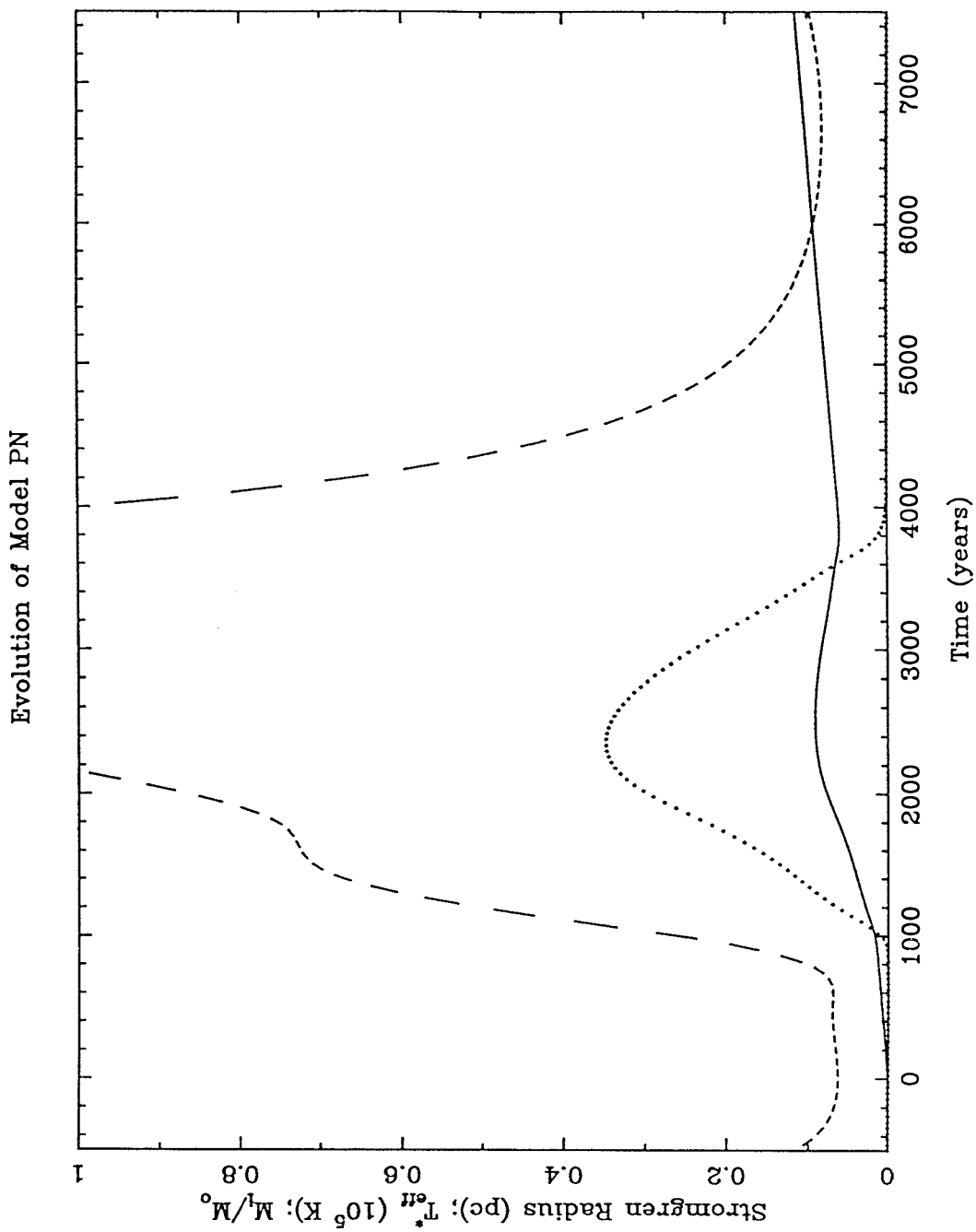
Evolution of Model PN
Time (years)
0
1000
2000
3000
4000
5000
6000
7000
Stromgren Radius (pc); T^*_{eff} (10^5 K); $M_l/M_\odot$
0
0.2
0.4
0.6
0.8
1

Figure 4-26

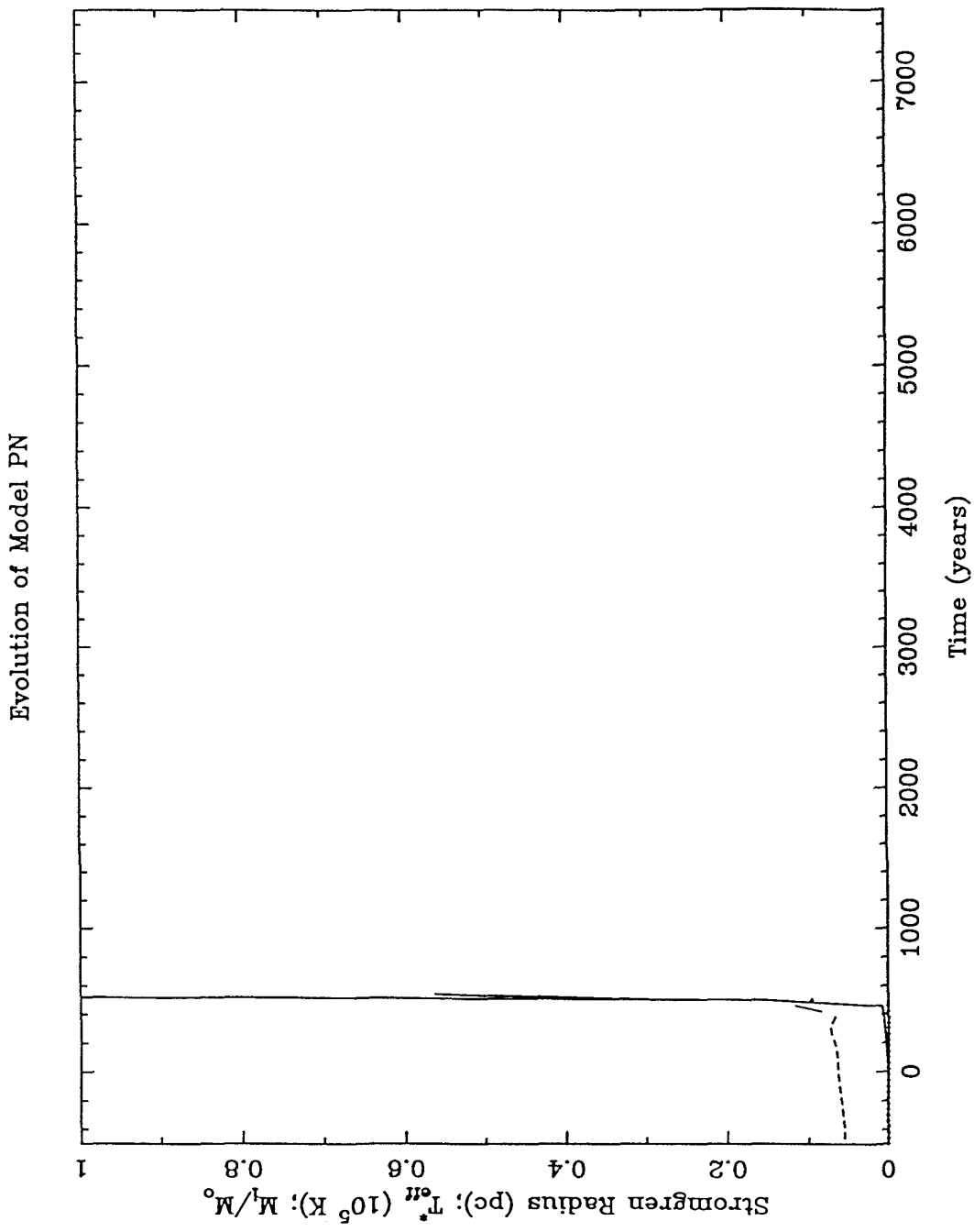
Evolution of Model PN
Time (years)
0
1000
2000
3000
4000
5000
6000
7000
0
0.2
0.4
0.6
0.8
1
Stromgren Radius (pc); T*eff (10^5 K); Mi/M⊙

Figure 4-27

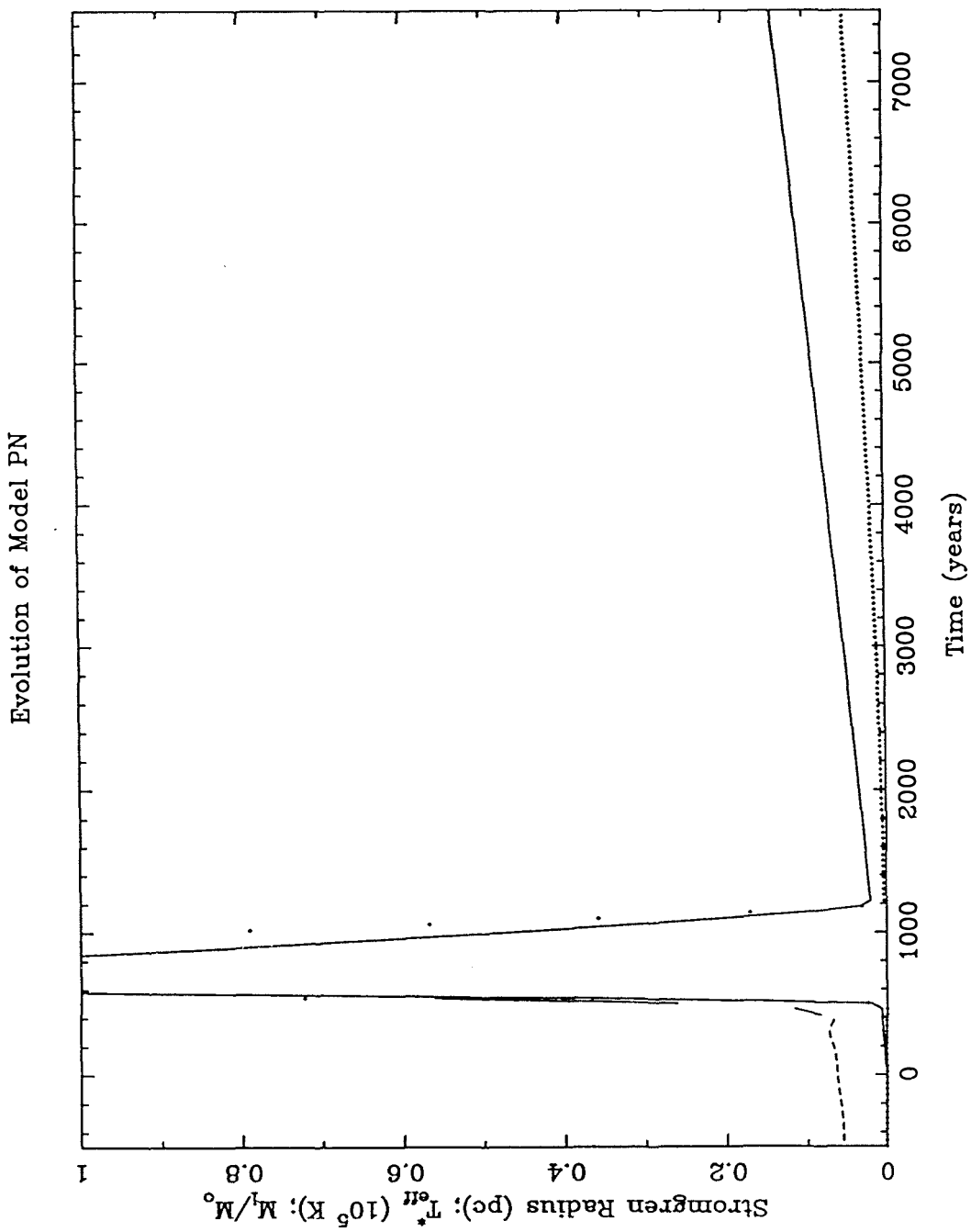
Evolution of Model PN
Stromgren Radius (pc); T^*_{eff} (10^5 K); $M_1/M_\odot$
0
0.2
0.4
0.6
0.8
1
0
1000
2000
3000
4000
5000
6000
7000
Time (years)

Figure 4-28

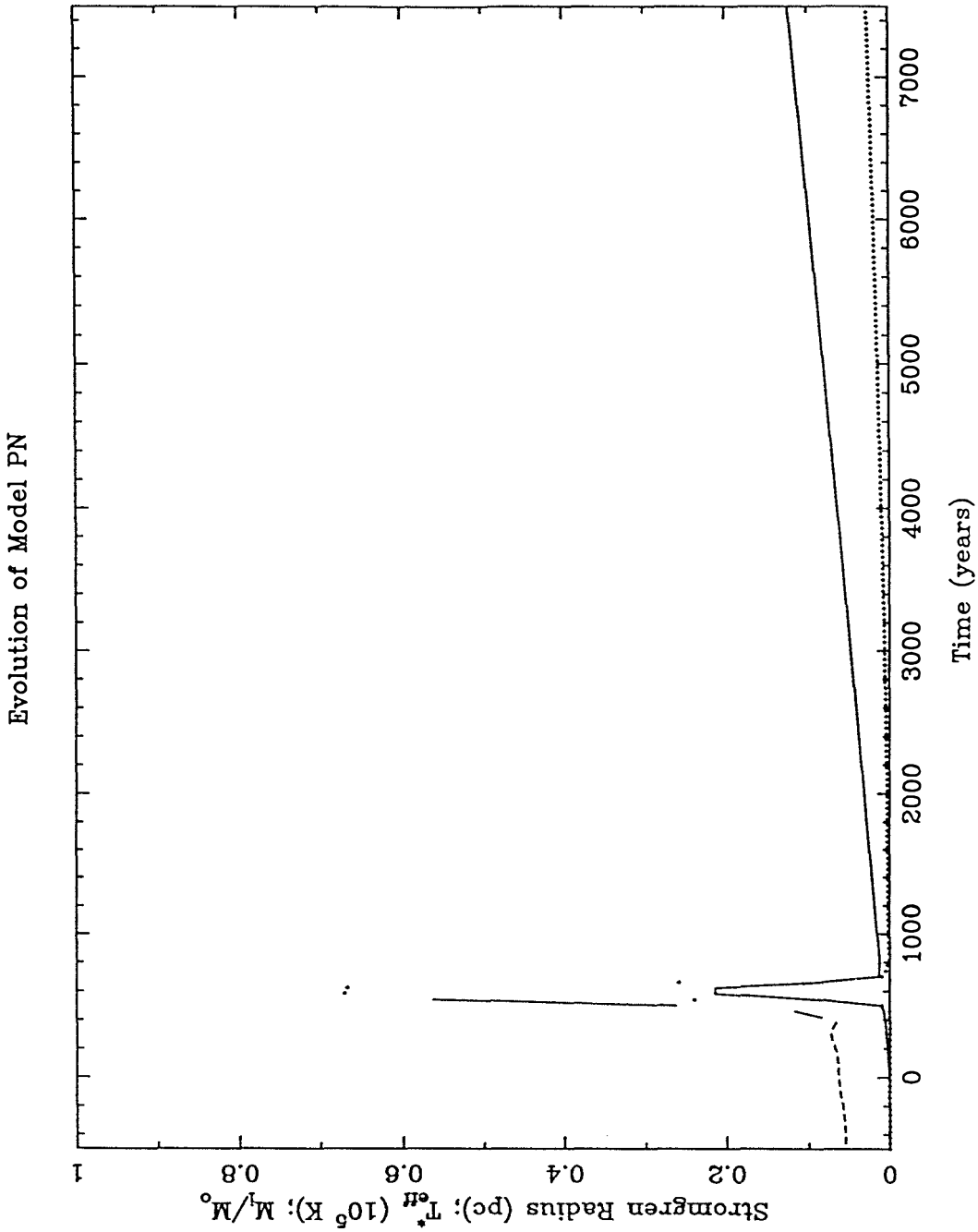
Evolution of Model PN
Stromgren Radius (pc); T*eff (10^5 K); Mf/Mo
Time (years)
0
0.2
0.4
0.6
0.8
1
0
1000
2000
3000
4000
5000
6000
7000

Figure 4-29

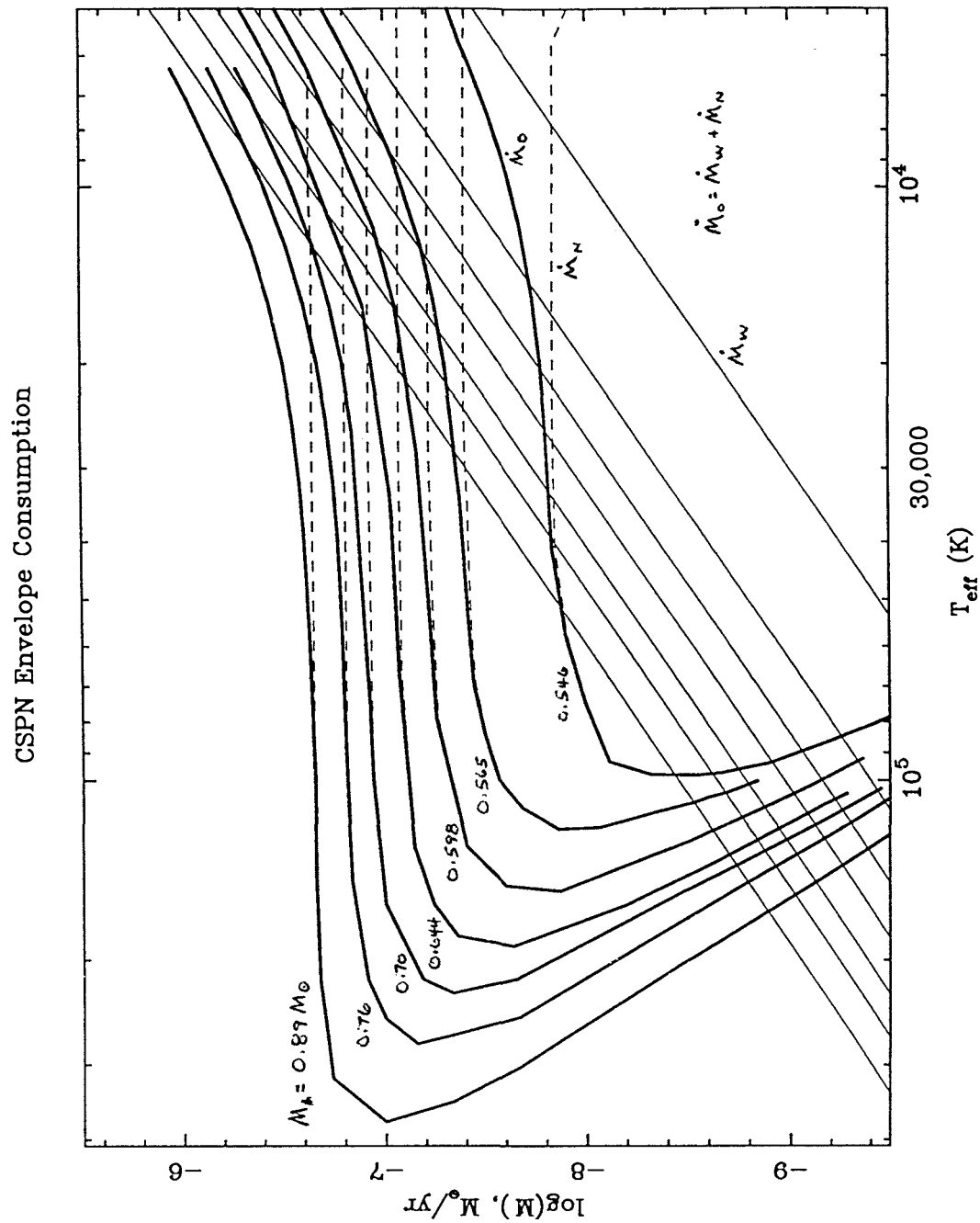
CSPN Envelope Consumption
log(Ṁ), M⊙/yr
−6
−7
−8
−9
10^5
10^4
30,000
T_{eff} (K)
$M_* = 0.89\,M_\odot$
0.76
0.70
0.644
0.598
0.565
0.546
$\dot{M}_o$
$\dot{M}_N$
$\dot{M}_w$
$\dot{M}_o = \dot{M}_w + \dot{M}_N$

Figure 4-30

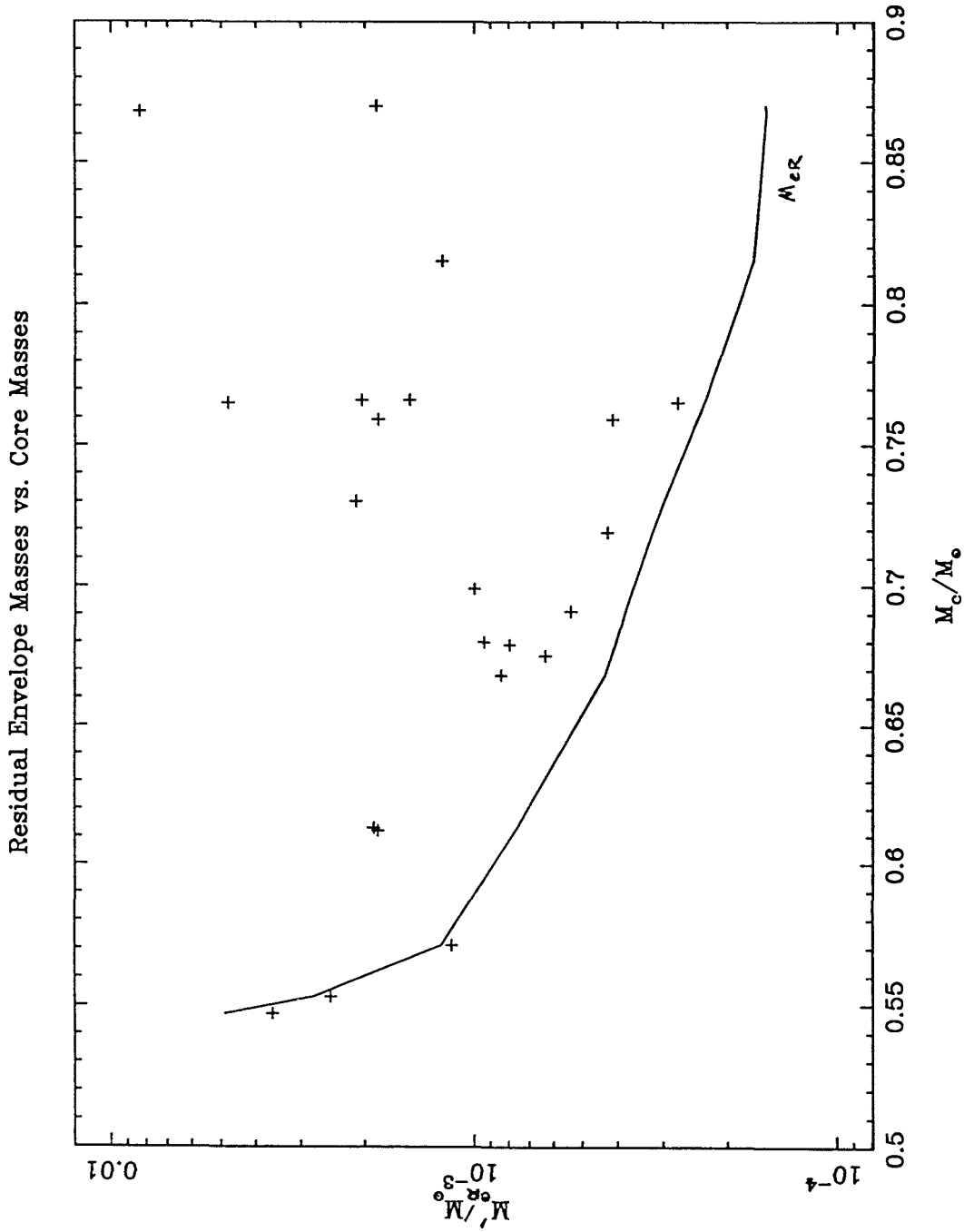
Residual Envelope Masses vs. Core Masses
M_{ER}
$M'_{OR}/M_\odot$
$M_c/M_\odot$
0.01
10^{-3}
10^{-4}
0.5
0.55
0.6
0.65
0.7
0.75
0.8
0.85
0.9

Figure 4-31

V. Future Work

A. The P60 Echelle Spectrograph

The most serious deficiency associated with the P60 Echelle Spectrograph at present is the lack of blue flat field light. Recall from §**III.C** above the considerable problems this caused for wavelengths shorter than 4500 Ångstroms, where division by the flat field exposure failed to remove the shape of the echelle blaze function from the raw counts, and this task fell upon the interactive mode of the reduction routine ECHXCONT. The problem has its origins in the fact that the spectrograph mounting base contains but a single incandescent flat field bulb with a spectrum that reaches a maximum longward of 7000 Ångstroms. Figure 5-1 shows a cross-section through a typical flat field exposure in the cross dispersion direction.

The solution is to use not one flat field lamp, but two, each with a color balancing filter in front of it. This arrangement would then be similar to that used in the 100-inch Dupont telescope echelle spectrograph, where the problems caused by only one unfiltered lamp would have been even more severe due to the limited dynamic range of the two-dimensional photon counting detector. Figure 5-2 shows one possible two lamp and two filter solution, using Schott filters UG 1 to provide light in the blue and BG 18 to better balance the light in the red. Note that the far red leak of the UG 1 filter will be important, and so a dichroic filter may have to be placed in front of it to divert all light with $\lambda > 5000$ Å out of the beam path.

A somewhat related problem has to do with the present lack of an adequate wavelength calibration arc lamp in the spectrograph mounting base. The temporary solution used to date has been to take a Th-Ar arc exposure at the beginning and end of each observing run, with the echelle spectrograph separated from the telescope and the Th-Ar bulb held above the slit of the spectrograph. The internal He, Ne,

Ar, and Hg lamps were then used during the run to monitor the zero-point shifts from the Th-Ar exposure caused by flexure as the telescope was moved away from the zenith (refer to Table 2-8 above).

The relatively large size of the Th-Ar lamp, 1.5 inches diameter × 6.0 inches long, prevents it from being incorporated into the existing spectrograph mounting base comparison lamp housing. Therefore the solution proposed is to build an auxiliary lamp housing to hold not only the Th-Ar lamp but also the two lamp two filter flat field combination, and to transmit the light of these two sources into the existing mounting base via fiber optic cables. Quartz fiber optics and condensing lenses are required in order to transmit this light down to the echelle spectrograph's 3200 Ångstrom short wavelength limit.

A third troublesome area in need of future work is the relay optics of the spectrograph mounting base T.V. guider. This optical path was diverted 90 degrees when the echelle spectrograph was mated to the telescope, and the quality and focal length of its relay lens was improved to better match the RCA CCD guider camera in use at the time. However, two problems remain as a result of this modification: (1) there is more than an acceptable amount of flexure in the guider optical system, caused either by movement of the relay lens or the heavy Quantex camera now used in place of the RCA CCD; (2) the change in focal length of the relay lens made to match the RCA CCD camera has caused a severe mismatch in image size when the Quantex camera is used in its place. This situation has been somewhat improved by the use of a 35mm photographer's "2x Teleconverter" placed behind the T.V. guider zoom lens, which doubles the magnification of the slit image in the T.V. guider. A better, more efficient solution, however, must await the final decision of which T.V. guider camera will be chosen as the long-term solution at the P60.

A fourth improvement to the observing conditions with the P60 echelle spectro-

graph at present would be to individually balance both the echelle spectrograph and the spectrograph mounting base around the optical axis of the telescope. This could be quite easily accomplished with the help of a few appropriate counterweights, and would greatly ease the task of rotating the instrument — usually necessary several times during the night in order to align the spectrograph slit with the direction of atmospheric dispersion — with the telescope pointed away from the zenith. It would also offer the added benefit that the telescope balance done with the spectrograph at one rotation would not be affected by later change to a different rotation; currently the compromise made in practice is to balance the telescope with the spectrograph slit North/South, since most observations are made at or near the meridian with a slit orientation not very different from N/S.

As far as the echelle spectrograph itself is concerned, performance of its internal optical and mechanical components has been equal to or better than the design objectives (see §**II.A** and §**II.D**), so no major design revisions are anticipated at this time. The only changes made to the echelle spectrograph itself since it was first assembled in August of 1986 have been: (1) the CCD sensor was moved forward slightly inside the Dewar in order to bring the images into focus; (2) the electronic interconnections between the shutter and rotating slit wheel mechanisms were re-designed due to space limitations; and (3) the manner in which the CCD Dewar bolts onto the spectrograph was re-designed to allow this to be done completely from the outside of the instrument. There are, however, two outstanding items which were part of the original design conception of the instrument but have as yet not been accomplished and therefore come under the heading of "future work." The first of these is relatively straightforward: namely, grinding smooth all external sharp or rough edges, anodizing the entire welded aluminum framework of the spectrograph, and painting its exterior surfaces. This work has been delayed until after the second item of unfinished work is done: implementing the low resolution,

long slit mode.

The low resolution, long slit mode is possible as a consequence of the fact that two cross-dispersing prisms are used, one prior to and one following the echelle grating. Were these two prisms each removed from the beam path (in practice, rotated out of the way), the collimator and camera optical axes would intersect alongside the echelle grating. It is at this new point of intersection (point "G" in Figure 2-2) that a low resolution, single order, "ordinary" diffraction grating can be placed and the highly efficient spectrograph optics and CCD9 used in the "low resolution, long slit mode."

The plan for implementing this new mode calls for a mounting flange and socket to be built for the rotating 3 × 3 inch grating mount from the existing P60 low resolution spectrograph (Figure 5-3). Note, however, that the reversed sense of camera and collimator directions will require that each of the gratings to be used with the P60 echelle spectrograph in this mode will have to be rotated 180 degrees in its cell in order to have the correct blaze direction. Finally, the cross-dispersing prisms mount is already equipped with spindles and bearings for the rotation required to move these prisms out of the way, but the spindle emerging from the bottom of the spectrograph housing presently lacks a crank, worm, and worm gear to manually accomplish this movement. A worm and worm gear is the transmission of choice since its low gear ratio will prevent even the most impatient observer from moving the prisms too quickly and possibly damaging them against the limits of motion.

The long slit disks to be used in this low resolution mode were fabricated along with the short slit disks for the echelle mode, and fit interchangeably in the spectrograph's rotating slit disk. The long slits are 0.929 inches in length, corresponding to 6 arcminutes on the sky at the image scale of the P60 Cassegrain.

Ten long slits exist, having unique widths of 0.7, 1.3, 2.0, 3.3, 4.0, 4.7, and 9.2 arcseconds (see Table 2-7). Note also that these long slits must be installed at 90 degrees to the nominal (i.e., $\chi = 0$) slit direction of the echelle spectrograph, since the echelle grating is used in the "Quasi-Littrow" mode (see §**II.B**), unlike the low resolution ordinary grating.

Finally, returning to the echelle mode of the spectrograph, note that although designed for a wavelength range 3200 to 7000 Ångstroms, the CCD sensitivity has constrained its usefulness to 3700 to 9000 Ångstroms. If one is in fact more interested in this latter wavelength range, the possibility exists to build a second set of cross-dispersing prisms which would be interchangeable with the existing set of quartz prisms. This new set of "red" prisms would consist of a denser glass, one that does not transmit very well below 3700 Ångstroms but is more dispersive, so that the fewer orders spanning the 3700 to 9000 Ångstrom range would have an increased order-to-order separation. Because the cost of a second set of prisms and a copy of the rotating prism mount to be interchangeable with the first would not be inexpensive, there are at present no plans for fabricating this set of "red" cross-dispersing prisms. Instead it is hoped that advances in CCD development will result in a detector sensitive over the original design wavelength range of 3200 to 7000 Ångstroms.

B. The Data Reduction

The data reduction process developed and used for this project has proven quite reliable and automatic; indeed, it only requires interaction at four phases from start to finish. These are: (1) interactively run SDIST; (2) from a cross-cut through the orders, telling ECHTRACT where to start fitting the first two orders to be extracted and what their order numbers are; (3) ECHXCONT; and (4) fitting the first few order arcs in ECHARC. While this has proved a viable compromise

between laborious interactive tedium on one hand and a completely automated mode in which all decision making is turned over to the program on the other, under this heading of "future work" it is appropriate to point out ways to make the data reduction process more automated and therefore more rapid.

Since the curvature of echelle orders is much less than S-distortion in image tubes, steps could be taken to automate SDIST. This would have the further advantage of no longer requiring the Grinnell image display. Whereas SDIST fits no more than 10 S-distorted "orders," there is no fundamental reason for this restriction, and a version of SDIST modified especially for use with echelle data could attempt to fit all orders and use only those it proves able to fit successfully.

ECHTRACT could easily be modified to start not expecting exact order centroids from the user, but instead start from a window within which it could find the order maxima itself. This would combine the best features of the FIT, SEARCH, and TEMPLATE modes of operation.

A second, but much more subtle, way in which ECHTRACT is not as automatic as one would ideally like it to be is how it computes the amount of order wings to subtract from adjacent orders. The process is equivalent to truncating the Gaussian fit it obtains for the order at a certain power of Y (in this case, the cross-dispersion direction; see equation (3.3) above) so as to simulate order wings broader than those of a true Gaussian profile, and then multiplying each of these wings by a scale factor different for the red wing and the blue wing. These scale factors were determined and written into the program code such that the atmospheric A-band of a sample test B star spectrum was successfully removed from the adjacent inter-order minima rows.

Although the expressions for the truncated Gaussian wings are quite naturally functions of the Gaussian fit parameters determined independently for each order

every time ECHTRACT is run (and so behave accordingly as the seeing and/or focus changes from spectrum to spectrum and from observing run to observing run), these multiplicative scale factors are not. An improved version of ECHTRACT might be able to look for the deepest absorption line feature in the data and re-determine these scale factors appropriately for each spectrum; a less ambitious solution would see these factors brought up from where they are buried deep inside the wing fitting subroutine in ECHTRACT and offered to the user as input parameters to be specified. Perhaps even a utility program could determine these factors for each night's B-star exposure (e.g.) and pass the values it finds along to ECHTRACT to be used for that night's data.

ECHXCONT's interactive mode is quite well suited to removing narrow lines from the echelle spectra of hot stars. However, its performance in the automatic mode or when presented with later type spectra leaves much to be desired, since these are based on a comparison between the uncorrected data and its median. When the lines become more numerous and the continuum regions narrower with reference to the median boxcar, the median ceases to be a reliable indicator of continuum regions. This requires that one find a more suitable test to determine what part of a given spectrum is continuum and what parts are lines than the median test employed by ECHXCONT. The data reduction system employed by Universität Sternwarte München University in their CASPEC work takes as the continuum level the maximum value from within the boxcar, but for CSPN this fails in the vicinity of any of the numerous nebular emission lines. But for late-type stars in which the problem is too many absorption lines, it ought to be considered. The IRAF continuum fitting options include one routine which fits the data with some polynomial or spline function, rejects all parts of the spectrum that deviate from this fit by more than a specified amount, and then iterates on this process using only the points remaining from the previous iteration. MIDAS uses a two-

dimensional model of the echelle grating blaze function to fit the continuum of all orders simultaneously, but whether it distinguishes from line and continuum regions in the process is not clear from the MIDAS documentation or published reports (Ponz, et al., 1986). Were ECHXCONT modified to work in wavelength coordinates instead of pixel coordinates, its PREVIOUS keyword could be used to take a master list of continuum regions and so bypass the need for an automatic continuum discriminator without having to resort to an interactive fit for each object in a set of similar objects.

The expansion of Keith Shortridge's one-dimensional interactive ARC program into ECHARC has proven very successful, as one can judge from the performance figures given in §**III.E** above. However, ECHARC's performance diminishes substantially when required to "extrapolate" as opposed to "interpolate" from the interactive fit inputs. A large part of its problem is deciding what action to take when it finds fewer than 4 arc lines (e.g.) when it is supposed to perform a 4th order fit. At present its instructions are to recompute the predicted wavelengths using all the line identifications it has up to that point, and try again. If still unsuccessful, it is to proceed onto the next order and come back to this order. But if the arc positions differ from the program's predictions for all subsequent "extrapolate" orders, ECHARC is not smart enough to give up but rather wastes a great deal of time computing these predictions over and over again trying to match the arc line positions. Clearly a greater degree of artificial intelligence is required.

A further improvement of ECHARC one could benefit from is to do away with the interactive order fit phase altogether as an option, using instead the results from a previous night or a previous run which ECHARC would cross-correlate order by order to find its own starting identifications. This would follow along the lines of the program ACROSS added to Figaro at Caltech by Josh Zucker as a one-dimensional improvement of ARC. A less ambitious step forward for ECHARC would be to

present the user with a menu initially for PREVIOUS=.TRUE. that includes the options to go directly to the automatic phase, rather than (as is true at present) requiring that one go through the interactive fitting to each order even if this is not necessary.

C. The Central Stars of Planetary Nebulae

The methodology for distance-independent study of the central stars of planetary nebulae presented in Chapter **IV** has demonstrated itself to be among the most reliable currently available (cf., §**IV.D**, which compares the results of this work with that of Mendez, et al., 1988). Currently the primary need is for a larger sample of CSPN; recall that in §**I.F** the Daub (1982) distance scale was analyzed in an attempt to define a distance limited sample, and 64 objects were identified as potential candidates for this study. Of these, 21 were observed (§**IV.A**) and model atmosphere fits have been so far performed to only five. Clearly much future work remains to increase the sample size.

Recall that the calculation of the spectroscopic distance requires as input the visual magnitude of the central star; the problems with currently available magnitudes were reviewed recently by Kaler (1987). In the future two dimensional CCD photometry should be undertaken to determine much more accurate magnitudes. By choosing a filter bandpass between the bright nebular emission lines, this approach reduces to a minimum the errors arising from their contribution to the stellar magnitudes. The two-dimensional nature of this technique is also capable of properly accounting for the nebular continuum. Both of these considerations are especially important for faint central stars embedded in nebulae of high surface brightness, which is the typical situation for the particularly important young and/or massive CSPN.

The measurement of dynamical ages could be improved by the use of inner nebular radii instead of outer radii. While monochromatic optical images are one way of obtaining inner radii, it has been pointed out (most recently by Masson, 1988a,b) that radio continuum maps are capable of revealing the shell structure of nebulae having complex optical morphology (e.g., NGC 7027). The greater angular resolution of radio telescopes such as the VLA would also increase the accuracy of dynamical age estimates, although as noted by Masson detailed modelling of the nebular geometry then becomes necessary to interpret these more accurate measurements in order to derive the dynamical age. Furthermore, the difference between the bulk motion of the nebula and the expansion of the ionization front, which was the subject of §**IV.I**, needs to be properly accounted for in order to derive meaningful dynamical ages. Whereas the treatment in §**IV.I** served to illustrate the important distinction between bulk motion and the expansion of the ionization front, the thermodynamical consequences of the nebular ionization — potentially important owing to the restructuring of the radial density distribution which would take place as a result — were left out of the discussion for the sake of simplicity. Likewise, the possible influence of a stellar wind was omitted (cf., the treatment by Giuliani, 1981).

Regarding the comparison of CSPN with evolutionary tracks presented in the latter half of Chapter **IV**, there was first the suggestion (Iben, et al., 1983; Iben, 1984) that some fraction of CSPN may have experienced a late helium shell flash. Although this was shown to be very unlikely for the majority of CSPN in the present sample (and dynamical ages revised downwards through the use of inner radii and ionization considerations as suggested above would reduce this possibility even more), the few objects uppermost in the lower panel of Figure 4-16 should be examined for evidence supporting or refuting this hypothesis, as the probability is perhaps as great as 0.3 that a late shell flash has occurred. Such supporting evidence

would likely take the form of an unusually high atmospheric helium abundance or perhaps an abundance gradient in the nebula; Iben, et al. (1983), interpret the existence of this latter evidence in the well known cases of Abell 30 and 78 as an indication that these objects may contain "born-again" central stars.

As far as the empirical residual envelope mass estimates are concerned, note first of all that they were derived by requiring agreement with the PN dynamical ages. Therefore the comments above applying to a better determination of the expansion ages are important here as well. Such efforts combined with a larger sample may help to better define observationally the heretofore unknown residual envelope mass as a function of core mass. Improved calculations of M'_{eR} might then be appropriate, dropping the assumption of a constant rate of envelope mass decrease during the additional transition time, which was made for the sake of simplicity in §**IV.I**.

While the discussion in the latter half of Chapter **IV** focussed on the predominance of "old" nebulae around "young" (i.e., massive) central stars, for the few low mass central stars in the present sample the problem is just the reverse. How is it possible for a 0.55 $M_\odot$ CSPN with an effective temperature T_{eff} = 75,000 K (e.g., NGC 1360) — for which the evolutionary age derived on the basis of the Schönberner (1983) model tracks is $\sim$ 140,000 years — to reside inside of a planetary nebula of much younger dynamical age (e.g., $\sim$ 20,000 years) ? This was precisely the question posed by Gathier (1984) for his sample of apparently less massive CSPN. Note that for low mass central stars "older" than the surrounding nebulae, the rapid ionization mechanism suggested by §**IV.I** is not able to reconcile the timescale disagreement as it can for higher mass CSPN younger than the nebulae.

Fortunately, the transition time dependence on residual envelope mass (equa-

tion 4.27) still offers a possible explanation. For these objects the empirical residual envelope mass estimate from equation (4.41) is only slightly *less* than that typically used in the evolutionary model calculations, and therefore the transition time to high effective temperatures is shortened. In other words, the empirical residual envelope mass estimate implies that the superwind mass loss mechanism removes more envelope material, and as a result the star evolves rapidly to high T_{eff} during the AGB to CSPN transition time (cf., Figure 3 of Schönberner, 1983, which gives T_{eff} as a function of envelope mass M_e, to Figure 4-31 of this work). Note that an absence of low mass stars with $T_{eff} \lesssim 50{,}000$ K would support this suggestion of a rapid transition to high T_{eff} through the removal of extra envelope material by the superwind; Mendez, et al. (1988), do remark that there is some evidence of this kind for their sample (their log(g) – log(T_{eff}) diagram is reproduced as Figure 5-4, with the results of this work added).

Were this lack of cool (50,000 K $\geq T_{eff} >$ 27,000 K) low mass central stars in the present sample to persist as the sample size is greatly increased, this would be strong evidence against the theoretical residual envelope masses — which lead to $t_{evol} > 100,000$ years — and in favor of those determined empirically as suggested in §**IV.I** above. Since the situation regarding high mass, "young" central stars within "old" nebulae can be reconciled in any of several ways, an observational test of the empirical residual envelope masses suggested in §**IV.I** is not as straightforward as for the low mass objects. It may be that statistical arguments such as those advanced by Shaw (1986, 1987) comparing the relative numbers of high and low mass CSPN for a well defined sample would be able to confirm or refute the postulated empirical residual envelope masses for the high mass CSPN.

Returning to the prospects for a distance limited sample, note that because the present sample was defined without respect to the spectral type of the central star, many of the CSPN in Tables 1-1 through 1-3 do not have pure absorption line

spectra which lend themselves to the model atmosphere fitting process explained in §**IV.C**. While it is currently possible to analyze Of-type as well as sdO type spectra (N.B. the work of Pauldrach, 1987, which addresses statistical equilibrium in radiation driven winds, building on the work of fellow colleagues at the Universität Sternwarte München), the WC category of carbon Wolf-Rayet stars must await the development of non-hydrostatic model atmosphere codes. Kudritzki (1987) claims that such codes are currently only one to two years away, citing the recent work by Puls (1987) at the Universität Sternwarte München on self-consistent radiation driven wind models. If this problem proves tractable, it will be a very important step forward for our understanding of the WC class of CSPN and the evolutionary role these stars fulfill. Note, however, the continuum flattening challenge Wolf-Rayet echelle spectra represent; the "future work" suggested in §**V.A** and §**V.B** will therefore be equally important in providing the highest quality observational material for comparison with these forthcoming models.

In a somewhat similar sense, a "self-consistent radiation driven wind model" ought to be a future objective of those developing post-AGB evolutionary models, although such stars are pulsationally unstable as well. It is quite clear from Chapter **IV** that mass loss plays an important and ultimately, of course, the dominant role governing the transition from OH/IR stars at the tip of the AGB to proto-planetary nebulae. The residual envelope mass and rate of surface mass loss then govern the crucial transitional timescale for the subsequent early evolution of the CSPN. Hopefully the empirical residual envelope mass estimates presented at the conclusion of Chapter **IV** will prompt much productive future work in this area, and our understanding of "clouds" will benefit as a result.

Bibliography

Daub, C.T., 1982. *Ap. J.*, v. **260**, p. 612.

Giuliani, J.L., 1981. *Ap. J.*, v. **245**, p. 903.

Iben, I., Kaler, J.B., Truran, J.W., and Renzini, A., 1983. *Ap. J.*, v. **264**, p. 605.

Iben, I., 1984. *Ap. J.*, v. **277**, p. 333.

Kudritzki, R.P., 1987. Private communication.

Masson, C.R., 1988a. *Ap. J.*, submitted.

Masson, C.R., 1988b. Preprint.

Mendez, R.H., Kudritzki, R.P., Herrero, A., Husfeld, D., and Groth, H.G., 1988. *Astron. Astrophys.*, v. **190**, p. 113.

Pauldrach, A., 1987. *Astron. Astrophys.*, v. **183**, p. 295.

Ponz, D., Brinks, E., and D'Odorico, S., 1986. *Proc. SPIE,* v. **627**, p. 368.

Puls, J., 1987. *Astron. Astrophys.*, v. **184**, p. 227.

Shaw, R.A., 1986. *Ph.D. Thesis,* University of Illinois.

Shaw, R.A., 1987. In *I.A.U. Symposium No. 131, Planetary Nebulae,* ed. S. Torres-Peimbert, in press.

Figure Captions

Figure 5-1: A cut through an echelle image of the incandescent flat field lamp in the cross-dispersion direction. Note the lack of blue light.

Figure 5-2: A proposed two filter combination to provide better balance between the blue and red light in the flat field lamp.

Figure 5-3: A design drawing for the 3×3 inch ordinary grating mount found in the existing P60 Spectrograph. It is expected that a receptacle for this grating mount can be built into the P60 echelle spectrograph, allowing it to be used in an alternate low dispersion, long slit mode.

Figure 5-4: The log(g) – log(T_{eff}) diagram from Mendez, et al. (1988), onto which the CSPN sample of this work has been added. Note the absence of low mass, low effective temperature objects.

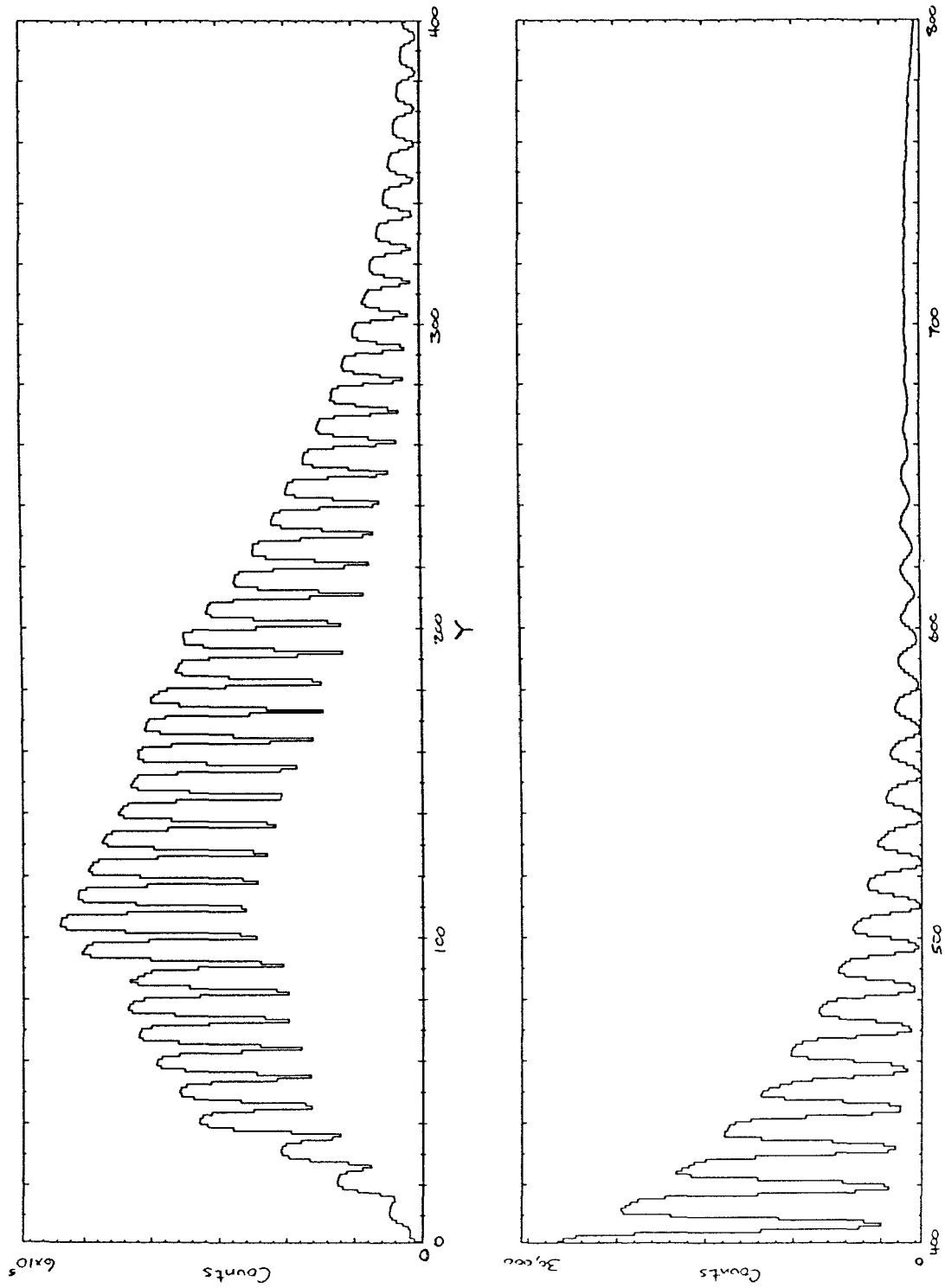
Counts
6x10^5
0
100
200
300
400
Y
Counts
3e,ccc
0
400
500
600
700
800

Figure 5-1

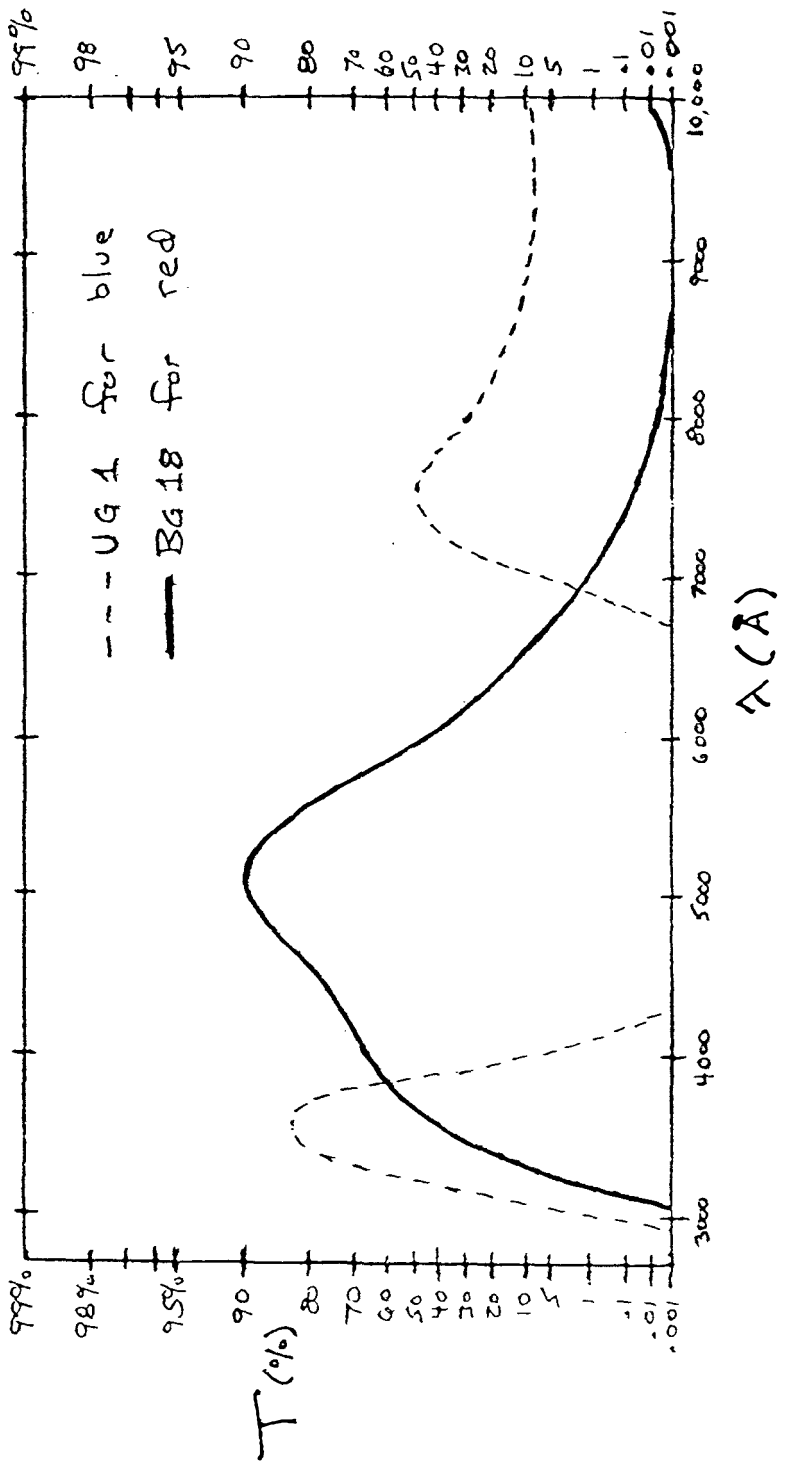
99%
98
95
90
80
70
60
50
40
30
20
10
5
1
.1
.01
.001
10,000
9000
8000
7000
6000
5000
4000
3000
λ (Å)
T (%)
--- UG 1 for blue
— BG 18 for red

Figure 5-2

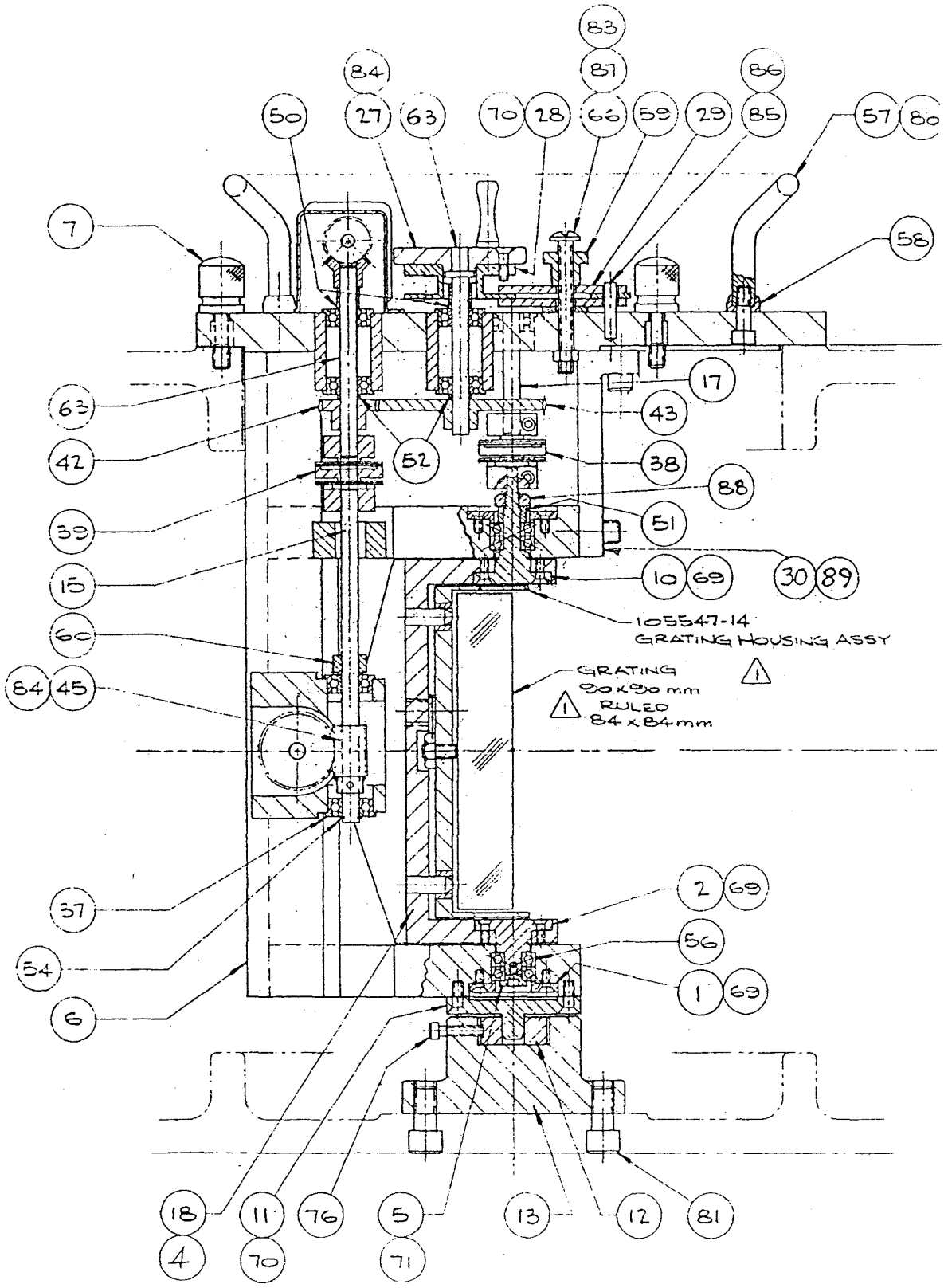
83
84
87
86
50
27
63
70
28
66
59
29
85
57
80
7
58
17
63
43
42
52
38
88
39
51
15
10
69
30
89
105547-14
GRATING HOUSING ASSY
1
60
GRATING
90 x 90 mm
84
45
1
RULED
84 x 84 mm
37
2
69
56
54
1
69
6
18
11
76
5
13
12
81
4
70
71

Figure 5-3

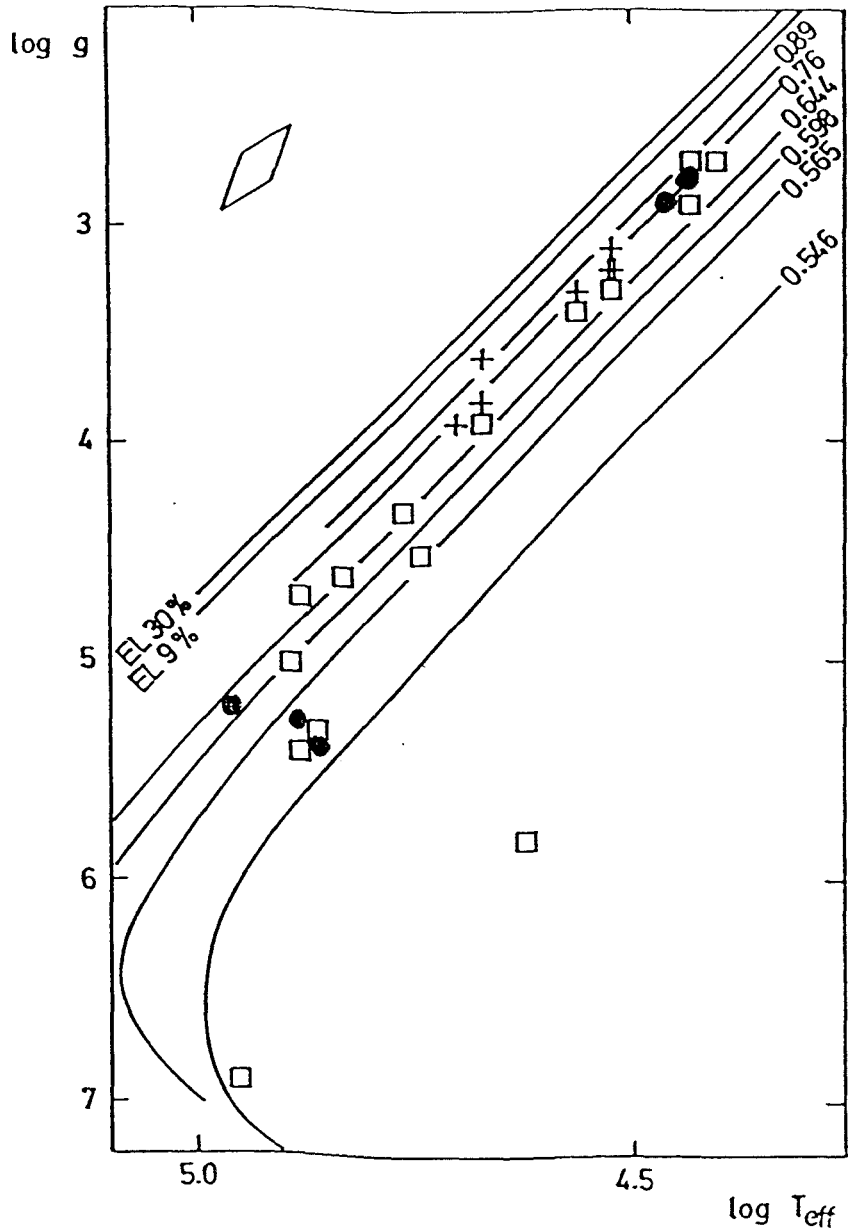

Fig. 3. The log g-log T_{eff} diagram. The two lines labeled EL are Eddington limits for photospheric He abundances of 30% and 9%. We have plotted 6 theoretical post-AGB evolutionary tracks, which are labeled with the corresponding value of the stellar mass, in solar masses. Plus signs and open squares indicate CSPN that show, respectively, He II λ4686 in emission and in absorption. A typical error box can be seen in the upper left corner of the figure.

● THIS WORK

Figure 5-4

Appendix A

P60 Echelle Spectrograph Commercial Components and Their Commercial Sources

1) Optical Components

Bausch & Lomb
Instruments and Systems Division
P.O. Box 25189
Rochester, NY 14625
(716) 338-8208

Echelle Diffraction Grating,
52.65 lines/mm, blaze angle 63 26′,
ruled length 76mm, ruled width 152mm,
actual blank size: 85mm x 165mm,
Zero-Dur low expansion substrate

Dow Corning Corporation
Corporate Center
CO2230
Midland, MI 48686-0997
(800) 432-3220
[attn. Ms. Nancy Didrichsons]

Sylgard 184 Elastomer,
used for cementing fused quartz and
calcium flouride optical elements

ESCO Products
171 Oak Ridge Road
Oak Ridge, NJ 07438
(201) 697-3700

Fused Quartz Blanks for Camera Lenses

Fair Optical Company
1258 N. San Antonio Ave.
Pomona, CA 91767
(714) 620-5515
[attn. Mr. Gene Fair]

Polishing of Stainless Steel Slit Disks

Harshaw Chemical Company
6801 Cochra Road
Solon, OH 44139
(216) 248-7400

Optical Grade A Calcium Fluoride Blank,
used in camera lens system triplet

Donald A. Loomis
Custom Optics
3624 Avenue de Montezuma
Tucson, AZ 85749
(602) 749-3371
[attn. Mr. Don Loomis]

Fabrication of Camera Lens System,
$\pm 0.1\%$ tolerance on radii,
$\pm 50\,\mu$m tolerance on thicknesses,
$\pm 25\,\mu$m tolerance on centering

Newport Thin Film Lab, Inc.
4534 Carter Court
Chino, CA 91710
(714) 591-0276
[attn. Mr. Jeff Dukes]

Custom Anti-Reflection Coatings,
3200 – 7000 Å wavelength range,
normal as well as 45° incidence

Optics Plus, Inc.
1351 Edinger Ave.
Santa Ana, CA 92705
(714) 972-1948
[attn. Mr. Lonnie Hoyle]

Custom Collimator Folding Mirror,
Pyrex, 3.00" ln., 1.25" wd., 0.375" th.,
flat to $\lambda/4$, 80-50, Al+SiO coated

Off-Axis Paraboloid Collimator,
Pyrex, 3.5" clear aperture, 0.75" th.,
18.00" F.L., 4.05" zonal radius center,
accuracy $\lambda/4$, 80-50, Al+SiO coated

United Lens Company, Inc.
259 Worcester Street
Southbridge, MA 01550
(617) 765-5421

UBK7 and LLF6 Glasses for Camera Lens

2) Mechanical and Electrical Components

ACME Bearing & Drives
13924 Valley Blvd.
City of Industry, CA 91744
(818) 961-4444

Slit Pulley Bearing,
NDH 773L01, 12mm bore, 28mm O.D.
Detent Cam Follower,
RBC S-24-LW, 0.75" O.D.
Detent Pivot Bearing,
NDH 55600, 0.394" bore, 1.378" O.D.,
double row of rollers, 2 shields

Gaston Araya Machining
2526 N. Highland
Altadena, CA 91001
(818) 798-4764
[attn. Mr. Gaston Araya]

Custom Machine Work,
performed throughout the
P60 echelle spectrograph

Automation Gages
850 Hudson Avenue
Rochester, NY 14621
(800) 922-0329

Triplet Camera Lens Mount Ball Slide,
part # RL-31, series L roller slide,
1-inch travel, 350 lb. capacity

Center Line Welding
1728 Tyler Avenue
So. El Monte, CA 91733
(818) 350-8117
[attn. "Dale"]

Custom Fabrication & Welding Work,
performed on P60 echelle spectrograph
aluminum mounting stand

EDM Labs
7525 Park Avenue
Garden Grove, CA 92641
(714) 894-5050
[attn. Mr. Richard Hunt]

EDM Machining (*recommended vendor*),
slit widths or dia. $\geq 0.002''$,
lengths up to 1.0" or larger (?)
($50.00 each; "Conventional EDM")

Johnson Products, Inc.
232 W. Maple Avenue
Monrovia, CA 91016
(818) 359-8353
[attn. Mr. Sam La Porte]

Slot Milling, Heat Treating, and Surface
Grinding of Slit Disks,
final membrane thickness $\leq 0.005''$

King Bearing 13324 E. Valley Blvd. City of Industry, CA 91746 (818) 330-3456 [attn. Mr. Manuel Villegas]	High Precision Bearings for Slit Wheel, NDH Q20201-DT-L 7A, 12mm bore, 32mm O.D., *matched pair*
Marshall Industries 9710 De Soto Avenue Chatsworth, CA 91311 (818) 407-4100	AMP CPC Series Plastic Connectors #206705-1 and #206705-2, #206708-1, #206966-1
Mertsoc Tool Co. 1165 Linda Vista San Marcos, CA 92069 (619) 744-4640 [attn. Mr. Frank Mertsoc]	EDM Machining (*not recommended, as this work was delayed indefinitely*), P.O. finally cancelled (see EDM Labs)
Minark Electric Company 224 E. 3rd Street Los Angeles, CA 90013 (213) 624-3161 [attn. Mr. Joseph Estrada]	Stepper Motor for Slit Wheel Rotation, Slo-Syn model number M061-FC02
New England Affiliated Tech. 620 Essex Street Lawrence, MA 01841 (617) 685-4900	Triplet Camera Lens Focus Micrometer, part # MMI-M10D digital head, 25.4mm travel, 0.001mm resolution
John B. Olson Co., Inc. 1845 N. Case Street Orange, CA 92665 (714) 998-9672 [attn. Mr. John Olson, Jr.]	Uniblitz Shutter, model 225L-0-0-T-5 25mm dia., no case, Teflon coated blades, plate design "X" cut
PIC Design P.O. Box 1004 Benson Road Middlebury, CN 06762 (800) 243-6125	— Misc. Parts for Slit Wheel Drive — Motor Drive Gear, # FD5-16, 16 tooth, 0.5" pitch dia. Drive Pully Belt, # FA-220, 220 pin, 21.598" pitch circ.

PIC Design (continued)

Drive Gear Clamp,
L4-15, set-screw type for 0.25" shaft

Don Richetts Company, Inc.
P.O. Box 730
828 East Valley Blvd.
San Gabriel, CA 91778
(818) 280-0470

Micrometer Head & Ball for Grating Tilt,
model numbers 263-P and 247-A

Westinghouse Electric Corp.
Industrial & Gov't Tube Div.
Westinghouse Circle
Horseheads, NY 14845
(607) 796-3386
[attn. Ms. Eileen Putnam]

Thorium Hollow Cathode Discharge Lamp,
type Q-A-A, low pressure Argon fill,
1.5" diameter quartz window

($325.00 each)

Appendix B

Commercial Literature and Technical Information Related to the P60 Echelle Spectrograph

Information about High Technology Silicone Materials

DOW CORNING

SYLGARD™ 184 SILICONE ELASTOMER, BASE & CURING AGENT

Type	Two-part silicone elastomer
Color	Transparent
Physical Form	
as supplied	Medium-viscosity liquid
as cured	Flexible elastomer
Cure	25 to 150 C (77 to 302 F)
Special Properties	Transparent; reversion resistant; stable dielectric; high physical properties
Primary Uses	Potting and encapsulating
Benefits	Low toxicity; repairability

DESCRIPTION

SYLGARD™ 184 silicone elastomer, base & curing agent, is supplied as a two-part kit comprised of liquid components. When the base and the curing agent are thoroughly mixed in a 10:1 by weight ratio, the medium-viscosity liquid mixture has a consistency resembling SAE No. 40 motor oil. The liquid mixture will cure to a flexible transparent elastomer ideally suited for electrical/electronic potting and encapsulating applications.

SYLGARD 184 silicone elastomer offers a flexible cure schedule from 25 to 150 C (77 to 302 F) and cures at a constant rate regardless of sectional thickness or degree of confinement, and without an exotherm. SYLGARD 184 silicone elastomer requires no post cure and can be placed in service immediately following the completion of the cure schedule at any operating temperature from -55 to 200 C (-67 to 392 F). See Table I for special features and benefits of this product.

USES

Because of its many special features, SYLGARD 184 silicone elastomer is ideal for a wide variety of electrical/electronic potting and encapsulating applications and provides environmental protection for:

- Equipment modules
- Relays
- Power supplies
- Magnetic amplifiers
- Transformers
- Ferrite cores
- Coils
- Connectors
- Fiber optic waveguide coatings
- Encapsulation of circuit boards

It is especially useful when clarity is desirable, such as:

- Encapsulation of solar cells
- Encapsulation of opto-electronic displays

HOW TO USE

Mixing

SYLGARD 184 silicone elastomer is supplied in two parts, a lot-matched base and curing agent, mixed in a ratio of 10 parts base to one part curing agent, by weight.

For best curing results, glassware or tinned cans and glass or metal stirring implements should be used. Mix with a smooth action that will minimize the introduction of excess air.

Pot Life – Working Time

Cure reaction of SYLGARD 184 silicone elastomer, base & curing agent, begins with the mixing process. Initially, cure is evidenced by a gradual increase in viscosity, followed by gelation and conversion to a solid elastomer. Pot life is defined as the time required for viscosity (in centipoise) to double, following addition of curing agent to base. At 25 C (77 F) the pot life of SYLGARD 184 silicone elastomer is 2 hours. Pot life of this product can be extended by refrigeration at 4 C (40 F); however, do not allow moisture from condensation to collect in the silicone elastomer.

SYLGARD 184 silicone elastomer will cure at 25 C (77 F) and will become a solid in 24 hours. At 25 C (77 F) SYLGARD 184 silicone elastomer will reach full cure in 7 days. See "Curing."

Processing

Thoroughly mix SYLGARD 184 silicone elastomer, base & curing agent, in a ratio of 10 parts base to one part curing agent, by weight. Agitate gently to reduce the amount of air introduced. Allow 30 minutes for the mixture to set before pouring.

Since air bubbles are usually present following mixing, vacuum deairing is recommended. Deair in a container with at least four times the liquid volume to allow for expansion of material. Entrapped air in the mixture can be removed by using a vacuum of 25 to 29

TYPICAL PROPERTIES
These values are not intended for use in preparing specifications.

As Supplied		
CTM 000 1A[1]	Specific Gravity at 25 C (77 F)	1.05
CTM 0050	Viscosity[2] at 25 C (77 F), centipoises	5500
As Catalyzed[3]		
CTM 0050	Viscosity at 25 C (77 F), centipoises	3900
CTM 0055	Pot Life[4], hours, minimum	2
As Cured – Physical[5]		
CTM 0176	Appearance	Transparent
CTM 0099	Durometer Hardness, Shore A	40
CTM 0137A	Tensile Strength, MPa (psi)	6.20 (900)
CTM 0137A	Elongation, percent	100
CTM 0159A	Tear Strength, die B, kN/m (ppi)	2.6 (15)
CTM 0022	Specific Gravity at 25 C (77 F)	1.05
CTM 0224	Thermal Conductivity, cal/cm²-sec-(°C/cm)	3.5×10^{-4}
CTM 0585	Linear Coefficient of Thermal Expansion, cm/cm per °C from -55 to 150 C	3.0×10^{-4}
CTM 0585	Volume Coefficient of Thermal Expansion, cc/cc per °C from -55 to 150 C	9.6×10^{-4}
MIL-I-16923G	Thermal Shock Resistance, from -49 to 68 C (-55 to 155 F)	Passes 10 cycles
	Weight Loss, percent	
	after 1,000 hours at 150 C (302 F)	1.6
	after 1,000 hours at 200 C (392 F)	3.2
ASTM D 570	Water Absorption, after 7 days immersion at 25 C (77 F), percent	0.10
ASTM D 746	Brittle Point, degrees	-65 C (-85 F)
CTM 0002	Refractive Index at 25 C (77 F)	1.430
	Radiation Resistance, cobalt 60 source	
	at 200 megarads	Still usable
	at 500 megarads	Hard and brittle
UL 94	Flammability[6] Classification	94 V-1
UL	Temperature Rating,	
	Mechanical, degrees	130 C (265 F)
	Electrical, degrees	130 C (265 F)
Electrical[7]		
CTM 0114A	Dielectric Strength, volts/mil[8]	450
CTM 0112	Dielectric Constant, at	
	60 Hz	2.7
	100 Hz	2.66
	100 KHz	2.65
CTM 0112	Dissipation Factor, at	
	60 Hz	0.001
	100 Hz	0.0009
	100 KHz	0.001
CTM 0249A	Volume Resistivity, ohm-cm	2.0×10^{15}
CTM 0171	Arc Resistance, track, seconds	115
Electrical – after heat aging for 1000 hours at 200 C (392 F)		
CTM 0114A	Dielectric Strength, volts/mil[8]	600
CTM 0112	Dielectric Constant at	
	60 Hz	0.001
	100 Hz	0.001
CTM 0249A	Volume Resistivity, ohm-cm	2.0×10^{14}

[1] *In most cases, CTMs (Corporate Test Methods) correspond to ASTM standard tests. Copies of CTM procedures are available upon request.*

[2] Brookfield Viscometer Model LVF, spindle #4 at 60 rpm.

[3] Mix ratio 10 parts base to 1 part curing agent, by weight.

[4] Time required to double catalyzed viscosity.

[5] Based on sample thickness of 125 mils and a minimum cure of 4 hours/65 C (149 F).

[6] Tests, claims, representations and descriptions regarding flammability are based on standard small scale laboratory tests.

[7] Properties obtained on 1.58-mm-thick (0.062-inch) specimens, cured 4 hours at 65 C (149 F).

[8] Measured with 1/4-inch standard ASTM electrode, 500 volts per second rate of rise.

Specification Writers: Please contact Dow Corning Corporation, Midland, Michigan, before writing specifications on this product.

inches of mercury. Large bubbles will form almost immediately and should be collapsed by introducing atmospheric pressure for 30 seconds. Then continue the vacuum until the liquid expands and settles to its original volume and bubbling subsides. This may take 15 minutes to 2 hours, depending on the amount of air introduced during stirring.

Clean and degrease all application surfaces using a solvent to remove all mold release agents, processing oils and surface contaminants. Dry and remove all solvent before application.

For best adhesion the application substrate should be primed with SYLGARD™ prime coat. Obtain a technical bulletin for proper application instructions. See "Bonding."

CAUTION: SYLGARD 184 silicone elastomer is flammable. Keep away from heat, sparks and open flame. Use only with adequate ventilation.

When pouring SYLGARD 184 silicone elastomer into the container in which it is to be cured, care should be taken to minimize air entrapment. When practical, pouring should be done under vacuum, particularly if the component being potted or encapsulated has many fine voids. If this technique cannot be used, the unit should be evacuated after SYLGARD 184 silicone elastomer has been poured.

After allowing time for the material mass to reach temperature, cure according to the cure time-temperatures listed in "Curing."

Repairability

In the manufacture of electrical/electronic devices it is often desirable to salvage or reclaim damaged or defective units. With most rigid types of potting and encapsulating materials, removal or entry is difficult or impossible without causing excessive damage to internal circuitry. SYLGARD 184 silicone elastomer, base & curing agent, offers excellent repairability as cure is to a transparent flexible elastomer allowing visual inspection of encapsulated or potted components. SYLGARD 184 silicone elastomer can be selectively removed with relative ease, repairs or changes completed, and the area repotted with additional product. SYLGARD 184 silicone elastomer, base & curing agent, can be removed by cutting with a sharp blade or knife and tearing material away from the area to be repaired. Thin sections of the adhesive elastomer are best removed from substrates and circuitry by mechanical action such as scraping or

rubbing and can be assisted by the application of isopropyl alcohol.

Before repotting a repaired device, if it is possible, roughen the exposed surface of the SYLGARD 184 silicone elastomer, base & curing agent, with an abrasive paper. This will enhance adhesion and permit the repair material to become an integral matrix with the existing elastomer. Silicone prime coats are not recommended for adhering SYLGARD 184 silicone elastomer, base & curing agent, to itself in repotting applications.

Reversion Resistance

Many types of potting and encapsulating materials, when heated under confinement or in deep sections, will depolymerize or revert to a more liquid state. This degradation process is commonly referred to as reversion. SYLGARD 184 silicone elastomer, base & curing agent, employs a unique "addition reaction" curing mechanism which produces no cure byproducts. This cure system provides excellent reversion resistance even when exposed to temperatures in excess of 200 C (392 F) while under confinement or in deep section.

Temperature Stability

SYLGARD 184 silicone elastomer, base & curing agent, cures chemically to a thermoset material that will not melt or appreciably soften even at elevated temperatures of 250 C (482 F). The material may harden or become brittle after prolonged exposure to these elevated temperatures. SYLGARD 184 silicone elastomer, base & curing agent, has a 130 C (265 F) UL yellow-card temperature index classification for both electrical and mechanical functional use.

Upon exposure to lower temperatures, SYLGARD 184 silicone elastomer does not approach a stiffening point until -55 C (-67 F). Overall, the cured elastomer will maintain its basic elastomeric flexibility over an extremely wide temperature range of -55 to 200 C (-67 to 392 F), making it the ideal selection for applications that may experience high or low temperature cycling.

PROCESSING TECHNIQUES

Curing

SYLGARD 184 silicone elastomer, base & curing agent, can be satisfactorily cured either by exposure to air or completely sealed, and at temperatures ranging from 25 to 150 C (77 to 302 F). Curing time can be appreciably decreased by elevating the cure temperature. Suggested cure cycles are one of the following:

25 C (77 F) for 24 hours
65 C (149 F) for 4 hours
100 C (312 F) for 1 hour
150 C (302 F) for 15 minutes

Relatively massive parts will require additional time in the oven to bring them up to the selected cure temperature. Satisfactory sources of heat include circulating and noncirculating ovens, infrared heating lamps and heat guns.

Full mechanical strength will not be achieved for 7 days when SYLGARD 184 silicone elastomer, base & curing agent, is cured at 25 C (77 F). The majority of its physical strength, however, is present after 24 hours.

Bonding

SYLGARD 184 silicone elastomer, base & curing agent, will not normally bond to clean nonporous surfaces such as metal or glass. A prime coat is required to insure adhesion to these surfaces. SYLGARD prime coat is recommended to obtain the best adhesion. The prime coat should be applied in a thin layer to clean, dry surfaces where adhesion is desired. It should be air dried 1 to 2 hours before the silicone elastomer is applied.

Lowering Viscosity

The viscosity of SYLGARD 184 silicone elastomer, base & curing agent, can be lowered by the addition of DOW CORNING® 200 fluid, 50 cSt. Quantities of 10 percent or less will have little or no effect on the physical or electrical properties. Quantities of 10 percent or greater may decrease the physical strength and hardness but will have no effect on the electrical properties. At concentrations greater than 10 percent the fluid may possibly bleed from cured SYLGARD 184 silicone elastomer. The addition of thinning fluid does not change the weight of curing agent required with a given weight of base.

Varying the Hardness

Variations of up to 10 percent in concentration of curing agent in SYLGARD 184 silicone elastomer have little effect on cure time or on the physical properties of the final cured elastomer. Lowering the curing agent concentration by more than 10 percent will result in a softer and weaker elastomer; increasing the concentration by more than 10 percent will result in an overhardening of the cured elastomer and will tend to degrade the physical and thermal properties. Any change in the curing agent concentration will have little or no effect on the electrical properties, however.

Release Agents

When SYLGARD 184 silicone elastomer, base & curing agent, is cured in a mold, the mold should first be treated with a release agent to prevent sticking. Suitable release agents include DUPONOL®[1] WAQ to a 5 percent concentration with isopropanol; DOW CORNING® 230 fluid to a 2 percent concentration with CHLOROTHENE®[2] or similar chlorinated solvent; a mild liquid detergent to a 2 to 5 percent concentration with water; or petroleum jelly to a 5 percent solution in a chlorinated solvent.

LIMITATIONS

Inhibition of Cure

SYLGARD 184 silicone elastomer, base & curing agent, cures rapidly and uniformly at a wide variety of temperatures, in thick or thin sections and under conditions of air exposure or in total confinement. It can be cured in molds of a variety of materials and in contact with most electrical insulation materials.

There are certain situations, however, where cure reaction cannot proceed normally. These conditions occur when materials called inhibitors are present. In the presence of inhibitors cure in the immediate vicinity is poor. In the inhibited area (usually less than 0.020-inch thick) the silicone elastomer remains in a liquid or tacky state even though the cure schedule has been completed. This material will remain uncured despite any subsequent attempts to convert it to a hard, dry, rubbery mass. Extremely minute quantities of inhibitor may be sufficient to produce this effect. The most notable causes of inhibition include:

- Organo-tin and other organometallic compounds
- Silicone rubbers containing organo-tin catalyst
- Sulfur, polysulfides, polysulfones and other sulfur-containing materials
- Amines, urethanes, amine-containing materials and other nitrogen-containing materials
- Unsaturated hydrocarbon plasticizers

[1]DUPONOL is a registered trademark of E.I. du Pont de Nemours & Company.
[2]CHLOROTHENE is a registered trademark of The Dow Chemical Company.

If a substrate or material is considered questionable in respect to potential inhibition of cure, a small scale compatibility test to ascertain suitability in the particular application is recommended. If inhibition is present it may sometimes be overcome by prebaking the unit at the highest tolerable temperature for approximately 1 to 4 hours to remove volatile chemicals. See bulletin no. 10-022, "How To Process SYLGARD™ Brand Elastomers" for a listing of inhibition-causing materials.

Thermal Expansion

SYLGARD 184 silicone elastomer, base & curing agent, has a notable volume coefficient of thermal expansion (9.6×10^{-4} cc/cc/°C; see Typical Properties chart). On this basis the volume of the cured elastomer will increase or decrease approximately 9.6 percent for each 100 degrees Centigrade (212 degrees Fahrenheit) of temperature differential. When using SYLGARD 184 silicone elastomer, base & curing agent, in applications that are highly confined or hermetically sealed, allowance should be made to accommodate volume expansion and prevent pressure build-up at higher temperatures. Normal thermal expansion and contraction stresses may be minimized by selecting a cure temperature close to the midway point of the high and low extremes of the thermal cycle.

Temperature limits may also be influenced by differences in the thermal expansion values between the silicone elastomer and encapsulated or potted components, and also by their configurations. Therefore, thermal operating limits should be determined by testing before large scale use.

SAFETY REQUIREMENTS

Handling

SYLGARD 184 silicone elastomer, base & curing agent, does not contain volatile solvents. Special ventilation is not required in the normal use or storage of this product. Base and curing agent liquid components or their cured mixture do not present any significant toxicological hazard incidental to normal industrial handling. Minimal eye protection, such as standard safety glasses, should be adequate for normal industrial use. Direct eye contact can cause temporary eye discomfort; flush thoroughly with copious amounts of water should contact occur.

Abnormal Exposures

CAUTION: The liquid curing agent component of SYLGARD 184 silicone elastomer, if contaminated with strong acids, bases or catalytic oxidizing materials, may generate hydrogen gas. If exposure is suspected, use appropriate caution to relieve hydrogen gas pressure. Keep away from sparks and flame, and supply adequate ventilation to reduce localized build-up of hydrogen gas.

Spills

Spills of the liquid base and curing agent components of SYLGARD 184 silicone elastomer can become extremely slippery. Sawdust or other absorbent material should be immediately applied to any liquid spill for temporary relief. The spill should be removed with high flash mineral spirits or other suitable solvent.

TABLE I: SPECIAL FEATURES AND BENEFITS

Special Feature	*Benefit*
• Low toxicity	• No special precautions required for normal industrial handling
• No solvents or cure by-products; no exotherm during cure	• Requires no special venting; will not cause corrosion; low shrinkage during cure
• Cures to a transparent flexible elastomer	• Provides stability and relief from mechanical shock; low transmission of vibration; visual inspection of components and easy repairability
• Environmental protection	• Low water absorption; good radiation resistance; little out-gassing in hard vacuum
• Excellent dielectric properties	• Maintains and protects existing electrical insulation requirements
• Stability over a wide temperature range; reversion resistant	• Maintains elastomeric flexibility and provides functional stability from -55 to 200 C (-67 to 392 F), even in confinement
• Flame resistant	• UL flammability classification of 94 V-1 and a temperature rating of 130 C (265 F)

SHIPPING LIMITATIONS

None.

STORAGE AND SHELF LIFE

When stored in original unopened containers at or below 32 C (90 F), SYLGARD 184 silicone elastomer, base & curing agent, has a shelf life of 12 months from date of shipment.

PACKAGING

SYLGARD 184 silicone elastomer, base & curing agent, is shipped in kits that contain both the base and curing agent liquid components in separate containers. Each kit contains the appropriate weight of curing agent for amount of base. Net weights of complete kits are:

1.1 pounds (0.5 kg)
11 pounds (5 kg)
55 pounds (25 kg)
495 pounds (225 kg)

DOW CORNING CORPORATION
MIDLAND, MICHIGAN 48640

Printed in U.S.A. Form No. 10-042A-84

DOW CORNING

Information about High Technology Silicone Materials

DOW CORNING

SYLGARD® PRIME COAT

Color	Clear
Type	Moisture-reactive ingredients in heptane
Physical Form	Dilute solution
Primary Use	Promotes adhesion of many Sylgard encapsulants to common reactive substrates

DESCRIPTION

Sylgard® prime coat is a dilute, moisture-reactive solution in heptane solvent. When properly applied, Sylgard prime coat provides a surface treatment that can promote an adhesive bond between selected Sylgard encapsulants and many surfaces. It is particularly recommended for clear, nonfilled Sylgards such as Sylgard® 182 and 184 encapsulants.

NOTE: To bond filled Sylgards such as Sylgard® 170 A & B silicone elastomer, Sylgard® 186 encapsulating resin, or Silastic® E & J RTV silicone rubbers, Dow Corning® 1200 prime coat is recommended.

Effective substrates include most reactive metals, glass and ceramics, as well as selected laminates, resins and plastics (see Limitations).

HOW TO USE

Surfaces to be primed with Sylgard prime coat should be clean, dry and free of contaminants, oil films, grease and mold release. To remove substrate contaminants, a two-step cleaning procedure is recommended; first, clean with toluene, then follow with an acetone rinse. Vapor degreasing is also a very effective cleaning procedure. Shiny or difficult-to-adhere-to surfaces should be roughened or abraded. Both the primer and the surfaces to be primed should be at room temperature.

Apply the prime coat sparingly by either wiping, brushing, spraying or dipping. Best results are obtained with mechanical application such as wiping. A very thin film is recommended. Do not allow the primer to collect in pools on the surface. Excessive caulk-like or flake-like films are not effective. Primed surfaces should be air-dried under standard ambient conditions and humidity for one to two hours. For the ultimate in adhesion, the Sylgard encapsulant can be cured or post-baked at 158 F (70 C).

LIMITATIONS

Good adhesion cannot be expected on nonreactive metal substrates or nonreactive plastic substrates such as Teflon*, polyethylene, or polypropylene. Special surface treatments such as chemical etching or plasma are required to provide a reactive surface and promote adhesion to these substrates. Poor adhesion is normally experienced on plastic or rubber substrates that are highly plasticized, since the mobile plasticizer can act as a release agent. Sylgard encapsulants or addition-reaction cured silicone products will not adhere to substrates that contain chemicals capable of inhibiting the cure reaction. Sulfur, amines and organometallics are the most commonly used chemicals capable of causing inhibition of cure. (See "How to Process SYLGARD® Brand Encapsulants," Bulletin No. 61-276A-80 for more details.)

CAUTION

The heptane solvent present in Sylgard prime coat is extremely flammable. Keep away from heat, sparks and open flame. Use only with adequate ventilation. Avoid prolonged or repeated breathing of vapor.

When using any solvent to clean substrate surfaces, always follow all handling precautions on container label.

SHIPPING LIMITATIONS

D.O.T. Classification: Flammable liquid.

*"Teflon" is a registered trademark of E.I. DuPont de Nemours.

STORAGE AND SHELF LIFE

For best results, Sylgard prime coat should be used within one year from date of shipment. Store it away from heat, sparks and open flame.

Containers of Sylgard prime coat should be kept tightly closed when not in use. Prolonged exposure to atmospheric moisture will cause the reactive material to precipitate from solution and destroy effectiveness of the primer. Excess Sylgard prime coat remaining after completion of the priming operation should be discarded or sealed in a separate container. Material which has been excessively exposed to air will contaminate fresh primer. Keeping stored containers as full as possible limits the amount of trapped air, and prolongs the effective life of the primer.

PACKAGING

Sylgard prime coat is readily available in various container sizes. Contact either Dow Corning Corporation, Midland, Michigan 48640, or your local authorized Dow Corning Electrical/Electronic distributor.

USERS PLEASE READ

The information and data contained herein are believed to be accurate and reliable; however, it is the user's responsibility to determine suitability of use. Since Dow Corning cannot know all of the uses to which its products may be put or the conditions of use, it makes no warranties concerning the fitness or suitability of its products for a particular use or purpose.

You should thoroughly test any proposed use of our products and independently conclude satisfactory performance in your application. Likewise, if the manner in which our products are used requires governmental approval or clearance, you must obtain it.

Dow Corning warrants only that its products will meet its specifications. There is no warranty of merchantability of fitness for use, nor any other express or implied warranties. The user's exclusive remedy and Dow Corning's sole liability is limited to refund of the purchase price or replacement of any product shown to be otherwise than as warranted. Dow Corning will not be liable for incidental or consequential damages of any kind.

Suggestions of uses should not be taken as inducements to infringe any patents.

The information and data contained herein are based on information we believe reliable. You should thoroughly test any application and independently conclude satisfactory performance before commercialization. Suggestions of uses should not be taken as inducements to infringe any particular patent.

DOW CORNING CORPORATION
MIDLAND, MICHIGAN 48640

Printed in U.S.A. Form No. 10-058-83

DOW CORNING

DIGICORD D2 AUTO-OFF

Digital
Micrometer
for Coordinates

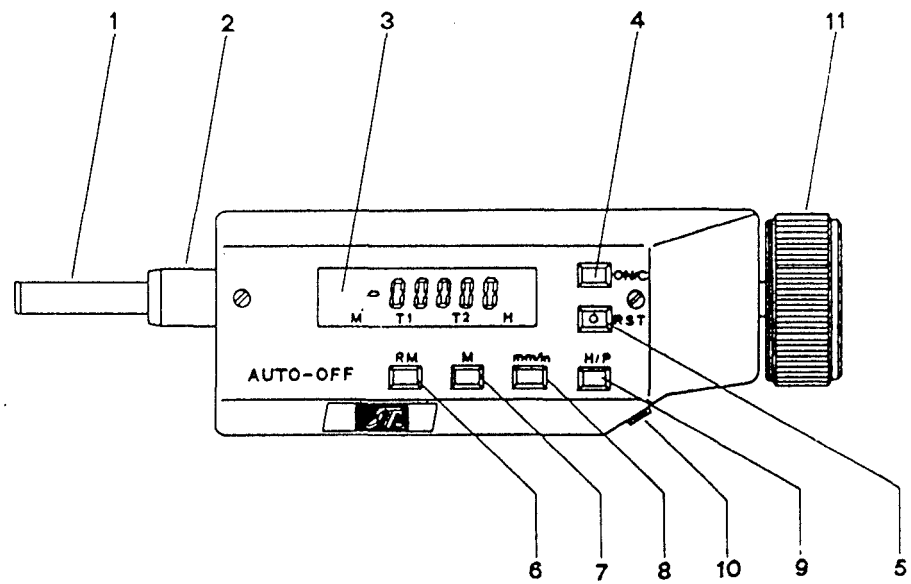

1. SCREW
2. ATTACHMENT CYLINDER
3. DISPLAY
4. ON/C KEY
5. RST KEY
6. RM KEY
7. M KEY
8. mm/inch KEY
9. H/P KEY
10. JACK SOCKET
11. TRAVERSE KNOB

OPERATING INSTRUCTIONS

MICRODIGIT M2 AUTO-OFF
MICRODIGIT M5 AUTO-OFF
DIGIVERT V2 AUTO-OFF
DIGICORD D2 AUTO-OFF

1) INTRODUCTION

This instrument is an electronic digital reading micrometer with LCD display. The combined use of a sophisticated electronics and a highly precise mechanics it a fine quality instrument. The numerous functions to be chosen make it remarkably versatileand adaptable to various requirements in the dimensional measuring field, both in laboratory and production.

2) FEATURES

- instant mm/inch conversion
- memorization of the reference value (zero relative) for relative measures at any point of the measuring range
- go - no go test for large quantity testing
- memorization of reading on display (Hold)
- automatic switch off after 4' of inactivity (Auto-Off)
- memorization of chosen function, of last registered value before switching off (continuous memory) and blocking of the micrometric screw travel
- series of micrometers with special measuring heads for measuring of particular surfaces
- improper use signal (Error)

3) DIRECTIONS FOR USE

- Accuartely clean the measuring surfaces of anvil and screw.
- Switch on the instrument by pressing the ON/C key: the last registered value and the functions chosen before switching off will appear (continuous memory). If necessary clear by pressing the ON/C key again.
- Release the micrometric screw by removing the lock key on ring nut.
- Bring the screw against the anvil by rotating the clutch knob only: the approach to the anvil or to the measuring surface must be accomplished with care so that the cluch force only is trasmitted, which will make the knob slide once the screw reaches the measuring surface; DO NOT OPERATE ON THE UNBLOCK CLUTCH RING. This ring allows to unblock the screw should it get blocked due to erroneous operation.
- Press the ON/C key (Clear operation); the display is zero set.
- For micrometezero setting is obtained on the setting gauge included with the instrument and the display will show the values 25.000, 50.000, 75.000 accordingly.
- The instrument in now ready to perform absolute measures.

4) RELATIVE MEASURES

- Bring the instrument to the reference value.
- Press the M key: the display is zero set and the M signal appears (the segment under the letter M).
- The measurements now refer to the memorized value.
- It is possible to recall the current absolute value at any time by pressing the

RM key. The M signal flashes indicating that the memory is still connected; move the screw in order to return to relative measures operation.
- To cancel such operation, press the RM key twice in succession.

5) **GO - NO GO**

- Visualize the reference value and press the M key; the display is zero set and the M signal is evidenced.
- Set the 1st tolerance (lower limit) and press M; the T1 signal is evidenced.
- Set the 2nd tolerance (higher limit) and press M; the T2 signal is evidenced and GO appears on display.

While measuring, if the values are in the set tolerance limits GO appears on display; if the values are out of tolerance NO GO appears on display alternatively with the difference (either positive or negative) from tolerance limits.

- To recall the absolute value press the RM key.
- To cancel the GO-NO GO operation press the RM key twice consecutively.

6) **mm/Inch CONVERSION**

- To convert the displayed value from one measuring unit to another, press the mm/inch key.
- The values expressed in inches are marked by two apexes (") on the right side of the displayed value.

7) **HOLD**

- When the H/P key is pressed the H signal appears and display is set on last visualized value.
- To return to the absolute value, eliminating the Hold operation, press the H/P key again.

8) **AUTO-OFF**

The instrument automatically switches off within 4' of inactivity, thus saving the accumulator's autonomy. Should the display visualize «Error», the auto-off function is disconnected. In order to re-establish te AUTO-OFF operation press the ON/C key to clear the display.

9) **ADDITIONAL SOFTWARE FUNCTIONS**

- Continuous memory
  When the instrument goes into OFF position, all previously selected functions and last measurement performed are held in memory. When the ON/C key is pressed the instrument turns on in the same measuring conditions as when it went off. Should it be necessary to cancel previous instructions clear the instrument by pressing the ON/C key again. The instrument is provided with a clutch blocking key which does not allow micrometric screw movement. Insert block key before the instrument goes into OFF position.
- Error indication when the screw is moved too fast or when the wrong keyboard functions are selected. (press the ON/C key to cancel the error condition).

10) **RESET**

A RESET key is provided which is protected against accidental movements

and accessible through a pinhole market RST. Press this key only when it is not possible to clear the instrument with the ON/C key.

11) SPECIAL MICROMETERS

MS1 Particularly suitable for the measurement of small pieces, grooves, etc. Measuring surface: Ø 2 x 5 mm.

MS2 Most suitable for the measurement of particular forms with conical and spherical surfaces, corners, etc. Conical measuring surfaces: 60° angle, length 5 mm.

MS3 Particularly suitable for measuring gears with minimum module 0,5mm, distance between centers, groves, etc. Disc measuring surface: Ø 22 mm.

MS4 Particularly suitable for the measurement of curved surfaces. The spherical contacts have Ø 6,5 mm and R – 4 mm.

MS5 Particularly suitable for measuring the thickness of soft materials. Disc shaped measuring surfaces: Ø 14 mm.

MS6 Most suitable for measturing hard to reach places and particular shapes. Wedge-shaped measuring surfaces: 60° angle, length 6 mm.

MS7 Particularly suitable for measuring narrow grooves, channels, etc. Knife blade shaped measuring surfaces: thickness 0,75 x 5 mm.

MS8 This micrometer includes a comparator, allowing both measuring and comparisons of round and flat pieces.

MS9 Suitable for measuring the average diameter of threads. Interchangeable measuring faces.

DIGIVERT Allows measuring of depths.

DIGICORD Micrometers for application on axial sliding tables for coordinates.

12) ACCUMULATORS RECHARGING OPERATION

When the accumulators are low recharge as follows:
- connect the adapter to the power main, checking for compatibility of power supply voltage;
- place the adapter plug in the jack socket properly;
- leave the instrument in change for approx. 12h avoiding extended charging, which can damage the accumulators.

It is possible to use the instrument during charging operation but the time required is extended. Do not store the instrument for long periods of time when the accumulators are discharged because they can be damaged. When storing the instrument it is recommended that it be recharged for approximately 6 hours every 6 months.
ATTENTION: The instrument is not to be used without the accumulators or with broken accumulators.
Time required for key response: 0.5 sec.

13) MAINTENANCE

This electronic LCD micrometer is a measuring instrument of fine quality, conceived to last in time; providing excellent service with minimum care. In case you should detect wear sings or any other defect on the instrument, inform

the Assistance Service of your distributor, by using the defect card included with the instrument. Use a dry cloth to clean the instrument. Never use solvents. Protect the instrument from humidity and from either too high or low temperatures, both when operating and when in its case.

14) REPLACING THE ACCUMULATORS

The accumulators generally last a long time. Whenever it is necessary to replace them procede as follows:

- remove the two screws from the back body separating it from the micrometer body;
- withdraw the accumulator connector from circuit;
- replace the back body and connect the accumulator pack to the circuit observing polarity (see figure 1);
- assemble the new back boby on micrometer body and tighten the two clamping screws.

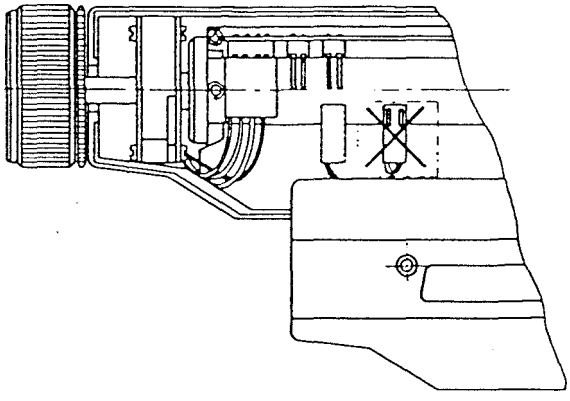

Fig. 1

15) WARRANTY

This micrometer has been carefully tested. However, should defects due to manufacturing errors or faulty material be detected, the after sale service of your distributor will repair or replace the faulty piece. Rechargeable batteries are not included in the above guarantee. This guarantee ceases should the instrument be touched by non-authorized persons, or in case of damages caused by improper use and by non-compliance to the instructions given.

SPECIFICATIONS \ CODES	UNIT	M2 25	M2 50	M2 75	M2 100	MS 1 ~ 9	V2	D2	D1
measuring range	mm	0 ÷ 25	25 ÷ 50	50 ÷ 75	75 ÷ 100		0 ÷ 25	0 ÷ 25	0 ÷ 25
	inch	0 ÷ 1"	1" ÷ 2"	2" ÷ 3"	3" ÷ 4"		0 ÷ 1"	0 ÷ 1"	0 ÷ 1"
resolution	µm	1							
	inch	0,00005"							0,00010"
accuracy (L = minimum opening)	µm	± (1,5 + L)					± (1,5 + L)		
	inch	± (0,00006" + L)					± (0,00006" + L)		
screw pitch	mm	0,5							
dimension of measuring faces	mm	Ø 6,5					Ø 6,5		
hardness of measuring faces	H.V.	≥760					≥760		
parallelism of measuring faces	µm	1,2		1,8					
uncertainty of measures		± 1 digit							
measuring force	N	5 ÷ 10				4 ÷ 7	5 ÷ 10		
repeatability		± 1 digit							
display		LCD, 8 digits with "-" sign plus function indicators							LED
zero setting		during any measuring range operation							
mm/inch conversion		automatically during any measuring range operation							preselection
memory		on all positive values							
GO-NO GO		on all positive values							
HOLD		during any measuring range operation							
operating time	h	50 (continuous operation)							
power source — AC adapter		220V 50Hz ~ 110V 60Hz							
power source — rechargeable accumulators	V;mAh	3 X 1,2 ; 250							
weight	g	390	490	640	780		400	270	270
reference gauge	mm		25	50	75				
storage temperature	°C	− 10 ÷ 50							
automatic switching off (AUTO-OFF)		after approximately 4' of inactivity							

Appendix C

A Compendium of Fortran Comment Sections and Connection Files for Echelle FIGARO Commands

OVERVIEW

-- ECH* ROUTINES FOR REDUCTION OF ECHELLE DATA --

ECHTRACT: Collapses a full echelle image into an extracted 2D format with one row per order. Simultaneously performs flat fielding (and normalizes flat field to unity in the center of each order). Order number becomes OUTPUT.Y.DATA while OUTPUT.X.DATA remains pixel number.

Related routines: TEMPLATE, YCADD, ECHPLOT, MBPLT. (see below)

ECHXCONT: Determines the continuum across "narrow" spectral features (i.e., features narrow enough that a spline fit in the X direction is a sufficiently accurate continuum estimate).

Related routines: ECHYCONT (see below); IDIV (standard FIGARO).

ECHYCONT: Determines the continuum across "wide" spectral features (i.e., not narrow enough to trust ECHXCONT result) by replacing ECHXCONT output at these locations by the average of the two adjacent orders, suitably normalized at the feature's boundaries.

Related routines: IDIV (standard FIGARO) used to actually perform the normalization by dividing the original input to ECHXCONT by the final output from ECHYCONT.

ECHARC: Automated version of ARC suitable for use on ECHTRACT'ed Th-Ar echelle arc frames. User does an interactive 1D fit to 3+ orders, and ECHARC identifies and performs fits to lines in all remaining orders. Output is to a WAVES image where WAVES.Z.DATA is the fit wavelength at each pixel.

Related routines: ICMULT, IADD (standard FIGARO) can be used to make a weighted average of multiple WAVES images from Th-Ar arcs which bracket an object image.

ECHXREBIN (see below).

ECHXREBIN:

Takes an object image and assigns wavelengths from a WAVES image (ECHARC output or a weighted average) to it by rebinning the object image in the X direction on to a constant Meff * Lambda scale. It creates a new data structure to hold the OUTPUT.Y.MEFF array, and writes into OUTPUT.X.DATA the product of Meff * Lambda.

Related routines: TEMPLATE, ECHPLOT, EXTRACT (see below).

... proposed: ECHICROSS, a routine which could cross-correlate a pair of ECHXREBIN'ed images in two dimensions as an alternative to separate SCROSS'es, one for each order.

ECHPLOT: Routine which makes a series of SPLOT-like plots from a collapsed echelle image, one per order over the specified range of orders. The X axis is Wavelength if the image has been through ECHXREBIN, pixel number otherwise. "-- Order # yy" is appended to the top label of each plot. Output to a BUILD file is in a form acceptable to the command MBPLT, although standard SOFT and HARD options exist.

Related routines: MBPLT (see below).

EXTRACT: Modified version of the standard FIGARO "EXTRACT" command, with the added feature of recognizing ECHXREBIN'ed data and able to reconstruct an output SPECTRUM.X.DATA = IMAGE.X.DATA / IMAGE.Y.MEFF = wavelength, since IMAGE.X.DATA is in this case Meff * Lambda.

--- Related Routines useful not only for Echelle Data ---

MBPLT: Literally, "M"ultiple "BPL"o"T" routine which routes a BUILD file from ECHPLOT or MPLOT (see below) to a hardcopy or softcopy device with the added option of having multiple plots per page. This is a vital feature for echelle data, in which every exposure typically results in up to sixty individual order spectra, each NX long.

TEMPLATE: Sets the user variable VARS.TEMPLATE to the specified TFILE input. At present only ECHTRACT and ECHXREBIN look to this variable in order to "do this time exactly what you did some time ago to the specified template file," but the idea has potential application to many other future FIGARO tasks.

YCADD
YCDIV
YCMULT
YCSUB: Routines which act on IMAGE.Y.DATA the same way XCADD, XCDIV, XCMULT, and XCSUB act on IMAGE.X.DATA ... namely, arithmetically by a constant factor. These were written to allow adjustment of IMAGE.Y.DATA = "Order Number" follow ECHTRACT, should the order number be incorrectly specified during ECHTRACT'ion.

--- Useful JKM "User" Routine Unrelated to Echelle Data ---

MPLOT: Modified version of the standard FIGARO "SPLOT" command, such that its BUILD file output is in a form acceptable to MBPLT for multiple plots per page. MPLOT is also capable of more sophisticated labels for each individual plot, to make identifying which output spectrum came from which input spectrum easier. For instance, if the parameter LABEL=".OBS.OBJECT", MPLOT will take SPECTRUM.OBS.OBJECT as the title of the plot.

SUBROUTINE ECHTRACT

E C H T R A C T

Adds a number of consecutive rows from an echelle image to produce a set of 1D spectra (1 from each order). A 'row' is all the pixels with a given y-value. Prior to this collapse, the user is given options of subtracting order-to-order contamination and also subtracting a smooth global background as determined from inter-order minima. The data is subsequently flat fielded, since flat fielding first would destroy inter-order information still present in the unflattened data.

Command parameters -

IMAGE The name of the image from which the order rows are to be taken.

NORDERS The expected number of orders to be found between YSTART and YEND. Needed only if TEMPLATE=FALSE.

MSTART The number of the first order in the range to be echtracted. Needed only if TEMPLATE=FALSE.

MDELTA The order number increment. The last order number, MEND, is found from MSTART+(NORDERS-1)*MDELTA. Needed only if TEMPLATE=FALSE.

FIT A keyword instructing the program to fit order cross-sections with Gaussian profiles in order to determine and subtract cross-talk from the wings of adjacent echelle orders.

YMAX1 The Y-row position of the first order peak to be fit. This value is used as an initial guess for the fit, and so should be close but needn't be exact. The value is required only if FIT=TRUE.

ZMAX1 An initial guess for the peak intensity of the first order to be fit. Needed only if FIT=TRUE.

YSIGMA An initial guess for the sigma (in pixels) of the order cross-section profile. Needed only if FIT=TRUE.

YMAX2 An initial guess for the Y-row position of the second order peak to be fit. The value is required only if FIT=TRUE. It doesn't matter whether YMAX2>YMAX1; in fact, the fit should begin at whichever Y extreme has orders farthest apart.

NFITS The number of X-positions at which the Gaussian order fitting should be done; the subtraction of adjacent order contamination will be based on interpolation between these NFITS solutions equally spaced in X, so in general lower S/N should use fewer NFITS. A value of NFITS is required only if FIT=TRUE.

TEMPLATE A keyword instructing the program to duplicate the echtraction process used on the template file. The template file has been set previously with the command TEMPLATE TF=_____. TEMPLATE is assumed FALSE if FIT=TRUE, and prompted for if FIT=FALSE.

SEARCH If TEMPLATE is .TRUE. and SEARCH is .TRUE. also, the program will pick out the highest value within the bounds specified by TEMPLATE.Y.ROW1 and .Y.ROW2; if both FIT and TEMPLATE are .FALSE., search will be automatically set to .TRUE. and the search will be carried out without the template bounds.

YSTART The Y-value of the first row to be used when looking for orders. If IMAGE has a .Y structure, the data from this is used. If not, the row numbers are used, starting from 1. YSTART is required only if FIT=FALSE and TEMPLATE=FALSE.

YEND The Y-value of the last row to be used. YEND is required only if FIT=FALSE and TEMPLATE=FALSE.

BCKGND A keyword instructing the program to determine and subtract a smoothed background as determined by the inter-order minima after subtraction of adjacent order contamination, if any.

YAVG The number of inter-order minima rows over which to smooth the background. If BCKGND=.TRUE., the inter-order minima rows will be first median filtered then smoothed by averaging; if BCKGND=.FALSE., only the median filtering will be performed.

XAVG The number of columns over which to smooth the background in the echelle dispersion direction. See the above YAVG description for BCKGND dependence.

SAVE A keyword instructing the program whether to save the smoothed background in a new .Z.BCKGND data structure. If SAVE=FALSE, the background will be output to a separate disk file that can easily be deleted or saved apart from the OUTPUT.Z.DATA image. The .Y information to be associated with

OUTPUT.Z.BCKGND is actually the .Y data + 1/2 order. That is, the first BCKGND row was found between the first and second DATA rows.

FLAT The name of the structure containing the flat field data. The actual data used is contained in the structure 'FLAT.Z.DATA'. No normalization of the flat field is required beforehand; ECHTRACT will normalize the center of each order to unity before dividing the data by it, so final counts in the center of each order will be representative of true counts, yet the echelle grating blaze function will be corrected by the flat yielding a straight continuum. Flat fielding will only be performed if the number of counts in the flat field rows exceeds the number of counts in the IMAGE data rows. The OUTPUT.Y.PROC array is a record of whether flat field processing has been done on a particular order (.Y.PROC[i]=0 indicates order i is un-flattened).

EXWIDTH The number of rows to be extracted per order. Actually the extraction range is from IYCENTER - HWHM to + HWHM, where HWHM = INTEGER((EXWIDTH-1)/2). This means that odd numbered values for EXWIDTH work as expected; even values default to the next lowest odd number. Required in all cases except TEMPLATE=.TRUE. and SEARCH=.FALSE.

OUTPUT The name of the resulting data, which will have the same X dimension as IMAGE and NORDERS Y entries. A new output format 'Echelle' will result from ECHTRACT, with this top-level file structure name associated with it.

Input data -

IMAGE is assumed to have a structure with the actual image data in IMAGE.Z.DATA; FLAT is checked to make sure it has the same dimensions as IMAGE. If TEMPLATE=TRUE, the row numbers to be echtracted are to be taken from TFILE.Y.ROW1 and TFILE.Y.ROW2 data structures. ECHTRACT checks to make sure that TFILE has the top-level structure name 'Echelle' (in other words, is an existing ECHTRACT output file).

Output data -

OUTPUT is created with the same structure as IMAGE, except that .Z.DATA will have only NORDERS Y entries, and if IMAGE has a .Y structure, this

will be omitted. Any .X structure will be copied over to OUTPUT.X unchanged.

User variables - (">" input, "<" output)

(>) TFILE The previously echtracted template file from which to take the rows to be echtracted, if the command keyword TEMPLATE is specified. 'TEMPLATE' =.FALSE. is the default. (Other user variables may be set by the command processor, in connection with the parameter default values).

originally EXTRACT: KS / CIT 29th June 1984
--rewritten for use as ECHTRACT: JKM / CIT 11th Nov 1986
-modified to use TEMPLATE file: JKM / CIT 18th Nov 1986

Modified:

JKM / CIT 9 December 1986:

WRUSER calls replaced with calls to PAR_WRUSER calls; The variable NOMAX renamed NORDERS for the sake of clarity. An OUTPUT.Y.DATA[] data structure was added to hold the order numbers "m" taken from user input.

JKM / CIT 29 April 1987:

The 'FIT' process was added to remove order-to-order cross-talk and so enable the true inter-order background to be determined. The 'BCKGND' subtraction process was therefore made possible, and set-up so that BCKGND subtraction could be done with or without order FITting and crosstalk removal. 'SAVE' was invented to allow the background to be inspected at some later time.

JKM / CIT 22 May 1987:

'EXWIDTH' was added as an input parameter, in the hopes that a wider extraction width would reduce the continuum undulations observed for data in which order width sigma varies along the order length.

JKM / CIT 17 June 1987:

The arrays OUTPUT.X.XFIT, OUTPUT.Y.YFIT, and OUTPUT.Z.SFIT were added to the output data structure so as to correct for these continuum undulations at a later time.

JKM / CIT 18 August 1987:

The array OUTPUT.Y.PROC was added to record whether or not flat fielding was done on a particular order. This decision is based on a comparison of the counts in the flat field image and in the input image.

JKM / CIT 24 August 1987:

The OUTPUT.Z.BCKGND (or OUTPUT_B.Z.DATA) arrays are median filtered in X and Y prior to smoothing by averaging in order to remove cosmic rays, bad columns, and bright emission lines from the inter-order minima rows before subtracting them from the data if BCKGND=.TRUE.

JKM / CIT 26 August 1987:

The SEARCH parameter is added to permit searching within the bounds specified by TFILE.Y.ROW1 and .ROW2, which is desirable for very low S/N data.

Parameter file for ECHTRACT command

```
COMMAND   ECHTRACT

       PARAMETER      IMAGE
            NAME      IM(AGE)
            TYPE      FILE
         OPTIONS      INPUT
          PROMPT      "(IMage) name of echelle image to
                      extract data from"-"

       PARAMETER      NORDERS
            NAME      NO(RDERS)
            TYPE      FLOAT
          PROMPT      "(NOrders) number of orders expected"

       PARAMETER      MSTART
            NAME      MS(TART)
            TYPE      FLOAT
          PROMPT      "(MStart) number of the first order in
                      range"

       PARAMETER      MDELTA
            NAME      MD(ELTA)
            TYPE      FLOAT
          PROMPT      "(MDelta) order number increment (-1 or
                      +1) ?"

       PARAMETER      FIT
            NAME      FIT
            TYPE      KEY
          PROMPT      "(FIT) orders with Gaussians to subtract
                      cross-talk?"

       PARAMETER      YMAX1
            NAME      YMAX1
            TYPE      FLOAT
          PROMPT      "(YMAX1) Y position of first order peak
                      to be fit"

       PARAMETER      ZMAX1
            NAME      ZM(AX1)
            TYPE      FLOAT
          PROMPT      "(ZMax1) Peak intensity of first order
                      to be fit"

       PARAMETER      YSIGMA
            NAME      YSIG(MA)
            TYPE      FLOAT
          PROMPT      "(YSIGma) Half width of first order to
                      be fit"
```

```
PARAMETER     YMAX2
     NAME     YMAX2
     TYPE     FLOAT
   PROMPT     "(YMAX2) Y  position of  second order to
              be fit"

PARAMETER     NFITS
     NAME     NF(ITS)
     TYPE     FLOAT
   PROMPT     "(NFits) number of fits to make  across
              image in X"

PARAMETER     TEMPLATE
     NAME     TE(MPLATE)
     TYPE     KEY
   PROMPT     "(TEmplate)  Base  echtraction  on  a
              template file?"

PARAMETER     SEARCH
     NAME     SE(ARCH)
     TYPE     KEY
   PROMPT     "(SEarch) Search  within template bounds
              for peak?"

PARAMETER     YSTART
     NAME     YST(ART)
     TYPE     FLOAT
   PROMPT     "(YSTart) Y  value to start search for
              orders"

PARAMETER     YEND
     NAME     YE(ND)
     TYPE     FLOAT
   PROMPT     "(YEnd)  Y  value  to  stop  search  for
              orders"

PARAMETER     BCKGND
     NAME     BCK(GND)
     TYPE     KEY
   PROMPT     "(BCKgnd) Smooth  and subtract global
              background?"

PARAMETER     YAVG
     NAME     YA(VG)
     TYPE     FLOAT
   PROMPT     "(YAvg) Number of ORDERS over which  to
              smooth in Y"

PARAMETER     XAVG
     NAME     XA(VG)
     TYPE     FLOAT
   PROMPT     "(XAvg) Number  of PIXELS over which to
              smooth in X"
```

```
PARAMETER     SAVE
     NAME     SAVE
     TYPE     KEY
   PROMPT     "(SAVE) Save  background as  part of
              OUTPUT.DST?"

PARAMETER     FLAT
     NAME     FL(AT)
     TYPE     FILE
  OPTIONS     INPUT
   PROMPT     "(FLat) name of flat field image"-"

PARAMETER     MONITOR
     NAME     MON(ITOR)
     TYPE     KEY
   PROMPT     "(MONitor)  ECHTRACT  process  on device
              'PGPLOT'?"

PARAMETER     EXWIDTH
     NAME     EXW(IDTH)
     TYPE     FLOAT
   PROMPT     "(EXWidth) Number of rows to extract per
              order"

PARAMETER     OUTPUT
     NAME     OUT(PUT)
     TYPE     FILE
  OPTIONS     OUTPUT
   PROMPT     "(OUTput) Collapsed  echelle image to be
              generated"
```

SUBROUTINE ECHXCONT

E C H X C O N T

This routine bridges narrow features in an image in X and then smoothes the result in X order to obtain a continuum image XCONT with these narrow features and noise removed. The FIGARO command ECHYCONT can then be used to bridge in Y wide features that still remain in the ECHXCONT output, and thereby one can create a continuum image that can be divided into the input image to rectify undulations in its continuum. To assist ECHYCONT, the present ECHXCONT routine compares each order to the average of the order(s) adjacent to it and so computes a trial mask that one can edit before turning it over to ECHYCONT for the final continuum calculation.

Command parameters -

IMAGE The name of the structure containing the image. The actual data to be operated on is assumed to be 'IMAGE.Z.DATA'

XMED (Numeric) The range in X used when median filtering the image to determine the local continuum.

INTERACT (Logical) If true, the user is given the option of fitting each order by hand on the currently defined SOFT device. If PREVIOUS=.TRUE., this option allows interactive corrections to the fits based on XMASK.ECH

PREVIOUS (Logical) If true, the program will look for a file XMASK.ECH from a previous ECHXCONT session and use it as a mask for interpolating the continuum across narrow features. If false, the following two input parameters are prompted for, and the mask determined based on their values.

CFACTOR (Numeric) The comparison factor between the input IMAGE and an X median filtered image, expressed as a fraction of the continuum level. Mismatches between the two images greater than CFACTOR are assumed to be narrow lines and interpolated across in X.

BWIDTH (Numeric) The bin width to be used when dividing the continuum regions into sections for cubic spline interpolation in X across narrow lines detected.

CMINIMUM (Numeric) The minimum size allowed for a continuum region detected. The default size is one (i.e., all continuum regions found are allowed), and CMINIMUM is not ordinarily prompted for.

XMASK (Logical) If true, the regions of the spectrum masked in X are written to the file XMASK.ECH -- note that this file can be changed with the editor and ECHXCONT repeated with PREVIOUS=.TRUE. if this first attempt is unsatisfactory in a few places.

CONTX (Logical) If true, the program will create a continuum file XCONT.ECH instead of the mask file XMASK.ECH (i.e., the file format used in X will be one giving regions of the continuum used, not regions of lines that were masked and not used). Note that only "X" is changed: the "Y" file remains YMASK.ECH. Note also that both output and input (for PREVIOUS=.TRUE.) in X are changed. Read "CONTX" as "context" to keep this straight.

XAVG (Numeric) The range in X used when smoothing the line- free orders to derive the final X continuum.

AFACTOR (Numeric) The fractional agreement required between an order and the average of its adjacent order, so as NOT to appear in YMASK.ECH (see below). For instance, if AFACTOR=0.01, YMASK.ECH will contain a list of all the places where an order disagrees with the average of its adjacent orders by more than 1 percent.

YMASK (Logical) If true, regions detected in disagreement by more than AFACTOR are written into the file YMASK.ECH -- note that this file can be changed with the editor and then given to ECHYCONT for final determination of the continuum across broad features in the spectrum.

XCONT The name of the continuum file to be created as a result of ECHXCONT's interpolation and smoothing in the X-direction.

-- Originally IXSMOOTH: KS / CIT 23rd Mar. 1983
-- Rewritten for use as ECHXCONT & modified:
JKM / ESO 24th Oct. 1987

Modified:

JKM / ESO 9. Nov. 1987

The YMASK trial comparison routines were added. The PREVIOUS and CMINIMUM parameters added. All known bugs were successfully exterminated.

Parameter file for ECHXCONT command

```
COMMAND ECHXCONT

      PARAMETER     IMAGE
           TYPE     FILE
           NAME     IM(AGE)
        OPTIONS     INPUT
         PROMPT     "(IMage) Name of input ECHELLE image"

      PARAMETER     XMED
           TYPE     FLOAT
           NAME     XM(ED)
         PROMPT     "(XMed) Number of PIXELS to median
                    filter in X"

      PARAMETER     CLEAN
           TYPE     KEY
           NAME     CLEAN
        OPTIONS     NOPROMPT
         PROMPT     "(CLEAN) image by median filtering in X
                    a small amount ?"

      PARAMETER     NCLEAN
           TYPE     FLOAT
           NAME     NC(LEAN)
        OPTIONS     NOPROMPT
         PROMPT     "(NClean) Number of PIXELS to clean
                    image in X"

      PARAMETER     INTERACT
           NAME     INTERACT
           TYPE     KEY
         PROMPT     "(INTERACT) Select line regions
                    interactively on "PGSOFT" ?"

      PARAMETER     PREVIOUS
           NAME     PREV(IOUS)
           TYPE     KEY
         PROMPT     "(PREVious) Use XMASK.ECH from a
                    previous ECHXCONT ?"

      PARAMETER     CFACTOR
           TYPE     FLOAT
           NAME     CF(ACTOR)
         PROMPT     "(CFactor) Fraction of continuum line
                    mask threshold"

      PARAMETER     WFACTOR
           TYPE     FLOAT
           NAME     WF(ACTOR)
         PROMPT     "(WFactor) by which to increase lines
                    masked widths"
```

```
PARAMETER       BWIDTH
     TYPE       FLOAT
     NAME       BW(IDTH)
  OPTIONS       NOPROMPT
   PROMPT       "(BWidth) Bin width for cubic spline
                interpolation"

PARAMETER       CMINIMUM
     TYPE       FLOAT
     NAME       CM(INIMUM)
  OPTIONS        NOPROMPT
   PROMPT       "(CMinimum)   Minimum  Continuum  region
                size for spline fit"

PARAMETER       XMASK
     NAME       XMASK
     TYPE       KEY
   PROMPT       "(XMASK) Write out masked  areas to file
                XMASK.ECH ?"

PARAMETER       CONTX
     NAME       CONTX
     TYPE       KEY
   PROMPT       "(CONTX) Use  XCONT.ECH file instead of
                XMASK.ECH file ?"

PARAMETER       XAVG
     TYPE       FLOAT
     NAME       XA(VG)
   PROMPT       "(XAvg) Number of PIXELS to smooth in X"

PARAMETER       AFACTOR
     TYPE       FLOAT
     NAME       AF(ACTOR)
   PROMPT       "(AFactor)      Fractional      adj-order
                agreement for continua"

PARAMETER       YMASK
     NAME       YMASK
     TYPE       KEY
   PROMPT       "(YMASK) Write out trial  YMASK areas to
                YMASK.ECH ?"

PARAMETER       MONITOR
     NAME       MON(ITOR)
     TYPE       KEY
   PROMPT       "(MONitor) ECHXCONT  processes on device
                'PGPLOT'?"
```

```
PARAMETER       YMIN
     TYPE       FLOAT
     NAME       YMIN
  OPTIONS       NOPROMPT
   PROMPT       "(YMIN) Minimum value for MONITOR plots"


PARAMETER       YMAX
     TYPE       FLOAT
     NAME       YMAX
  OPTIONS       NOPROMPT
   PROMPT       "(YMAX) Maximum value for MONITOR plots"

PARAMETER       XCONT
     TYPE       FILE
     NAME       XC(ONT)
   PROMPT       "(XCont) Name of smoothed  X_CONTinuum
                output image"
```

SUBROUTINE ECHYCONT

E C H Y C O N T

This routine determines the continuum in places where there are broad features by comparison with the continua of adjacent orders. It is assumed that the input has first been through ECHXCONT, thus is devoid of narrow features, and has already been sufficiently smoothed in the X direction also.

Command parameters -

XCONT The name of the input image, assumed to be the output from the FIGARO command ECHXCONT. The actual input continua to be further processed by ECHYCONT is taken from the structure 'XCONT.Z.DATA'.

XRANGE (Numeric) The number of pixels on each side of a YMASKed feature to be used to normalize the adjacent order average to the local continuum.

SMOOTH (Logical) If true, in addition to using adjacent orders to bridge broad features, ECHYCONT will use several of the adjacent orders to smooth each order. This might be requested to reduce the amplitude of residual undulations in XCONT from shallow dips not removed by ECHXCONT.

YRANGE (Numeric) The range in Y used to determine the local continuum during smoothing. Needed only if SMOOTH=true.

YWTS (Numeric Vector) The set of YRANGE weights to be applied over YRANGE during smoothing. Needed if SMOOTH=true.

MONITOR (Logical) If true, intermediate results are plotted on the device with logical name 'PGPLOT'. MONITOR is not prompted for, so must be specified explicitly in order to be invoked (was designed for debugging use only).

YCONT The name of the final resulting continuum. This ought not be the same as XCONT, since several iterations may be required to get YCONT right ....

-- Originally IXSMOOTH: KS / CIT 23rd Mar. 1983
-- Rewritten for use as ECHYCONT: JKM / ESO 6th Nov. 1987

Parameter file for ECHYCONT command

```
COMMAND ECHYCONT

      PARAMETER     XCONT
           TYPE     FILE
           NAME     XC(ONT)
        OPTIONS     INPUT
         PROMPT     "(XCont) Name of X CONTinuum input
                    image"

      PARAMETER     XRANGE
           TYPE     FLOAT
           NAME     XR(ANGE)
        OPTIONS     NOPROMPT
         PROMPT     "(XRange) Number of PIXELS to use for
                    normalizaton"

      PARAMETER     SMOOTH
           NAME     SMOOTH
           TYPE     KEY
         PROMPT     "(SMOOTH) Further smooth orders in the
                    Y-direction ?"

      PARAMETER     YRANGE
           TYPE     INT
           NAME     YR(ANGE)
         PROMPT     "(YRange) Number of orders to use for
                    Y-smoothing"

      PARAMETER     YWTS
           NAME     YW(TS)
           TYPE     FLOAT[15]
         PROMPT     "(YWts) Relative order weights_ "

      PARAMETER     MONITOR
           NAME     MON(ITOR)
           TYPE     KEY
         PROMPT     "(MONitor) ECHYCONT processes on device
                    'PGPLOT'?"

      PARAMETER     YMIN
           TYPE     FLOAT
           NAME     YMIN
        OPTIONS     NOPROMPT
         PROMPT     "(YMIN) Minimum value for MONITOR plots"

      PARAMETER     YMAX
           TYPE     FLOAT
           NAME     YMAX
        OPTIONS     NOPROMPT
         PROMPT     "(YMAX) Maximum value for MONITOR plots"
```

```
PARAMETER     YCONT
     TYPE     FILE
     NAME     YC(ONT)
   PROMPT     "(YCont)  Name  of  Y  CONTinuum  output
              image"
```

SUBROUTINE ECHARC

E C H A R C (Version 1.0, 18-NOV-1987 ff.)
(Version 1.5, 08-DEC-1987 ff.)

This substantially revised version of ECHARC0 performs the 1D ARC process on 3-10 orders of a collapsed echelle image, and then automatically detects lines and performs fits to all the remaining orders. The output from the program is a complete listing of all lines found (ARLINES.ECH) and an output image with WAVES.Z.DATA containing the fitted wavelengths. One can then use ICMULT and IADD to compute a weighted average of two or more such output fits, and then ECHXREBIN to rebin the data onto a constant "Meff * Lambda" .X.DATA scale.

Command parameters -

IMAGE The arc data. This should be a .dst file with a two-dimensional .z.data component (pixels,orders). ECHARC assumes there is a .y.data component giving order numbers "m" (such as produced as output from the command ECHTRACT). If there is a .x.data component the information it contains will be used during the program, although usually the .x.data will simply be pixel number.

ARCTYPE The type of arc that was used - eg HELIUM, NEON, etc. ARC will look for a file called ARCTYPE.ARC which should hold the line list for the arc.

INTERACTIVE The number of orders to be fit interactively.

ORDERS The array of INTERACTIVE order numbers to be fit.

NCOEFF The initial number of polynomial fit coefficients.

SIGMA The initial value for the line width.

ARFILE The name of the list file from which the previous fit is to be read. Only used if PREVIOUS is specified. Note that the output is always written to ARLINES.ECH. Default extension is .ECH.

WAVES An output image with WAVES.Z.DATA containing the fitted wavelengths from this ECHARC solution.

Command keywords -

PREVIOUS If specified, ARC will read in the line list from the previous session as a starting point.

User variables -

(>) SOFT (Char) The device/type to be used for graphics soft plots. See the SOFT command for details. The device must support a cursor.
(>) HARD (Char) The device/type for graphics hard plots.

Input -

As named May use the lines from a previous run. If so by ARFILE these are read from the previous run's output file. See below.

Output -

ARLINES.ECH
File containing the lines used in the final fit. Format is as follows - Number of lines used in fit (I5)
1 blank record, then one header record.
Then one record for each line, giving order, channel number, wavelength, calculated wavelength, wavelength discrepancy, line number, and auto flag (I3,4F13.4,I7,A4). The auto flag is either " (A)" for a single order Auto fit, " (E)" for complete echelle order auto fit, or is a blank string for lines explicitly identified by user. Then one blank record, then a record giving the RMS error and the value of SIGMA used (12X,F10.2,19X,F5.2). Then one blank record, then one record giving the number of coefficients of the fit (15X,I3).

Functions / subroutines used -

ECH_ARINTR (FIGARO)
Plots an order section by section and allows user to identify lines, fit a polynomial to those lines, and repeat. When an order is finished, the lines identified within it are written to the file ARLINES.ECH in case of problems during the fit to the next order.

ECH_ARGETL (FIGARO)
Reads order, channel, wavelength, etc., information from an existing ARLINES.ECH -format file to use as a starting point for fits to the current order.

Originally ARC : KS / CIT 13th June 1984
Modified:

28th Nov 1984 KS/AAO

Test for only one line added before fit.

10th Dec 1984 KS/AAO

Number of arc lines allowed increased.

5th Sept 1985 KS/AAO

Dispersion plot facility added and menu operation adopted for the fit, edit, refit sequence. ARFILE parameter added. Output file name now output. Line number added to output file format. RMS now output after 'C'. Weights array now incorporated everywhere, but only really used in ARFIT for the 'RMS without this line' figure. Autofit added, together with class array. Defaults for order and sigma now taken from previous file, if used.

12th Sept 1985 KS/AAO

Now checks dispersion and decides if a double precision X array has to be created. Error actions modified to follow later Figaro style using FAULT and FIG_DTAERR. WRUSER calls changed to PAR_WRUSER.

30th Sept 1985 KS/AAO

'Modify' added to menu options. Order may now be specified as 0.

22nd Nov 1985 KS/AAO

Occasional bug causing access violation in final hardcopy plot traced to failure to remap Z array after creation of new X array. Fixed.

30th June 1986 KS/AAO

Initially requested order is now remembered until enough lines have been selected.

-- Rewritten for use as ECHARC0: JKM / CIT 9 Dec 1986

Modified for use with 2D input data, one order at a time. "ORDER" (of polynomial fit) renamed "NCOEFF" and all occurences of [real] ORDER+1 ---> ORDER [NCOEFF] changed to a consistent NCOEFF def'n.

Output file renamed "ARLINES.ECH" and format of file changed to include order number for each line identified. All subroutines affected by this revision renamed ECH_AR...

--Modified for use as ECHARC (v. 1.0): JKM / ESO 18 Nov 1987

The highly interactive loop through all orders was replaced by interactive fits required for only three orders, with the program then identifying lines and performing fits automatically for all the remaining orders in the input image. WAVES image added.

Modified: --> ECHARC: v. 1.5 JKM / ESO 8. Dec 1987

The automatic search sequence was changed, so that instead of starting with order 1 and going to order NY, it starts mid-way between the first and last order interactively fit and proceeds from the center outward in four stages. It then makes three additional attempts to fit orders previously unsatisfactory.

Parameter file for ECHARC command

```
COMMAND ECHARC

      PARAMETER     IMAGE
           NAME     IM(AGE)
           TYPE     FILE
        OPTIONS     INPUT
         PROMPT     "(IMage) Collapsed echelle arc  image to
                    be fitted"

      PARAMETER     ARCTYPE
           NAME     AR(CTYPE)
           TYPE     CHAR
         PROMPT     "(ARctype) Type of arc"

      PARAMETER     INTERACTIVE
           NAME     INT(ERACTIVE)
           TYPE     INT
         PROMPT     "(INTeractive) Number  of orders to fit
                    interactively"

      PARAMETER     ORDERS
           NAME     ORD(ERS)
           TYPE     FLOAT[10]
         PROMPT     "(ORDers) Order numbers_ "

      PARAMETER     SIGMA
           NAME     SI(GMA)
           TYPE     FLOAT
         PROMPT     "(SIgma) Arc line half width in pixels"

      PARAMETER     NCOEFF
           NAME     NC(OEFF)
           TYPE     FLOAT
         PROMPT     "(NCoeff)  Number  of  polynomial
                    coefficients"

      PARAMETER     PREVIOUS
           NAME     PRE(VIOUS)
           TYPE     KEY
         PROMPT     "(PREvious) Use  arc lines from previous
                    fit?"

      PARAMETER     MONITOR
           NAME     MON(ITOR)
           TYPE     KEY
         PROMPT     "(MONitor) ECHARC  autofitting on device
                    'PGPLOT'?"
```

```
PARAMETER     ARFILE
     NAME     ARF(ILE)
     TYPE     CHAR
   PROMPT     "(ARFile) Name of file giving previous
              fit"

PARAMETER     WAVES
     NAME     WA(VES)
     TYPE     FILE
   PROMPT     "(WAves) Name of wavelength output
              image"
```

SUBROUTINE ECHXREBIN

E C H X R E B I N

This routine transfers wavelengths from WAVES.Z.DATA to the x-axis scale OUTPUT.X.DATA after multiplying wavelength by order number and computing an average M*LAMBDA scale. Then for each order, and "effective" order number OUTPUT.Y.MEFF[ ] is calculated and the INPUT.Z.DATA rebinned to this new scale according to WAVES.Z.DATA.

Command parameters -

IMAGE The name of the structure containing the image. The actual data to be operated on is assumed to be ´IMAGE.Z.DATA´

WAVES The name of the file containing wavelength data as ´WAVES.Z.DATA´ for each pixel of IMAGE. This can be obtained from ECHARC, and manipulated with ICDIV and IADD to obtain a weighted mean scale from two or more arcs if necessary.

TEMPLATE (Logical) If true, the program looks to TFILE.X.DATA and TFILE.Y.MEFF to establish the wavelength scale onto which INPUT.Z.DATA should be rebinned; otherwise ECHXREBIN calculates these based on WAVES.Z.DATA. The command TEMPLATE TFILE=xxxx can be used to specify the name of the template file.

LINEAR (Logical) If true, the output file will be rebinned with a constant wavelength difference between adjacent pixels in a given order, otherwise there will be a constant velocity difference between adjacent pixels of all of the orders (default). Required only if TEMPLATE=.FALSE.

IQUAD (Logical) If true, quadratic interpolation is used when rebinning, otherwise linear interpolation is used.

CFLUX (Logical) If true, flux is conserved during rebinning, otherwise the mean value will be conserved (default).

OUTPUT The name of the resulting output file, which can be the same as IMAGE.

-- JKM / ESO 18th Nov. 1987

Parameter file for ECHXREBIN command

```
COMMAND ECHXREBIN

      PARAMETER     IMAGE
           TYPE     FILE
           NAME     IM(AGE)
        OPTIONS     INPUT
         PROMPT     "(IMage) Image  to be rebinned onto a
                    wavelength scale"

      PARAMETER     WAVES
           TYPE     FILE
           NAME     WA(VES)
        OPTIONS     INPUT
         PROMPT     "(WAves) Image containing wavelength
                    information"

      PARAMETER     TEMPLATE
           NAME     TEMPLATE
           TYPE     KEY
         PROMPT     "(TEMPLATE) Rebin  to same scale as a
                    template?"

      PARAMETER     LINEAR
           NAME     LINEAR
           TYPE     KEY
         PROMPT     "(LINEAR) Use a linear  not logarithmic
                    wavelength scale ?"

      PARAMETER     IQUAD
           NAME     IQUAD
           TYPE     KEY
        OPTIONS     NOPROMPT
         PROMPT     "(IQuad)   Rebin   using   quadratic   not
                    linear interpolation ?"

      PARAMETER     CFLUX
           NAME     CFLUX
           TYPE     KEY
        OPTIONS     NOPROMPT
         PROMPT     "(CFLUX) Rebin data conserving  flux not
                    mean intensity ?"

      PARAMETER     OUTPUT
           TYPE     FILE
           NAME     OUT(PUT)
         PROMPT     "(OUTput) Name  of wavelength calibrated
                    OUTPUT image"
```

SUBROUTINE ECHPLOT

E C H P L O T

Produces a build file of 1D plots from data in a collapsed 2D echelle data structure.

Command parameters -

IMAGE The data to be plotted. This should be a .dst file with a .z.data component. If there is a .x.data component this will be used to give the x-axis. If not, the x-axis will just have to be the numbers from 1 to n. Note that in either case, XSTART and XEND refer to pixel numbers (since wavelengths differ each order).

YSTART The first order number to be plotted.

YEND The final order number to be plotted. (YSTART and YEND are not required if the WHOLE keyword is specified.)

WLENGTH The length in Angstroms for each plot, which if specified and is less than the length of an order will cause two or more plots to be produced ... cumbersome, so WLENGTH is hidden.

XSTART The x-pixel at which plotting is to start.

XEND The x-pixel at which plotting is to end. (XSTART and XEND are not required if the WHOLE keyword is specified.)

MFACTOR If AUTOSCALE, HIGH=MFACTOR*(Order Median) & LO=0.

HIGH The maximum value to be used for the plot.

LOW The minimum value to be used for the plot.

BIAS A value used to displace the plot - BIAS is effectively a value added to the data before it is plotted. (It is implemented as a value subtracted from both HIGH and LOW.) (HIGH,LOW and BIAS are not required if the AUTOSCALE keyword is specified.)

LABEL A label for the plot.

COLOUR The colour for the plot (only meaningful for the Grinnell - later may be extended to map onto different line types). The axes are always white.

THICKNESS The width of the lines used for the plot. This should really be 1 for anything other than a high-resolution device like the Versatec.

BFILE Only used for a 'build' plot. The name of the file to be used.

Command keywords -

AUTOSCALE The program is to work out the values for HIGH and LOW, using the maximum and minimum values in the data over the specified range.

WHOLE The program is to display all of each order.

CONTINUUM If true, the program draws a reference line at the continuum=1.00 level. Useful only for data that has been normalized.

AXES Axes will be plotted.

LINES The plot is not done as a histogram, but as a 'join the dots' line plot.

User variables - (">" input, "<" output)

(<) TVXST Is set to the starting x-value for the plot.

(<) TVXEN Is set to the final x-value for the plot.

(<) TVHIGH Is set to the same value as HIGH.

(<) TVLOW Is set to the same value as LOW.

(<) TVFILE Is set to the value of SPECTRUM.

(<) TVCOLOR Is set to the GRPCKG code for the plot colour. (The TV.. variables are intended for use by cursor routines, and reflect the settings for the last plot made, even if XSTART etc are changed.)

(Other user variables may be set by the command processor, in connection with the parameter values.)

-- Based on SPLOT command: KS / CIT 30th April 1984
-- First ECHPLOT version: JKM / CIT 24th Nov. 1986

ECHPLOT Modified:

17th Nov 1987 - JKM / ESO
YSTART and YEND parameters added; definition of WHOLE changed to mean all of every order. CONTINUUM keyword added. Order number added to the title of each plot.

28th Nov 1987 - JKM / ESO
XSTART and XEND redefined strictly in terms of pixel number. Plotting wavelengths now possible if IMAGE.Y.MEFF data structure can be found. WLENGTH hidden parameter added to make possible plots with constant A/cm_of_paper.

Parameter File For ECHPLOT Command

```
COMMAND ECHPLOT

       PARAMETER      IMAGE
            NAME      IM(AGE)
            TYPE      FILE
         OPTIONS      INPUT
          PROMPT      "(IMage) Collapsed  echelle image to be
                      plotted"

       PARAMETER      WHOLE
            NAME      WH(OLE)
            TYPE      KEY
          PROMPT      "(WHole) Plot all of every order ?"

       PARAMETER      YSTART
            NAME      YS(TART)
            TYPE      FLOAT
          PROMPT      "(YStart)  First  order  number   to  be
                      plotted"

       PARAMETER      YEND
            NAME      YE(ND)
            TYPE      FLOAT
          PROMPT      "(YEnd) Last order number to be plotted"

       PARAMETER      WLENGTH
            NAME      WL(ENGTH)
            TYPE      FLOAT
         OPTIONS      NOPROMPT
          PROMPT      "(WLength) Length  in  Angstroms desired
                      for every plot"

       PARAMETER      XSTART
            NAME      XS(TART)
            TYPE      FLOAT
          PROMPT      "(XStart)  First  X-pixel  number to be
                      plotted"

       PARAMETER      XEND
            NAME      XE(ND)
            TYPE      FLOAT
          PROMPT      "(XEnd)  Last  X-pixel   number   to  be
                      plotted"

       PARAMETER      AUTOSCALE
            NAME      AU(TOSCALE)
            TYPE      KEY
          PROMPT      "(AUtoscale) Scale  so all of spectrum
                       fits?"
```

```
PARAMETER     MFACTOR
     NAME     MF(ACTOR)
     TYPE     FLOAT
  OPTIONS     NOPROMPT
   PROMPT     "(MFactor) Autoscale median factor"

PARAMETER     HIGH
     NAME     HI(GH)
     TYPE     FLOAT
   PROMPT     "(HIgh) Maximum data value to be
              plotted"

PARAMETER     LOW
     NAME     LO(W)
     TYPE     FLOAT
   PROMPT     "(LOw) Minimum data value to be plotted"

PARAMETER     CONTINUUM
     NAME     CONT(INUUM)
     TYPE     KEY
   PROMPT     "(CONTinuum) Draw line at CONTINUUM=1.00
              level?"

PARAMETER     BIAS
     NAME     BI(AS)
     TYPE     FLOAT
  OPTIONS     NOPROMPT
   PROMPT     "(BIas) Bias value to be added to data"

PARAMETER     LABEL
     NAME     LAB(EL)
     TYPE     CHAR
   PROMPT     "(LABel) Label for plot"

PARAMETER     AXES
     NAME     AX(ES)
     TYPE     KEY
  OPTIONS     NOPROMPT
   PROMPT     "(AXes) Plot and label axes?"

PARAMETER     LINES
     NAME     LIN(ES)
     TYPE     KEY
  OPTIONS     NOPROMPT
   PROMPT     "(LINes) Use a line plot (not a
              histogram)?"

PARAMETER     COLOUR
     NAME     COL(OUR)
     TYPE     CHAR
  OPTIONS     NOPROMPT
   PROMPT     "(COLour) Plot colour (Bl, Wh, R, G, B,
              Cy, Ma, Y)"
```

```
PARAMETER     THICKNESS
     NAME     TH(ICKNESS)
     TYPE     INT
   PROMPT     "(THickness) Plotted line width"

PARAMETER     BFILE
     NAME     BF(ILE)
     TYPE     CHAR
   PROMPT     "(BFile) File to use to build the plot"
```

SUBROUTINE EXTRACT

E X T R A C T

Adds a number of consecutive rows from an image to produce a 1D data object. (A 'row' is all the pixels with a common given y-value.) This version of EXTRACT (28.NOV.1987ff) looks to see whether the image is in "Echelle" format, and if so then it checks to see whether it can compute an OUTPUT.X.DATA wavelength scale from IMAGE.X.DATA and IMAGE.Y.MEFF information, if of course only one order is requested (YSTART=YEND).

Command parameters -

IMAGE The name of the image from which the rows are to be taken.

YSTART The Y-value of the first row to be used. If IMAGE has a .Y structure, the data from this is used. If not, the row numbers are used, starting from 1.

YEND The Y-value of the last row to be used.

SPECTRUM The name of the resulting 1D data frame.

Input data -

IMAGE is assumed to have a structure with the actual image data in IMAGE.Z.DATA

Output data -

SPECTRUM is created with the same structure as IMAGE, except that .Z.DATA will only have one dimension, and if IMAGE has a .Y structure, this will be omitted. Any .X structure will be copied unchanged.

KS / CIT 29th June 1984

Modified:

28. Nov. 1987 - JKM / ESO.

The "Echelle" specific operations were added. The lengths of IMAGE, SPECT, etc., character variables were increased to 64 to allow room for directory name as well as filename.

Parameter file for EXTRACT command

```
COMMAND   EXTRACT

      PARAMETER      IMAGE
           NAME      IM(AGE)
           TYPE      FILE
        OPTIONS      INPUT
         PROMPT      "(IMage) name of image to extract  data
                     from"-"

      PARAMETER      YSTART
           NAME      YS(TART)
           TYPE      FLOAT
         PROMPT      "(YStart) first y-value to be used"

      PARAMETER      YEND
           NAME      YE(ND)
           TYPE      FLOAT
         PROMPT      "(YEnd) last y-value to be used"

      PARAMETER      SPECTRUM
           NAME      SP(ECTRUM)
           TYPE      FILE
        OPTIONS      OUTPUT
         PROMPT      "(SPectrum) name  of spectrum  to be
                     generated"
```

SUBROUTINE MBPLT

M B P L T

Creates a plot from a 'build' file as output by SPLOT then multiple MPLOTs.

Command parameters -

DEVICE a character string in the form used by PGPLOT and GRPCKG - ie has the form device/type, eg 'PPLT.DAT/PR'.

BFILE the name of the build file to be plotted.

NXSUB the number of plots per page in the x direction.

NYSUB the number of plots per page in the y direction.

Command keywords -

SPOOL if specified, any hardcopy files are spooled automatically to the appropriate printer. Note: A number of special strings are recognised for device -
SOFT - the current soft plot device.
HARD - the current hard plot device.
PRINTRONIX - the printronix printer.
VERSATEK - the versatek printer.
RETRO - the current terminal, as a Retrographics 640
VT125 - the current terminal, as a VT125
TEK - the current terminal, as a Tektronix 4010
GRINNELL - the Grinnell image display.

These can be abbreviated.

User variables used - (">" input)

(>) SOFT The current soft plot device
(>) HARD The current hard plot device

JKM / cit 8 Oct 1985
based on BPLOT by KS / CIT 29th Sept 1983

Parameter file for MBPLT command

```
COMMAND MBPLT

      PARAMETER     DEVICE
           NAME     DEV(ICE)
           TYPE     CHAR
         PROMPT     "(DEVice) Device/type for plot output"

      PARAMETER     BFILE
           NAME     BF(ILE)
           TYPE     CHAR
        OPTIONS     NOPROMPT
         PROMPT     "(BFile) Build file to be plotted"

      PARAMETER     NXSUB
           NAME     NX(SUB)
           TYPE     FLOAT
         PROMPT     "(NXsub) Number  of page subdivisions in
                    X"

      PARAMETER     NYSUB
           NAME     NY(SUB)
           TYPE     FLOAT
         PROMPT     "(NYsub) Number of page  subdivisions in
                    Y"

      PARAMETER     SPOOL
           NAME     SP(OOL)
           TYPE     KEY
        OPTIONS     NOPROMPT
         PROMPT     "(SPool) Automatically  spool file to
                    printer?"
```

SUBROUTINE TEMPLATE

T E M P L A T E

Sets the user variable (TFILE) that specifies the echtraction template file, from which ECHTRACT takes .Y information

Command parameters -

TFILE a character string giving the echtracted file name.

Command keywords -

None.

originally HARD: KS / CIT 31st Dec 1982
rewritten for use as TEMPLATE: JKM / CIT 18th Nov 1986

Parameter File For TEMPLATE Command

```
COMMAND TEMPLATE

      PARAMETER     TFILE
           NAME     TF(ILE)
           TYPE     FILE
        OPTIONS     INPUT
         PROMPT     "(TFile) Echtracted  image to use as a
                    template"
```

SUBROUTINE ICONST

I C O N S T

This routine is the main body of ICMULT,ICDIV,ICADD and ICSUB, and of XCMULT, XCDIV, XCADD and XCSUB, and most recently of YCMULT, YCDIV, YCADD, and YCSUB. The Ixxxx routines operate on the data in an image, the Xxxx routines operate on the data in the X array of the input file, and the Yyyy routines operate on the data in the Y array of the input file. *CMULT multiplies by a constant. Since the constant can be less than 1., these functions will also divide by a constant, but *CDIV saves the caller from having to calculate a reciprocal. *CADD adds a constant, while *CSUB subtracts a constant.

Command parameters -

IMAGE (Character) The name of the structure containing the image. The actual data to be operated on is assumed to be 'IMAGE.Z.DATA' for the Ixxxx routines, 'IMAGE.X.DATA' for the Xxxx routines, or 'IMAGE.Y.DATA' for the Yyyy routines.

FACTOR (Numeric) The value of the constant factor.

OUTPUT (Character) The name of the result of the operation. This can be the same as for IMAGE. If not, a new structure is created, with everything but the data a direct copy of the input. The command name is used to distinguish between the possible operations.

KS / CIT 12th June 1984

Modified:

30th Dec 1985. KS / AAO. ICSUB added.
10th July 1986. KS / AAO. Xxxx routines added.
07th Sept. 1987 JKM / CIT. Yyyy routines added.

Parameter file for YCADD command

```
COMMAND YCADD

      PARAMETER     IMAGE
           TYPE     FILE
           NAME     IM(AGE)
        OPTIONS     INPUT
         PROMPT     "(IMage) Image  with Y  data to be added
                    to"

      PARAMETER     FACTOR
           TYPE     FLOAT
           NAME     FAC(TOR)
         PROMPT     "(FACtor) Additive constant"

      PARAMETER     OUTPUT
           TYPE     FILE
           NAME     OUT(PUT)
        OPTIONS     OUTPUT
         PROMPT     "(OUTput) Name of resulting image"
```

Parameter file for YCDIV command

```
COMMAND YCDIV

      PARAMETER     IMAGE
           TYPE     FILE
           NAME     IM(AGE)
        OPTIONS     INPUT
         PROMPT     "(IMage) Image with Y data to be divided
                    into"

      PARAMETER     FACTOR
           TYPE     FLOAT
           NAME     FAC(TOR)
         PROMPT     "(FACtor) to be divided by"

      PARAMETER     OUTPUT
           TYPE     FILE
           NAME     OUT(PUT)
        OPTIONS     OUTPUT
         PROMPT     "(OUTput) Name of quotient image"
```

Parameter file for YCMULT command

```
COMMAND YCMULT

      PARAMETER     IMAGE
           TYPE     FILE
           NAME     IM(AGE)
        OPTIONS     INPUT
         PROMPT     "(IMage) Image with Y data to be
                    multiplied by"

      PARAMETER     FACTOR
           TYPE     FLOAT
           NAME     FAC(TOR)
         PROMPT     "(FACtor) to be multiplied by"

      PARAMETER     OUTPUT
           TYPE     FILE
           NAME     OUT(PUT)
        OPTIONS     OUTPUT
         PROMPT     "(OUTput) Name of product image"
```

Parameter file for YCSUB command

```
COMMAND YCSUB

      PARAMETER     IMAGE
           TYPE     FILE
           NAME     IM(AGE)
        OPTIONS     INPUT
         PROMPT     "(IMage)  Image  with  Y  data  to  be
                    subtracted from"

      PARAMETER     FACTOR
           TYPE     FLOAT
           NAME     FAC(TOR)
         PROMPT     "(FACtor) to be subtracted"

      PARAMETER     OUTPUT
           TYPE     FILE
           NAME     OUT(PUT)
        OPTIONS     OUTPUT
         PROMPT     "(OUTput) Name of resulting image"
```

SUBROUTINE MPLOT

M P L O T

Produces a plot of a spectrum, several per page, as defined LATER by nxsub and nysub (see mbplt.for). The plot is directed to the device defined by the user variables 'SOFT' and 'HARD', and by the value of the command keyword 'HARDCOPY', so will appear immediately if these specify a video device (VT125, Grinnell, etc.). If a hardcopy device is specified, the file for that device will be produced, but SPLOT does not attempt to spool it off for printing.

Command parameters -

SPECTRUM The data to be plotted. This should be a .dst file with a .z.data component. If there is a .x.data component this will be used to give the x-axis. If not, the x-axis will just have to be the numbers from 1 to n.

XSTART The x-value at which plotting is to start. XEND The x-value at which plotting is to end. (XSTART and XEND are not required if the WHOLE keyword is specified.)

HIGH The maximum value to be used for the plot.

LOW The minimum value to be used for the plot.

BIAS A value used to displace the plot - BIAS is effectively a value added to the data before it is plotted. (It is implemented as a value subtracted from both HIGH and LOW.) (HIGH,LOW and BIAS are not required if the AUTOSCALE keyword is specified.)

LABEL A label for the plot.

COLOUR The colour for the plot (only meaningful for the Grinnell - later may be extended to map onto different line types). The axes are always white.

THICKNESS The width of the lines used for the plot. This is only used for 'hard' & 'build' plots, and should really be 1 for anything other than a high-resolution device like the Versatec.

BFILE Only used for a 'build' plot. The name of the file to be used.

Command keywords -

AUTOSCALE	The program is to work out the values for HIGH and LOW, using the maximum and minimum values in the data over the specified range.
WHOLE	The program is to display all of the spectrum.
HARDCOPY	The plot is to produce a hard copy.
BUILD	The routine is to create a 'build' file.
AXES	Axes will be plotted.
ERASE	The screen will be erased before the plot.
LINES	The plot is not done as a histogram, but as a 'join the dots' line plot.

User variables - (">" input, "<" output)

(>) SOFT	Specifies the device and type to be used for soft plots. See the SOFT command for more details.
(>) HARD	Specifies the device and type to be used for hard plots. See the HARD command for more details.
(<) TVXST	is set to the starting x-value for the plot.
(<) TVXEN	Is set to the final x-value for the plot.
(<) TVHIGH	Is set to the same value as HIGH.
(<) TVLOW	Is set to the same value as LOW.
(<) TVFILE	Is set to the value of SPECTRUM.
(<) TVCOLOR	Is set to the GRPCKG code for the plot colour. (The TV.. variables are intended for use by cursor routines, and reflect the settings for the last plot made, even if XSTART etc are changed.)

(Other user variables may be set by the command processor, in connection with the parameter values.)

based on SPLOT: KS / CIT 30th Apr. 1984
-- rewritten for use as mplot: JKM / CIT 7th Oct. 1985

Parameter file for MPLOT Command

```
COMMAND MPLOT

      PARAMETER     SPECTRUM
           NAME     SP(ECTRUM)
           TYPE     FILE
        OPTIONS     INPUT
         PROMPT     "(SPectrum) Spectrum to be plotted"

      PARAMETER     HARDCOPY
           NAME     HA(RDCOPY)
           TYPE     KEY
         PROMPT     "(HArdcopy) Produce plot as a hard
                    copy?"

      PARAMETER     BUILD
           NAME     BU(ILD)
           TYPE     KEY
         PROMPT     "(BUild) Build plot in a disk file?"

      PARAMETER     WHOLE
           NAME     WH(OLE)
           TYPE     KEY
         PROMPT     "(WHole) Plot all of spectrum?"

      PARAMETER     AUTOSCALE
           NAME     AU(TOSCALE)
           TYPE     KEY
         PROMPT     "(AUtoscale) Scale so all of spectrum
                    fits?"

      PARAMETER     XSTART
           NAME     XS(TART)
           TYPE     FLOAT
         PROMPT     "(XStart) First X-value to be plotted"

      PARAMETER     XEND
           NAME     XE(ND)
           TYPE     FLOAT
         PROMPT     "(XEnd) Last X-value to be plotted"

      PARAMETER     HIGH
           NAME     HI(GH)
           TYPE     FLOAT
         PROMPT     "(HIgh) Maximum data value to be
                    plotted"

      PARAMETER     LOW
           NAME     LO(W)
           TYPE     FLOAT
         PROMPT     "(LOw) Minimum data value to be plotted"
```

```
PARAMETER     BIAS
     NAME     BI(AS)
     TYPE     FLOAT
   PROMPT     "(BIas) Bias value to be added to data"

PARAMETER     LABEL
     NAME     LAB(EL)
     TYPE     CHAR
   PROMPT     "(LABel) Label for plot"

PARAMETER     ERASE
     NAME     ER(ASE)
     TYPE     KEY
  OPTIONS     NOPROMPT
   PROMPT     "(ERase) Erase screen before plotting?

PARAMETER     AXES
     NAME     AX(ES)
     TYPE     KEY
  OPTIONS     NOPROMPT
   PROMPT     "(AXes) Plot and label axes?"

PARAMETER     LINES
     NAME     LIN(ES)
     TYPE     KEY
  OPTIONS     NOPROMPT
   PROMPT     "(LINes) Use a  line  plot  (not  a
              histogram)?"

PARAMETER     COLOUR
     NAME     COL(OUR)
     TYPE     CHAR
  OPTIONS     NOPROMPT
   PROMPT     "(COLour) Plot  colour (Bl, Wh, R, G, B,
              Cy, Ma, Y)"

PARAMETER     THICKNESS
     NAME     TH(ICKNESS)
     TYPE     INT
  OPTIONS     NOPROMPT
   PROMPT     "(THickness) Plotted line width"

PARAMETER     BFILE
     NAME     BF(ILE)
     TYPE     CHAR
  OPTIONS     NOPROMPT
   PROMPT     "(BFile) File to use to build the plot"
```